# Tool Condition Monitoring of Diamond-Coated Burrs with Acoustic Emission

Thomas Howard Jessel

**Cardiff University**
**School of Engineering**

**A thesis submitted for the degree of Doctor of Philosophy**

**September 2025**

# Abstract

Within manufacturing there is a growing need for autonomous Tool Condition Monitoring (TCM) systems, with the ability to predict tool wear and failure. This need is increased, when using specialised tools such as Diamond-Coated Burrs (DCBs), in which the random nature of the tool and inconsistent manufacturing methods, create large variance in tool life. This unpredictable nature leads to a large fraction of a DCB's life being underutilised, due to premature replacement, a significant concern considering the mass-manufacturing scale of DCB usage. To combat this widespread wastage, this thesis presents Acoustic Emission (AE) as an on-machine and indirect sensing technology, which through a range of processing and Machine Learning (ML) methods can monitor the wear state of DCBs.

A developed DCB wear test methodology, allowed the systematic wearing of a ⌀1.3 mm #1000 DCB, whilst acquiring continuous AE and direct tool wear measurements. Over this thesis, 22 wear tests were conducted with constant machining parameters. Therefore, enabling the identification of DCB wear mechanisms and phases, through monitoring DCB radial wear, and in turn quantifying the inherent variability of DCBs. Additionally, investigation into the effect of varying initial DCB runout levels, between $1-77\,\mu m$, identified a clear correlation between increased runout and variability in total life. These wear tests also allowed extracted AE features, from both the time and frequency domain, to be validated as useful indicators for both a DCB's Remaining Useful Life (RUL) and its grinding effectiveness. Frequency domain partial powers within the AE Power Spectral Density (PSD) were seen to align well with overall DCB wear, whilst $AE_{RMS}$ and $AE_{kurt}$ indicated a DCB's contact and runout.

With this knowledge, three TCM approaches were developed, each framing the problem differently. A threshold-based criterion method, using a transformation of selected AE features, to indicate a DCB's transition into its final phase of wear was developed.

Resulting in a computationally inexpensive and indirect warning system to indicate the decline of a DCB. Additionally, a regression and classification Artificial Neural Network (ANN), trained on the obtained TCM dataset, are able to predict a DCB's mean radius with a Root Mean Square Error (RMSE) = 1.407 µm, and a balanced accuracy of 0.938 when predicting the geometric tolerance of the ground workpiece. Both of which, providing valuable information to the operator about the state of grinding; enabling tool compensation or changes to occur with no measurement downtime. The completed work therefore, demonstrates the potential for developing an indirect TCM system to simultaneously reduce tool wastage, improve cycle times, and prevent unexpected tool failure.

# Acknowledgements

I would like to express my gratitude to the team of supervisors I have shared the last four years of Monday afternoons with; Prof. Rhys Pullin, Dr. Mark Eaton, and Dr. Carl Byrne thank you all for your advice, guidance, and laughter. Mark, thank you for your level-headedness, whether talking through technical points or assuring me that I'm on track. Carl, your plethora of anecdotes have been amazing, and I'm sorry for never knowing any of the references; from teaching me how to use a CNC machine, to highlighting my many grammatical errors, thank you. Rhys, I'm glad to say you can now leave early on a Monday. Your support has been unwavering, thank you for fostering a working environment which has made my time fly-by, and for always having the answer.

I am also indebted to the team at Renishaw who have supported my research endlessly. Whether it be trusting me to use a CNC milling machine, reviving prototypes or answering my never ending questions. Ben, Stu, Nathan, and the many others, thank you for enabling all of this work.

Next, I have to thank all the people of Cardiff University's school of engineering. All the technical staff, students and lecturers, who it has been great to get to know and better to work alongside with. Of course, it would be amiss not to mention the rotating sitcom cast of friends I have shared the CUSP lab with, thank you all for enabling my tea addiction and making the lab a brilliant place to be a part of.

Additionally, thank you to my friends and family, who have provided a needed balance during my PhD, forcing me to stop working. Finally, to Vicky, thank you for your belief and support, underpinning my entire studies, without which this thesis would have never of come together. Having you as my sounding board, even if you have no idea what I'm saying, has been a privilege.

# Contents

# List of Figures

# List of Tables

# List of Abbreviations

**A/D** Analogue to Digital

**AE** Acoustic Emission

**$Al_2O_3$** Aluminium Oxide

**ANN** Artificial Neural Network

**BiGRU** Bidirectional Gated Recurrent Network

**BiLSTM** Bidirectional LSTM

**cBN** Cubic Boron Nitride

**CCD** Charge Coupled Device

**CNC** Computer Numerical Control

**CNN** Convolutional Neural Network

**CNT** Carbon Nanotube

**CV** Cross-Validation

**DAQ** Data Acquisition

**DCB** Diamond-Coated Burr

**DIO** Digital Input/Ouput

**ELM** Extreme Learning Machine

**EOL** End Of Life

**FFT** Fast Fourier Transform

**FN** False Negative

**FP** False Positive

**HDT** Hit Definition Time

**HLT** Hit Lockout Time

**HMM** Hidden Markov Model

**JD** Jingdiao

**LDA** Linear Discriminant Analysis

**LSTM** Long Short-Term Memory

**MAE** Mean Absolute Error

**MCC** Matthews Correlation Coefficient

**ML** Machine Learning

**MLP** Multi-Layer Perceptron

**MLP-WIN** MLP with sliding window

**MSE** Mean Square Error

**NC4** Renishaw NC4+ Blue

**NI** National Instruments

**Ni** Nickel

**Ni-diamond** Nickel-diamond

**OMP600** Renishaw OMP600 spindle probe

**PCC** Pearson Correlation Coefficient

**PDT** Peak Definiition Time

**PLB** Pencil Lead Break

**PSD** Power Spectral Density

**PZT** Lead Zirconate Titanate

**$R^2$** coefficient of determination

**ReLU** Rectified Linear Unit

**RF** Random Forest

**RMSE** Root Mean Square Error

**RNN** Recurrent Neural Network

**ROC** Receiver Operating Characteristic

**RUL** Remaining Useful Life

**S/N** Signal to Noise ratio

**SEM** Scanning Electron Microscope

**SiC** Silicon Carbide

**STFT** Short Time Fourier Transform

**SVM** Support Vector Machine

**TCM** Tool Condition Monitoring

**TN** True Negative

**TP** True Positive

**WD** Wideband Differential

**WPT** Wavelet Packet Transform

# List of Symbols

$\phi$ activation function

$AE_{AMP}$ maximum amplitude of the AE signal

$AE_{kurt}$ kurtosis of the AE signal

$AE_{raw}$ raw AE signal

$AE_{RMS}$ root mean squared of the AE signal

$AE_{skew}$ skewness of the AE signal

$a_p$ axial depth of cut

$\boldsymbol{b}$ neuron bias vector

$\boldsymbol{c}$ LSTM long-term cell state

$n$ cutting speed

$F_1$ F1 score of a classification model

$F_{1\,macro}$ Macro F1 score of a classification model

$F_{1\,micro}$ Micro F1 score of a classification model

$F_{1\,weighted}$ Weighted macro F1 score of a classification model

$\boldsymbol{f}$ LSTM cell forget gate vector

$V_f$ feedrate

$r_{fe}$ form error from an NC4 2D scan

$G$ grinding ratio

$L$ grinding length

$\boldsymbol{h}$ LSTM short-term hidden state

$\boldsymbol{i}$ LSTM cell input gate vector

$k$ Number of data splits for a $k$-fold CV resampling method

$\boldsymbol{h}$ ANN layer output

$r_{mean}$ mean radius of NC4 2D scan

$n_{repeats}$ Number of repeats undertaken in a repeated $k$-fold CV resampling method

$\boldsymbol{o}$ LSTM cell output gate vector

$r_{peak}$ peak radius of NC4 2D scan

$PP$ partial power of the PSD

$a_e$ radial depth of cut

$r_{runout}$ runout from an NC4 2D scan

$\alpha$ offset angle

$\rho$ offset distance

$\tau$ tilt angle

$\phi$ location angle of the tilt angle

$\sigma$ logistic sigmoid function

$\mathbf{tanh}$ hyperbolic tangent function

$\tilde{\boldsymbol{c}}$ LSTM temporary cell state

$a_e'$ true radial depth of cut

$V_s$ volumetric wheel wear

$V_w$ volumetric workpiece removal

$V_{ref}$ reference voltage

$\boldsymbol{W}$ neuron weight matrix

$\boldsymbol{X}$ input data matrix

$\boldsymbol{x}$ single input data vector

$x_c$ x-coordinate of fitted circle

$\hat{\boldsymbol{y}}$ model output vector/predictions

$\boldsymbol{y}$ model target vector

$y_c$ y-coordinate of fitted circle

# 1 Introduction

The subject of this thesis is the Tool Condition Monitoring (TCM) of single-layer electroplated Diamond-Coated Burrs (DCBs), used in the manufacturing of ceramic and glass components. Acoustic Emission (AE) is investigated as a passive, indirect, and on-machine monitoring technique, from which a range of TCM approaches can be based upon. This chapter introduces the motivations behind the research, and its aim and objectives. Additionally, the novelty of the thesis and outline of the subsequent chapters are presented.

## 1.1 Motivation

Grinding is used extensively throughout manufacturing for a multitude of different applications. Utilising an abrasive wheel/tool, that when rotated at high speeds, removes material, often from difficult to machine workpiece materials, through a network of small cutting edges, made up of a large number of abrasive grains [1]. Grinding is typically used when one of three factors is required: high accuracy, high surface quality or the machining of hard materials [2]. Due to the increasing use cases of brittle ceramics within aerospace [3–5], electronic components [6, 7], and biomedical applications [8, 9], the grinding of hard materials has become steadily more important and widespread. As a finishing operation, grinding is an inherently expensive process, incurring between $60-95\,\%$ of the overall manufacturing costs, due to the significant machining time required while using specialist tooling [10]. Additionally, as the final step in the production chain, component damage occurring in this finishing operation is particularly expensive [11, 12]. Consequently, to combat the high expense associated with the increased prevalence of grinding, TCM

approaches are becoming more desirable and cost-effective within the manufacturing industry.

TCM systems aim to monitor and predict the wear state of machine tooling, to optimise their use and replacement strategies, and have been utilised for a range of applications, including lathe inserts [13, 14], milling cutters [15, 16] and abrasive tooling [17–19]. Within the broader manufacturing space, tool wear and failure are major concerns, impacting the machined surface's quality and geometric precision, as well as the overall process efficiency, with 20 % of a machine tool's downtime being attributed to tool failure [20]. This problem is further exacerbated when using small diameter mono-layer electroplated DCBs. Not only does the grinding behaviour of a DCB change throughout its life, due to the removal of diamond grains from its single abrasive layer, but the dressing of its grinding surface, to re-condition or remove runout, is not possible [21, 22]. Additionally, the stochastic nature of a DCB's electroplating fabrication method, causes the abrasive grain density, spacing, and protrusion all to vary across a DCB's surface [23]. Fig. 1.1 show Scanning Electron Microscope (SEM) images of an unused DCB in which the natural variation in grain distribution and protrusion can be observed. All of these factors combine to result in a grinding wheel that's life can vary significantly between tools of the same specification, which is further compounded when utilising DCBs with smaller diameters [24]. As a result of this, the tool replacement strategy for DCBs is often time-based and very conservative, opting in favour of wasting the Remaining Useful Life (RUL) of a DCB to prevent potential tool failure and workpiece damage.

To better inform TCM systems, methods of measuring a DCB's RUL, both directly and indirectly, are critical to enable the optimisation of a tool's usage, on an individual basis [25]. Ideally, the tool state would be monitored continuously, via a non-intrusive and indirect method, therefore not requiring stopping of the grinding process or removal of the DCB for measurements. Of all the indirect sensing methods, AE has long been the most promising and widely used technique for on-machine grinding process monitoring [26, 27]. Allowing developed TCM approaches to be inherently passive and actionable in real-time, due to AE resulting directly from material removal mechanisms during grinding

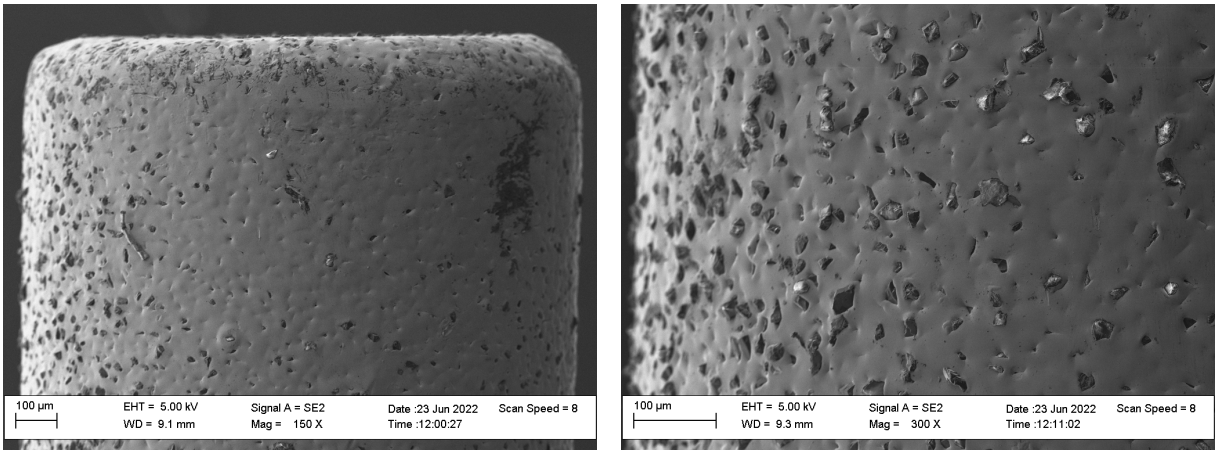


**(a)** 150X **(b)** 300X

**Fig. 1.1:** SEM images of an unused DCB at (a) 150X and (b) 300X magnification..

[28]. In addition, AE also maintains its high Signal to Noise ratio (S/N) and sensitivity, for small scale grinding operations, where other indirect methods are limited [29–31], because of its intrinsically high frequency range (>10 kHz) preventing background machine noise from dominating the acquired signals [32]. Consequently, AE has been utilised for the monitoring of a range of grinding specific applications; from the detection of grinding burn [33] to the identification of nano-scale deformation modes [34, 35]. Furthermore, with the advancements in Machine Learning (ML) techniques, data-driven approaches sufficiently complex to fully utilise the information available in AE, have made significant improvements to TCM systems [36, 37]. Therefore, this thesis investigates AE and ML approaches, for the TCM of DCBs.

## 1.2 Aim & Objectives

This thesis has the overarching aim of leveraging AE, as an indirect and on-machine sensing technology, to both monitor and predict the wear state of DCBs. Therefore, enabling the optimisation of existing tool replacement strategies, simultaneously reducing wastage, improving cycle times, and preventing unexpected tool failure. A series of objectives to enact this aim, are as follows:

- Review of current TCM approaches employed for grinding tools, utilising AE as a sensing technique.
- To develop a DCB wear test methodology that systematically induces tool wear through repeated grinding operations, while simultaneously acquiring AE data and direct measurements of both tool wear and workpiece condition.
- Gain an understanding of the DCB wear mechanisms, through the analysis of inspection data collected over multiple wear tests.
- Identification and validation of useful AE features, correlating to key tool wear metrics.
- Quantification and analysis of the variability in a DCB's setup and runout, and its impact on both tool wear and the resulting AE signals.
- Development and utilisation of a variety of TCM prediction approaches to make informed assessments of a DCB's wear state.

## 1.3 Thesis Novelty

The points of novelty for this thesis are as follows:

- Development of a fully autonomous DCB wear test methodology, capturing on-machine direct tool and workpiece measurements and indirect AE [38].
- Identification of macro wear mechanisms resulting in final DCB failure and a detailed understanding of the wear development [39, 40].
- Quantification of the effect runout has on a DCB's overall lifespan and wear mechanisms [41].
- The use of AE features to indirectly infer a DCB's wear state and runout level [41, 42].
- Validation of the inferred wear through a high number of direct tool measurements, generating a continuous representation of a DCB's RUL [38].
- Development of a visualisation technique, leveraging AE power over a single tool revolution, to quantify runout level and track wear [41, 43].

- Application of a regression Artificial Neural Network (ANN) on this specification of DCB [38].
- Use of direct geometric workpiece measurements to enable TCM to be framed as a classification problem [41, 43].

### 1.3.1 List of Publications

As of Feburary 2026 aspects of this work have been published as follows:

#### Journal Publications

[38] T. Jessel, C. Byrne, M. Eaton, B. Merrifield, S. Harris, and R. Pullin, 'Tool condition monitoring of diamond-coated burrs with acoustic emission utilising machine learning methods', *Int J Adv Manuf Technol*, vol. 130, no. 3, pp. 1107–1124, Jan. 2024, doi: 10.1007/s00170-023-12700-7.

[39] T. Jessel, C. Byrne, M. J. Eaton, and R. Pullin, 'The capability of Acoustic Emission features to monitor diamond-coated burr grinding wear and effectiveness', *e-Journal of Nondestructive Testing*, vol. 29, no. 10, Art. no. 10, Oct. 2024, doi: 10.58286/30231.

[41] T. Jessel, C. Byrne, M. Eaton, and R. Pullin, 'Monitoring the effect of runout on a Diamond-Coated Burrs' wear progression with Acoustic Emission', *Wear*, vol. 584-585, Jan. 2026, doi: 10.1016/j.wear.2025.206420.

[42] T. Jessel, C. Byrne, M. Eaton, and R. Pullin, 'Predicting the wear state of diamond-coated burrs, using acoustic emission features and machine learning techniques', *Procedia CIRP* [Accepted, Pending Publication].

#### Conference Publications

[44] T. Jessel, C. Byrne, M. Eaton, and R. Pullin, 'Utilising Machine Learning for Tool Condition Monitoring of Diamond-Coated Burrs with Acoustic Emission', presented

at the BSSM 17th International Conference on Advances in Experimental Mechanics, Glasgow, UK, Aug. 31, 2023.

[40] T. Jessel, 'The monitoring of diamond-coated burrs with acoustic emission techniques', presented at the CIRP UK Meeting, Cardiff, UK, May 23, 2024.

[43] T. Jessel, 'A machine learning approach to tool state classification utilising in-process acoustic emission features', presented at the 65th Acoustic Emission Working Group (AEWG) Meeting, Chicago, USA, May 14, 2025.

## 1.4 Thesis Organisation

This thesis comprises seven chapters, inclusive of this introduction, a brief summary of each chapter is listed below:

- **Chapter 1** is an introduction to the thesis, detailing the motivations for this research, the aim and objectives of the thesis, and the novelty achieved during its course.
- **Chapter 2** details the theory behind DCB wear mechanisms, as well as their manufacture and usage. Followed by a review of the current state of AE based TCM approaches and ML methods for wear state predictions.
- **Chapter 3** sets out a methodology to systematically wear a DCB, whilst acquiring indirect AE, for sensing, and direct tool and workpiece measurements, for validation, to produce a TCM dataset.
- **Chapter 4** presents the analysis of the acquired TCM dataset. Developing an understanding of the mechanisms and influencing factors of a DCB's wear, whilst also introducing a range of AE features as indicators of a DCB's wear state.
- **Chapter 5** further builds upon the analysis of Chapter 4, to utilise three different TCM approaches, enabling the monitoring of DCB wear to aid tool replacement strategies.
- **Chapter 6** discusses the findings of the thesis, summarising both the outcomes and limitations of the research.

- **Chapter 7** concludes the thesis, encapsulating the final state of work and outlining future avenues for continuation.

# 2 Literature Review & Theory

Chapter 1 presents the motivations and objectives of this research, leading the following chapter to detail the relevant background information and prior literature on the subject. The first section of which details the manufacture, usage, and wear mechanisms of DCBs, followed by a section covering the fundamentals of AE monitoring. Finally, a review of existing TCM approaches for grinding processes is presented, outlining the key techniques and limitations of the current research area.

## 2.1 Diamond-Coated Burrs

In order to investigate the wear of DCBs, an understanding of their composition, manufacturing, wear mechanisms and use cases is first required. This work defines a DCB as a mono-layer diamond grinding wheel that uses an electroplated Nickel (Ni) bond layer to hold abrasive diamond grains onto a steel shank mechanically. Fig. 2.1 shows a selection of electroplated superabrasive grinding wheels, with tools of varying grain sizes and tool profiles.


**Fig. 2.1:** A selection of electroplated superabrasive grinding wheels. Reprinted from [45].

### 2.1.1 DCB Composition & Manufacture

Grinding wheels are characterised by two key properties: their abrasive grain and bond method. Unlike most commonly used grinding wheels (conventional) with Silicon Carbide (SiC) or Aluminium Oxide ($Al_2O_3$) abrasive grains, DCBs are a superabrasive wheels utilising diamond abrasive grains. Superabrasive wheels, whilst being more expensive than conventional wheels, offer distinct advantages as a result of their superior hardness. The grinding of otherwise impossible workpiece materials and the significantly reduced wear, have made superabrasive wheels commonplace [22]. The diamond grains utilised by DCBs allow for the grinding of engineering ceramics and glass, but being a form of carbon, are ill-suited for grinding steels.

DCBs are manufactured with a single layer of abrasive grains held onto a steel shank with a metal bond. Desired wheel forms can therefore be machined into the steel shank prior to coating, allowing for complex and cost-effective form grinding tools at a vast range of sizes [46]. Fig. 2.2a shows a diagram of a DCB's axial cross-section, with Fig. 2.2b showing the radial cross-section of an unused ⌀1.3 mm #1000 DCB through an optical microscope. Metal-bonded mono-layer wheels are manufactured through two processes,

brazing and electroplating. Brazing creates a strong chemical bond between the grain and tool shank, allowing for greater grain exposure than electroplating methods. However, the required high temperature (up to 1000 °C) for brazing leads to weakened grains and the potential for distorted steel tool shanks [2]. Electroplating is widely adopted across the manufacturing industry due to the reduced production costs whilst still maintaining high quality and dimensional precision [47].

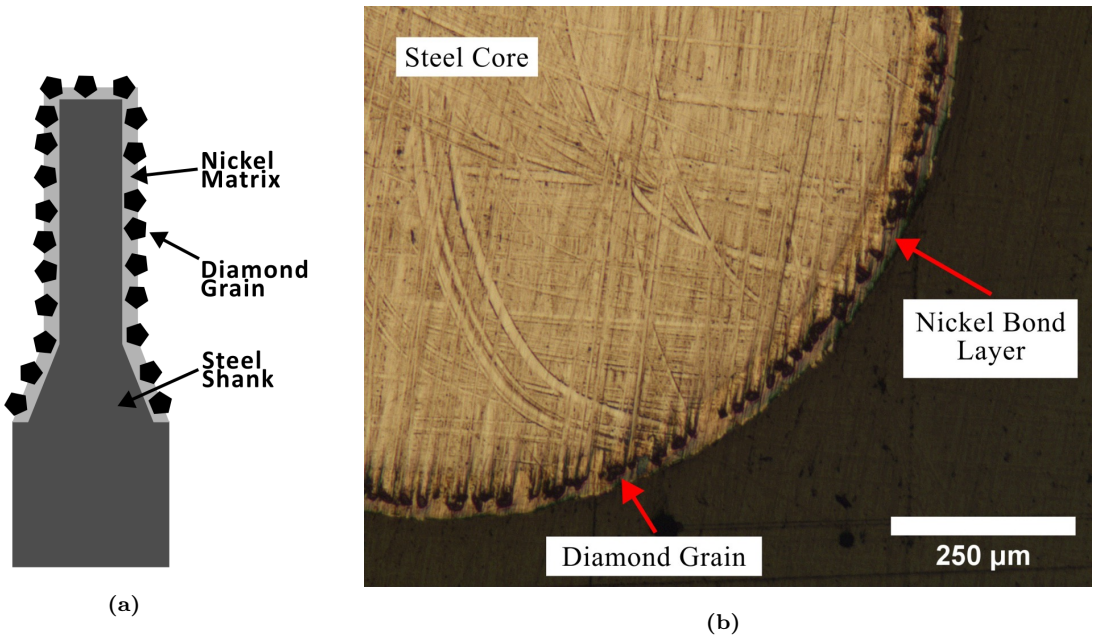


**Fig. 2.2:** DCB cross-section visualisation (a) axial diagram and (b) optical microscope image of an unused ⌀1.3 mm #1000 DCB having been radially sectioned.

Electroplated wheels utilise composite electrodeposition to mechanically hold diamond grains within a Ni bond matrix. Nickel is used for its wettability with diamond, an important factor for obtaining good layer adhesion onto the cathode (steel shank) [48]. To enable this, a Watts bath is used first to deposit a thin layer of Ni onto the tool shank before the Nickel-diamond (Ni-diamond) co-deposition [49]. The addition of diamonds into the Watts bath then allows diamonds to adsorb positive Ni ions, which, along with mechanical stirring, transports the grains onto the cathodic tool shank. Once adhered onto the tool shank, diamond grains are further coated in Ni engulfing the abrasive grains [50, 51]. This electroplating process occurs at <100 °C, resulting in a mechanical bond

covering between 30 – 50 % of the grain height to obtain the required bond strength [2, 48].

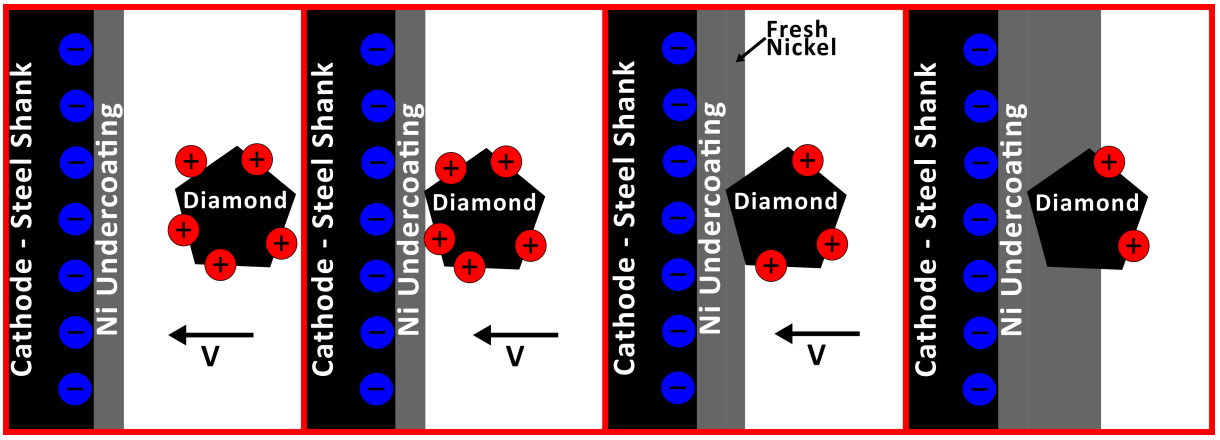


**Fig. 2.3:** Schematic of Ni-Diamond electroplating process. Adapted from [51].

Multiple factors affect the manufacturing quality of DCBs. From the start, the steel tool shank must be machined to a high quality; inaccuracy at this stage can lead to an imbalanced wheel as a result of runout and incorrect grinding profiles [52]. Additionally, the size of the abrasive layer must be taken into account when machining the shanks to form. The Ni-undercoating layer is also crucial in preventing the delamination of the Ni-diamond layer, and providing adequate material to absorb the grinding forces. Huang *et al.* [47] showed the effect of increasing Ni-undercoating layer thickness through the manufacture and wearing of DCBs with 150 µm average grain size and varying Ni-undercoating layer thickness, between 30 – 150 µm. The authors found an increase in workpiece removal of four times between tools manufactured at the extremes of the undercoating range.

Another factor affecting a DCB's performance is the distribution of abrasive grains around the tool's circumference and through the Ni-diamond layer's thickness. DCBs are prone to defects as a result of the plating process, particularly due to their small diameter, leading to regions of missing plating, varying grain concentration, high spots, and thin coating. To limit these defects and improve form accuracy, the abrasive grains for electroplated wheels are often resized to obtain a smaller distribution of grain sizes [48, 53]. However, the plating process itself is still the dominant factor in these defects

and still remains a challenge to uniformly disperse particles within a matrix [54]. Multiple authors [49–51, 55] have identified the stirring rate of the Watts bath as a key parameter to optimise plating for any given DCB specification. Unlike other bath parameters, e.g. temperature, current density, pH, and grain concentration, stirring rate has a distinct optimal value. Stirring is critical in transporting diamond grains towards the cathodic steel shank within the plating bath. Insufficient stirring can lead to a low amount of particles reaching the tool shank, particularly when using diamond grains above 100 µm. However, excessive stirring can result in the grains accelerating beyond a velocity that overcomes the initial adhesion when plating [51]. Additionally, achieving a uniform current density around the tool's geometry is particularly difficult. A thicker Ni layer is deposited in areas of higher current density, and as such, improper distancing/sizing of the anode can lead to variations in layer thickness. Furthermore, the "edge effect" leads to higher plating thickness around protruding edges or corners, requiring complex forms to be carefully considered [48].

But potentially the most important factor in determining a DCB's total useful life is the wear resistance of the Ni bond matrix. Electroplated wheels only mechanically hold onto abrasive grains, meaning wear of the bond matrix leads to accelerated failure through grain pullout [56, 57]. Improving the Ni bond layer's residual stress, hardness, and ductility all play a role in its wear resistance an as a result have become an active area of research. The bond layer's properties can be modified through the plating bath chemistry yielding small benefits, increases in both pH and chloride concentration within the Watts bath increase the hardness of the plated layer [58]. The addition of cobalt ions ($Co^{2+}$) were found to aid particle co-deposition and reduces agglomeration in Ni-diamond plating [59], which improves both the mechanical and tribological properties of the matrix. Both Wang *et al.* [60] and Pushpavanam *et al.* [61] found large increases in micro-hardness and wear resistance with the inclusion of $Co^{2+}$ in Ni-diamond coatings, owing the improvements to a better distribution of diamond particles through the matrix. Ni-boron alloy coatings have also been investigated as a superior surface coating to both nickel and chromium [62]. Along with the increased hardness associated with addition

of boron to the Ni, the effect of annealing to reduce residual stress within the composite layer has shown improved ductility in nanoindentation testing [63]. Huang *et al.* [49, 64] utilised this Ni-boron alloy as the bond metal within DCBs to investigate its effect on grinding performance and overall life. A range of DCBs with differing concentrations of boron were manufactured, resulting in an increase in the abrasive layer's hardness by 650 Hv with the inclusion of $8\,\mathrm{g\,L^{-1}}$ trimethylamine borane within the Watts bath. Following this, each DCB was used to grind slots in an $Al_2O_3$ ceramic plate until failure, the addition of boron led to the doubling of the total grinding length prior to failure. Additionally, a series of Ni-boron DCBs were annealed at 300, 400 and 500 °C for 30 min and then followed the same evaluation process. Annealing was seen to further increase the total useful life of each DCB, increasing the grinding length from 110 mm for an as-plated Ni-boron DCB to 1375 mm for one annealed at 500 °C. Suzuki and Konno [65] utilised Carbon Nanotubes (CNTs) within the Ni bond layer to improve the grain bonding strength. In which, a Ni-CNT composite layer (15 µm) was plated on top of an existing Ni-diamond layer (15 µm) to embed 50 µm diamond grains onto a ⌀3 mm DCB. A side-milling operation on white plate glass was used to assess the improvement in grain strength via in-process force measurements. Results showed an increase in tool life of approximately eight times compared with normal Ni-diamond DCBs, additionally the maximum normal force increased by 1.3 time prior to failure of the Ni-CNT DCBs. Suggesting a significant improvement in grain bond strength through the addition of CNTs.

### 2.1.2 Grinding Wear Mechanisms

Wear has many effects on the grinding process, most of which are detrimental and hard to control, therefore it is important to understand the contributing mechanisms of grinding wheel wear. Grinding wheel wear is the loss of tool volume, and is the cumulative result of many interactions between abrasive grains and the workpiece material [21]. A variety of mechanisms lead to wheel wear depending on the grain geometry, grinding forces and temperature as a result of the programmed grinding pass [66]. Both the abrasive grains and bond matrix undergo wear simultaneously, leading to macro and micro scale

changes of the wheel geometry and grinding effectiveness. The macroscopic wear of a grinding wheel is associated with geometric errors to its form, either through decreasing grain protrusion, profile deviation or roundness deviation. Microscopic wear concerns the abrasive grains and impacts the grinding output, i.e. grinding forces, workpiece surface roughness and thermal damage [21]. The microscopic wear mechanisms that cumulate into macro wear can be divided into two categories: attritious and fracture wear.

Attritious wear results in the dulling or flattening of abrasive grains, occurring from the interaction between grinding wheel and workpiece material at the atomic scale [67]. Grain flattening occurs as a complex interaction of mechanical, chemical, and temperature factors. A grain's hardness determines its resistance to frictional wear and plastic deformation as a result of mechanical factors. The chemical reactions are intensified at this scale as the newly cut surfaces are highly reactive, which when coupled with the high localised temperatures due to friction, enable superabrasive grains to experience attritious wear that would not through solely mechanical factors. One such instance of this is the graphitisation of diamond at high temperatures (>700 °C), leading to a reduction in grain hardness, enabling the attritious wear to occur [21]. Fig. 2.4 shows the resulting wear flats on abrasive grains from attritious wear.

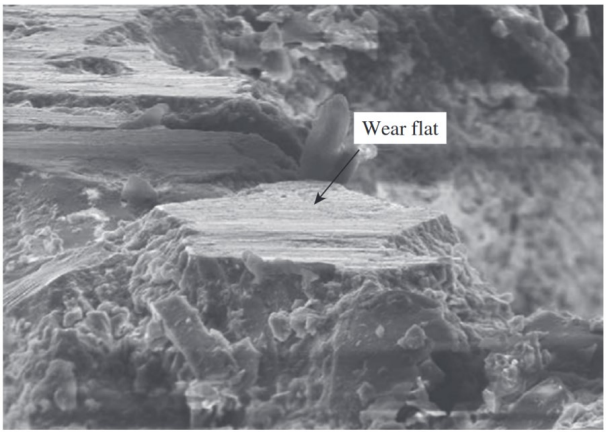


**Fig. 2.4:** 700 X magnification SEM image of a wear flat on the grains of a grinding wheel. Reprinted from [68].

With proper grain selection for a given application, attritious wear arises as a result

of frictional effects from low grinding forces on individual grains [66]. Wear flats produced by attritious wear lead to the progressive loss of grain form, lowering the cutting ability of the grinding wheel and generating further frictional heating. A by-product of this is the increase in grinding force with increasing wear flat area [69], inciting grain or bond fracture mechanisms. If fracture does not occur to re-sharpen the wheel, attritious wear will continuously increase the contact area between grain and workpiece, which in turn can cause total failure of the tool or damage to the workpiece.

As the grinding force per grain increases, the wear mechanism moves from attritious wear into fracture wear [21]. Fracture wear concerns the removal of abrasive grain volume through fracturing within the grain or bond matrix. Grain fracture exposes new sharp edges on the abrasive grains, allowing the wheel to self-sharpen. This self-sharpening effect reduces the grinding forces and temperatures, enabling a regulation of the effects of grain flattening. The extent of grain fracture is dependent on both the grain itself, the magnitude of forces, and the grinding environment. Under ideal conditions, micro-fracturing of the grain takes place instead of macro-fracture, achieving the same self-sharpening with minimal abrasive volume loss [67]. Fig. 2.5 shows SEM of both micro and macro-fractures in abrasive grains.

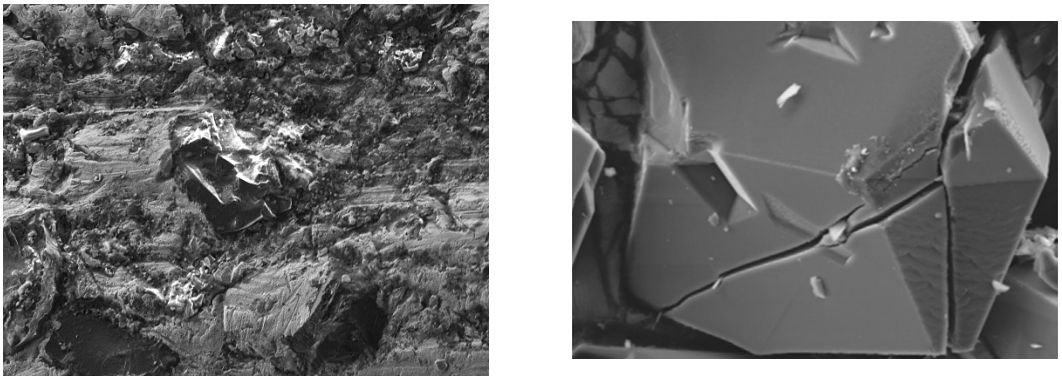

**(a)** Grain micro-fracture.

**(b)** Grain macro-fracture.

**Fig. 2.5:** SEM images of grain micro and macro fractures. Reprinted from [66].

On top of the fracturing of abrasive grains, the bond material is subject to fracture also. If the grain has a fracture toughness much greater relative to the holding strength of the bond matrix, or the force per grain is exceptionally high, the DCB can experience

grain pull-out through fracture of the bond material. Abrasion wear of the bond also occurs, which is necessary to maintain the required grain protrusion for grain penetration, however if excessive protrusion arises grain pull-out can emerge [70]. The space between grains, chip pockets and grain protrusion can all affect the level of bond wear that occurs.

In addition to attrition and fracture, adhesive wear also occurs, whereby the workpiece material has bonded to the wheel surface. This can occur due to chemical adhesion or surface deformation at high temperatures [2]. Whilst it is not wear, in the sense of reduction in radius or profile, it prevents grains from cutting into the workpiece as effectively. Some metals such as aluminium and titanium are highly prone to adhesion and can even be redeposited back onto the workpiece. Adhesive wear creates a very poor surface finish on the workpiece and greatly increases grinding forces and temperatures. However, it can normally be avoided or reduced with adequate cooling and proper selection of wheel materials [68].

As a result of the stochastic nature of grinding and the cumulative effect of wear, macroscopic wear is never the result of a sole mechanism but rather a mixture. However, there is a distinct effect of grinding parameters on the prevalence of individual wear mechanisms. Additionally, there are favourable wear mechanisms, the grinding ratio ($G$) evaluates a grinding wheel's material removal effectiveness as the volumetric ratio of workpiece material removal ($V_w$) to wheel wear ($V_s$).

$$G = V_w/V_s \tag{2.1}$$

Fig. 2.6 shows the effect of grinding parameters on inciting different wear mechanisms, and how favourable each mechanism is through the grinding ratio. For grinding stability, there must be a balance between abrasive grain wear and bond wear. If bond wear is significantly larger than abrasive wear, radial wear of the tool is drastically increased, leading to geometrical inaccuracies. But if abrasive wear is larger than bond wear, then grain protrusion increases alongside the grinding forces and temperatures, leading to grain pull-out. Therefore, the ideal cycle of a wheel's wear is a small amount of attritious

wear limited by the self-sharpening of grain micro-fracture. As such, the correct selection of grinding parameters is paramount for a DCB to work effectively, as it only contains a single layer of abrasive grains [71].

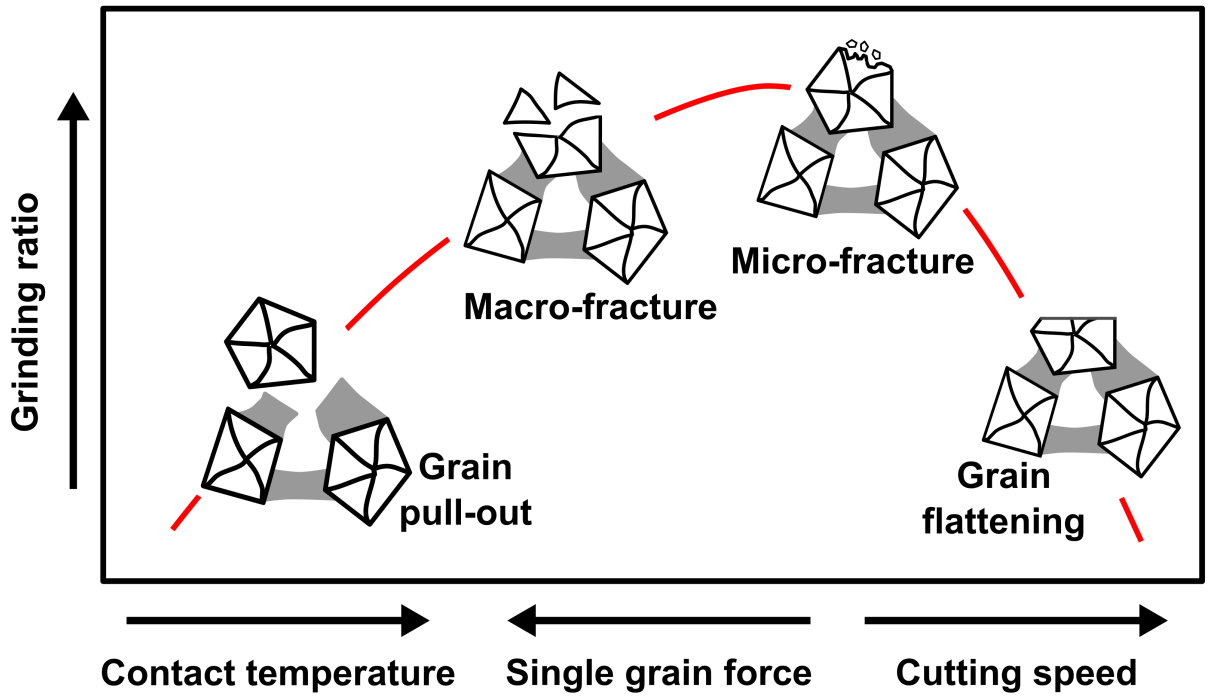


**Fig. 2.6:** Grinding wheel wear mechanism depending on grinding parameters. Adapted from [21].

### 2.1.3 Wear Cycle

Dressing is typically carried out to prepare a grinding wheel for grinding by removing a small amount of material from the wheel's surface. For conventional wheels, dressing is a crucial step to obtain optimum performance and meet workpiece tolerances [2]. Performed both prior to grinding and on a periodic basis for a variety of purposes [72]:

- **Truing**: To remedy deviations of wheel form, straightness or concentricity
- **Sharpening**: To produce a sharp cutting surface
- **Conditioning**: To remove superfluous bond material

- **Cleaning**: To remove adhered material from a loaded wheel

DCBs as electroplated mono-layer tools, are not typically dressed to preserve the limited number of grains present on the wheel. This lack of dressing is seen as an advantage to the overall process efficiency, removing the need for additional dressing equipment and the downtime associated with dressing. However, a consequence of not being able to dress DCBs, is the inability to correct for the changing behaviour due to their wear [2]. Variation in grinding forces/power, radial wheel wear rate, and workpiece roughness all follow a three-phase cycle, similarly to single-point metal cutting tools, even when operating within the ideal grinding parameters [73, 74]. Fig. 2.7 shows this characteristic three-phase cycle of tool wear, plotting a tool's $V_s$ against $V_w$.

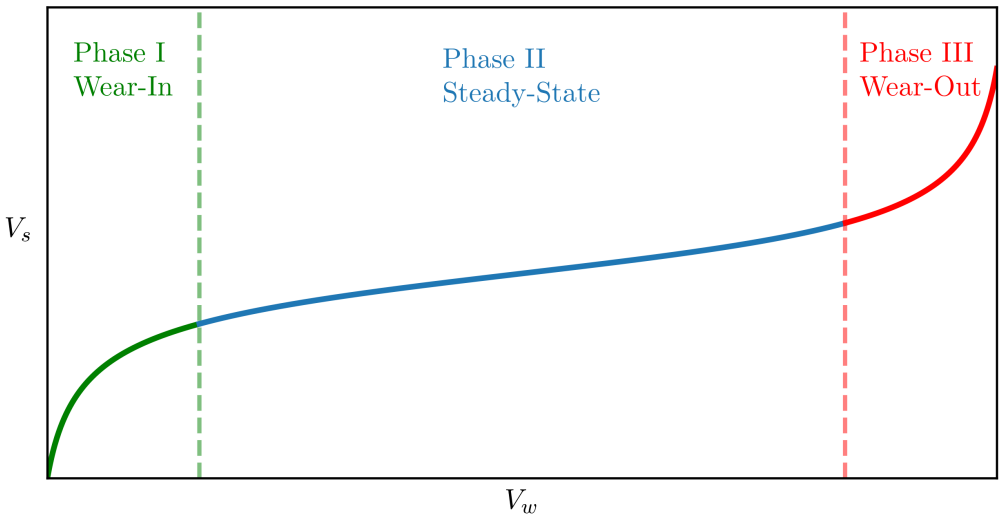


**Fig. 2.7:** Typical wear curve for material removal tools.

Initially, a period of accelerated wear occurs as the wheel undergoes phase I - "Wear-In", during which weakly adhered grains are quickly removed along with any superfluous Ni bond material [75, 76]. Shi and Malkin [71] estimated that 60 – 80 % of the wheel wear associated with the initial transient phase is the result of grain pull-out, with the remaining wear being grain or bond fracture. The wheel wear then slows and stabilises through grain flattening and fracture, leading into phase II - "Steady-State". This phase lasts the majority of the DCB's life, resulting in good grinding output, and is crucial

in effectively utilising a mono-layer wheel [74]. Finally, once the DCB has reached it's End Of Life (EOL), failure occurs through either wheel-burn or the complete stripping of the abrasive layer, phase III - "Wear-Out" [52]. Identifying this last phase is critical, for traditional wheels, as this point signifies the need for re-dressing, for DCBs this normally results in damage or failure of the tool's steel core. A DCB can be re-plated for reuse multiple times, provided grinding is stopped prior to reaching EOL [48, 77].

### 2.1.4 DCB Usage & Limitations

DCBs are used for a range of grinding operations due to their changeable form and small diameter. A by-product of both their use at small scales, commonly employing DCBs with a diameter of $<5\,\text{mm}$, and mono-layer composition is the relatively low number of grains present on a DCB's surface, resulting in inconsistent wear rates and difficult to predict failure points [71]. As previously discussed, electroplated wheels are not commonly dressed to preserve the single abrasive layer [72], which gives rise to both advantages and disadvantages. The removed requirement of dressing dramatically increases the usability of DCBs, enabling them to be used in non-grinding specific machine tools and dramatically reducing the associated costs and downtime required for the dressing of traditional grinding wheels [2, 78]. A consequence of this, however, is the inability to correct the grinding tool's form, minimise runout or condition the surface to remove excess bond material and workpiece build-up [72].

A tool's runout describes the error between its geometric centre and its rotational centre. The runout of a tool is the summation of multiple sources of deviation between the tool, tool-holder and machine spindle. As a result, the final state of runout can be described completely by two terms, axial offset and tilt. Axial offset describes the tool's translation by an offset distance ($\rho$) applied at an offset angle ($\alpha$), and the axial tilt term describes the tool's rotation by an tilt angle ($\tau$) applied at an location angle of the tilt angle ($\phi$). Fig. 2.8 shows how each runout term transforms a tool's rotational axis. Attanasio [79] provides a comprehensive overview of the quantification of runout for

small-scale tooling.

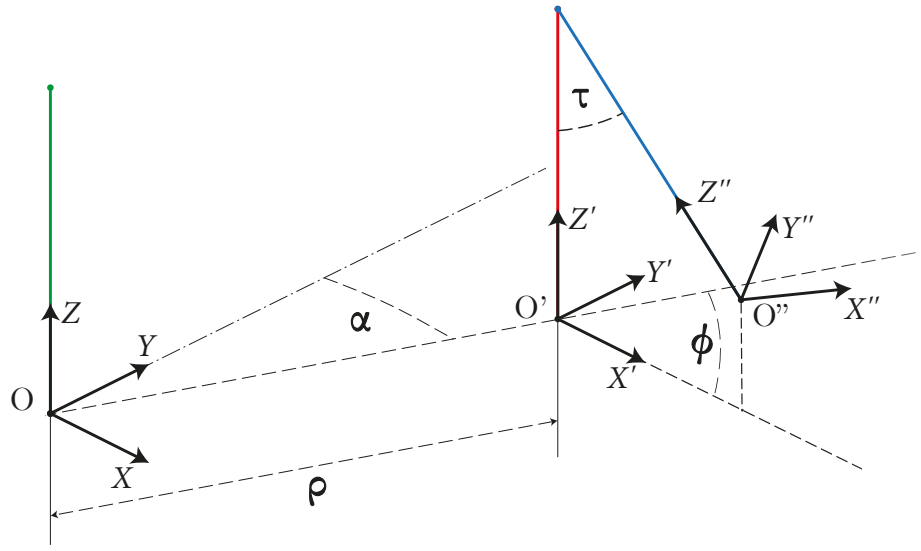


**Fig. 2.8:** Tool axis runout and its terms. Adapted from [79, 80].

Common causes of runout include incorrect clamping of the tool within its tool-holder, inaccuracy during tooling manufacture, and poor mating of the tapered contacts [80, 81]. In addition, electroplated tools experience another source of runout originating from the plating process, allowing a non-uniform distribution of the abrasive layer around the circumference of the tool [55]. The runout of grinding wheels as with all tooling should be minimised, when unmanaged runout can lead to uneven wear around a tool's circumference, poor surface quality as a result of chatter, and in extreme cases complete wheel failure due to uneven stress distributions [79, 82]. These adverse effects are more prevalent as the size of the tool decreases, especially as the runout can be larger than the programmed radial depth of cut for a given grinding pass [79, 83]. An aspect of this work is the variation and measurement of runout for small diameter grinding wheels, to determine its effect on a tool's overall useable life.

To investigate the effect of runout on any tool, its level must first be set and measured prior to verifying its impact on tool wear or workpiece quality. Badger *et al.* [82] added runout back to a dressed large diameter vitrified-bond grinding wheel by remounting the wheel on the machine spindle. Through dial indicator measurements around the

tool's circumference, an increase in runout from 0 µm to 81 µm was introduced. This method allowed for runout to be investigated via a realistic scenario without any additional equipment, however this limited the author's ability to set a specific value of runout. Grinding forces indicated significant wheel chatter and periodic burn marks were seen on the workpiece, a result of the induced runout. Additionally, the authors reported an increase in wheel wear of 60 % for a highly eccentric grinding wheel. To further develop this methodology, Diez *et al.* [81] used an adjustable boring head to experimentally simulate the effect of runout on a ⌀12 mm fluted end mill. This allowed the authors to vary the tool's runout continuously between 0 – 40 µm, verifying the effect of runout across the feasible range. A dial indicator was utilised to measure the true runout level of the tool between its cutting edges prior to conducting milling operations, during which the cutting forces were measured to validate simulated results. Similarly to the measurement of micro-milling tools, runout should not be measured at the tool's shank, as there is a machined taper down to the working diameter which can introduce an additional source of runout [84]. Therefore, measurement of runout for DCBs should be conducted over the grinding surface, to avoid errors from the runout introduced through the taper and electroplating process.

### 2.1.5 Measurement Techniques

Since grinding wheel wear has a major impact on the ground workpiece, compromising dimensional accuracy and surface quality, TCM is essential to reversing the changing wheel topology. A multitude of measurement techniques have been used for TCM approaches, classified through their operation method: direct and indirect measurements. Direct methods utilise optical or physical means to obtain measurement values directly, whereas indirect methods make inferences based on other signals correlating to the wear. The use of cameras, laser beams, radioactive isotopes, electrical resistance and contact probes all enable the direct measurement of grinding wheels. Due to their nature, direct measurements provide unparalleled accuracy across a range of conditions, and often act as ground truth for other TCM approaches to be validated against [85]. Si *et al.* [86]

utilised a laser displacement sensor to directly quantify the radial wheel wear of a white corundum grinding wheel after every grinding cycle, which enabled the authors to develop a regression model based on radial wheel wear.

However, these direct methods are expensive and difficult to apply effectively within any machining environment [87]. Contact methods are at risk of wear when measuring abrasive tooling, and coolant usage can have a severe impact on vision and laser based systems. As such, direct measurements are often conducted off-line or during breaks in the process, impacting production efficiency. Lee *et al.* [88] utilised a Charge Coupled Device (CCD) camera to image an electroplated Cubic Boron Nitride (cBN) point grinding tool after every $10^{\text{th}}$ grinding pass during a wear test. Image capture was conducted off-line on a separate image capture station, using a rotary chuck, CCD sensor and light source. Statistical features of the images were then used to train three different ML regression models, to predict the number of passes a wheel had completed. Leading to coefficient of determination ($R^2$) scores of greater than 0.92 for each architecture. To combat the usability issues of the work, Lee *et al.* [89] then presented a methodology allowing real-time image capture with a linear CCD sensor, through which a similar post-processing technique could be applied in the future. However, given the high operating costs of precision grinding, factors that slow down production should be minimised.

To combat these drawbacks, indirect measurements sacrifice raw precision for the ability of real-time and on-machine monitoring, presenting a more practical sensing solution [90]. Furthermore, indirect sensing encompasses the effect of the whole grinding zone, in contrast to the random sampling of direct measurements [91]. A number of external factors affect the ability of indirect sensors, and as such validation of their use across a broad range of scenarios is critical to ensure consistent outputs [25]. A host of sensors have been utilised for indirect measurement of tool wear, commonly researched approaches include cutting forces [92–94], motor power/current [95–97], vibration [30, 98], audible acoustics [99], temperature [100] and AE [101–103]. Fig. 2.9 shows a comparison in usage between the main sensing methods within abrasive machining processes [91].

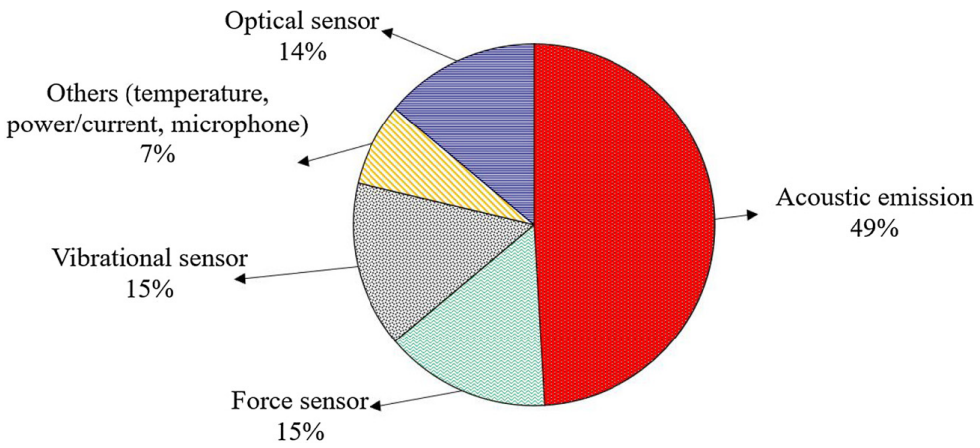


**Fig. 2.9:** Proportion of abrasive processes utilising sensors for monitoring approaches. Reprinted from [91].

Traditionally, cutting force and vibration sensors have both been heavily used for research in monitoring of turning and milling processes [25]. However, when applied to grinding operations, these techniques lose sensitivity to the higher frequency range which are associated with material removal on this submicrometre scale, see Fig. 2.10. By comparison, the S/N of AE improves at the micro-scale, whereby the high frequency nature of AE dominates the lower frequency noise [26]. Because of this, AE is the most frequently used sensing method for the monitoring of abrasive processes because of its sensitivity compared to other indirect methods. Leading to it having been used to monitor grinding wheel chatter, contact detection, dressing, burn, cutting modes and recently wheel wear [104, 105].

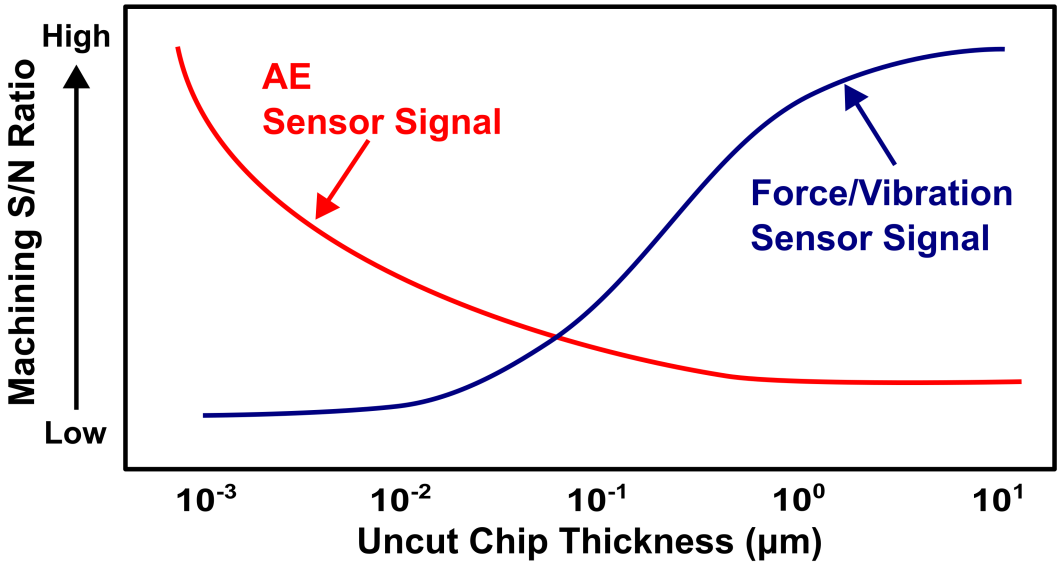


**Fig. 2.10:** S/N characteristics of AE vs. force and vibration sensors at different uncut chip thickness. Adapted from [26].

## 2.2 Acoustic Emission

Of the indirect monitoring methods, AE has become one of the most promising and widely used methods for grinding process monitoring [27]. The AE technique utilises the phenomenon in which as a material experiences damage, energy is released spontaneously in the form of elastic stress waves. Within grinding, a large range of mechanisms can generate these stress waves, deemed AE sources [105]. These high frequency elastic waves are monitored and recorded to form the basis of AE monitoring. This section covers the fundamentals of AE, its acquisition from grinding sources, and a brief overview of signal processing approaches for the extraction of AE features.

### 2.2.1 AE Fundamentals

AE pertains to the transient elastic stress waves generated by the energetic micro-structural changes of a material. Localised sources produce waves in the ultrasonic range,

>20 kHz, that propagate throughout the material, resulting in tiny surface displacements on the material surface. A range of AE sources occur during the grinding process, including but not limited to material deformation, friction, phase transitions, crack formation and propagation, and thermally induced changes [106]. Which are then recorded and leveraged for monitoring or source location through a variety of signal processing techniques. AE presents as either "burst" or "continuous" signals, examples of which are shown in Fig. 2.11. Most AE sources generate "burst" AE, in which there is a sharp increase in energy followed by a damped oscillating decay. "Continuous" AE signals, on the other hand, maintain their amplitude over much longer durations, often times as a result of the superposition of many individual "burst" signals.

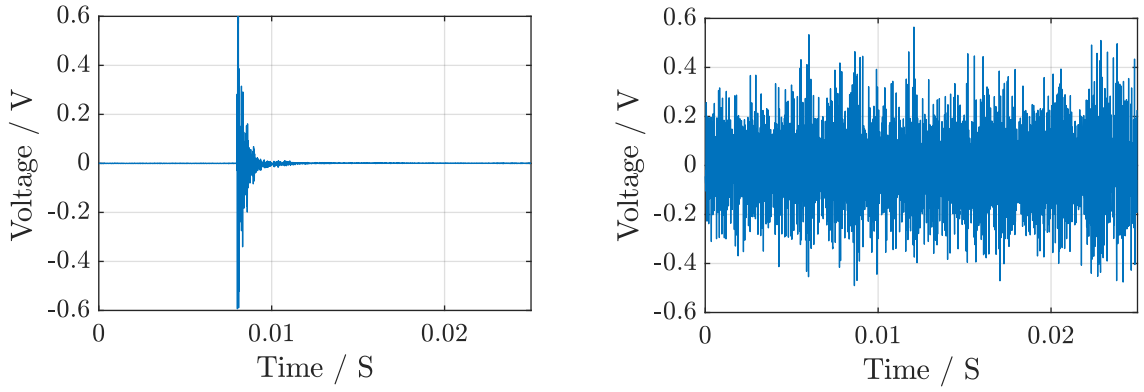


**(a)** Burst AE

**(b)** Continuous AE

**Fig. 2.11:** Example AE signals: (a) burst and (b) continuous.

AE generated from outside the grinding material removal mechanisms is deemed AE noise, stemming from machinery or electricity, is typically a concern impacting the monitoring capabilities of any system [107]. The main advantage of AE as a sensing method for precision machining is the high frequency range of the generated signals, markedly higher than the range of detrimental noise, minimising the impact on the acquired AE [72, 108]. The pseudo-continuous nature of grinding, compounded by the AE noise, make the identification of source mechanisms for individual AE bursts very difficult [109].

Unlike most other sensing methods, AE can be generated by very small interactions between the tool and workpiece. Lee [28] was able to identify changes between brittle and

ductile regimes in an atomic force microscope based nano-machining operation with traditional AE analysis techniques utilising both AE time and frequency domain features. A series of single grain cBN scratch tests, with increasingly dulled grains, allowed Yiming *et al.* [34] to compare a grain's sharpness through the energy within certain frequency ranges. AE energy within the $0-90\,\text{kHz}$ frequency band was found to increase as the grain dulled, with the authors' theorising this was due to increased frictional contact. Pandiyan and Tjahjowidodo [18] identified changing material removal mechanisms (rubbing, ploughing, and cutting) of a single aluminium oxide abrasive grain during a series of scratch tests, from the Short Time Fourier Transform (STFT) of acquired continuous AE. With the mode of material removal, validated through 3-Dimensional profliometry of each scratch.

Overall, AE is a non-destructive sensing method that occurs directly due to material removal mechanisms or microstructural changes from loading. Its passive nature, in which the elastic wave is formed through a small proportion of the overall interaction energy, allows monitoring in real-time. Additionally, the high frequency content of AE generated at the micro-scale creates a natural barrier to the low frequency noise [105].

### 2.2.2 AE Acquisition

AE monitoring is centred on the measurement of the minute surface displacements that result from the propagation of AE stress waves. Piezoelectric transducers are commonly employed to convert the AE into a analogue output voltage that can be amplified and recorded. Small disks of Lead Zirconate Titanate (PZT), that generate voltage under compression, are embedded within an AE sensor housing, which through a combination of different sizes, shapes, and dampening methods, result in sensors sensitive to different frequency ranges. In order for these AE sensors to operate, they must be physically coupled to a material's surface that AE will propagate through. Therefore, the acquired signals are highly sensitive to not only the specification of sensor used, but also the propagation pathway from the AE source to the piezoelectric element. The material surface and properties, applied sensor pressure, coupling medium, wave incident angle, source distance and

sensor properties all combine to transform the generated AE during acquisition [109–111]. Fig. 2.12 shows a diagrammatic view of this measurement pathway.

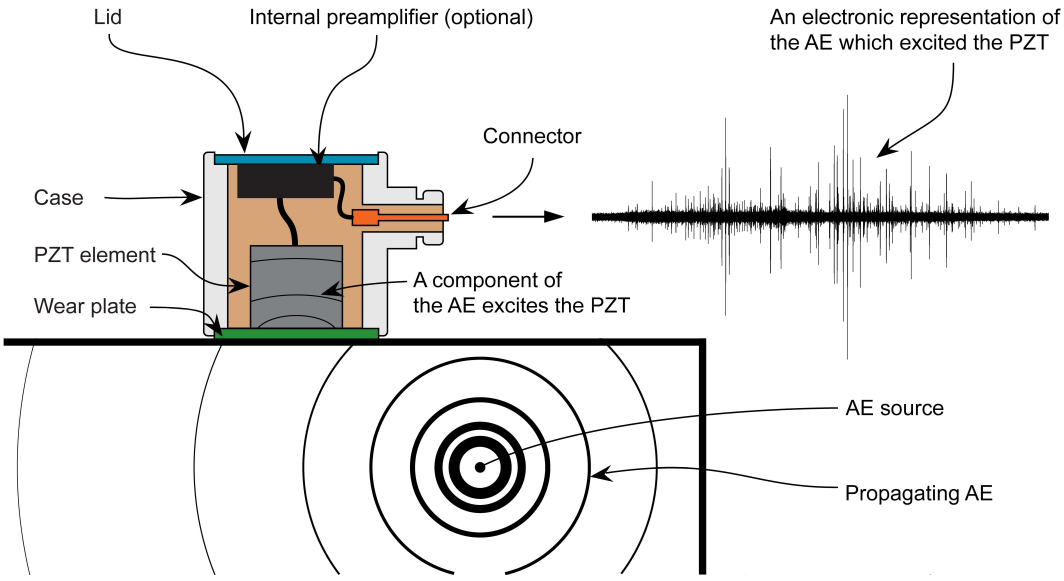


**Fig. 2.12:** Diagram of the measurement pathway of an AE sensor. Reprinted from [107].

AE sensor selection is primarily based on their frequency response, with size and environmental protection being secondary considerations [112]. Sensors fall into two categories based on their unique frequency response:

- **Resonant:** Characterised by a large peak sensitivity at a specific resonant frequency, with typically low sensitivity outside this region. The resonance frequency can be modified through the size and shape of the PZT element, with a standard range for resonant sensors falling between 100 – 400 kHz.
- **Wideband:** Sensors that exhibit a uniform response across a range of frequencies, potentially up to 2 MHz. Typically resulting in a lower peak sensitivity compared to resonant sensors.

The choice of which is highly dependent on the application, resonant sensors distort the frequency content of the received signals and as such are mainly used when only the time domain features are of interest. But this distortion also allows for an inbuilt bias towards certain frequencies, potentially isolating key mechanisms from a further distance

[111]. Wideband sensors are utilised if the frequency of interest is unknown or if different frequency ranges within signals are to be analysed. Shen [113] utilised two different Vallen resonant sensors mounted to the machine bed, to simultaneously monitor the grinding of a steel workpiece. This enabled the comparison of sensor selection for a particular grinding based application. The two sensors, a low frequency 30 – 120 kHz VS75S sensor and a standard frequency 100 – 400 kHz AE104A sensor, were both used separately to train a classification Support Vector Machine (SVM) model, for labelling input data as "sharp" or "worn". The authors found that the standard frequency range AE sensor (100 – 400 kHz) scored on average 5 – 7 % higher in classification accuracy, with lower variation during a 10-fold Cross-Validation (CV) process.

Coupling of the AE sensors' face to the material is required to improve the transfer of acoustic energy from the material surface to the PZT element [112]. Couplant aims to remove pockets of air between the sensor and material, a result of their combined surface roughness. The acoustic impedance of air is roughly five orders of magnitude less than the PZT element and most materials, and a such couplant can have a large effect on the recorded AE [114]. Theobald *et al.* [114] compared the effects of five different couplants, including a dry contact application, of an AE sensor's response to a longitudinal wave, shown in Fig. 2.13. As expected, a clear improvement in sensitivity across the frequency range (0 – 900 kHz) was seen between dry contact and all other couplants. Additionally, below 400 kHz differences between couplant were deemed to be within the random variability associated with the coupling process. A standard guide to the mounting of AE sensors, including coupling considerations, can be found in the ASTM *E650/E650M - 17* [112].

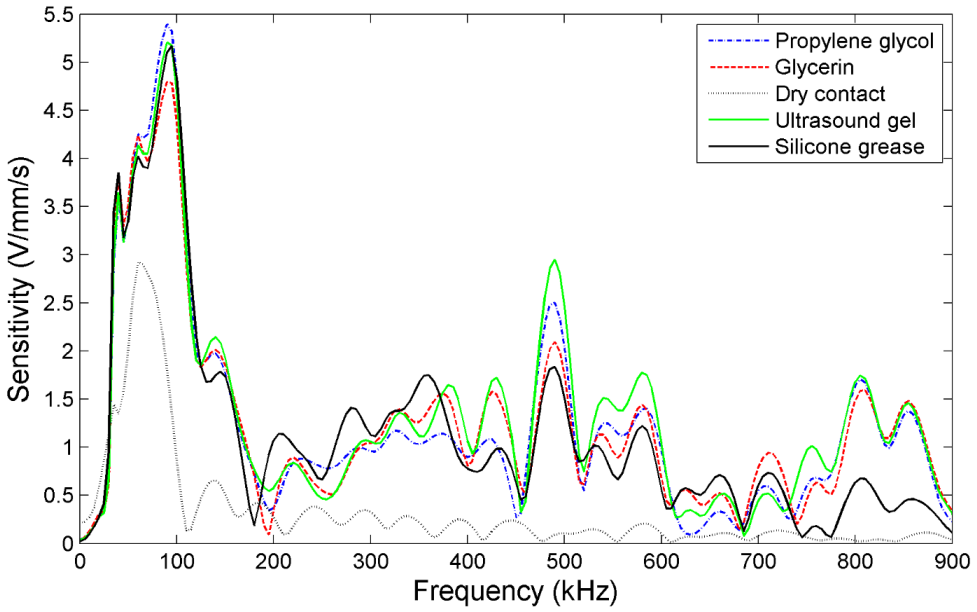


**Fig. 2.13:** Sensitivity of an AE sensor to a longitudinal wave using different couplants. Reprinted from [114].

Another consideration for the application of AE within a machine tool is the location of the AE sensor. High frequency signals, such as AE, attenuate with distance and surface boundaries, consequently AE sensors operate best when mounted along a transmission pathway as close to the source as possible [106]. Practical limitations also play a large role in sensor location, with considerations to the workpiece holding and replacement, cable organisation, spatial constraints and environmental protection all important alongside AE sensitivity. Typically within machine tools, AE sensors are bonded to the workpiece directly [102, 115], the work-holding device [27, 116] or spindle head [117, 118]. Sensors mounted to the machine bed or workpiece encounter limitations due to the changing relative position between the grinding zone and sensor location. This changing relative position can dramatically change the acquired AE signals generated through similar scenarios [25]. Kon *et al.* [119] concluded that acquiring AE through a static sensor on the hydrostatic bearing of a machine spindle was favoured over one coupled to the tailstock, as it provided consistent and effective correlation to grinding wheel deterioration despite the reduced signal sensitivity. Additionally, it is possible to acquire AE through a

coolant stream during grinding, by coupling the sensor close a coolant nozzle [120]. This pseudo non-contact approach removes the limitations of other sensor locations, changing source location and mounting to a rotating surface. Rowe *et al.* [121] and Inasaki [120] verified the sensitivity of AE sensors coupled in this way for both contact sensing during grinding wheel dressing and chatter detection during milling operations. Sutowski *et al.* [122] went on to utilise this approach to monitor internal cylindrical grinding operations. The authors found that hydro-acoustic coupling enabled wear monitoring and surface evaluation during a process with limited access.

Alongside sensor selection, coupling and location, multiple other effects impact the acquisition of AE. One such example is the "aperture" effect, whereby a larger sensor diameter can lead to a decrease in amplitude at higher frequencies, as multiple wavelengths are averaged over the sensor face [123]. In addition to all these presented considerations, the performance of a AE system may degrade over time as a result of physical or environmental factors. Therefore, the verification of an AE system as a whole unit is critical and should be conducted routinely throughout it's deployment [124].

To verify a system's performance, it is subjected to a number of repeatable AE sources, that should produce a known response from a working AE system. Pencil Lead Breaks (PLBs) are a commonly used method to generate repeatable artificial AE sources, with a short duration, fast risetime and high peak amplitude. A standard for PLBs was established by Hsu and Breckenridge [125] and Nielsen [126] as the breaking of a 0.3 mm or 0.5 mm diameter, 2H hardness pencil lead with a 2.5 mm extension from the mechanical pencil on the material surface at a fixed distance, known as a Hsu-Nielsen source. Hsu-Nielsen sources are used to investigate signal propagation, check sensor coupling and define signal processing parameters [127]. Multiple verification methods utilising PLBs for different aspects of AE monitoring can be found in ASTM *ASTM E976-15(2021)* [128]. Table 2.1 shows an example verification method through the measured peak amplitude of AE generated from artificial PLB sources.

**Table 2.1:** Example of peak amplitude verification for evaluating AE system performance.

| | |
|---|---|
| Waveform parameter of interest | Peak amplitude |
| Verification method | PLB (Hsu-Nielsen source) |
| No. of sources | 3 – 5 |
| Source distance | >100 mm |
| Specified acceptable range | >70 $\mathrm{dB_{AE}}$ |
| Acceptable repeatability | <3 $\mathrm{dB_{AE}}$ |

The final step in the acquisition of AE is the amplification, filtering and conversion of the analogue voltage signals prior to storage and processing. Pre-amplifiers are often used prior to Analogue to Digital (A/D) conversion of the signal, in which the signal is conditioned through a bandpass filter and amplified. Filtering and amplification of the signals at this stage allows for a significant increase in S/N prior to a potentially long transmission path to the acquisition board [124, 129]. Modern pre-amplifiers allow for selective filtering and amplification gains to be chosen based on the application's requirement. Typical filtering varies between 1 kHz - 2 MHz, with gains typically set to 0, 20, 40 and 60 $\mathrm{dB_{AE}}$. Where the unit dBAE describes the ratio between the signal voltage and a reference voltage, $V_{ref}$, of 1 µV:

$$\mathrm{dB_{AE}} = 20 \log_{10}(V/V_{ref}) \tag{2.2}$$

A/D converters are then necessary to convert the high frequency AE signals. These converters are required to be fast-acting allowing bursts of AE to be measured with short time delays, and have a sufficient resolution and sampling rate to accurately capture the signals [124, 129].

### 2.2.3 Signal Processing of AE

Signal processing of AE signals aims to extract relevant features or patterns relating to desired objective functions. In grinding, these TCM objectives are typically process metrics or a measure of the tool's state. Two schools of processing exist for AE signal processing, hit/parameter-based and signal/waveform-based analysis, from which a host of methods can be applied to extract useful meaning.

Hit-based analysis starts with the separation of transient AE bursts from the background noise or continuous AE. To do so a detection method is utilised, traditionally the crossing of an amplitude threshold along with other timing parameters (Hit Definition Time (HDT), Hit Lockout Time (HLT) and Peak Definiition Time (PDT)), are used to isolate individual AE hits, as can be seen in Fig. 2.14. From these isolated hits, AE features are derived to describe the AE burst without the need for storing the raw waveform. Features include AE amplitude, risetime, duration, counts, energy and many more [107]. Hit-based processing arose due to limitations of acquisition hardware. With time, significant developments in computing power have enabled AE hardware that is capable of storing waveforms of each segmented AE hit, or even the continuous acquisition of raw AE (wavestreaming) for set amounts of time [130].

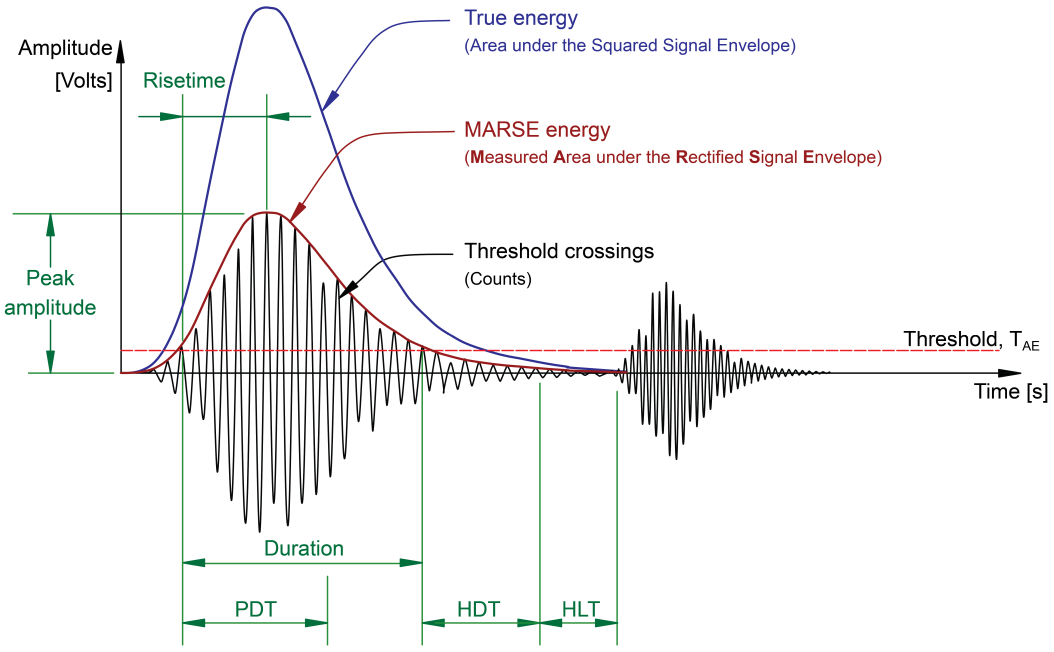


**Fig. 2.14:** Diagram of the threshold and timing based hit detection method, with common AE features illustrated. Reprinted from [107].

Signal-based processing utilises these advancements in acquisition technology to record whole AE waveforms, from which the analysis can be based on. This methodology is inherently more complicated and resource consuming, however results in a comprehensive and flexible analysis method. Signal processing directly with waveforms has become widespread due to both its application in continuous systems and for ML evaluation techniques [124]. Grinding processes like other continuous processes, such as rotating machinery [98, 131], tribological contact [132], and turning operations [14, 29], are preferably monitored with signal-based analysis.

AE waveform processing methods fall into three domains; time, frequency and time-frequency. A reliable TCM method to monitor any processes condition based on a sole signal feature is not feasible, and therefore, a common strategy is to calculate a host of potentially useful features [25]. A feature selection criteria can then be used to determine each signal's significance/usefulness, for transformation, removal, or use within an evaluation method. With the prevalence of ML approaches in intelligent manufacturing and

advancements in the training of deep learning models, waveform-based analysis can also be employed to better enable data-driven models [14]. Section 2.3.1 details other works utilising evaluation methods through a range of signal processing techniques.

## 2.3 Tool Condition Monitoring of Grinding

With an understanding of the DCB tools, grinding process and their subsequent wear as well as an overview of measurements techniques, this section presents a review of literature based around AE-based TCM approaches of grinding processes. Including signal processing techniques to evaluate the grinding process indirectly with AE, and model architectures to produce actionable information from the acquired signals.

### 2.3.1 AE Evaluation of Grinding Processes

The effectiveness of AE as a monitoring technique for grinding at the precision scale has been established for a long time, owing to it's many advantages over other techniques, as discussed in Section 2.2.1. Initially in the 1980s, AE was used for the detection of wheel contact, sparkout and loading during grinding processes, with the overarching aim of identifying ideal dressing times automatically. Dornfeld and Cai [17] and Inasaki and Okamura [133] both showed the ability of AE to monitor the dressing process through the use of the root mean squared of the AE signal, $AE_{RMS}$. Both works showed a clear correlation between the enveloped $AE_{RMS}$ signal and the uncut chip thickness, or dressing depth. With Dornfeld and Cai [17] concluding that $AE_{RMS}$ was a feasible method to monitor wheel condition as part of an adaptive process control system, owing to its sensitivity to wheel loading, depth of cut and contact. At the time the use of $AE_{RMS}$ was necessary as it allowed for slower acquisition cards, commonly implemented for vibration analysis, to be used with analogue signal conditioning. A limitation of this low-frequency enveloping, that $AE_{RMS}$ produces, is the loss of frequency content at the high end and a loss of temporal resolution [104, 134].

Despite this, $AE_{RMS}$ is still utilised as a condition feature as an indirect measure of overall grinding contact. De Oliveira and Dornfeld [135] used a diamond dresser, coupled with a wideband AE sensor, to monitor the dressing process of a traditional grinding wheel using $AE_{RMS}$. The authors were capable to identify three stages of dressing (turbulence prior to contact, elastic deformation of the bond material and brittle contact due to dressing) through increasing levels of $AE_{RMS}$, alongside direct wheel displacement measurements with a laser interferometer.

$AE_{RMS}$ was then investigated as a technique to monitor the wear and surface profile of traditional grinding wheels. Denkena *et al.* [136] used $AE_{RMS}$ to indirectly measure wheel wear, the authors artificially bevelled the wheel's edge and added a groove to its surface. Reductions in the measured $AE_{RMS}$ identified both types of artificial wear, allowing for an optimised dressing cycle to be conducted. Sutowski and Plichta [137] applied this technique to monitor wheel wear during peripheral surface grinding operations. Both grinding forces and AE were collected during grinding to be related to post-process workpiece surface roughness and wheel wear measurements. $AE_{RMS}$ was seen to be a sufficient metric to evaluate the cutting ability of a grinding wheel whilst grinding. Lin *et al.* [138] investigated a fluid-coupled AE sensor for the monitoring of diamond grinding wheels whilst grinding sapphire workpieces. Collected $AE_{RMS}$ presented a clear trend inline with theoretical wheel wear phases, supported by spindle load measurements. Across two wear tests, $AE_{RMS}$ showed a clear increase during the initial phase of wear, as well as indicating a point of grain self-sharpening during the steady-state phase. The authors concluded that $AE_{RMS}$ presents as a fine-grained feature for evaluating a grinding wheel's status.

To combat the limitations of using $AE_{RMS}$, in the 1990s, multiple studies arose utilising more advanced acquisition systems capable of recording raw AE signal, $AE_{raw}$. With the hope of better understanding the source mechanisms of AE during grinding and producing a more reliable TCM approach [101, 104, 134, 139]. Liu [134] utilised the kurtosis of the AE signal, $AE_{kurt}$, as a metric for identifying instantaneous changes within $AE_{raw}$ signals. $AE_{kurt}$ represents the "tailedness" of the $AE_{raw}$ distribution, indicating the proportion of the signal occurring at its maximum voltage. Kurtosis has also been used

widely within fault diagnosis of rotating machinery, within all three domains of vibration signals [98, 140]. Webster *et al.* [101] showed the ability to capture wavestreams of $AE_{raw}$ over long time periods. Through this, the authors were able to identify grit contact with the workpiece during spark-in and spark-out phases of each grinding pass. The rate at which the $AE_{raw}$ signal develops into continuous AE, also gave the authors indications of the workpiece geometric error. Additionally, periodicity of the $AE_{raw}$ indicated the cylindrical workpiece was elliptical in profile and experiencing chatter at twice it's rotational frequency. Akbari *et al.* [139, 141] utilised parameter-based AE acquisition to investigate the effect of grinding parameters. During the grinding of alumina with diamond wheels, the authors linked brittle-mode material removal with high-amplitude, long-duration hits and found a strong positive correlation between AE activity and the abrasive grain depth of cut.

Hwang *et al.* [142] investigated AE as a means for monitoring high speed grinding with a ⌀203.2 mm #180 (90 µm) DCB. A wear test was conducted using the DCB to take repeated surface grinding passes from a sintered silicon nitride ceramic workpiece. Alongside the $AE_{raw}$ acquired during each grinding pass, grinding force, spindle power and frequent micrograph images were acquired. Throughout the wear test, the grinding wheel experienced significant wear, with micrographs showing the dulling of abrasive grains through attritious wear. The amplitude of collected AE signals were seen to progressively increase with grinding time, and distinct peaks were identified throughout the experiment within the Power Spectral Density (PSD). Mokbel and Maksoud [143] utilised the Fast Fourier Transform (FFT) to investigate the effect of changing grit sizes, wheel speeds and wear states on the frequency domain of acquired AE signals. Increases in AE spectral amplitude were attributed to reduced grinding ability of the grinding wheels, observed through direct wheel surface profile measurement.

With the advent of Wavelet Packet Transform (WPT) within the field of AE [144, 145], Liu *et al.* [146] isolated the AE signals relating to grinding burn mechanisms. The methodology was validated across artificial burn conditions, through laser irradiation, and real grinding scenarios. Liao *et al.* [147] also demonstrated the ability of WPT to produce

useful AE features alongside other frequency based features, which in combination with a genetic algorithm produced good clustering accuracy, 97 %.

Yesilyurt *et al.* [27] monitored plunge grinding with AE, and was able to identify healthy and burn-damaged conditions from time-frequency processing methods. Additionally, the sensitivity of AE allowed changes in operating conditions, radial depth of cut, $a_e$, and feedrate, $V_f$, to be identified. When cutting conditions were changed, the frequency spectra's shape remained consistent, but its power at certain peaks were altered. Wan *et al.* [102] identified high correlation frequency bands between 0–300 kHz from AE signals collected during the grinding of alumina ceramics. Signal features were then extracted, and a Random Forest (RF) optimisation algorithm then enabled the prediction of grinding wheel wear states. Leading to a classification accuracy of 90.6%, when using features from within these frequency bands. Bi *et al.* [116] employed Linear Discriminant Analysis (LDA) in which samples of AE from tools of varying wear levels were projected into a low-dimensional feature space. LDA was capable of showing division between states of wear, and with the addition of sub-states allowed the real-time prediction of wear state based solely on samples from the current grinding wheel.

Recently Li *et al.* [148] utilised a range of time, frequency and time-frequency techniques to characterise and identify surface damage during grinding of carbon-carbon composites. A side-milling operation was conducted with a ⌀6 mm #120 bronze sintered DCB, with the authors varying parameters after each pass. A R6α AE sensor acquired $AE_{raw}$ wavestreams at 2 MHz through each grinding pass, with a Zeiss ultra-depth-of-field microscope, and SEM used to understand the material removal mechanisms. Through the $AE_{RMS}$ of the signals, the non-homogeneous nature of the composite were identified, as well as observing periods of stable grinding during each pass. Grinding parameters, cutting speed, $n$, and axial depth of cut, $a_p$, both showed statistical significance influencing $AE_{RMS}$. The authors then used both the FFT and STFT methods and workpiece imaging to identify frequency bands relating to different material removal mechanisms.

Similarly, Huang *et al.* [149] demonstrated the ability of AE to determine a DCB's tool state when grinding a zirconia ceramic workpiece. A ⌀10 mm #120 (106 – 120 µm)

DCB was used to grind shallow slots within the workpiece without cutting fluid. An ultra-depth-of-field microscope was used to obtain direct measurements of the tool's state, alongside an optical profilometer and electron microscope to analyse the workpiece surface. Transitions between wear phases were identified via abrasive grain fracture and eventually pull-out, with clear differences in grinding mechanisms seen through the workpiece morphology after grinding. Both AE amplitude and the wavelet packet energy correlated well with the tool's increasing wear, with power levels varying across the frequency spectrum as different wear mechanisms become more prevalent.

### 2.3.2 Prediction Approaches

To effectively predict traditional grinding wheel wear, a range of methods have been developed, consisting of physics-based models and data-driven/statistical models [150]. Physics-based models require in-depth knowledge of the system to generate models based on the fundamental failure mechanisms. Accurate analytical models are rare due to the complexity and incomplete understanding of the wear process, and as such are typically limited in scope and applications. Data-driven models require significant data in order for the models to be trained, but require little expertise about the process [14]. Due to the random nature of grinding processes, statistical or data-driven models are more commonly employed and successful, as these models can easily be updated in real-time when the process inherently changes [150, 151]. Additionally, as the increase of collected data to monitor machine tools becomes more prevalent, advancements in ML and deep learning methods that can exploit this information are highly desirable [152].

ML approaches stand out within the data-driven category, consisting of many methods and architectures, all of which allow for the training of a model based on inputted raw data or extracted features. A range of ML architectures have been employed and validated within TCM, for a variety of problems. The most popular category of which are ANNs, mainly Multi-Layer Perceptron (MLP), Recurrent Neural Network (RNN) and Convolutional Neural Network (CNN). TCM models are commonly employed for either

regression or classification problems. Classification models output discrete labels for each input, which for TCM applications is usually the tool's wear state, i.e. worn or unworn, or the phase of wear. Regression models, however, allow for a continuous value to be outputted, which typically represents a tool's radius or RUL. To enable the supervised training of these models, direct measurements of the tool's wear are typically acquired, acting as the model's target. A crucial consideration is the frequency of acquired direct measurements during a wear test, especially when using regression models.

Having been shown as an effective feature for contact detection and wheel state evaluation, $AE_{RMS}$ has also been used as the basis for multiple TCM evaluation approaches utilising ML methods. Nakai *et al.* [85] conducted a thorough study evaluating the performance of multiple different ANN architectures when predicting the tool wear of a resin-bonded diamond grinding wheel. Three wheels were worn grinding alumina workpieces, each with a different depth of cut, during which both $AE_{RMS}$ and spindle power measurements were acquired. Radial wheel wear measurement were conducted at set intervals, to enable regression models to be trained. Evaluation of both ANN type and feature selection was conducted. Inclusion of $AE_{RMS}$ as an input feature for a MLP model reduced prediction errors by $>15\,\%$. Leading to final prediction errors of $<4.8\,\%$ across the three depth of cuts, but due to the required dataset size, training occurred offline. Sachin Krishnan and Rameshkumar [153] monitored the repetitive surface grinding operation of an $Al_2O_3$ grinding wheel through an AE sensor mounted to the workpiece. With wear measurements occurring after every grinding pass, the three phases of wear were identifiable through the changing rate of wear. $AE_{RMS}$ collected through the wear test, showed clear correlation with the grinding wheel's wear. From this data, a Hidden Markov Model (HMM) was trained to classify the dataset, based on the $AE_{RMS}$ and frequent wheel wear measurements, resulting in an accuracy of $94\,\%$.

MLP neural networks are a standard yet effective architecture for a range of applications, being capable of handling large datasets and multiple inputs. Defined as a feed-forward neural network comprised of at least three fully-connected ("Dense") layers: an input layer, hidden layer/s and an output layer. Abu-Mahfouz [154] demonstrated the

capability of an MLP architecture to classify the type and state of wear of twist drills based on vibration signals. A combination of time and frequency domain features were extracted and used as inputs, leading to a classification rate of 80 % in drill wear type. A detection model for grinding wheel burn from AE was developed by Wang *et al.* [33]. Two feature groups from AE were selected as inputs to MLP models, autoregressive features and averaged statistical properties, from which regions of burn could easily be identified, even when trained on a small dataset. Moia *et al.* [155] used three AE time domain statistics, including $AE_{RMS}$, to classify grinding wheel condition. AE was acquired during the dressing process, leading to a mean classification error of $<$0.3 %. However, a limitation of this application, was the binary classification labels of dressed or undressed.

CNNs are a widespread and advanced deep learning method, having been successful for computer vision, image recognition and classification tasks. CNNs require 2-Dimensional input data, which typically takes the form of images. Through three main layers, convolutional, pooling and fully-connected, CNN models are able to classify 2D data based on similar patterns or features [152, 156]. Gouarir *et al.* [94] used an encoded representation of each force component as inputs to a unique CNN. Force data was taken from a milling operation using a 6 mm ball nose end mill over 315 cutting passes. The CNN was trained to classify the data into three states (rapid initial wear, uniform wear and failure wear), leading to an overall accuracy of 90 % without any feature extraction or selection having taken place. However, due to the shorter nature of the initial and failure wear states, misclassification rates were higher when labelling data in these categories. Bi *et al.* [115] utilised a CNN model for grinding wheel classification based on raw AE waveform inputs. The selected model contained two convolutional layers, a max-pooling layer and two additional fully-connected layers before the output layer, leading to a prediction accuracy of $>$90 %. This result however is of more interest, the authors used 19 prediction labels representing 19 sequential wear states, instead of three states. Additionally, visualisation of the outputs of the two convolutional layers was conducted, which indicated the layers focused on differing frequency ranges of AE (150 – 200 kHz and 0 – 50 kHz respectively). Showing the capability of CNNs to extract differing AE components from the raw

time-domain signal. Recently the use of CNN models has allowed for the direct use of time-frequency domain representations, such as the STFT and various wavelet transform methods, potentially allowing a more informationally dense input feature [157–160].

A limitation of both MLP and CNN models is their lack of consideration for the temporal nature of certain input data types. RNNs were developed to fill this void, enabling models to have access to the history of previous inputs. This memory allows RNNs to learn representations across sequenced or time-series data [161]. Long Short-Term Memory (LSTM) networks have prevailed as the most useful and applicable RNN, allowing long-term and short-term dependencies to be captured [162]. LSTMs have been applied to a range of problems, including speech recognition [163], genome modelling [164] and natural language processing [165]. Zhao *et al.* [150] compared multiple ML architectures against both basic and deep LSTM models for regression of flank wear of a ball nose end mill. The dataset comprised of input data of force and vibration signals collected during milling, and flank wear measurements were conducted offline after every cut as the desired output. Without feature selection, deep LSTM models (comprising of 21-21-28 LSTM cells) performed well across the two metrics, with a Root Mean Square Error (RMSE) of 13.73 and a Mean Absolute Error (MAE) of 10.73 across three datasets. When compared against the entire measured dataset, the trained model showed the capability to predict and follow the trend of wear across the whole cycle. Guo *et al.* [166] applied a similar experimental procedure to grinding wheel wear. With a combination of data from force, vibration and acoustic emission sensor, a LSTM model was able to achieve a RMSE of 0.240 and a $R^2$ score of 0.994. This is a large improvement in prediction scores compared to Zhao *et al.* [150] but does require the selection and processing of input features prior to training. Si *et al.* [86] combined a transformer model with a Bidirectional Gated Recurrent Network (BiGRU) RNN aiming to further improve model capability for sequenced tasks. Utilising a current sensor for inputs to the Trans-BiGRU model, and a laser displacement sensor as a measure of a grinding wheel's true wear. K-fold CV was employed to evaluate the regression architecture, leading to a RMSE of 3.262 µm and a $R^2$ of 0.9338 predicting radial wear across a validation set. With the Trans-BiGRU model

increasing in error over the initial wear-in phase of all three wheels worn.

Multiple different processing techniques and architectures can all lead to good results for any given application, and as such it is good practice to compare the prediction capabilities of different ML models and training strategies. De Barrena *et al.* [14] conducted a series of elaborate wear tests to compare the capability of different ML architectures to predict the RUL of a lathe cutting insert. Alongside the authors' aim to compare prediction models, a range of indirect sensors were employed to evaluate the optimum features for each model input. Indirect sensors included, two 3-axis accelerometers, one on the tool holder and one situated on the lathe chuck, a directional microphone at the cutting region, a dynamometer recording cutting forces at the tool holder, spindle and motor power sensors, and a single AE sensor coupled to the tool holder. To gather sufficient data for analysis, twelve inserts were worn through repeated operations. Measurements of flank wear were conducted at a set frequency during each wear test, with a direct optical profilometer, to obtain a measure of the tool's RUL. The authors then trained and optimised seven different ML architectures, comparing the validation scores and time to train of each model. Of which the MLP, Bidirectional LSTM (BiLSTM) and BiGRU models resulted in RMSE scores lower than 30 s. Both RNN models achieved the lowest prediction scores and variation during CV, however the MLP model required a third of the time to train.

Liu *et al.* [167] used an Extreme Learning Machine (ELM) ANN optimised through the mayfly algorithm to classify the wear state of DCBs grinding a C/SiC Composite. The ELM was trained using a variety of time and frequency domain AE features acquired during the wear test. The authors found similar correlations between the AE features and wheel wear as Huang *et al.* [149]. The final trained model resulted in a classification accuracy of 96 % when asked to predict the tool's current stage of wear. However, the work used $AE_{RMS}$ as a wear metric in-place of direct tool wear measurements, and a limited number of passes, 90 in total, were completed across the wear test.

Overall, AE is presented as a highly adaptable and sensitive sensing technology, that due to its direct link to material removal mechanisms, is an effective input for a

range of ML approaches, for the TCM of DCBs. The use of wear tests has become a widespread procedure to aid the development of TCM system, acquiring both indirect sensing signals during a tool's wear and direct tool wear measurements for validation. A variety of data-driven ML models have been investigated for their predictive capability, both as regression and classification approaches for the problem of TCM. However, at the time of writing, only a handful of literature has been published focusing on the TCM of small diameter DCBs, despite their widespread use in manufacturing; and only three studies [148, 149, 167] have investigated the use of AE as a sensing method for the TCM of DCBs. Additionally, due to each study's wear test methodology, a low number of direct measurements are captured throughout each wear test, resulting in none of the current works presenting a useful and reliable TCM approach, with sufficient validation. A further limitation arises when considering each study has conducted only a single wear test, therefore not enabling the consideration of variations in DCB manufacture or tool setup for any identified wear indicators. Both of these limitations are addressed in this thesis, through the use of an autonomously controlled wear test, enabling a larger number of direct wear measurements and tests to be conducted.

# 3 Methodology: Wear Tests

Wear tests allow for the controlled and systematic wearing of machine tooling. These laboratory-based machining trials are crucial steps to understand machining processes, as well as developing and validating TCM approaches. To obtain a sufficient and representative dataset, a detailed wear test methodology was both designed and implemented to study the wear of DCB. Autonomous operation and data capture enabled regular direct measurements of the tool's wear and continuous AE acquisition for the analysis presented in subsequent chapters. This chapter covers the principal methodology used to conduct DCB wear tests and extract useful data features.

## 3.1 Wear Test Overview

In total, accounting for all test series, 22 DCB full wear tests were conducted. A generic methodology was developed and evaluated during an initial feasibility series of four tests, from which adaptions were made to investigate additional aspects of the grinding process. During each wear test, a new DCB was worn progressively to failure through a repetitive grinding cycle. Each cycle of which consisted of two distinct phases; grinding and inspection. The grinding phase consisted of a single grinding pass, in conjunction with continuous AE acquisition. Then followed by a direct measurement of the tool or workpiece, the inspection phase, to capture the result of the preceding grinding operation. Fig. 3.1 presents a simplified flowchart of the conducted wear tests, showing the order of operations and stopping criteria. Sections 3.2 and 3.3 detail the grinding and inspection phases, respectively. An aim of this methodology was to enable frequent on-machine direct measurements, which as seen in Section 2.3 is a limitation of recent studies looking to

validate indirect TCM approaches. To enable this, wear tests were implemented through machine G-code without operator input, with a stopping criteria based on a reduction in tool length by $\geq$0.5 mm. A value of 0.5 mm was chosen as a tradeoff between accurately stopping, after small tool failures near a DCB's tip, and preventing false triggers due to coolant droplets. Basing the stopping criteria on a reduction in tool length instead of radius, ensured each DCB's Ni-diamond layer has been fully worn prior to stopping, as the side-milling operation does not utilise the end face for material removal. The G-code can be found in Appendix A for reference. Fig. 3.2 shows the experimental layout within the machine tool during each wear test.

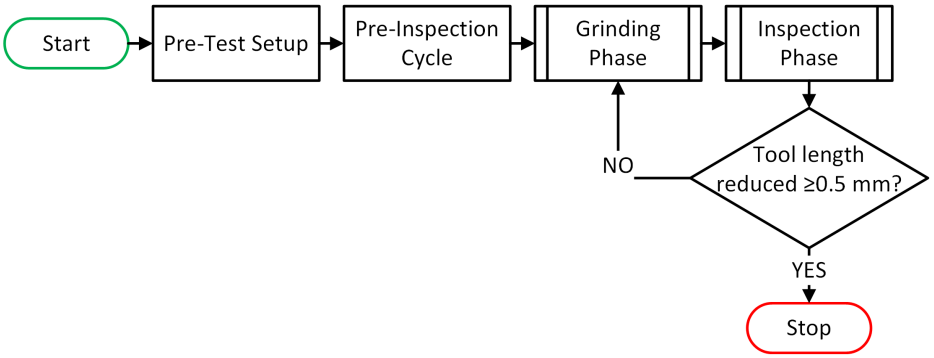


**Fig. 3.1:** Flowchart of the wear test procedure.

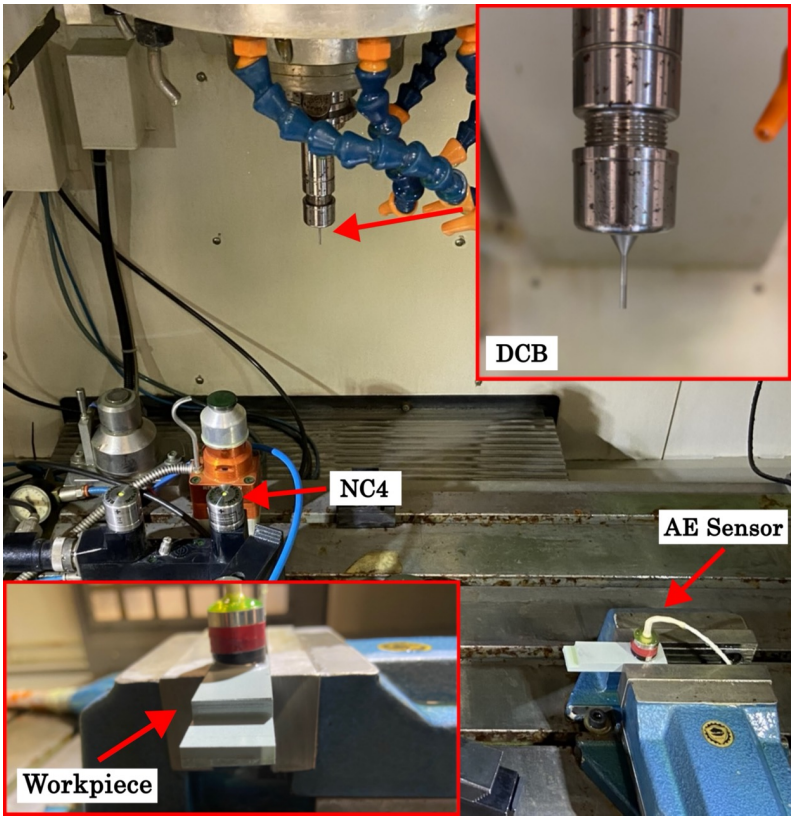


**Fig. 3.2:** Experimental layout within the machine tool.

## 3.2 Grinding Phase

The grinding phase of every wear test cycle consisted of a single grinding pass, during which continuous AE was wavestreamed and recorded. Fig. 3.3 shows a flowchart of the grinding phase operations.

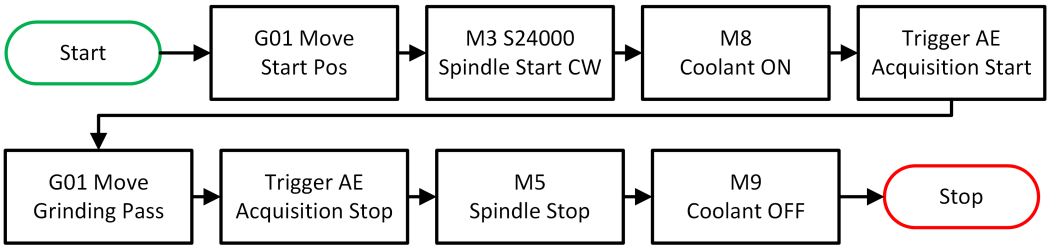


**Fig. 3.3:** Flowchart of the grinding phase subprocess.

### 3.2.1 Grinding Pass

A side milling operation was selected to wear each DCB, allowing easier observation and access, whilst being a good representation of a range of common mill-grinding operations. Fig. 3.4 shows the side milling operation with the relevant grinding parameters labelled from Table 3.1. The side-milling pass was programmed as a linear move in the y-axis, with the tool path starting and ending out of contact with the workpiece.

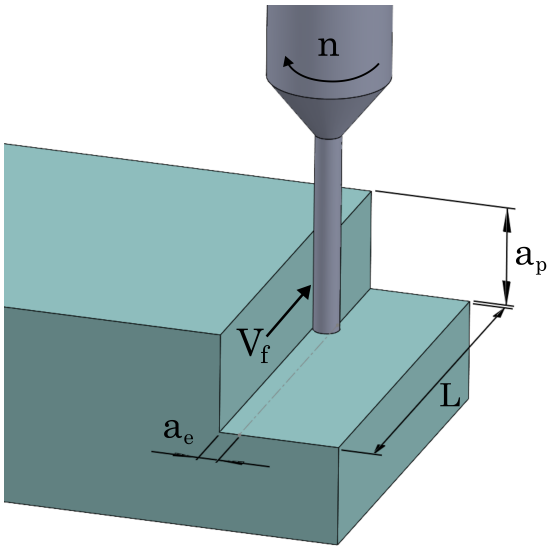


**Fig. 3.4:** Diagram of a DCB conducting a side milling operation, with labelled parameters.

**Table 3.1:** Side milling operation parameters.

| | |
|---|---|
| Grinding Machine | Jingdaio VT600 A12S |
| Machining Operation | Side Milling |
| | Up-cut grinding |
| Cutting Speed, $n$ | 98 m/min |
| Feedrate, $V_f$ | 60 mm/min |
| Depth of Cut - Axial, $a_p$ | 5 mm |
| Depth of Cut - Radial, $a_e$ | 0.03 mm |
| Grinding Length, $L$ | 20 mm |

Wear tests were conducted with Genentech ⌀1.3 mm #1000 DCBs of cylindrical form, Table 3.2 lists their specification. This specification of DCB was chosen as it represented the smallest diameter available, with a #1000 abrasive grain size to match finishing operations. When using small diameter wheels, a machine tool with a high spindle speed is required to reach recommended cutting speeds. Grinding was conducted in a Jingdiao (JD) VT600 A12S milling machine tool, suitable due to its maximum spindle speed of 24 000 rpm. The JD VT600 A12S is a 3-axis vertical milling machine with positioning accuracy of 5 µm and repeatability of 4.5 µm in all axes. Being commonly used for the precision manufacture and engraving of consumer electronics (3C) products out of ceramics or hard metals, including the housing, heat sinks and small components within mobile phones or other electronic devices. Fig. 3.5 shows an image of the machine tool used throughout. The JD machine tool was operated with a water-based coolant throughout all wear tests, aiming to reduce DCB wear through thermal degradation and clear away grinding debris from the tool-workpiece contact zone. The coolant specification is presented in Table 3.3.

**Table 3.2:** DCB specification.

| | |
|---|---|
| Tool Form | Cylindrical |
| Type | Electroplated Mono-layer |
| Tool Diameter | ⌀1.3 mm |
| Plated Surface Length | 10 mm |
| Mesh size | #1000 |
| Nominal Abrasive Grain Size | 15 µm |


**Fig. 3.5:** JD VT600 A12S machine tool.

**Table 3.3:** Coolant specification and parameters.

| | |
|---|---|
| Coolant | Supergrind Ultra |
| Supplier | Morris Lubricants |
| Type | Synthetic Water-based |
| Concentration | 2.5 – 3.0 % |
| Operating Temperature | 18 °C |
| Flow rate | 4 L $\text{min}^{-1}$ |

The DCBs were used to grind a green SiC workpiece, as a representative workpiece material for the commonly utilised engineering ceramics used with DCBs. The vitrified SiC workpieces were very abrasive and resulted in high DCB wear rates, whilst being inexpensive to purchase. Table 3.4 details the workpiece's specification. A milling vice

was used to fixture the workpiece to the machine bed. Importantly, prior to every wear test, the SiC workpiece was re-surfaced with a sacrificial #400 DCB.

**Table 3.4:** SiC workpiece specification.

| | |
|---|---|
| Material | Green Silicon Carbide |
| Bond type | Vitrified |
| Dimensions | 100 x 20 x 10 mm |
| Grain Size | #240 |
| Knoop Hardness | $2840\,\mathrm{kg_f\,mm^{-2}}$ |
| Relative Toughness | 1.6 |

A single grinding pass comprised of removing material across the 20 mm full width of the workpiece, $L$. The axial depth of cut, $a_p$, of 5 mm was purposely set to be less than both the workpiece thickness, 10 mm, and tool length, 10 mm. This choice allowed a consistent reference surface to be maintained on the workpiece throughout each wear test, crucial for setting work co-ordinates. Additionally, by only wearing halfway down each DCB's length a clear step in the abrasive layer was worn throughout each test. This step height between a worn and unworn section of the same DCB, allowed for easy comparison during each wear test and acted as a reference for 3D tool scans within the analysis.

### 3.2.2 AE Acquisition

To record the AE during each grinding pass, a MISTRAS Wideband Differential (WD) sensor was bonded to the workpiece's top face. The WD sensor has a superior wideband response over the 100 – 900 kHz range, due to the two PZT elements housed inside with opposite polarisation. As such, it is commonly used for research applications where a high resolution wideband response enables improved frequency analysis. Therefore, as the frequency content of the AE was initially unknown, and to enable a wider range of post-processing analysis techniques, the WD was selected. The datasheet of a WD sensor is available in Appendix B.

LOCTITE SI 595 [168] silicone sealant was utilised for both AE sensor couplant and environmental protection. The AE sensor was first coupled to the SiC workpiece's top face with a small amount of silicone sealant, which both adhered the sensor and improved signal transmission. More silicone sealant was then used to encase the AE sensor to prevent water damage from the flood coolant. Fig. 3.6 shows the position of the WD AE sensor in relation to the workpiece and grinding face. The location was chosen to minimise signal attenuation without compromising on ease of installation.

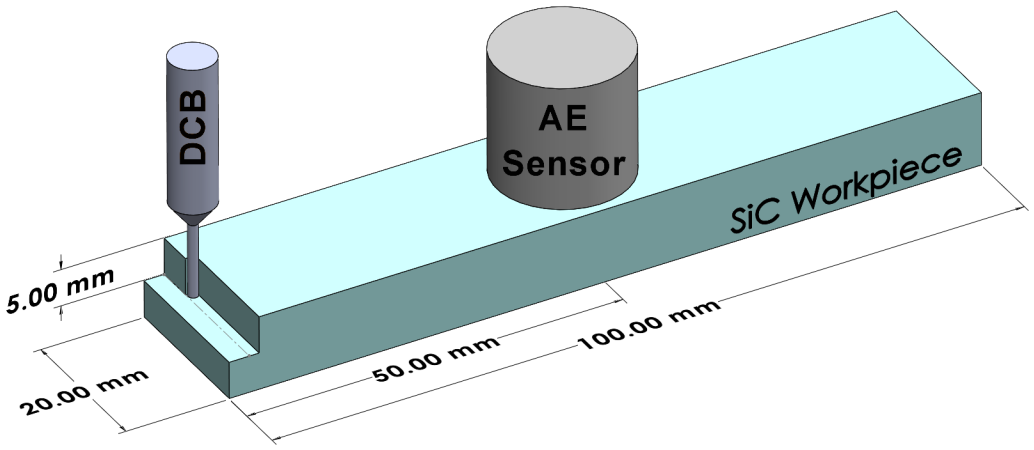


**Fig. 3.6:** Diagram showing the AE sensor's location on a SiC workpiece with dimensions annotated.

Prior to the Data Acquisition (DAQ) system, a MISTRAS 2/4/6 pre-amplifier was utilised to amplify and condition the AE signal. The pre-amplifier filtered the signal through an analogue 20 – 1200 kHz bandpass filter, as well as amplifying with a gain of 20 $dB_{AE}$. A National Instruments (NI) PXI DAQ system was used for the triggering and acquisition of AE during each grinding pass, the configuration of which is detailed in Table 3.5. The DAQ system allowed for AE to be acquired continuously at a sample rate of 2 MHz, with trigger signals controlled through the machine g-code. The sample rate of 2 MHz crucially satisfied the Nyquist criteria to prevent aliasing when using WD AE sensors with an operating frequency range of up to 1 MHz [169].

**Table 3.5:** NI PXI DAQ system configuration.

| **Controller** | |
|---|---|
| **Model** | **Description** |
| NI PXIe-8840 | Intel i7 5700EQ (2.6 GHz quad-core), 8 GB memory, 512 GB storage |
| **Modules** | |
| **Model** | **Description** |
| NI PXI-6515 | 64 channel DIO, ±30 V DC |
| NI PXI- 5922 | 2 channel oscilloscope, 15 MS/s max sample rate, 24 bit max resolution |
| **Chassis** | |
| **Model** | **Description** |
| NI PXIe-1071 | 4-Slot 3U, 3 GB/s bandwidth |

To interface with and control the NI DAQ system, a LabVIEW program was created, linking the machine's G-code with the oscilloscope card. A single oscilloscope channel was used for both the AE (CH 0) and the Renishaw NC4+ Blue (NC4) scans (CH 1), detailed in Section 3.3.1. The G-code was capable of setting a digital trigger signal to; "HIGH" (5 V) - acquire or "LOW" (0 V) - stop, for each of the oscilloscope channels through a programmable m-code command. The Digital Input/Ouput (DIO) card within the DAQ was used to monitor each digital trigger signal to inform the oscilloscope when to start and stop acquisition on each channel. To enable this, the LabVIEW code utilised an edge trigger to detect changes in state within the trigger signals, whereby a "rising" trigger signal started acquisition on its respective oscilloscope channel, and "falling" trigger signal stopped acquisition. Once acquisition was started, the LabVIEW code streamed the raw waveform into a binary .TDMS file. The resultant AE signal captured during every grinding pass lasted ∼20 s, with acquisition starting prior to the tool making contact and stopping after being out of contact. Fig. 3.7 shows a simplified flowchart of this process.

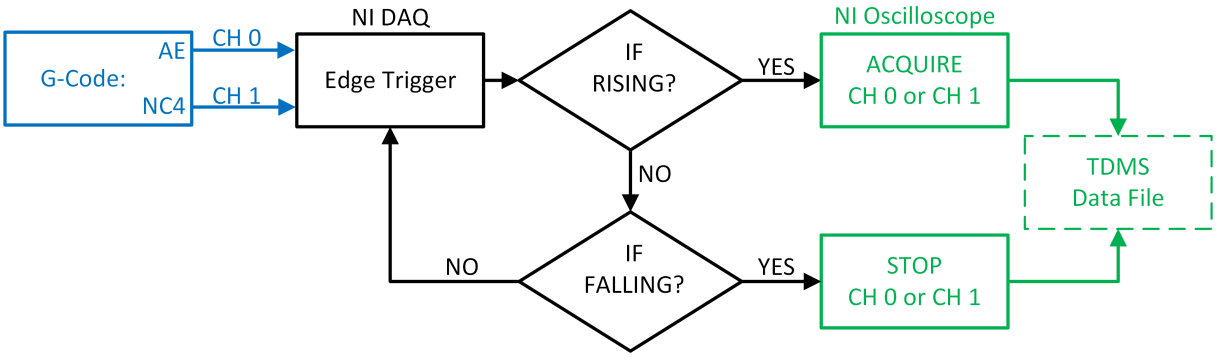


**Fig. 3.7:** Overview of the LabVIEW program control process.

## 3.3 Inspection Phase

To relate the acquired AE during the grinding to the resultant tool wear and workpiece condition, an on-machine inspection cycle was conducted after every grinding pass using an NC4 and a Renishaw OMP600 spindle probe (OMP600). The NC4 system enabled on-machine tool wear measurements, with the OMP600 allowing on-machine workpiece geometric measurements. Both systems were used as they were previously integrated into the machine tool for the tool and workpiece co-ordinate setting process. The inspection phase comprised of a range of direct measurement techniques including, a 2D circumferential surface scan of the DCB at a fixed position, a 3D surface scan of the entire tool's length, a probe measurement of the true radial depth of cut, $a_e'$, and a measure of the machine tool's thermal drift. The use of each measurement technique varied across each wear test, as the operational and processing code was developed alongside testing. Fig. 3.8 shows the order of operations during the inspection phase in its final and complete form. Wear tests varying from this procedure are detailed in Chapter 4. Each measurement's functionality, operation, and output are described in the subsequent section.

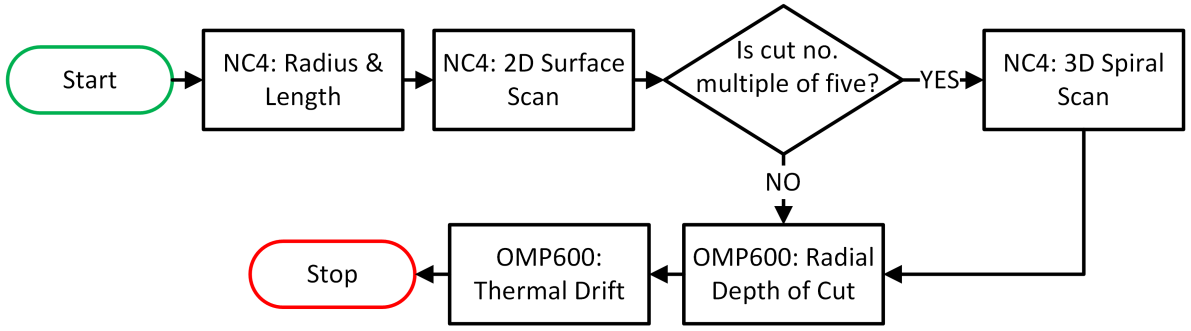


**Fig. 3.8:** Flowchart of the inspection phase subprocess.

### 3.3.1 NC4: DCB Measurements

An NC4 [170] was used to obtain on-machine tool radius measurements throughout all the wear tests. As an on-machine system operated through the machine G-code, the NC4 system enables frequent and unintrusive measurements of the DCBs without operator input. This functionality allowed wear tests to be conducted autonomously without direct user supervision, enabling wear tests to be continued indefinitely if required.

The NC4 is a non-contact tool setting system that determines the radius of a tool by using it to obscure a laser beam, the specification of which can be found in Appendix D. It consists of a transmitter tower and a receiver tower, housing a sensor used to measure the incident laser power across its face [171]. In a normal radius measurement macro, the NC4 operates through a trigger mode, in which a rotating tool is moved perpendicularly into the laser beam. When the tool blocks the beam sufficiently to reduce the incident power by a preset threshold, typically 50%, a trigger is sent to the machine controller to stop movement. The tool's radius is then calculated from the difference in machine and beam co-ordinates, outputting a single value for the tool radius. Fig. 3.9 shows a schematic of the NC4 with a representative rotating tool positioned at the 50 % radial laser obscuration position. Additionally, this method can be used to determine a tool's length by moving the tool in the z-axis to block the tool through axial movement rather than radial movement. This technique provide a quick but precise average value of the

tool's radius, however as it outputs a single value it only provides a limited view of the tool's wear state, limiting its usefulness.

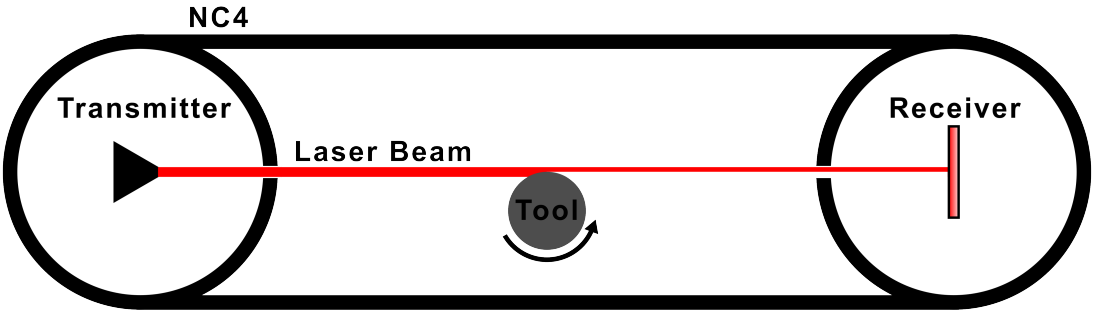


**Fig. 3.9:** Schematic of an NC4 with a tool obscuring the laser beam.

### 2D Surface Scan

To provide more information relating to the DCB's wear, the NC4 system can be used in an alternative strategy. This approach takes advantage of the concept that the radius of a rotating tool can be measured through the changing incident laser power levels. If a tool is moved so that its edge is within the beam and then rotated but not translated, any change in the measured power level is the result of the beam becoming more or less obstructed, from which the radius of a tool required to block the beam by an equivalent amount can be determined. The transmitter produces a beam which at its centre point, the midpoint between the two towers, is approximately 40 µm in diameter [172], over which the sensor will detect a drop in power if obscured. Through the calibration process of an NC4 a linear function is derived to convert the output sensor voltage into a radius that results in the equivalent beam obstruction. Using an external oscilloscope, the NC4 receiver's voltage can be polled whilst the tool is rotating, to obtain a 2D measurement of the tool's circumferential radius. The same NI PXI oscilloscope and acquisition process as used for the capture of AE outlined in Section 2.2.2, was used to record the NC4 output voltage at a sample rate of 50 kHz. A spindle of speed of 60 rpm was used to rotate the tool within the beam, resulting in measuring 7958 samples/rad about the tool's circumference. Fig. 3.10 shows an example of the converted 2D surface scan.

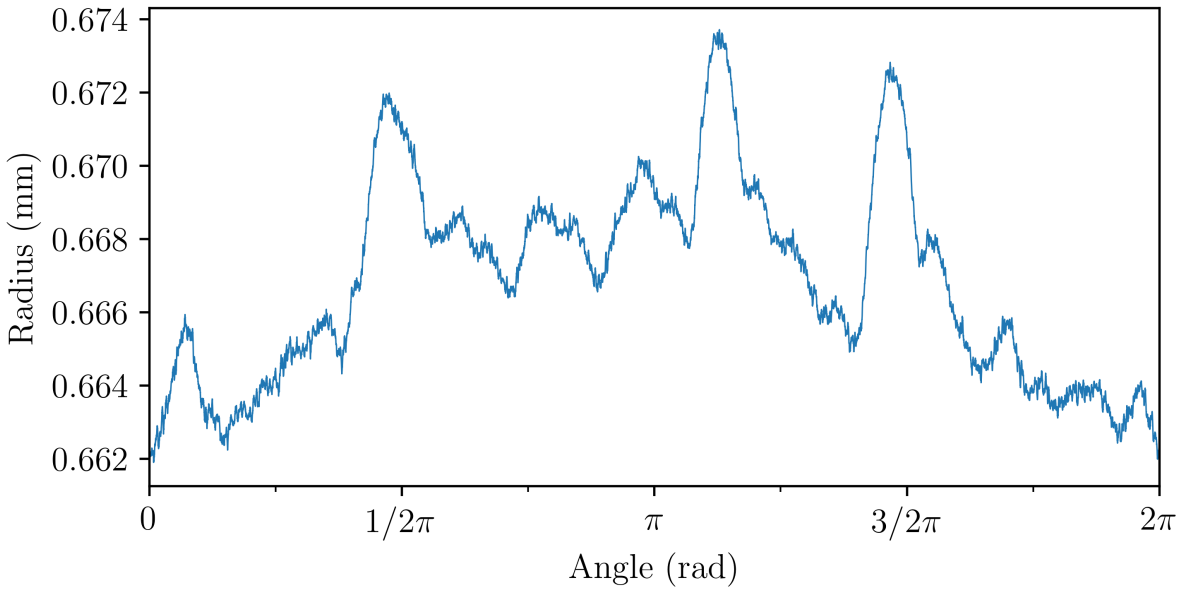


**Fig. 3.10:** A processed NC4: 2D surface scan of a new ⌀1.3 mm #1000 DCB.

In every wear test, the 2D surface scans were conducted halfway up the axial depth of cut, $a_p$ (2.5 mm from the end of the tool). By measuring at the same position, these measurements enable the progression of wear to be observed around the tool's circumference. The axial location of each measurement at 2.5 mm from the DCB's tip was recommended by Renishaw as a standard operating procedure, minimising the chance of not measuring the region of interest due to thermal drift or misalignment. To improve the output, small modifications to the above method were included, for example, the tool was measured rotating in the beam on both sides through three full rotations. By measuring on both sides of the laser beam and then averaging, thermal drift of the machine in the axis perpendicular to the beam should be minimised. Measuring multiple rotations of the DCB's circumference allowed for improved reliability in alignment between the two sides prior to this averaging operation, as well as ensuring a full revolution of the tool was captured. Lastly, to enable the full width of the NC4 receiver to detect changes in radius, the DCBs should be scanned with their surface inline with the laser beam's centreline. To account for deviation in this alignment, the multiple tool rotations occurred at 10 µm steps along the y-axis, perpendicular to the laser direction. The step outputting a voltage closest to

2.5 V during its three rotations, was extracted for the measurement. Each 2D NC4 surface scan took ∼1 min to complete without the need for a tool change operation. Therefore, these scans were conducted after every grinding pass in every wear test, forming the basis of the DCB direct monitoring.

From these 2D surface scans, a large amount of information can be deduced about the tool's wear state. Four main features were extracted from each scan; mean radius, peak radius, runout and form error. Each of which provided a simplified view of a DCB's wear state. The mean radius, $r_{mean}$, was determined by calculating the mean of the radius scan, $r$:

$$r_{mean} = \frac{1}{n}\Big(\sum_{i=1}^{n} r_i\Big) \tag{3.1}$$

The peak radius, $r_{peak}$, is the maximum value within the radius scan:

$$r_{peak} = max(r) \tag{3.2}$$

Form error, $r_{fe}$, is the range of the radius scan:

$$r_{fe} = max(r) - min(r) \tag{3.3}$$

An implementation of the hyper least squares fitting algorithm [173] was employed to fit a circle to each 2D surface scan, from which the fitted centre coordinates, ($x_c$, $y_c$), are used to calculate the DCB's runout, $r_{runout}$.

$$r_{runout} = 2\Big(\sqrt{{x_c}^2 + {y_c}^2}\Big) \tag{3.4}$$

**3D Spiral Scan**

A major downside of the 2D NC4 scans is that the circumferential measurements only occur at one axial position up the DCB's length. As a result, there is still the possibility of missing large parts of the tool's overall wear, which will still impact both the ground workpiece surface and the produced AE during grinding. Therefore, to obtain a more detailed view of the wear process, a pseudo 3D scan was implemented with the NC4 system. To generate this 3D plot, the DCB was both rotated and translated in the z-axis simultaneously, making the measurement point follow a spiral path up the tool's

surface. The acquisition and conversion of the NC4 incident laser power follows the same process as the previously described 2D NC4 scan. Through varying the spindle speed and z-axis feedrate, higher resolution scans can be produced with the penalty of scan time increasing. To acquire a sufficiently detailed scan for qualitative measurements, a spindle speed of 60 rpm with a Z-axis feedrate of 2 mm/sec was employed. Unlike the 2D NC4 surface scans, the 3D spiral scans did not employ the improvements for error reduction to reduce the total scan time. Once acquired, the spiral measurements can be sectioned by revolution to produce a pseudo 3D image of the tool's surface. Fig. 3.11(a) shows an example of this type of 3D measurement taken of a new ⌀1.3 mm DCB, in which the tool has been measured from it's tip to 7 mm up its length. Each NC4 spiral scan measures from below the tip of the tool (at Z = 0.2 mm) to beyond the axial depth of cut asked of the DCB shown by the horizontal black dotted line, showing a clear contrast between the wear of a worn and un-worn section of each DCB. For comparison, a scan of the same tool after 75 grinding passes is shown in Fig. 3.11(b), in which the tool's wear can clearly be identified across the grinding region. The large protrusion at the tip of the tool, above 0.68 mm, is a narrow band of coolant and can be ignored.

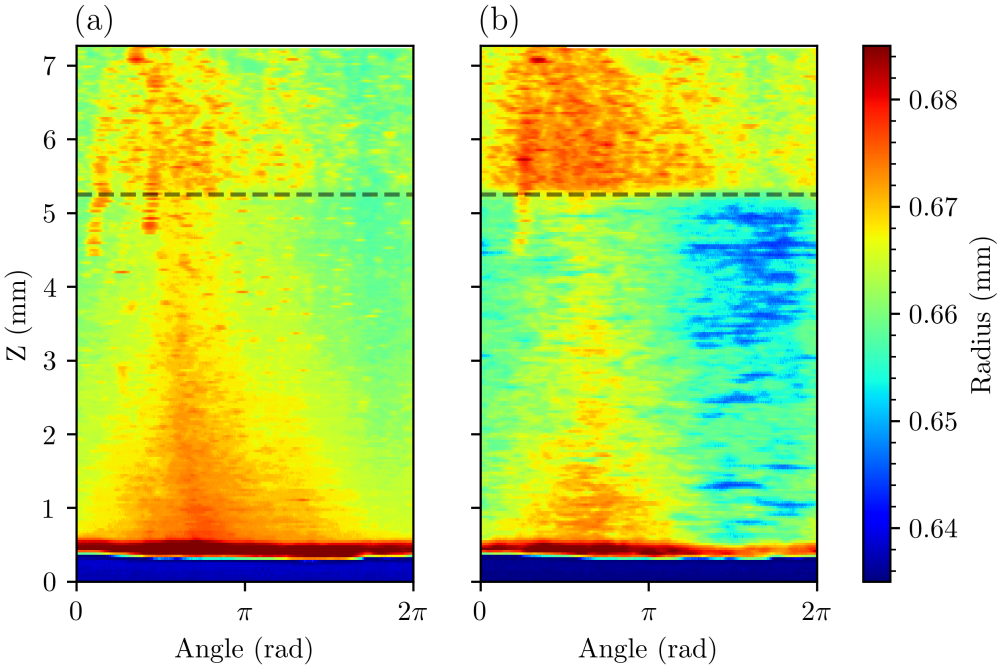


**Fig. 3.11:** 3D NC4 spiral scans of a ⌀1.3 mm #1000 DCB after (a) zero and (b) 75 grinding passes.

Overall, the 3D spiral scans enable monitoring of the DCB's macro wear across its whole surface. In comparison to the 2D NC4 surface scans, the 3D spiral scans take approximately four times longer to measure the DCB. Resulting in an overall lower precision as a result of the additional axis movement, reduced cycle optimisation and limitation of sectioning the scan per revolution based on a set number of samples. Despite these downsides, the benefit of the 3D spiral scans, enabling monitoring of the DCB's macro wear across its whole surface, meant that once developed this technique was deployed for all wear tests. To reduce the impact of cycle time, when employed, the 3D spiral scans were conducted at a reduced frequency of 5 passes/measurement.

### 3.3.2 OMP600: Workpiece Measurements & Thermal Drift

In addition to the NC4 used for direct measurements of the DCB, an OMP600 spindle touch probe was used to gather direct measurements from the workpiece. Strain

gauge touch probes such as the OMP600 are commonly used for both workpiece setup and dimensional verification [174, 175]. The OMP600 is controlled through the machine tool's g-code, using the probe's displacement, due to contact with its ⌀4 mm ruby ball stylus and the measurement surface, as a reliable trigger for positional measurement. As a result, the OMP600 is a "high-accuracy" probe with an adequate 2D repeatability of ±0.25 µm, two order of magnitudes below the specified $a_e$ of 30 µm. The datasheet of the OMP600 can be found in Appendix E. In this work the OMP600 probe was utilised to measure both the true radial depth of cut, $a'_e$, removed during a grinding pass and the machine bed's thermal drift during a wear test.

**Workpiece Removal Monitoring**

To gain understanding of a DCB's grinding ability as it wears, the OMP600 was used to measure the true radial depth of cut, $a'_e$, removed after every grinding pass. During the wear tests radius compensation, commonly employed with the NC4, was not utilised to replicate the worst case scenario whereby the user does not have the ability to measure the tool within the machine tool. Without tool radius compensation, the tool wear will result in $a'_e$ deviating from the programmed $a_e$. To enable this measurement, two surface planes were measured on the SiC workpiece, the reference, and cut surfaces, from which a relative measurement of $a'_e$ is obtained. By making these measurements relative across the workpiece, it removes a possible avenue of error relating to the thermal drift of the machine tool. Four equally spaced position measurements were taken along each surface to obtain a locating position. Fig. 3.12 shows the position of both the cut and reference surface on the SiC workpiece. Crucially, the reference surface remained untouched throughout each wear test, making the difference between each measured surface location equal the $a'_e$.

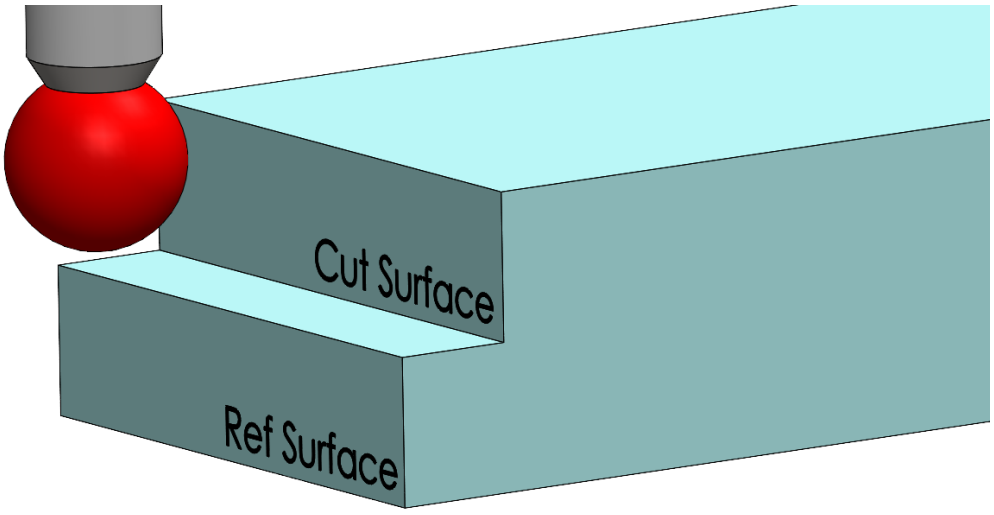


**Fig. 3.12:** Layout of probing process, showing the two measured surfaces on a SiC workpiece.

### Thermal Drift

Within a machine tool, multiple factors affect the dimensional and geometric errors in workpieces, including the machine's stiffness, tool wear and thermal deformations of the machine tool. Thermal drift describes the displacement between tool and workpiece as a result of thermal deformation of the machine axes [176]. The OMP600 was used to measure a ⌀24.998 mm precision reference bore mounted to the machine bed, from which thermal drift could be tracked throughout the wear tests. A measure of thermal drift in both the x and y machine axes was taken after every grinding pass, when used during wear tests.

Alongside this monitoring, thermal drift can be minimised through a thorough warm-up procedure. Warming up the spindle is common practice due to the large amount of heat generated by high-speed spindles, with other authors showing increases in spindle temperature of ∼50 °C during the warm-up procedure operating at lower spindle speeds than used in this work [177–179]. To determine the length of time required to run the spindle prior to conducting a wear test, a thermal drift study was carried out with an unworn tool mounted into the spindle. The spindle was rotated unloaded at 24 000 rpm

for 3 h, with measurements of the tool's length occurring every 15 min with the NC4. Fig. 3.13 shows the effect of thermal drift on the tool's measured length during this warm-up study. The tool's length showed a clear trend of logistic growth, as expected when an axis warms up significantly. An increase in the tool's length of 43 µm was measured over the 3 h period. After 60 min the tool length stabilises and variation is within the expected error of the measurement system, indicating that a warm-up period of 60 min is sufficient to minimise z-axis thermal drift. Prior to each wear test, the machine tool underwent a thorough warm-up procedure, including the spindle warm-up, to minimise the effects of thermal drift. Under load the spindle will generate heat at a higher rate, however the effect of this will be negligible once the spindle has warmed up due to the low grinding forces and spindle cooling loop.

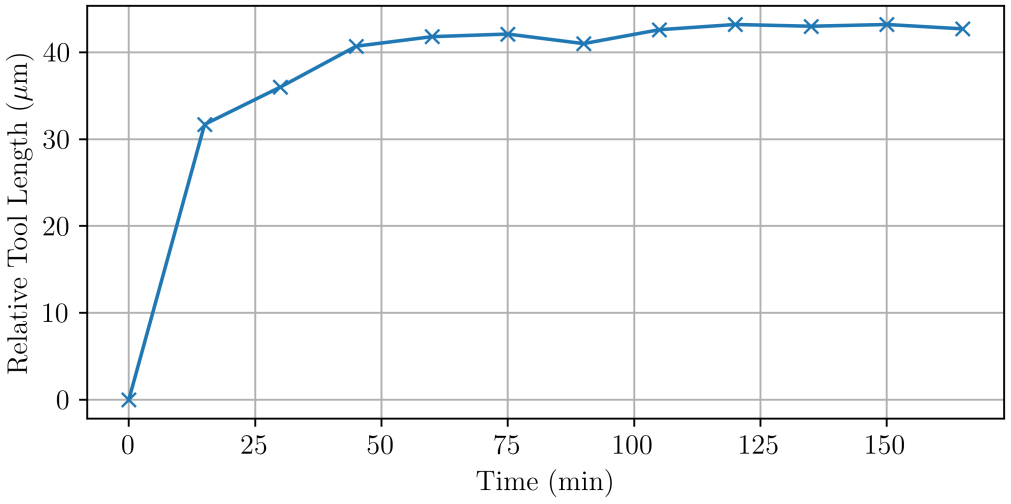


**Fig. 3.13:** Relative change in measured tool length during spindle warm-up cycle.

## 3.4 Runout Variation

As part of this work, a series of wear tests were conducted to investigate the effect of a DCB's initial runout level on its overall life. A specialised tool holder (NIKKEN BT30-SZF10-90 zero-fit) was employed to adjust the DCB's runout to a desired range prior to conducting the wear test. NIKKEN zero-fit tool holders are commonly employed

to reduce a given tool's runout. An inbuilt cam allows for a variable force to be applied to a given region of a tool's circumference, which when aligned with the tool's radial high spot, reduces the overall runout. To carry out this reduction on a typical machining tool, i.e a fluted end mill, a dial indicator is used on the tool's shank to identify the severity of runout and also determine the radial high spot location. In this application, however, the effect of both reduced and increased levels of runout were of interest and as such the runout was increased by applying the cam's adjustment to the radial low spot of the tool's circumference. The datasheet of the NIKKEN zero-fit tool holders can be found in Appendix F.

To obtain an accurate value for a DCB's runout measurement, a dial indicator was not applicable, due to the small tool diameter, concern for damaging the indicator tip and limitation of the JD machine tool's spindle preventing manual rotation As such, the NC4 was used to measure 2D surface measurements at multiple locations along the DCB's length from which the runout was extracted. The process of measuring 2D scans with the NC4 is detailed in Section 3.3.1. Before each wear test was conducted, the tool's initial runout was adjusted to a pre-determined amount. Three "levels" of runout were chosen to represent the full range of feasible runout values [24, 81, 82, 180]. The first of which adjusted a DCB's initial runout to $<15\,\mu m$. This range was considered to be a "low" level of runout for a DCB of this specification. The second level of runout, labelled as "medium", set the initial runout to between $25-35\,\mu m$. Finally, a "high" level of runout was defined as DCBs set to between $75-80\,\mu m$, whereby $80\,\mu m$ was the maximum value capable of being reached using the NIKKEN zero-fit tool holder.

## 3.5 AE Verification & Processing

### 3.5.1 AE Verification

Prior to conducting any DCB wear tests, verification of the WD AE sensor and DAQ was critical. Following standard practice as described in Section 2.2.2, three PLBs

were conducted on the top face of the SiC workpiece at a distance of 50 mm from the sensor's face, requiring an $AE_{AMP}$ of $\geq$95 $dB_{AE}$. This procedure was utilised whenever the sensor was recoupled to a new workpiece, adjusted within the machine vice or after a long period of downtime. Table 3.6 shows an example of the verification results from the initial experimental setup.

**Table 3.6:** PLB results.

| PLB No. | $AE_{AMP}$ ($dB_{AE}$) | Duration (ms) | Risetime (µs) |
|---|---|---|---|
| 1 | 96.474 | 1.752 | 61.0 |
| 2 | 96.341 | 3.054 | 61.5 |
| 3 | 96.475 | 2.960 | 60.5 |
| Average | 96.475 | 2.589 | 61.0 |

### 3.5.2 AE Background Noise

Alongside verifying that the AE sensor and DAQ are operating correctly, another important consideration for all AE applications is the quantification of background noise. To enable this AE was recorded during a range of scenarios common to the process. For context, the JD machine is located in a busy machine shop surrounded by >10 other large Computer Numerical Control (CNC) milling machines and lathes, a important consideration when understanding this work's feasibility. Table 3.7 shows the scenarios investigated as unwanted noise, as well as the maximum AE amplitude, $AE_{AMP}$, and the root-mean squared of each AE signal, $AE_{RMS}$. The $AE_{AMP}$ of a noise scenario signal indicates the strength of transient AE bursts, whilst $AE_{RMS}$ gives an insight to the overall continuous level of AE. All the acquired AE signals present as mixed mode AE, showing both a low amplitude continuous component, and higher amplitude bursts interspersed throughout.

**Table 3.7:** AE background noise from a range of scenarios.

| No. | Noise Scenario | $AE_{AMP}$ ($dB_{AE}$) | $AE_{RMS}$ ($dB_{AE}$) |
|---|---|---|---|
| 1 | Baseline 1 | 44.969 | 28.726 |
| 2 | Baseline 2 | 50.502 | 31.556 |
| 3 | Baseline 3 | 45.743 | 28.189 |
| | Average | 47.071 ($\pm$2.259) | 29.490 ($\pm$1.195) |
| 4 | Coolant Far | 45.617 | 29.087 |
| 5 | Coolant Near | 60.208 | 40.220 |
| 6 | Spindle (20.000 rpm) | 54.654 | 34.797 |
| 7 | Spindle (24.000 rpm) | 53.798 | 34.225 |
| 8 | Y-axis Travel | 55.750 | 36.230 |
| 9 | Coolant & Spindle (24.000 rpm) | 59.099 | 40.501 |
| 10 | Y-axis Travel, Coolant & Spindle (24.000 rpm) | 56.564 | 37.866 |

First to establish a measure of the noise "floor", three baseline measurements were collected, scenarios 1 – 3. These baseline measurements were conducted when the machine was on but idle, each acquiring AE for 2.5 s. The time domain signals of each baseline measurement can be seen in Fig. 3.14, with their respective PSD seen in Fig. 3.15. The baseline measurements resulted in an average $AE_{RMS}$ = 29.490 ($\pm$1.195) $dB_{AE}$. The frequency content of each baseline signal exhibit similar spectrum shapes, with distinct peaks at both 130 kHz and 505 kHz. Additionally, the impact of the WD sensor's frequency response can be seen by the large loss in power outside the 100 – 900 kHz range.

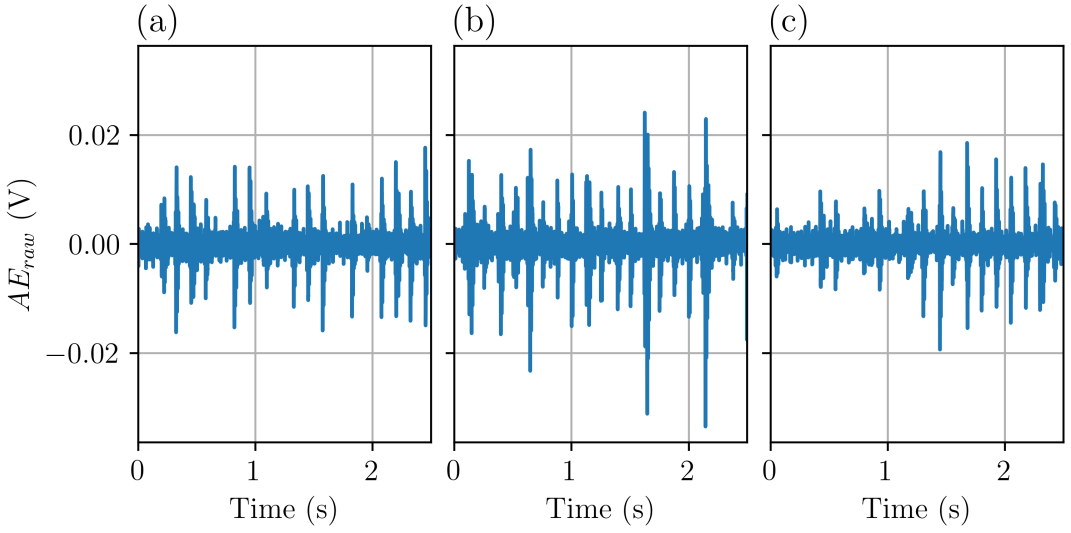


**Fig. 3.14:** Baseline AE noise measurements in the time domain.

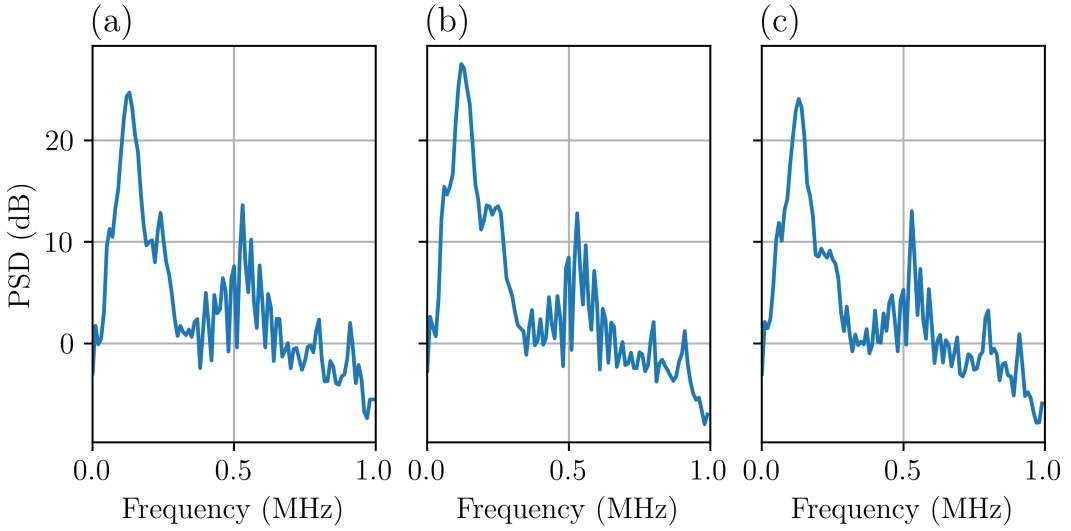


**Fig. 3.15:** Baseline AE noise measurements in the frequency domain.

To investigate the effect of coolant on the acquired AE, two further scenarios were measured. Both of which used coolant as specified in Table 3.3, differing by their targeted output location. The first coolant scenario (4), applied coolant to the opposite side of the machine bed, isolating the effect of coolant delivery on the acquired background noise. The second coolant scenario (5), opposed this and applied coolant directly on top of the

sensor, acting as a worst case scenario. As expected, the two scenarios result in different noise signals, as seen in Figs. 3.16–3.17. The AE from scenario 4, in which the coolant was directed away from the workpiece, is similar to the baseline measurements and falls within the average range of both $AE_{RMS}$ and $AE_{AMP}$. By comparison, the AE collected during scenario 5, resulted in a significantly higher amplitude time-domain signal. With the $AE_{AMP}$ and $AE_{RMS}$ increasing by 14.591 $\mathrm{dB_{AE}}$ and 11.133 $\mathrm{dB_{AE}}$ respectively between scenarios 4 and 5. The same can be seen in the frequency domain, Fig. 3.17, as both scenarios follow the spectral shape as seen in the baseline measurements. However, there is a change in power across the spectrum leading to an increase in 10 dB, with the 130 kHz peak becoming less pronounced.

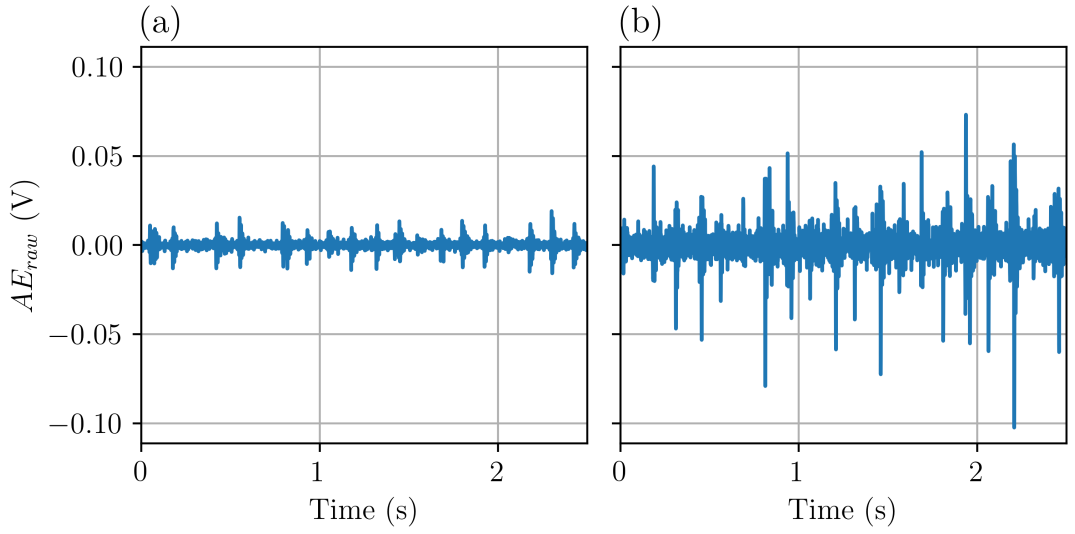


**Fig. 3.16:** Time domain AE signal with coolant running (a) far from and (b) on top of the AE sensor.

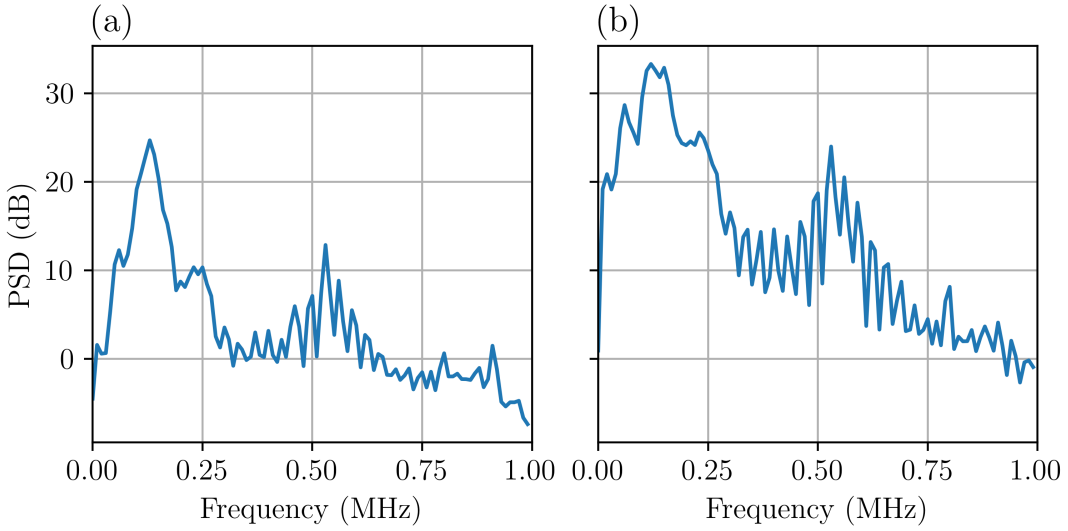


**Fig. 3.17:** Frequency domain AE signal with coolant running (a) far from and (b) on top of the sensor.

Scenarios 6 and 7 aim to look at the effect of the spindle's rotation on the acquired background noise. Whilst a DCB was held within the spindle just off from the cutting surface of the workpiece, AE was recorded while the spindle was rotating at 20 000 rpm and 24 000 rpm. The time and frequency domain signals for each scenario can be seen in Figs. 3.18–3.19. Both scenarios increased the $AE_{AMP}$ and $AE_{RMS}$ by $\sim$7 $\mathrm{dB_{AE}}$ and $\sim$5 $\mathrm{dB_{AE}}$ from the baseline. Within the frequency domain, aside from the overall increase in power across the spectrum, no noticeable influence could be identified relating to the spindles rotational speed. This is due to the spindle rotation frequency, of 333 Hz and 400 Hz respectively, being significantly lower than AE sensor's sensitivity range.

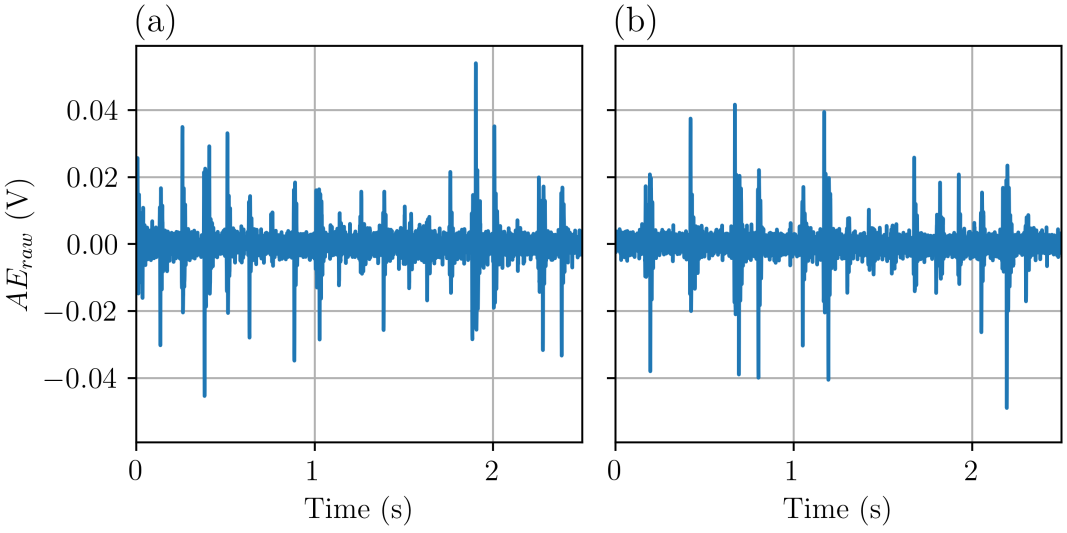


**Fig. 3.18:** Time domain AE signal with the machine spindle rotating out of contact at (a) 20 000 rpm and (b) 24 000 rpm.

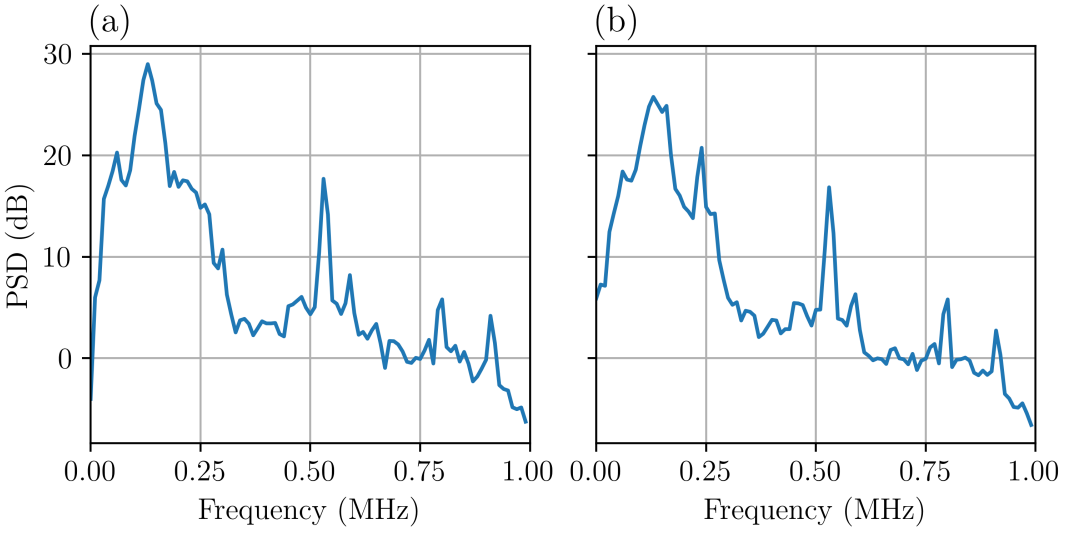


**Fig. 3.19:** Frequency domain AE signal with the machine spindle rotating out of contact at (a) 20 000 rpm and (b) 24 000 rpm.

A further scenario investigating the effect of machine bed movement was conducted. During scenario 8, the machine bed was moved in the Y-axis matching the tool path for a single grinding pass as described in Table 3.1. Figs. 3.20–3.21 shows a comparison

between an additional baseline measurement (a) and the noise generated during Y-axis travel (b). Similarly to scenarios 6 and 7, the only observable difference in acquired AE whilst the machine bed is moving is the overall increase in signal energy, seen by increases of $\sim$7 $\mathrm{dB_{AE}}$ in both $AE_{RMS}$ and $AE_{AMP}$.

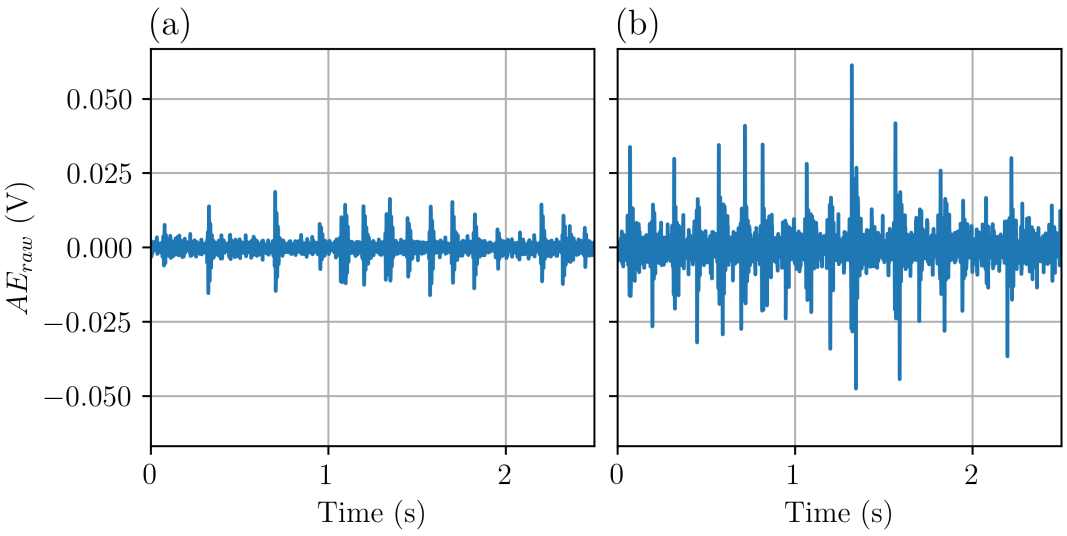


**Fig. 3.20:** Time domain AE signals of the machine bed (a) not moving and (b) moving in the y-axis at 60 mm/min.

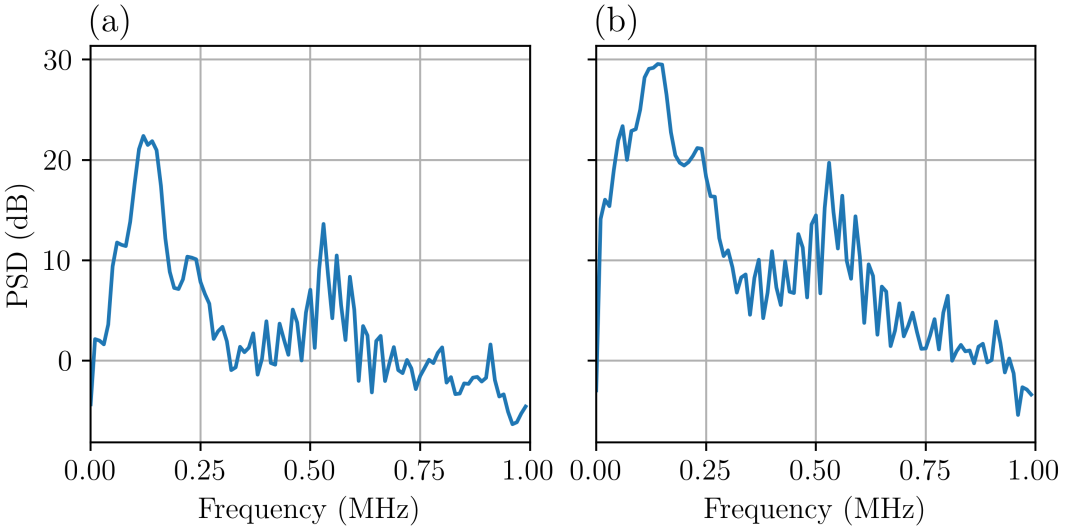


**Fig. 3.21:** Frequency domain AE signals of the machine bed (a) not moving and (b) moving in the y-axis at 60 mm/min.

The previous noise scenarios consider single aspects of the grinding process on the generated noise. However, in reality all of these components combine to form more complex generated noise. To measure the effect of compounding noise components, two additional scenarios, 9 and 10, were conducted simulating a grinding pass "dry" run. Scenario 9 combined both the spindle rotation at 24 000 rpm with flood coolant on top of the workpiece surface. Adding Y-axis travel to scenario 9, scenario 10 conducted a "dry" run of a single grinding pass, with 1 mm of clearance to prevent tool contact with the workpiece. Figs. 3.22–3.23 show the generated noise during scenarios 9 and 10, within the time and frequency domain. The resultant AE signals form a complicated PSD, with multiple distinct peaks at 100, 505, 760 and 900 kHz. Of the two scenarios, scenario 9 resulted in the highest energy AE signal, with a $AE_{AMP}$ of 59.099 $\mathrm{dB_{AE}}$ and a $AE_{RMS}$ of 40.501 $\mathrm{dB_{AE}}$. Whilst, scenario 10 generated AE with an $AE_{AMP}$ of 56.564 $\mathrm{dB_{AE}}$ and a $AE_{RMS}$ of 37.866 $\mathrm{dB_{AE}}$. This difference in amplitude is likely due to the changing coolant application location in scenario 10, as the coolant is fixed relative to the spindle.

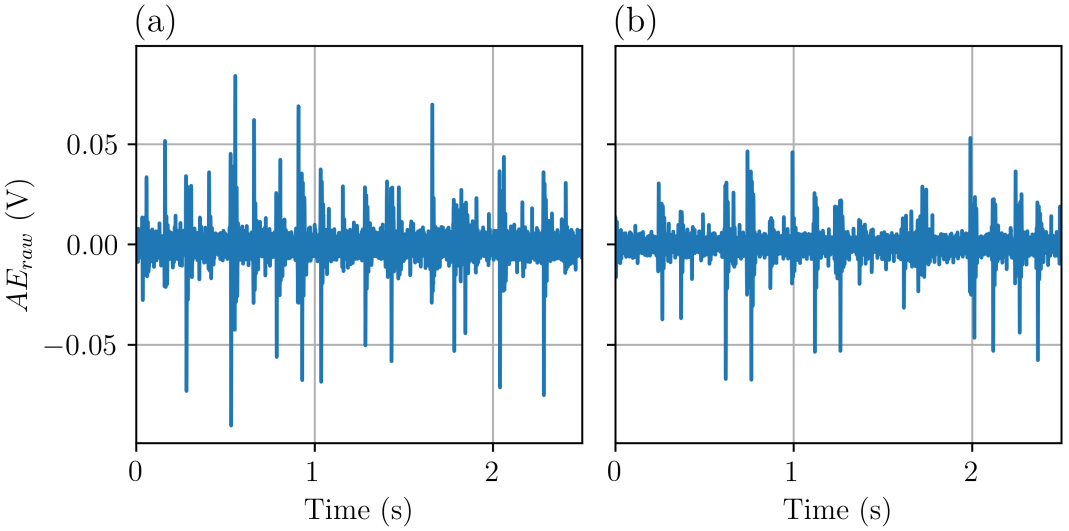


**Fig. 3.22:** Time domain AE signal while (a) the spindle is rotating at 24 000 rpm and flood coolant is on, as well as (b) with y-axis travel at 60 mm/min.

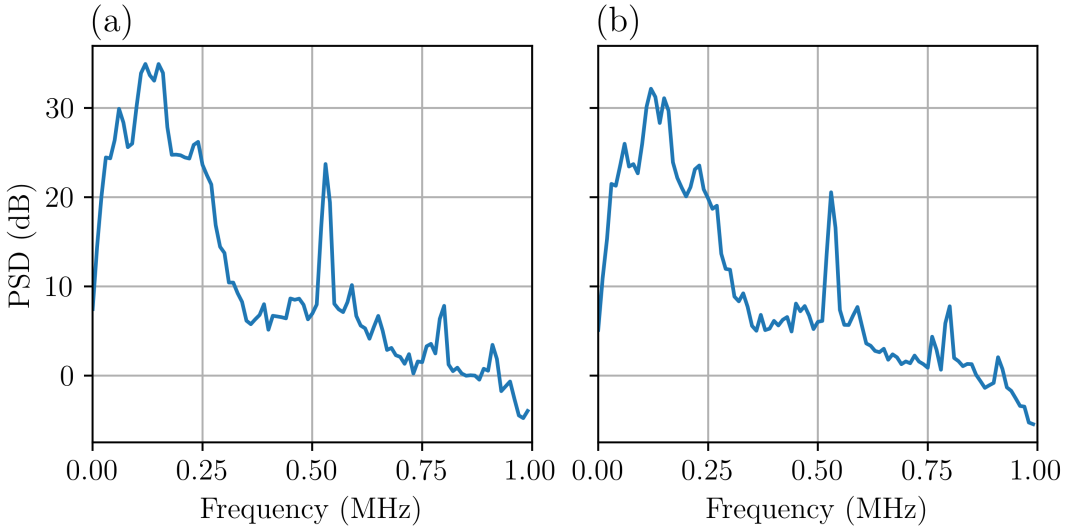


**Fig. 3.23:** Frequency domain AE signal while (a) the spindle is rotating at 24 000 rpm and flood coolant is on, as well as (b) with y-axis travel at 60 mm/min.

Overall, the level of background noise is low considering the environment and scenarios investigated. A baseline $AE_{RMS}$ noise level of 29.490 $dB_{AE}$ is acceptable and common within AE field-testing. Machine operations, such as spindle rotation, coolant and axis travel, all resulted in higher noise level than background. Of which, coolant applied close to the sensor location resulted in the largest increase in AE energy levels, with scenario 5 resulting in a $AE_{AMP}$= 60.208 $dB_{AE}$. However, as seen by the PLBs conducted in Table 3.6 and preliminary acquired grinding signals seen in Fig. 2.11, AE is expected to be acquired above the noise floors presented in all scenarios.

### 3.5.3 AE Sectioning

The AE acquired during each grinding pass, purposely recorded both before and after the DCB was making tool-workpiece contact. This decision was to ensure the entire grinding pass was captured within the AE waveform. A side effect of this choice, however, is the inclusion of between 0.5 – 1.0 s of AE acquired out of contact. These additional and unwanted sections of the AE, sandwich the useful grinding signal and as

such a method of reliably isolating the region of interest was developed. Without this sectioning, any extracted AE features will be impacted by noise and potentially impact further insights into the grinding process. To extract the grinding section, two triggers must be determined, "Trigger Start" and "Trigger End", signifying the start and end of the grinding pass. Fig. 3.24 shows the flowchart to determine both trigger points within any given uninterrupted grinding signal.

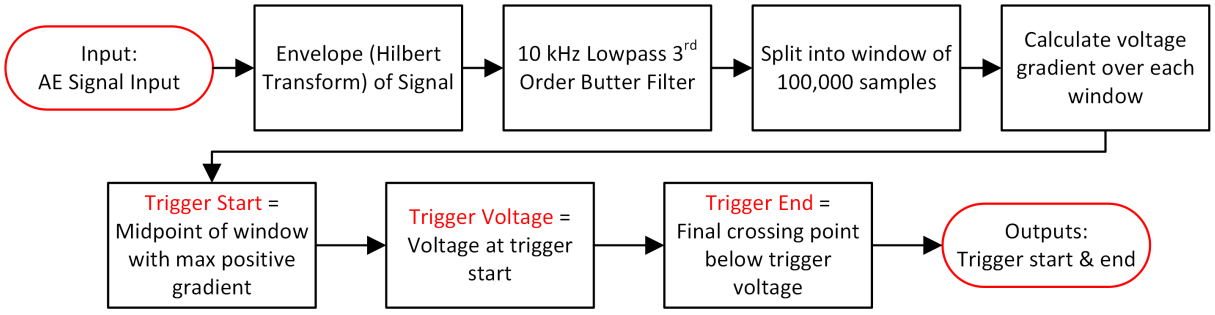


**Fig. 3.24:** Flowchart of the AE sectioning process.

The result of this sectioning process can be seen in Fig. 3.25, whereby the triggers of an example AE signal during a grinding pass are shown throughout the process. Fig. 3.25(a) shows the raw AE signal, in which a clear increase in the continuous AE signal's amplitude can be seen when grinding. The enveloped and filtered AE signal is shown in Fig. 3.25(b), as well as the "Trigger Start", "Trigger Voltage" and "Trigger End" thresholds, as described in Fig. 3.24, overlaid in red. Enveloping a signal with the Hilbert transform, by obtaining the instantaneous amplitude of the analytic signal, is a robust but computationally expensive method. Which then requires some post-processing to remove the high frequency components from the enveloped signal, to better pick the trigger points. Through trial and error, a zero-phase application of a 10 kHz low-pass digital filter, was found to be most effective for this application. Finally, the raw AE signal can be trimmed on either side of these triggers isolating the grinding period, as seen in Fig. 3.25(c).

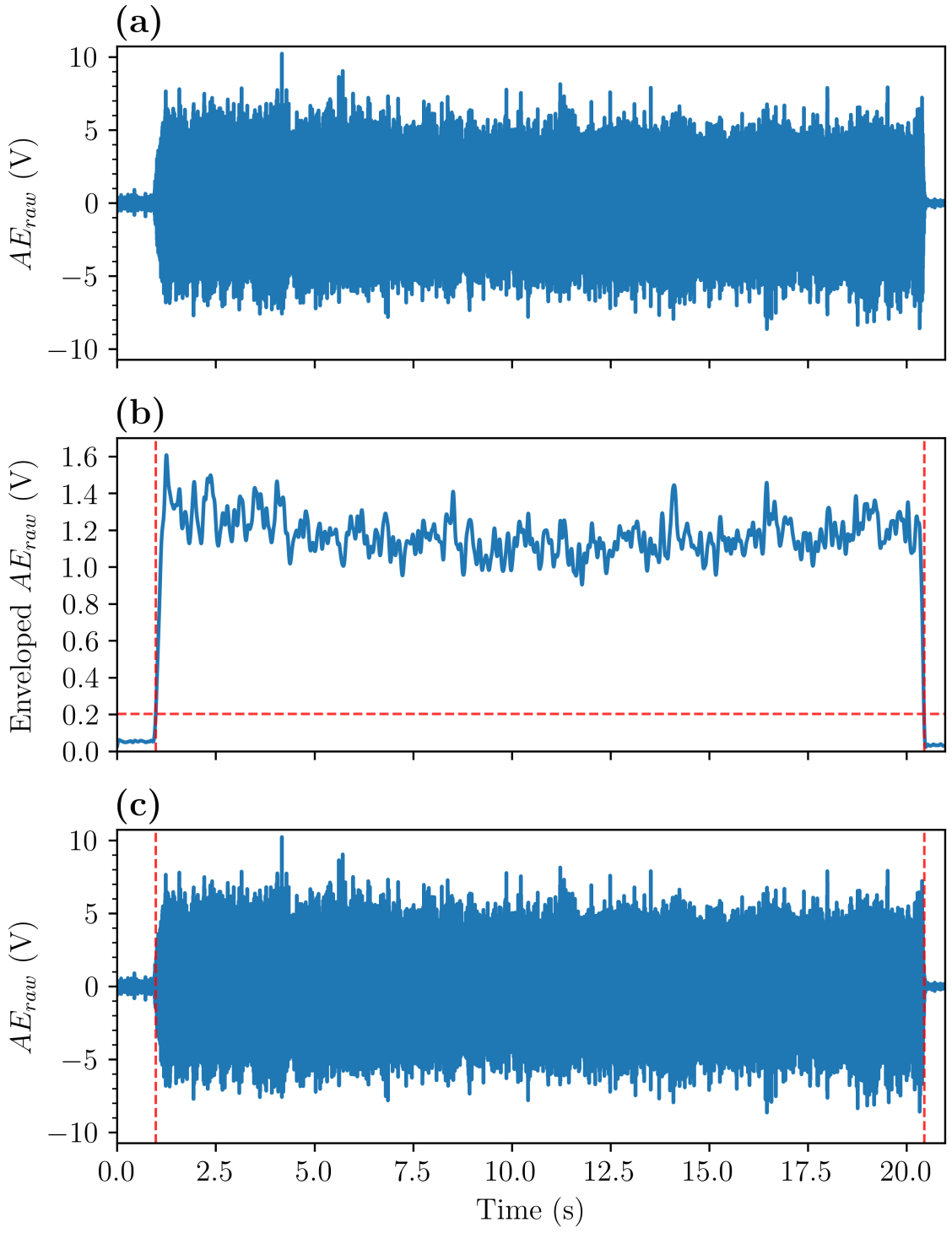


**Fig. 3.25:** The AE sectioning process on an example signal. (a) raw AE from a single grinding pass, (b) enveloped and filtered signal with triggers showed by red dashed lines and (c) showing the location of the triggers on the original raw AE signal.

A window size of 100,000 samples, equating to 50 ms, to calculate the envelope gradient over, was used as a trade-off between resolution in the picking of each trigger point in time, and reliability due to fluctuations in amplitude over smaller time windows. Therefore, the developed triggering process, is not perfectly precise, but importantly robust and accurate across all wear tests. This sectioning process was carried out on each acquired AE signal, and all results based on AE were calculated during this defined grinding period. Additionally, by only windowing a smaller section of the signal to envelope when obtaining the "Trigger Start" threshold, the process was sufficiently fast to not hold up post-processing over the large number of signals.

### 3.5.4 AE Features

Once sectioned, relevant features are extracted from both the time and frequency domain signals. From the time domain, four main features were utilised. The root mean square of the AE signal, $AE_{RMS}$, indicates the overall power across the specified window size, $n$ (Eq. (3.5)). Normally, this window is taken over the whole signal to gain a signal value for $AE_{RMS}$. But by using a rolling window with a smaller size, instantaneous changes in power can be seen, resulting in a similar looking output to the enveloping and filtering in Fig. 3.25(b).

$$AE_{RMS} = \sqrt{\frac{1}{n}\sum_{i=1}^{n} {y_i}^2} \tag{3.5}$$

The maximum absolute value of an AE signal is its amplitude, $AE_{AMP}$ (Eq. (3.6)).

$$AE_{AMP} = \max \|y_i\| \tag{3.6}$$

Both skewness and kurtosis are statistical measures of a distribution. Skewness measures a distribution's symmetry about its mean, $\bar{y}$. The skewness of a normal distribution is zero, with negative values indicating a left-biased skew. The skewness of an AE signal,

$AE_{skew}$ (Eq. (3.7)), is often low due to the oscillating nature of AE. Kurtosis is a measure of a distribution's "tailedness" relative to a normal distribution. The kurtosis of a normal distribution is equal to three, and distributions with heavier tails or more outliers lead to larger kurtosis values. When applied to continuous AE kurtosis, $AE_{kurt}$ (Eq. (3.8)), indicates the proportion of the signal occurring near it's maximum and minimum voltage.

$$AE_{skew} = \frac{\frac{1}{n}\sum_{i=1}^{n}(y_i - \bar{y})^3}{\sigma^3} \tag{3.7}$$

$$AE_{kurt} = \frac{\frac{1}{n}\sum_{i=1}^{n}(y_i - \bar{y})^4}{\sigma^4} \tag{3.8}$$

where $\bar{y}$ is the mean, $\sigma$ the standard deviation and $n$ the number of data points in the signal, $y$.

The FFT was used to transform the time domain AE signals into the frequency domain. A Hanning window was applied to each 1 kHz frequency bin to reduce spectral leakage. From the FFT the PSD was calculated as its modulus squared. PSD partial powers could then be determined as the power within a given frequency bin. Due to the windowing, the PSD was formed of 1000 1 kHz bins. A frequency bin's partial power, $PP$, represents the energy present within a certain frequency range of the AE signal, which can lead to distinguishing and monitoring individual source mechanisms.

# 4 Results

Chapter 3 laid out the foundation to wear a DCB systematically, with regular direct on-machine tool wear and workpiece measurements. The following chapter details the results from three series of wear tests enacting that methodology. Through which a greater understanding of how a DCB wears, and when it should stop being used, was established. Additionally, the capability of AE as an indirect TCM sensing method was investigated, highlighting several time and frequency domain AE features that reliably indicate a DCB's state of wear. The impact of increased DCB $r_{runout}$ on tool lifespan, grinding performance and the generated AE is also quantified.

## 4.1 Wear Test Series

During this thesis, 22 wear tests were conducted under three main testing series; feasibility, runout variation, and control. Table 4.1 shows the numbering of wear tests during each series and details the relevant inspections methods, detailed in Section 3.3, are used.

**Table 4.1:** Wear test numbering and utilised inspection methods.

| Series | Test No. | Inspection Methods | | | |
|---|---|---|---|---|---|
| | | NC4 2D | NC4 3D | OMP600 $a_e'$ | Thermal Drift |
| Feasibility | 1 – 4 | X | | | |
| Probe Test | 5 | X | | X | X |
| Runout Variation | 6 – 17 | X | X | X | X |
| Control | 18 – 22 | X | X | X | X |

Each series was developed to achieve a specific aim as the work evolved. First, a feasibility series was conducted, during which four wear tests were performed to verify the initial methodology. Following this series, a partial test was conducted to validate the developed OMP600 probe cycle before its use, which is not detailed in the following sections. Afterwards, a further series was undertaken using the NIKKEN adjustable tool-holder to investigate the effect of varying DCB runout. During this series, the complete inspection phase methodology was used, following the flowcharts shown in Figs. 3.1, 3.3 and 3.8. Finally, an additional five wear tests were conducted within the control series, using the full inspection suite to collect additional data without the NIKKEN adjustable tool-holder.

### 4.1.1 Initial Feasibility Study

Initially, four wear tests were performed to understand the process and the acquired data. During each test, AE and 2D NC4 scans were acquired in each cycle of the wear test. Table 4.2 shows the total number of grinding passes completed by each DCB prior to failure, as well as the change in DCB mean radius across each test. The variation in a DCB's total useable life is apparent through the difference between each wear test's completed grinding passes. Across the four tests, a range of 55 passes was observed, which due to the consistent methodology and tool/workpiece specification must be the result of varying DCB wear rates. The inbuilt stochastic nature of a DCB's abrasive layer is likely the main factor in this discrepancy. This is further supported by considering the amount of radial wear experienced in each wear test. Comparing test 1 and 3, both of which started with a tool of approximately the same radius, the DCB used during test 1 completed 37 more passes with 24 µm less overall radial wear.

**Table 4.2:** Feasibility series overview.

| Test No. | Total No. Passes | DCB Mean Radius | | |
|---|---|---|---|---|
| | | Initial (mm) | Final (mm) | Wear (%) |
| 1 | 213 | 0.676 | 0.636 | 5.980 |
| 2 | 163 | 0.662 | 0.635 | 4.504 |
| 3 | 176 | 0.674 | 0.610 | 10.085 |
| 4 | 158 | 0.665 | 0.610 | 8.670 |

Fig. 4.1 shows the 2D NC4 scans throughout each wear test, in which the degradation of each DCB's surface due to wear can be monitored. From these plots, high spots on the DCB's surface can be identified as a result of each tool's runout. Runout presents as a prominent high spot across half the tool's circumference, as seen in Fig. 4.1(a) and Fig. 4.1(b). Whereas, the DCB during test 3, shown in Fig. 4.1(c), experienced a $r_{runout}$ of $<$10 µm for the majority of its life, seen through the consistent radius of $\sim$0.67 mm around its circumference.

Additionally, Fig. 4.1 also shows the formation of "surface craters" during each test, seen as the dark blue regions. Fig. 4.1(a) shows this effect at 4.2 rad after 75 passes have been completed, whereby a small region on the tool's circumference is worn significantly below the mean surface height during 1–2 passes. Following the formation of this large but isolated step height, the crater expands radially around the tool's circumference, which leads to it encompassing over a third of the DCB's surface in test 1. Each DCB used during the feasibility series formed a surface crater on it's surface as it was worn, resulting in craters of varying circumferential width and radial depth. These craters form as a result of the complete removal of the Ni-diamond abrasive layer in localised regions. This explains their rapid circumferential expansion as the loss of diamond grains in isolated spots forces the surrounding areas to bear higher grinding forces, removing more material, and consequently undergoing accelerated wear. The width and depth of each surface crater appears to be linked to the DCB's $r_{runout}$, likely the consequence of sections of the DCB experiencing increased grain penetration into the workpiece as a

result of its $r_{runout}$.

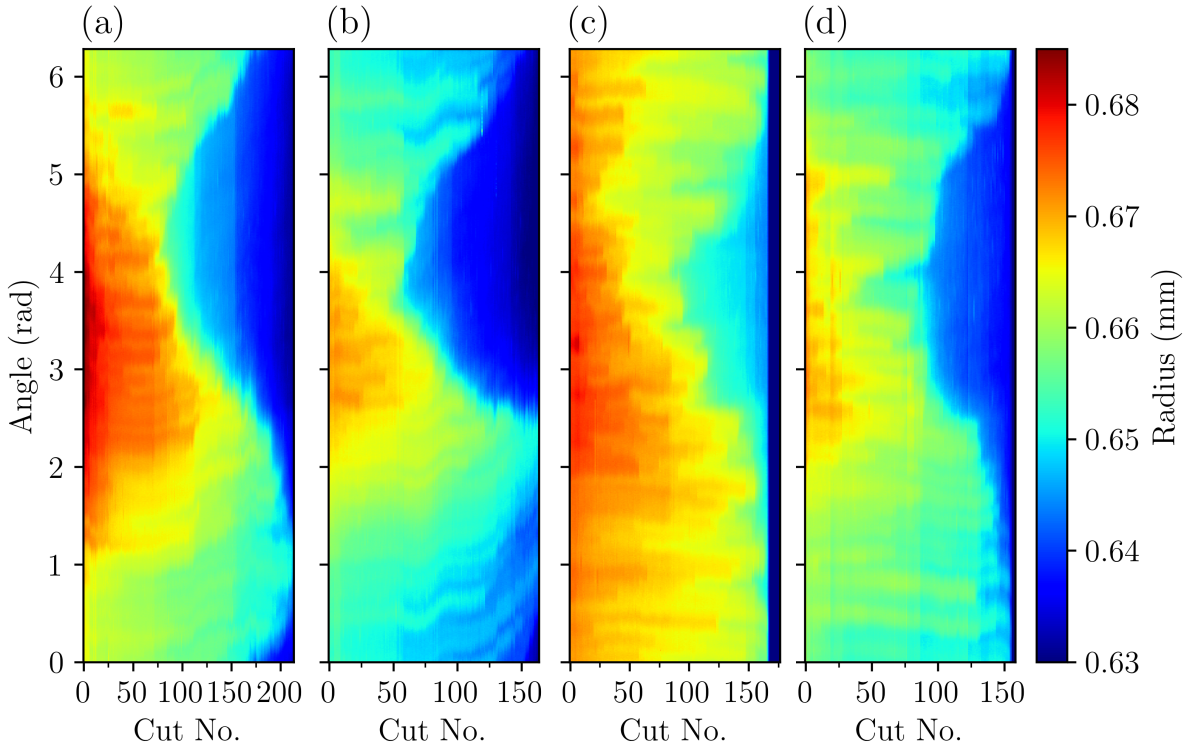


**Fig. 4.1:** 2D NC4 circumferential surface scans of each DCB during the feasibility series, with tests 1 – 4 shown in (a – d).

Fig. 4.2 shows two images from either side of the DCB used during test 2, after the g-code had determined tool failure, from which multiple observations of the process can be seen. Firstly, a clear transition between the worn and unworn regions of the DCB can be seen along its axis. The unworn section is shiny with diamond grains clearly adhered within. The worn region, however, is darker where diamond grains remain, a result of adhered workpiece particulate. The surface crater formed during test 2 has resulted in roughly half of the DCB's abrasive layer being removed, exposing the Ni undercoating and steel core on one side. Oxidation of the steel core where exposed, due to the use of a water-based coolant, gives a visual indication of the regions in which the entire Ni-diamond layer had been removed. The patchy nature of the oxidation also shows how inconsistent the wear is along the DCB's length. Fig. 4.2(a) shows that in this state of

wear, regions of the tool have penetrated to the steel core. But other sections have only removed the Ni-diamond layer, leaving the Ni undercoating intact, seen by regions lacking oxidation but void of abrasive grains. Failure of this DCB resulted from a small region of the tool, at its tip, being worn at an accelerated rate, leading to partial fracture.

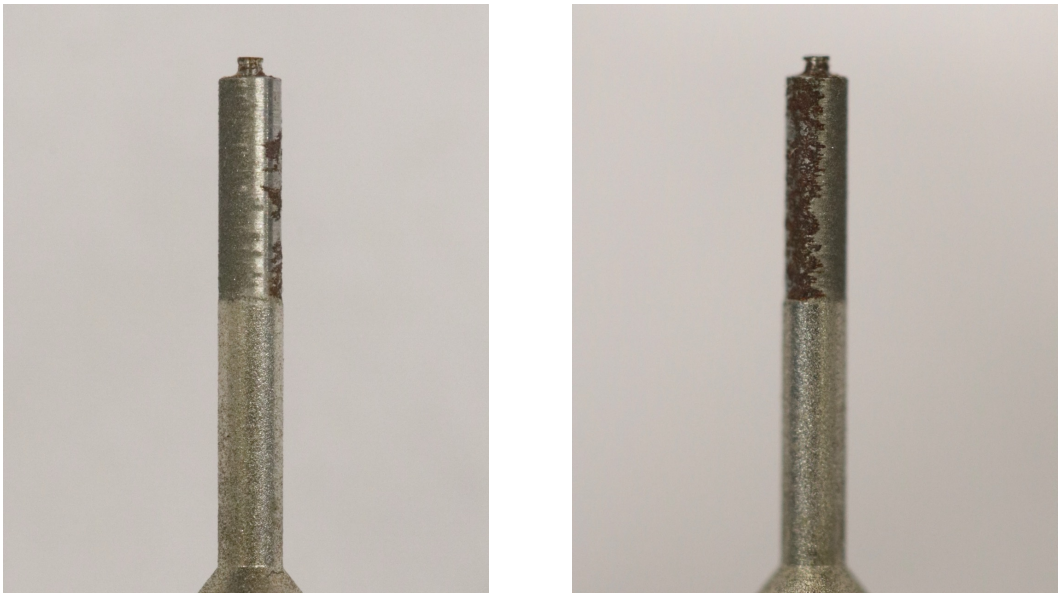

(a) (b)

**Fig. 4.2:** Images from two opposite sides of the DCB used in test 2 post-failure.

Fig. 4.3 shows the four extracted NC4 attributes during each wear test. Both the mean and peak radius of each DCB follow the three-phase wear curve trend, as presented in Section 2.1.3. The mean radius shows a smoothed trend when compared to the peak radius, whilst still enabling identification of the wear phases. Phase I - wear-in of all four tests occurred rapidly, lasting between 1–2 passes, as seen by the sharp drop in both radius attributes initially. During this phase, the peak radius is reduced significantly, indicating that weakly adhered grains or superfluous Ni bond material are quickly removed. Following this phase, every DCB transitioned into phase II - steady state, whereby the tool slowly reduced in radius at a consistent rate. This phase lasted the majority of each DCB's total life. During the steady-state phase, each DCB used in the feasibility series formed their respective surface craters. Leading up to their failure points, tests 3 and 4 presented signs of phase III - wear-out, through the instantaneous and large reduction in

mean radius in Fig. 4.3(c – d). Tests 1 and 2, however, failed without prior indication from any of the extracted NC4 features shown in Fig. 4.3(a – b). Overall, mean radius from the 2D NC4 surface scans can be seen as a clear indicator of the DCB wear state. However, even with regular measurements of a DCB's $r_{mean}$ does not provide sufficient information to predict failure to optimise a tool change strategy on its own. This is partially due to the large variation in initial tool state and varying wear rates. Whilst the nominal radius of each DCB was 0.65 mm, all four tools did not reach that value until having completed at least 100 grinding passes.

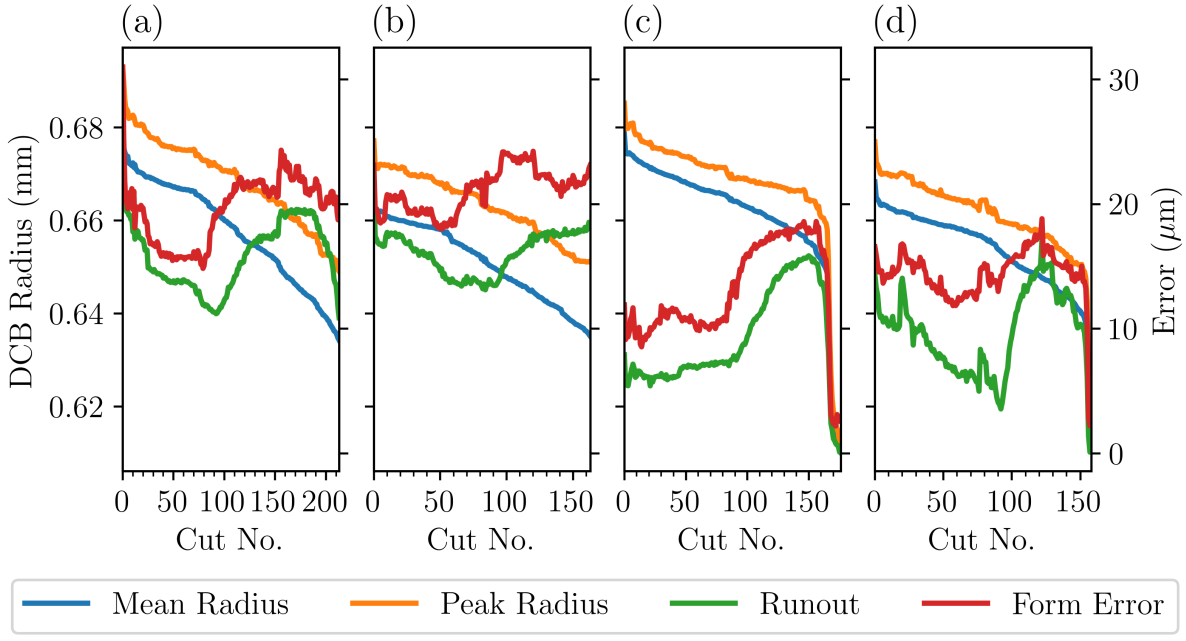


**Fig. 4.3:** NC4 attributes from each DCB during the feasibility series, with tests 1 – 4 shown in (a – d).

Alongside the variation between each DCB's initial radius, Fig. 4.3 also shows the large variation in runout between each wear test. During the series, a DCB's initial runout ranged between 7.9 – 23.2 µm. As each DCB wears, it's runout reduces as a result of the high spot wearing at an accelerated rate to the rest of the surface. However, once a crater has formed on the surface the trend changes, and the $r_{runout}$ starts increasing from the local minimum. The $r_{runout}$ during test 3 differs and instead stays constant, after the

initial wear-in phase, rather than decreasing to a minimum. This effect is because the DCB used during test 3 has the lowest initial runout level of the four initial wear tests, as seen in Fig. 4.1(c), whereby there is no distinct high spot around its circumference. The change in trend of $r_{runout}$ in each test indicates a surface crater has formed and worn below the mean surface height.

The inspection cycle employed during the feasibility series was restricted in two primary ways.

- Firstly, it gave no indication of whether a DCB was still effective in removing material from the workpiece. Each wear test continued for at least 50 passes once a surface crater had been formed on the DCB, however without tracking of the workpiece's removal rate it's unclear whether the DCB is still useful. This problem led to the development of the OMP600 probe measurement cycle for further wear tests.
- Secondly, another limitation stemmed from the 2D nature of the NC4 scans. By only measuring at one axial position along the DCB's length, a large part of the tool's wear can be missed. This resulted in the measurements from tests 1 and 2, in Fig. 4.1(a – b) and 4.3(a – b), indicating the DCBs had not reached the wear-out phase. However, in reality the tools had worn significantly outside the axial measurement position, leading to unforeseen failure. This issue is compounded when trying to relate AE acquired during the grinding passes to any of these NC4 attributes. To remedy this problem, the 3D NC4 scans were developed and implemented for following wear tests to better understand the DCB's overall wear state.

Fig. 4.4 shows the $AE_{raw}$ signal of the $50^{\text{th}}$ grinding pass of test 3, as a randomly selected example of the acquired AE throughout each wear test. Fig. 4.4 additionally shows the $AE_{RMS}$ calculated with a rolling window of 0.125 s overlaid. As seen previously, the AE produced during grinding is both high energy and continuous in nature. The point of tool-workpiece contact can be seen in both the $AE_{raw}$ and $AE_{RMS}$ signals as a large increase in amplitude from the noise floor. Due to the length of the recorded AE and the high sampling rate, 2 MHz, viewing the whole $AE_{raw}$ signal of any pass does not reveal much about the process.

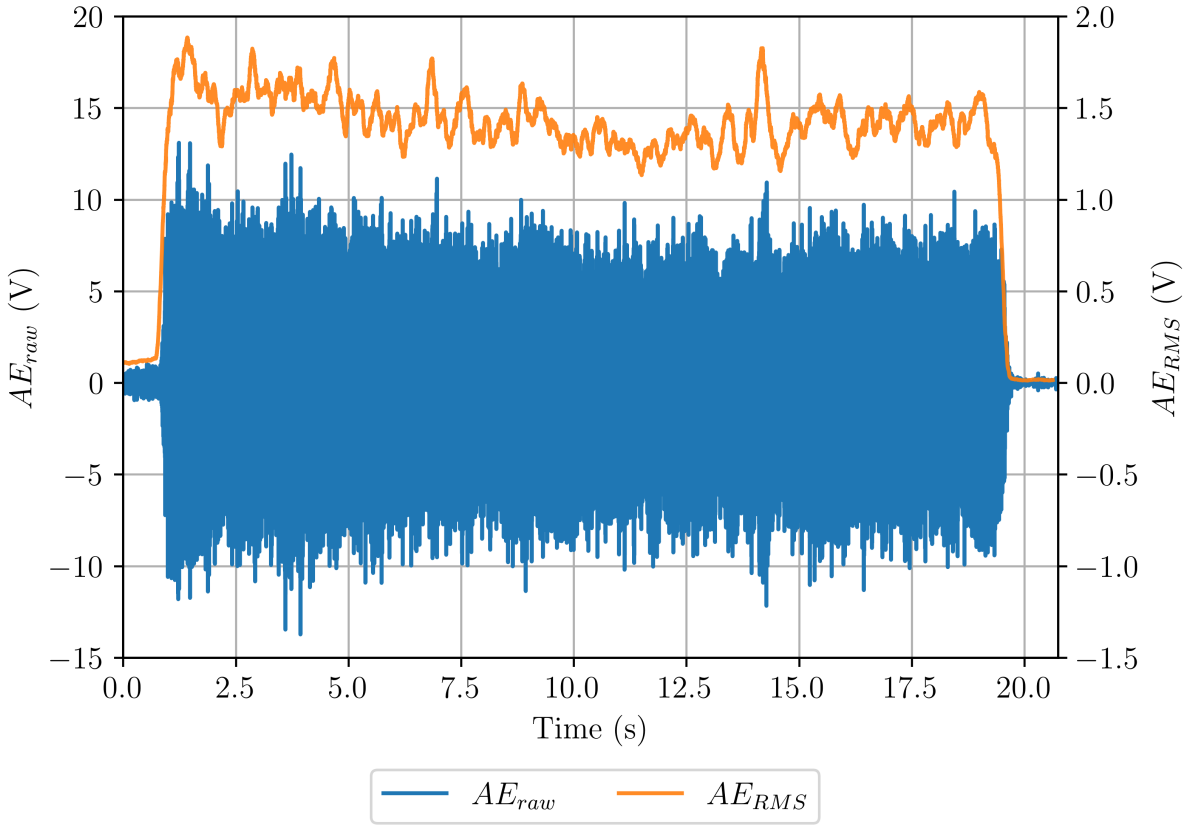


**Fig. 4.4:** The $AE_{raw}$ and $AE_{RMS}$ of the 50$^{\text{th}}$ grinding pass of test 3.

Fig. 4.5 shows a 15 ms period, between 5 – 5.015 s, of the $AE_{raw}$ signal from the 100$^{\text{th}}$ grinding pass of each wear test in the series. This focused view of the AE signal reveals much more information about the given grinding pass. The first observation is the large periodic pulsing of the $AE_{raw}$, especially prevalent in tests 1 and 2, Fig. 4.5(a – b). The pulsing occurring at a frequency of 400 Hz, every 2.5 ms, equating to the rotational speed of the DCB. Therefore, these large amplitude pulses of AE are due to a DCB's $r_{runout}$ induced high spot. A tool with higher $r_{runout}$ will present a singular high spot around its circumference, as seen in Fig. 4.1(a – b), which when grinding will result in a disparity in a DCB's workpiece penetration as it rotates. This disparity in contact then results in varying AE levels during each DCB revolution, presenting as the pulsing $AE_{raw}$ seen in Fig. 4.5.

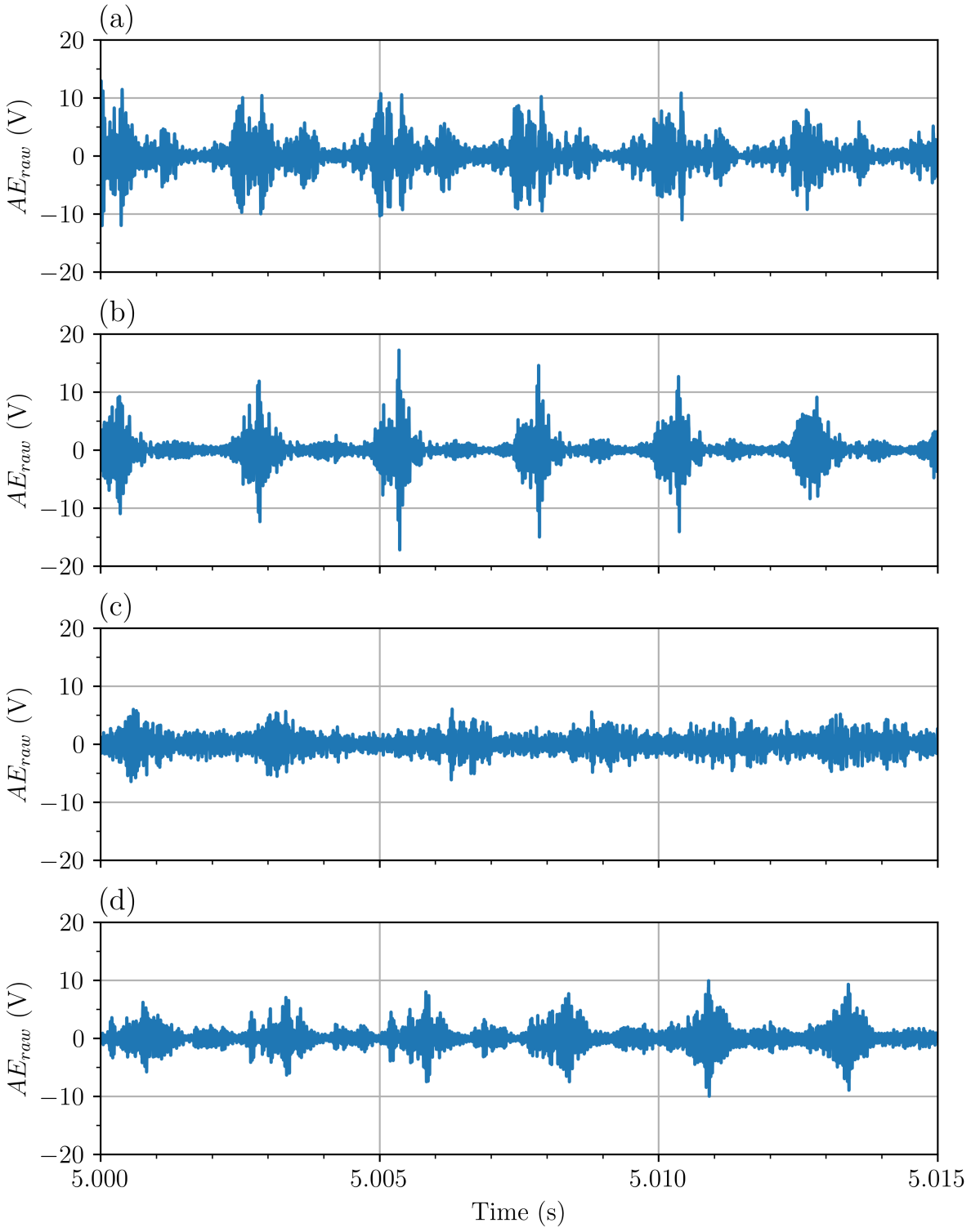


**Fig. 4.5:** A 15 ms section of $AE_{raw}$ from the 100$^{\text{th}}$ grinding pass of each wear test in the feasibility series, with tests 1 – 4 shown in (a – d).

This can be verified through looking at the difference between each DCB's state of wear to generate the AE in Fig. 4.5. Fig. 4.6 shows the 2D NC4 surface scans of each DCB after the $100^{\text{th}}$ grinding pass. The four DCBs were clearly in varying states of wear, with each showing a surface crater around its circumference of varying sizes. The wear state can clearly be seen to link to the produced AE. The DCB from test 3 produced the most continuous $AE_{raw}$ signal, in Fig. 4.5(c), with minimal difference in amplitude around the DCB's revolutions. The surface measurement of this DCB, in Fig. 4.6, shows a consistent surface with no distinct high spot and only a small surface crater covering less than 1 rad of the circumference. Resulting in the DCB after this pass having a $r_{runout} = 9.388\,\mu\text{m}$ and $r_{fe} = 16.012\,\mu\text{m}$. In stark contrast, test 2 produced the largest amplitude and most distinct pulses of $AE_{raw}$ during each DCB revolution of the four wear tests. Which aligns well with the NC4 surface measurement of the DCB from test 2 in Fig. 4.6. The surface scan shows a distinct and prominent high spot at 2.5 rad, as well as a deep surface crater encompassing half the DCB's circumference. Both of which combine to produce a high amplitude pulse with a large drop-off on each tool revolution. The DCB in test 2 had a $r_{runout} = 15.512\,\mu\text{m}$ and a $r_{fe} = 24.057\,\mu\text{m}$.

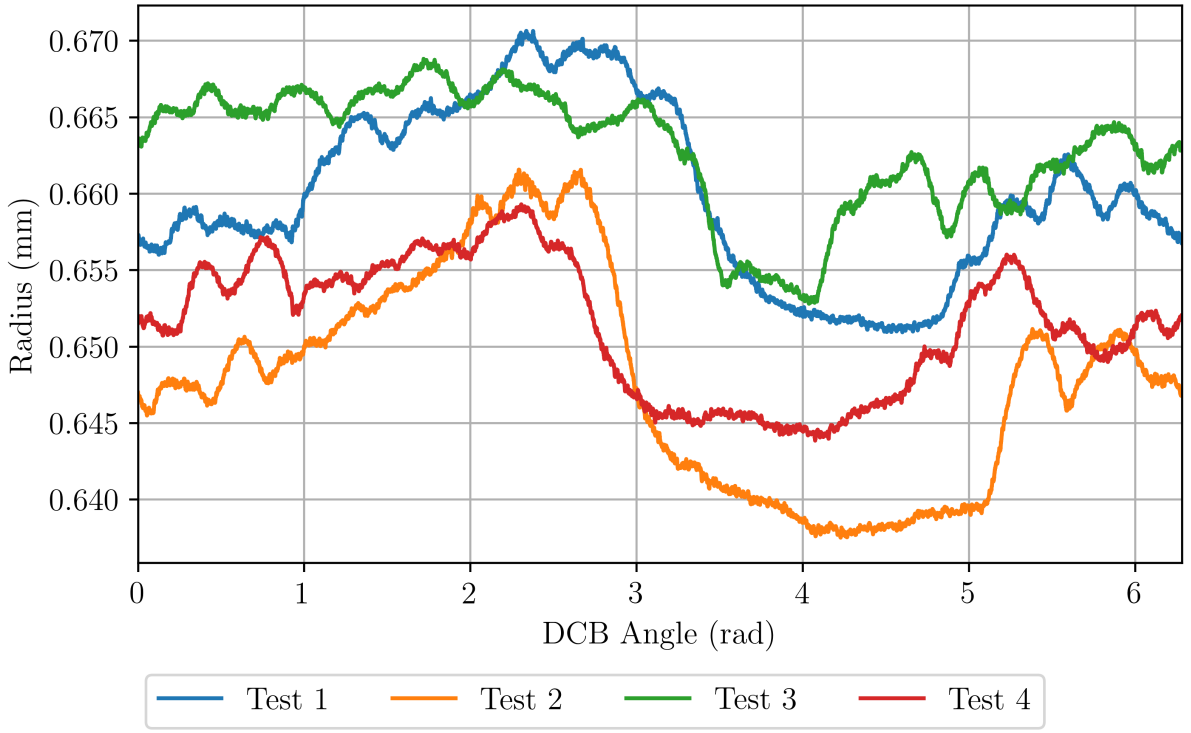


**Fig. 4.6:** 2D NC4 surface scan of each DCB in the feasibility series after the 100$^{\text{th}}$ grinding pass.

The time-domain AE features extracted across each grinding pass in the feasibility series are shown in Figs. 4.7–4.10, each of which also showing a moving average over five data points as a black dashed line. Looking at the $AE_{RMS}$ generated during each test, shown in Fig. 4.7, there is significant variation in energy as each wear tests progresses but also between the wear tests themselves. Across each of the four tests, following the initial variation of $AE_{RMS}$, due to the DCB's wear-in phase, the $AE_{RMS}$ reaches a baseline. Taking test 1 as an example, the first grinding pass resulted in a $AE_{RMS}$ of 1.33 V rising to 2.23 V during the sixth pass. Other tests in the series experienced a similar level of change over the initial period, with some falling to a baseline instead of rising. This variation is inline with a grinding wheel undergoing phase I - wear-in, during which the DCB's surface will change significantly, seen in both Figs. 4.1 and 4.3. The extent of this surface change, indicated through the change in $AE_{RMS}$ is perhaps not shown through the 2D NC4 scans, whereas AE captures the impact of the whole DCB.

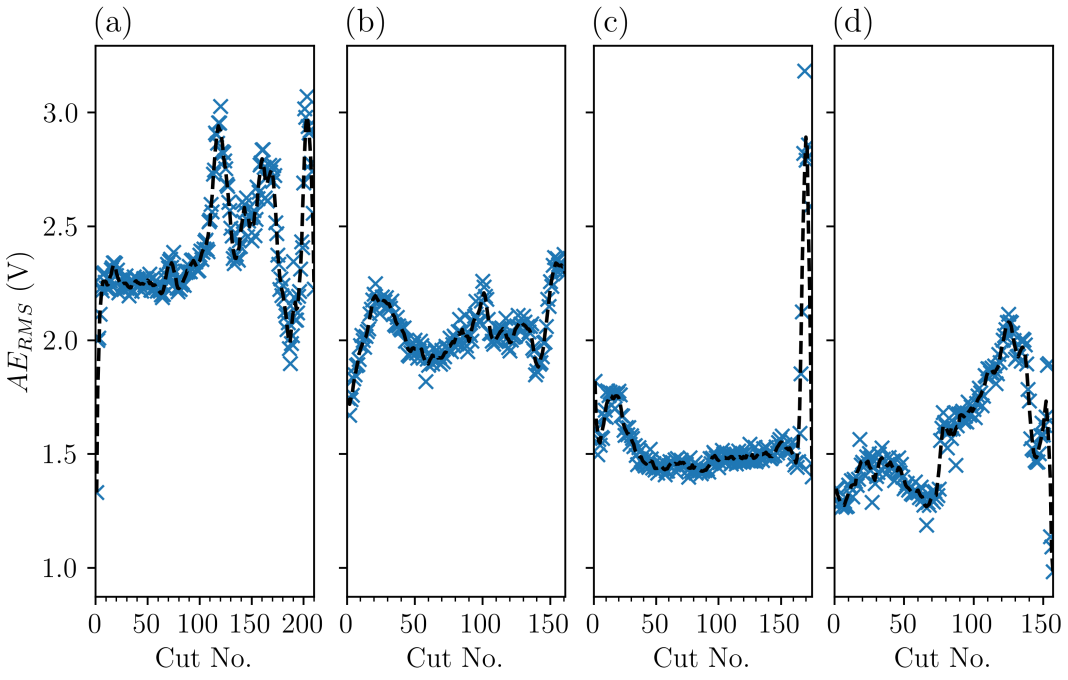


**Fig. 4.7:** $AE_{RMS}$ across each wear test in the feasibility series, with tests 1 – 4 shown in (a – d).

The creation of surface craters, in all tests, resulted in increases to the $AE_{RMS}$, most prominently seen after cuts 100 and 75 in tests 1 and 4. The $AE_{RMS}$ during test 2 also increases after cut 50 when the crater forms, in Fig. 4.1(b), but the increase is not as clearly linked to the crater, potentially indicating that other regions of the tool are wearing differently, making the $AE_{RMS}$ less clear to interpret.

The most interesting $AE_{RMS}$ data comes from test 3, in Fig. 4.7(c). Due to the DCB's low runout and therefore more consistent wear, the $AE_{RMS}$ produced throughout closely follows the three phase wear cycle. The initial variation of $AE_{RMS}$ due to the wear-in phase lasts ∼30 passes, explained by a greater proportion of the tool's surface undergoing wear-in simultaneously rather than just the high spot. Following this, the DCB's steady-state phase produced a more regular and consistent level of $AE_{RMS}$ compared to the other three tests. Which aligns with the steady rate of wear around the DCB's circumference, in contrast to the other wear tests in which a high spot due to higher levels of runout leads to varying wear rates around the circumference. In Fig. 4.1(c) a surface

crater can be seen to start forming after 100 passes, resulting in a less severe step in radius, at 100 passes in Fig. 4.7(c) the trendline shows a slight increase in the baseline $AE_{RMS}$. Suggesting that potentially the entire DCB surface has started to reach wear-out at around the same time. Supporting this is the dramatic increase in $AE_{RMS}$ as the tool reaches its failure point.

Fig. 4.8 shows the $AE_{AMP}$ during each test of the feasibility series. The $AE_{AMP}$ is an inherently more noisy signal due to no averaging in its calculation. Both tests 1 and 2, Fig. 4.8(a – b), shows a gradual increase in $AE_{AMP}$ as the wear test progresses. The $AE_{AMP}$ from tests 3 and 4 showed more variation inline with the DCB's wear seen across Figs. 4.1 and 4.3. The increased DCB $r_{runout}$ of tests 1 and 2 appear to also increase the $AE_{AMP}$, an advantage of not averaging the AE signal as seen in $AE_{RMS}$.

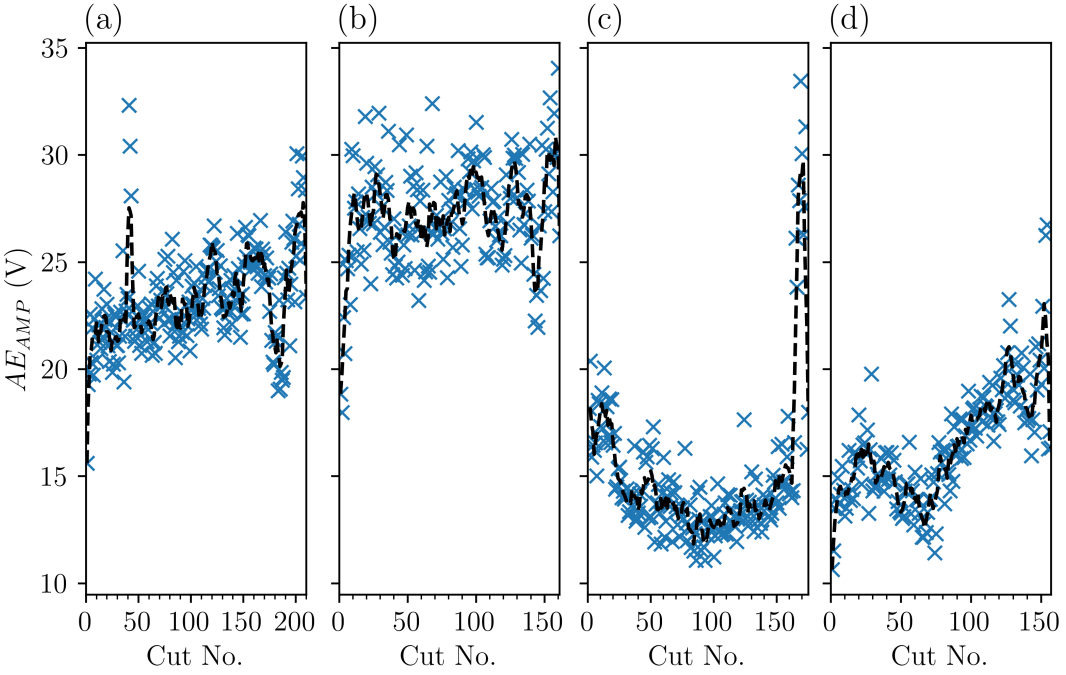


**Fig. 4.8:** $AE_{AMP}$ across each wear test in the feasibility series, with tests 1 – 4 shown in (a – d).

The two statistical AE features, $AE_{kurt}$ and $AE_{skew}$, calculated across each wear test, are shown in the Figs. 4.9 and 4.10. An idealised DCB with no surface defects,

consistent grain distribution and a low level of $r_{runout}$, should produce a consistent level of continuous AE resulting in a symmetrical normal distribution of AE, resulting in a low $AE_{kurt} = 3$, and a $AE_{skew} = 0$. Both Figs. 4.9 and 4.10 show variation in $AE_{kurt}$ and $AE_{skew}$, with the $AE_{kurt}$ also varying in overall level across the four tests.

The $AE_{kurt}$ during each wear test appears to be intrinsically linked to the level of contact/grain penetration a DCB makes with the workpiece, around its circumference. The $AE_{kurt}$ of each signal shown in Fig. 4.5 are; (a) Test 1: 8.404, (b) Test 2: 14.927, (c) Test 3: 4.636 and (d) Test 4: 8.742, aligning well with the indicated contact from the $AE_{raw}$ signal. And as seen in Fig. 4.9 changes in $AE_{kurt}$ are often accompanied by changes in the DCB's $r_{runout}$ and $r_{fe}$, acting as a useful metric to track the formation of surface craters. Fig. 4.10 shows a similar link between $AE_{skew}$ and the tool's level of contact and surface crater formation, with less clarity than presented by the $AE_{kurt}$.

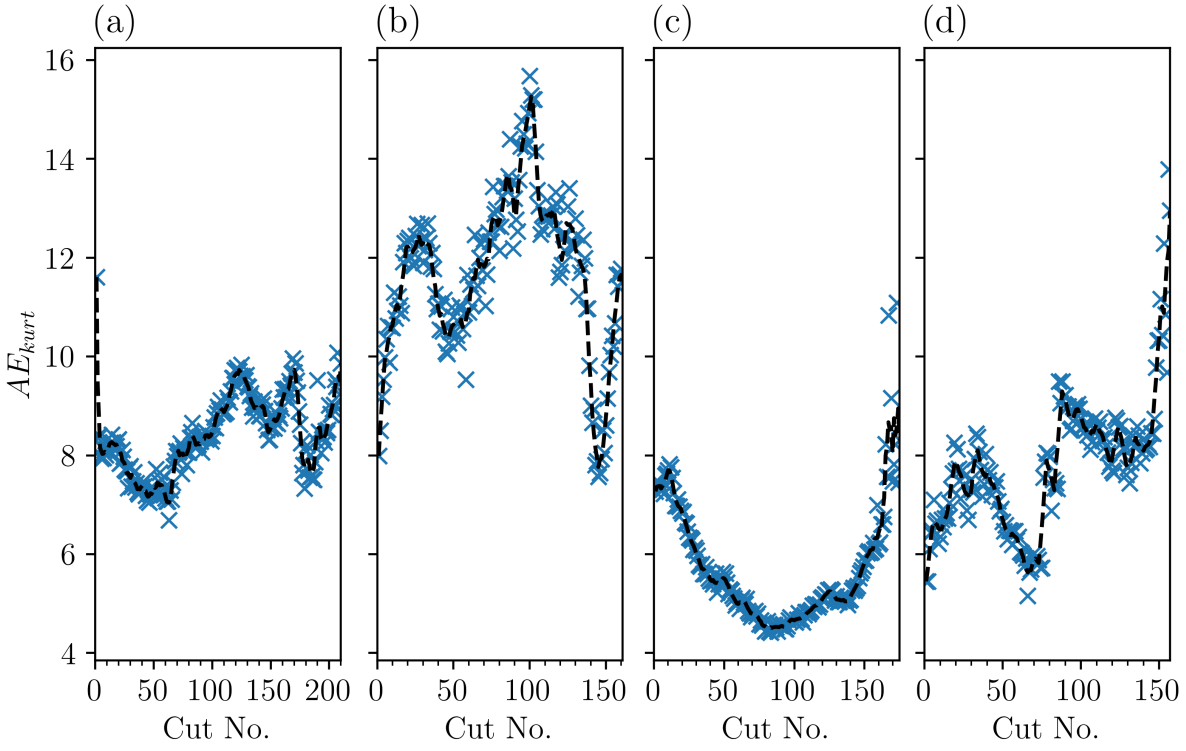


**Fig. 4.9:** $AE_{kurt}$ across each wear test in the feasibility series, with tests 1 – 4 shown in (a – d).

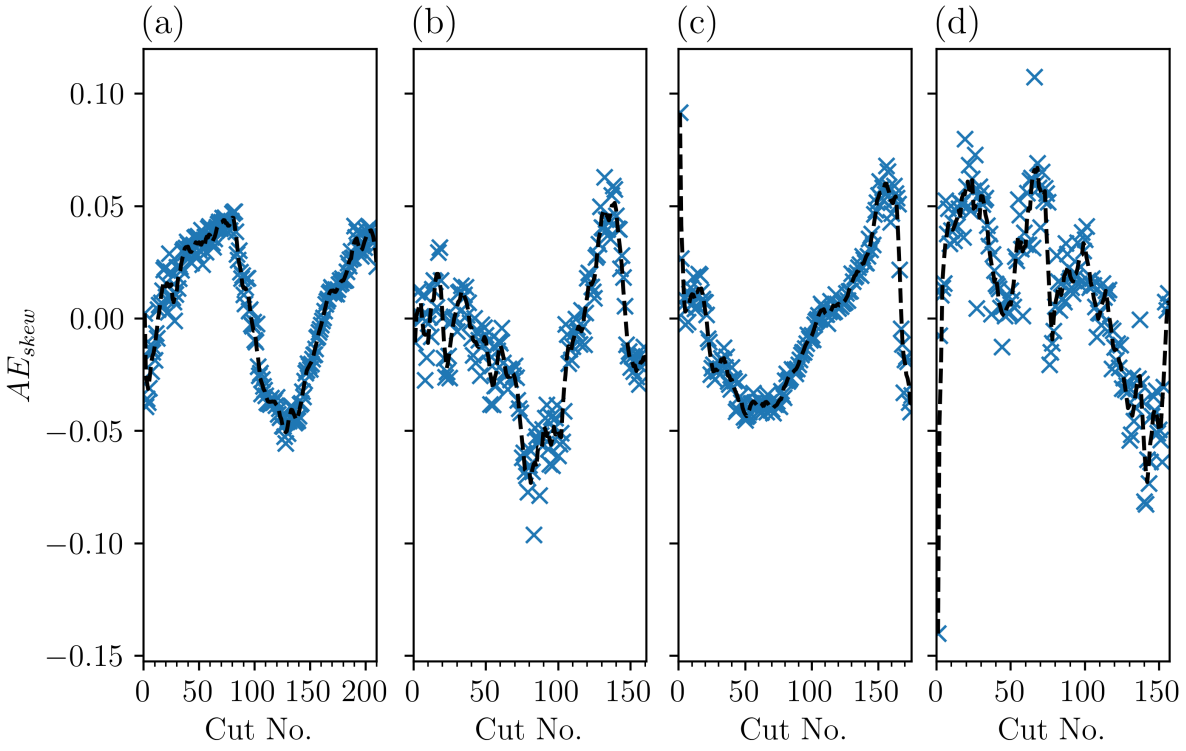


**Fig. 4.10:** $AE_{skew}$ across each wear test in the feasibility series, with tests 1 – 4 shown in (a – d).

Fig. 4.11 shows the PSD from the 100$^{\text{th}}$ grinding pass of each wear test in the series. With Fig. 4.12 showing a pseudo-spectrogram throughout each test's duration, by stacking the PSD from each grinding pass. All four PSDs follow a similar spectrum shape, differing in amplitude at certain frequencies. Importantly, peaks and troughs are consistent in their frequency across the four tests, such as at 100, 240, 291 and 520 kHz, implying a similar process has been used to generate the AE. The observed loss in amplitude is expected as frequency increases, due to the higher attenuation rate of high frequency signals over the distance between source and sensor. Seen in Fig. 4.12, the amplitude at given frequencies are not constant during the wear test, suggesting the frequency content of the AE contains relevant information about the tool's changing wear level throughout the test.

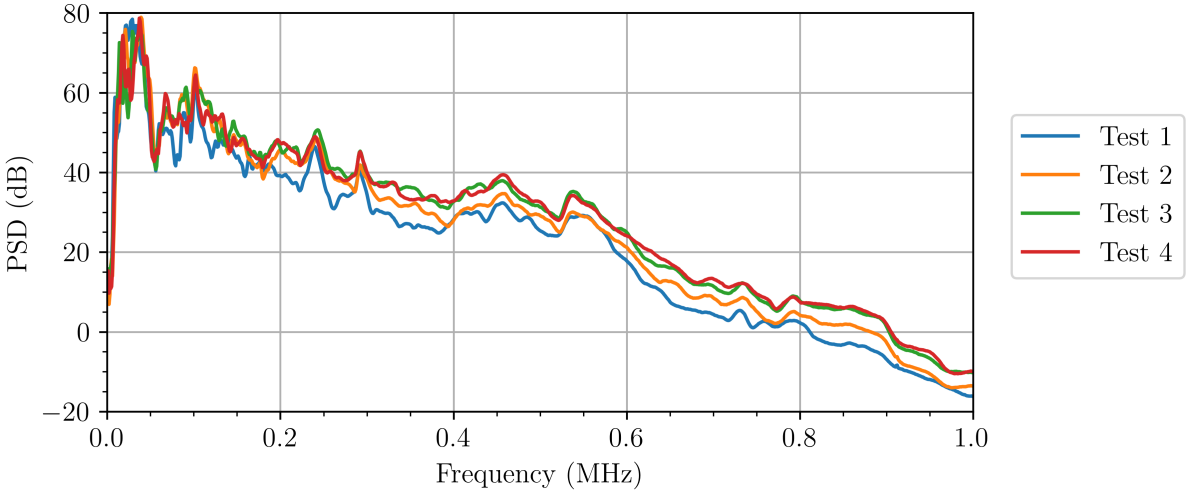


**Fig. 4.11:** PSD from the 100$^{\text{th}}$ grinding pass of each wear test in the feasibility series.

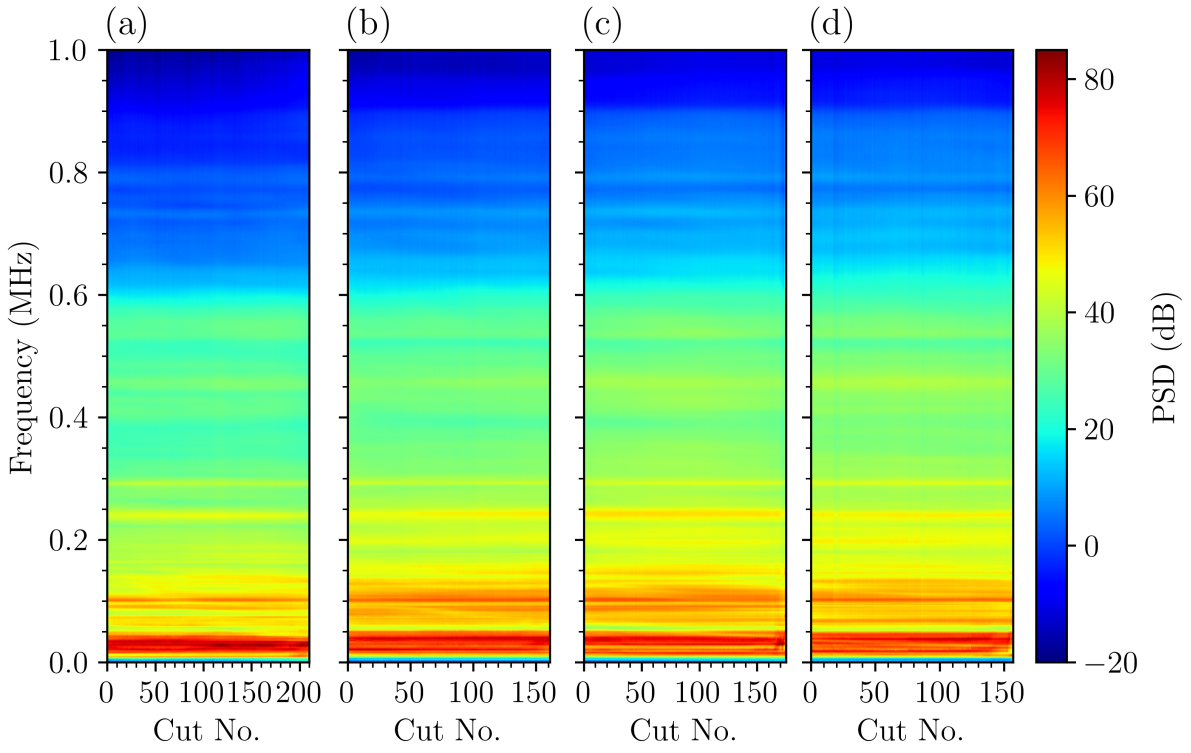


**Fig. 4.12:** Pseudo spectrogram of the PSD from each grinding pass during each wear test of the feasibility series, with tests 1 – 4 shown in (a – d).

Compared to the investigated AE time domain features, AE frequency domain fea-

tures showed a much higher level of correlation to the DCB wear metrics. Figs. 4.13–4.17 each show the $PP$ of a specific frequency bin during each wear test, from the spectrogram in Fig. 4.12. The trends of all the five presented $PP$s vary significantly across each test. As an example, Fig. 4.14 shows $PP_{35}$, the partial power within the 35 kHz frequency band, which during tests 1 and 4 shows a distinct correlation to the DCBs overall wear. The same correlation can be seen by the $PP_{134}$ in Fig. 4.15, whereby tests 3 and 4 show clear inflection points aligned to surface crater formation and therefore a reduction in tool contact, whilst tests 1 and 2 present contrasting trends. However, the trends during these two wear tests are opposing, with the $PP_{35}$ in test 1 falling over the DCB's life and it rising during test 4. This variation makes it difficult to isolate potential source mechanisms within set frequency ranges or set DCB limits based on these features. Therefore, whilst a large amount of information relating to the wear of each DCB is present within the $PP$ features, it is hard to make useful decisions about the tool's wear state.

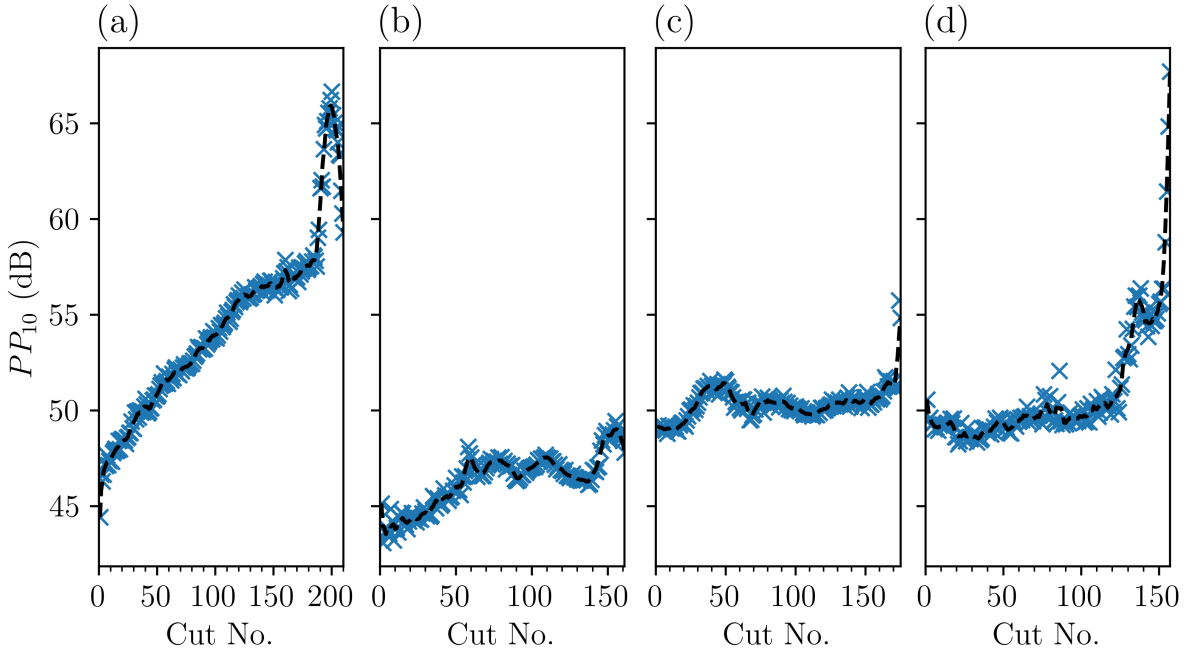


**Fig. 4.13:** $PP_{10}$ during each wear test in the feasibility series, with tests 1 – 4 shown in (a – d).

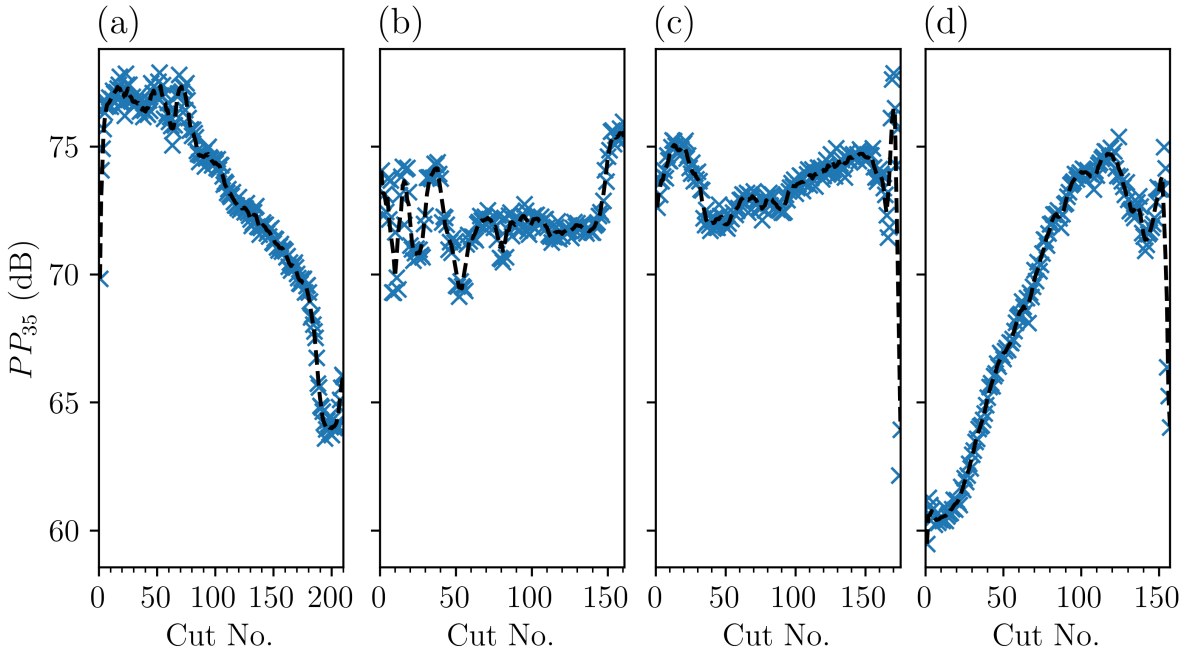


**Fig. 4.14:** $PP_{35}$ during each wear test in the feasibility series, with tests 1 – 4 shown in (a – d).

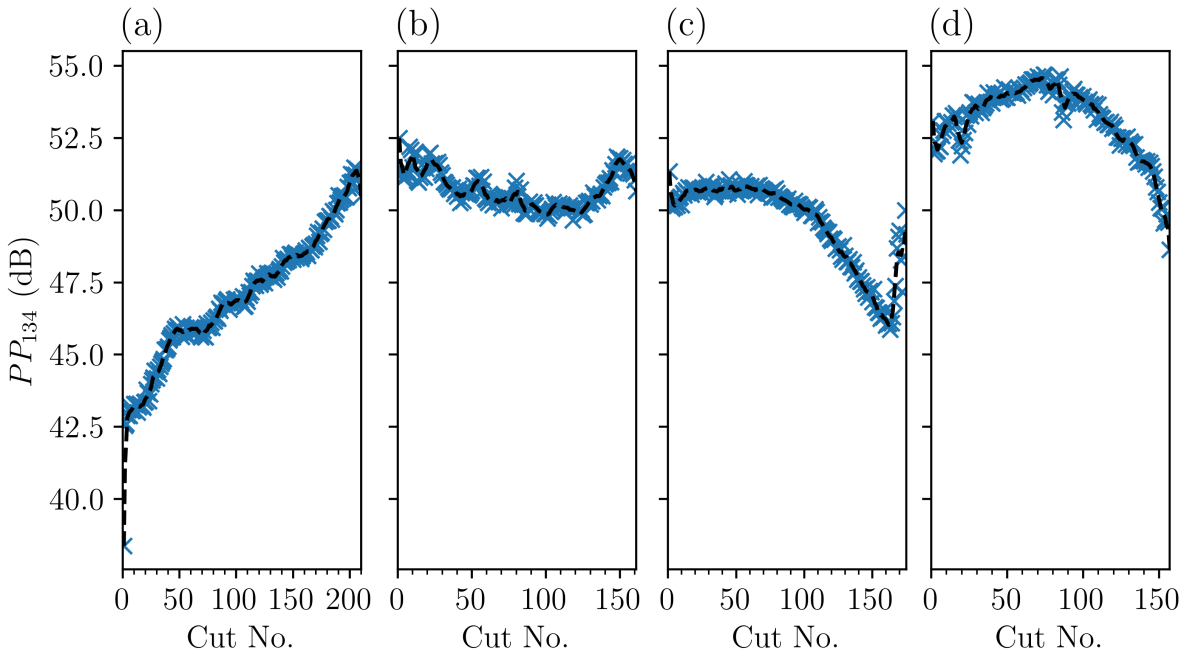


**Fig. 4.15:** $PP_{134}$ during each wear test in the feasibility series, with tests 1 – 4 shown in (a – d).

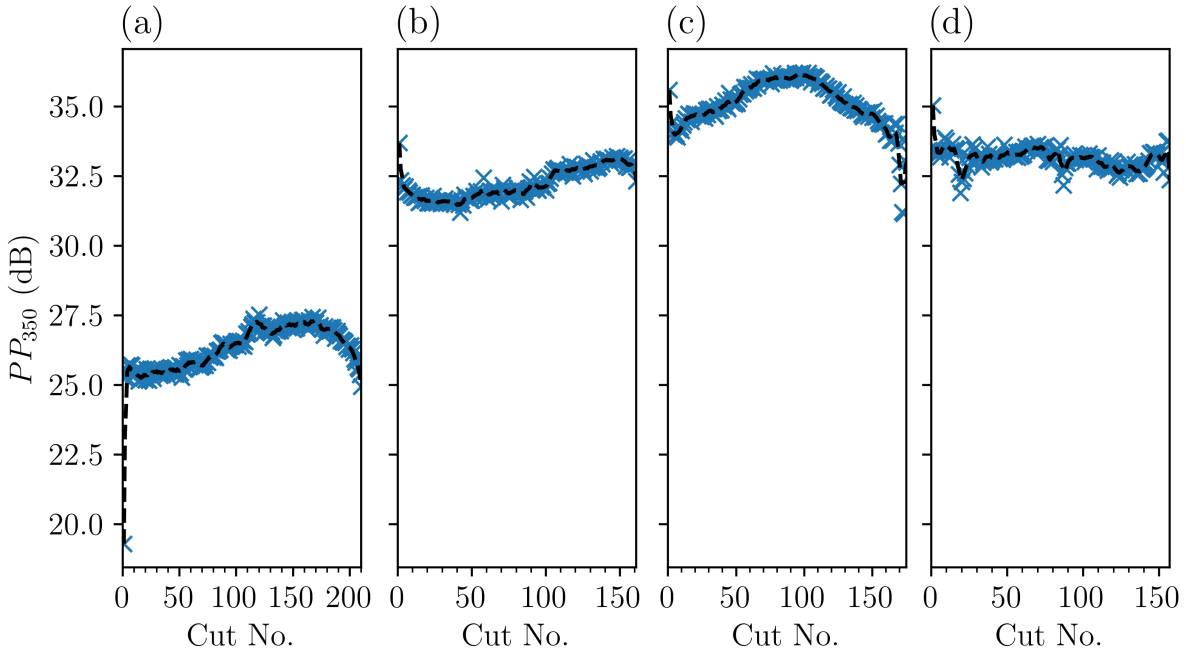


**Fig. 4.16:** $PP_{350}$ during each wear test in the feasibility series, with tests 1 – 4 shown in (a – d).

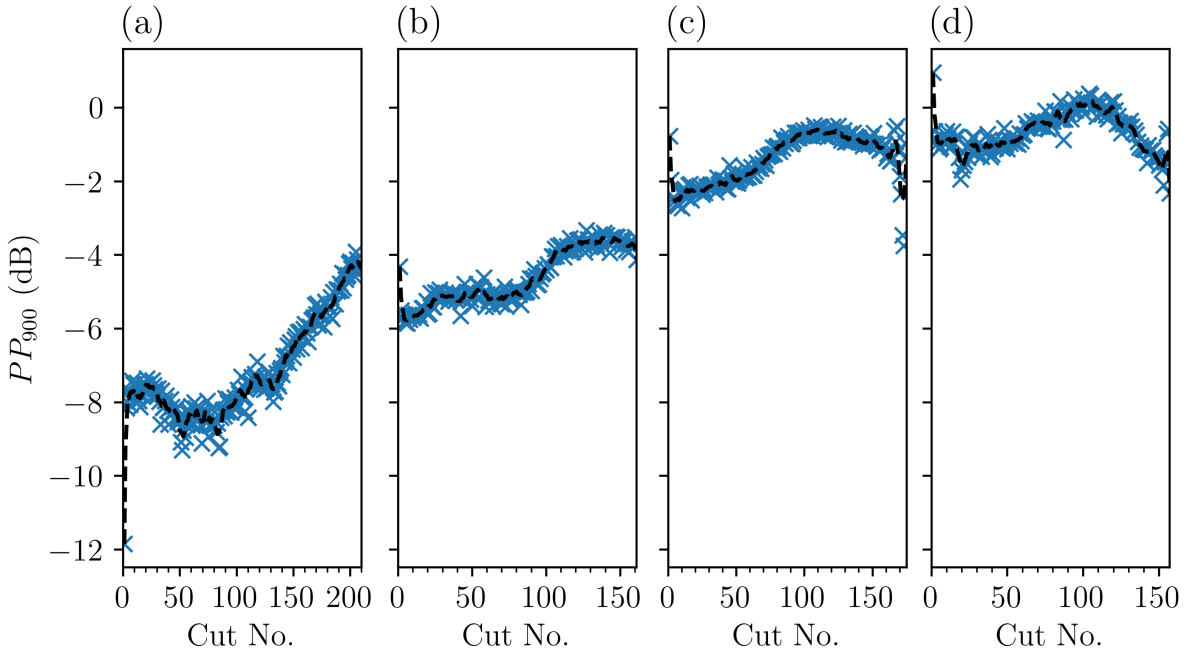


**Fig. 4.17:** $PP_{900}$ during each wear test in the feasibility series, with tests 1 – 4 shown in (a – d).

The feasibility series of wear tests confirmed that the overall methodology, particularly the repetitive grinding operation, was capable of consistently wearing a DCB to failure, whilst acquiring a direct tool measurements after every grinding passes. Whilst the wear test methodology and parameters were constant during each of the four wear tests, a large variation in the number of grinding passes completed prior to each DCB's failure was seen across the series. This variation in RUL was deemed to be the combination of differing DCB grain concentration/distribution, and inconsistent levels of DCB $r_{runout}$. Highlighting the importance of this work to prevent conservative tool replacement strategies underutilising a DCB, a core reason as to why this research was initiated by Renishaw.

From the in-situ NC4 2D surface scans, the DCBs were shown to follow a traditional three-phase wear cycle. Surface craters were formed on the tool's circumference during each DCB's steady-state phase, in which a large step height was worn through the Ni-diamond abrasive layer. The severity of the produced surface crater was linked to each DCB's $r_{runout}$. Two main limitations of the inspection cycle were observed: the lack of any workpiece measurement meant no indication of the DCB's grinding ability was monitored, and the 2D nature of the NC4 scans meant only a limited view of the DCB's overall wear was captured.

The collected AE data during each grinding pass, clearly showed that the period of tool-workpiece contact through a large increase in both $AE_{raw}$ and $AE_{RMS}$. The extent of a given DCB's $r_{runout}$ and contact area could be observed through the change in signal amplitude over the period of a single tool revolution. $AE_{kurt}$ presented as a useful feature indicating a DCB's level of $r_{runout}$ and the formation of surface craters around its circumference. Phase I - wear-in of each DCB could be seen through the initial increase in $AE_{RMS}$ until reaching a plateau, indicating a transition into phase II - steady-state. Also, the $AE_{RMS}$ seemed closely related to the DCB's progression through the wear cycle, with large changes aligning with the NC4 tool measurements across the multiple tests. The grinding pass produced a consistent PSD spectrum across all four wear tests, with specific $PP$s seemingly correlating to DCB wear attributes, despite producing varying

results across the series.

### 4.1.2 Runout Variation Study

From the feasibility series of wear tests, a DCB's $r_{runout}$ emerged as a crucial component, seemingly impacting how each tool wears and forms surface craters. Imaging of the final state of the DCB used during wear test 2, showed a stark difference in wear on opposite sides of the same DCB due to its $r_{runout}$. Whilst one half showed a complete removal of the single abrasive Ni-diamond layer, the opposite side still contained abrasive diamond grains adhered to its circumference, highlighting a loss of grinding potential. In addition to not fully utilising each DCBs abrasive layer, and potentially accelerating wear rates through surface crater formation, the effect of $r_{runout}$ on the removal of workpiece material and the resultant surface quality was not investigated but likely significant. AE showed promise as an indirect sensing method to monitor a DCB's $r_{runout}$ through both the $AE_{raw}$ signal and $AE_{kurt}$ feature. Therefore, the following series was aimed at observing the effects of differing runout levels on tool wear mechanisms and overall useful life.

Twelve full wear tests were completed during the runout variation series. Of these twelve tests, six of the DCBs used were set to a "low" level of runout, with three DCBs set to both the "medium" and "high" ranges, by utilising the NIKKEN adjustable toolholder as previously set out in Section 3.4. Fig. 4.18 shows the initial level of $r_{runout}$ each DCB was adjusted to, prior to conducting a wear test, the colouring of each bar representing the respective $r_{runout}$ level. Throughout each wear test, the full inspection cycle was utilised, as detailed in Section 3.3.

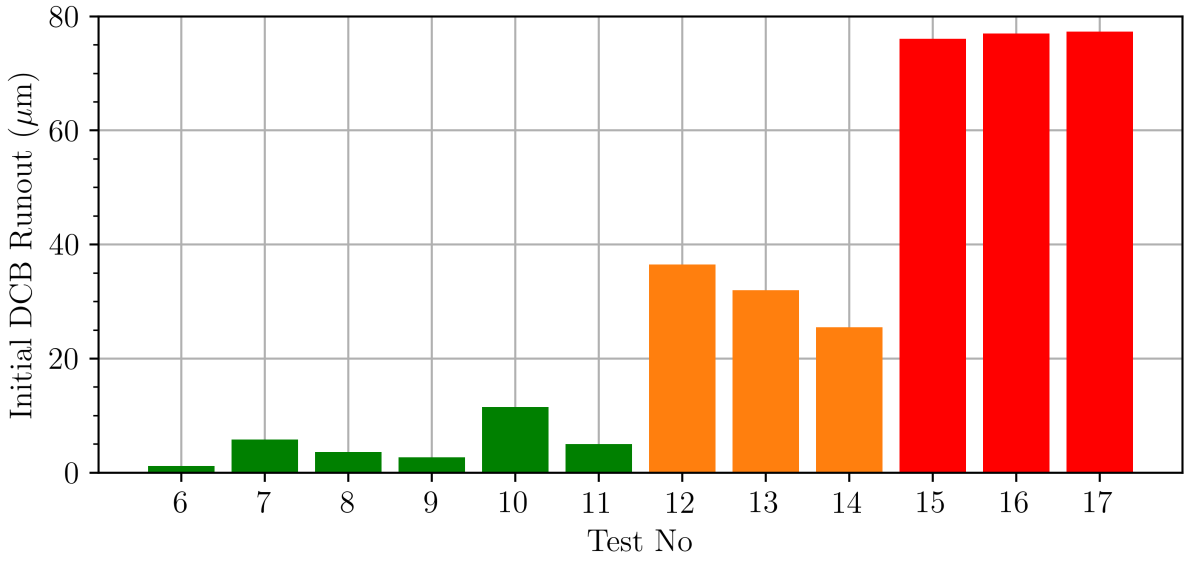


**Fig. 4.18:** The initial DCB $r_{runout}$ set prior to each wear test, within the runout variation series.

As with the feasibility series, the only variable across the wear tests was the initial condition of the DCB, be it varying grain distribution, DCB defects, or the preset level of $r_{runout}$. Table 4.3 shows the overview of results from each wear test within the runout variation series, with Fig. 4.19 showing the relationship between a DCB's initial $r_{runout}$ and the total number of grinding passes it was able to complete. Fig. 4.19 shows that the variability of a DCB's total useful life dramatically increases with its level of $r_{runout}$. As with all grinding wheels, there is an inherent baseline level of variation of their total life due to the stochastic nature of grinding and wheel manufacture, which can be observed across the wear tests conducted at the "low" runout level, producing a range of 16 grinding passes. But at the "high" level of runout, the three wear tests showed a range of 99 grinding passes. This increase in the unpredictability of a DCB's failure point is a major concern when considering the normal use case of these tools, within machine tools without any in-process tool measurements at the mass-manufacturing scale. Therefore, without the evaluation and consideration of a DCB's $r_{runout}$ level, it is very difficult to implement any basic tool replacement strategy with minimal wastage. However, a DCB that has had its $r_{runout}$ adjusted to $<$15 µm leads to a reduced range in total tool life, enabling a

simple confidence interval method to be employed as a DCB replacement strategy without excessive wastage. The variability in life between the three DCB's set to a "medium" level of $r_{runout}$, led to a range of 20 grinding passes, much closer to the range seen between the "low" level $r_{runout}$ wear tests. But reducing a DCB's $r_{runout}$ from "medium" to "low", a decrease of 20 µm, resulted in an increase to the total number of passes completed by the DCB by 39 % on average. This demonstrates how crucial gaining knowledge of a DCB's $r_{runout}$ level is, even if the runout cannot be removed in-situ, as it enables the operator to make a more informed prediction on the DCB's usable life and reduce the risk of unexpected failure.

**Table 4.3:** Runout variation series overview.

| Test No. | DCB Initial Runout (µm) | DCB Mean Radius | | | Total No. Passes |
|---|---|---|---|---|---|
| | | Initial (mm) | Final (mm) | Wear (%) | |
| 6 | 1.16 | 0.667 | 0.615 | 7.732 | 125 |
| 7 | 5.85 | 0.667 | 0.623 | 6.508 | 141 |
| 8 | 3.64 | 0.668 | 0.626 | 6.384 | 141 |
| 9 | 2.71 | 0.669 | 0.611 | 8.593 | 139 |
| 10 | 11.52 | 0.678 | 0.624 | 8.085 | 135 |
| 11 | 5.01 | 0.668 | 0.611 | 8.557 | 140 |
| 12 | 36.49 | 0.660 | 0.611 | 7.524 | 107 |
| 13 | 32.01 | 0.670 | 0.613 | 8.475 | 101 |
| 14 | 25.49 | 0.660 | 0.611 | 7.361 | 87 |
| 15 | 76.05 | 0.689 | 0.610 | 11.382 | 158 |
| 16 | 77.01 | 0.688 | 0.633 | 7.876 | 59 |
| 17 | 77.36 | 0.687 | 0.615 | 10.495 | 110 |

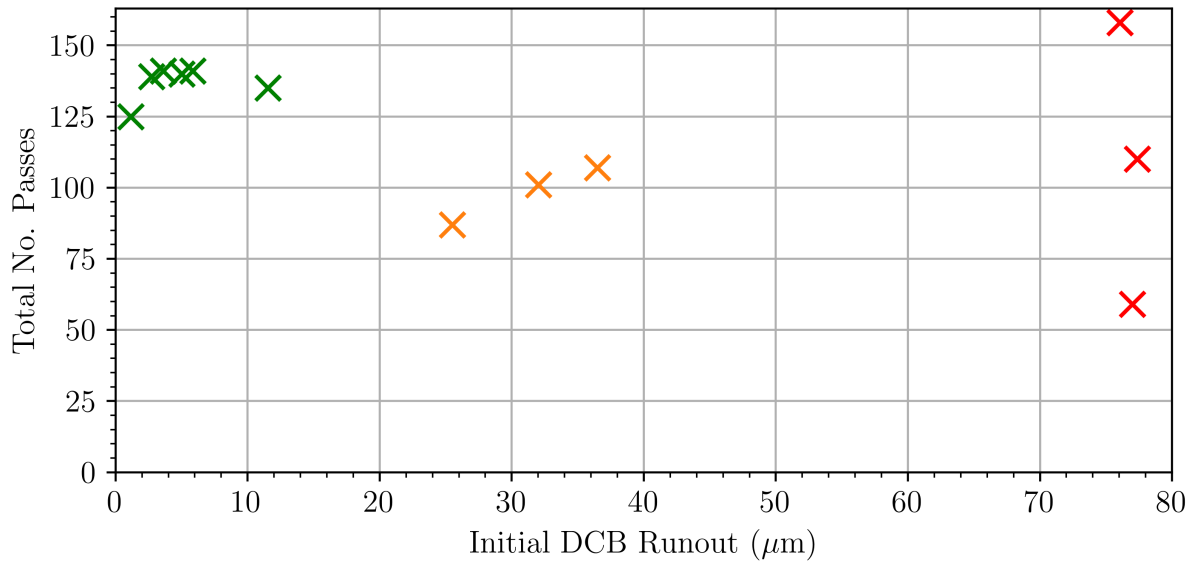


**Fig. 4.19:** Number of completed grinding passes completed by each DCB in the runout variation series, against its initial $r_{runout}$.

This increased variability and decrease in overall life of the DCBs as a result of increasing levels of $r_{runout}$, can be explained through the changing mechanisms of wear. Figs. 4.20–4.22 show every other NC4 spiral scan measurement throughout wear tests 9 ("low" $r_{runout}$), 12 ("medium" $r_{runout}$) and 15 ("high" $r_{runout}$) respectively. Across the three figures, there are stark differences in both the mechanism of wear and contact regions of each DCB. A limitation of the 3D NC4 spiral scans can be seen in Fig. 4.22 whereby the measured radius reaches the lower limit of its range, ~0.635 mm, seen by the dark blue regions of either side of the axial high spot of the DCB. This is the result of the tool's surface moving completely outside the NC4's laser beam as it is rotated due to its high levels of $r_{runout}$. The measurements of the high spot of these tools however is uneffected, allowing the tracking of wear around at least half of the tool's circumference. For this reason, attributes have not been extracted from the NC4 spiral scans for use in a quantitative sense, rather the scans have been used for a visual and qualitative understanding.

Phase I - wear-in of the DCB's life cycle is seen to occur during the first 10 grinding

passes of test 9, Fig. 4.20(a – b), in which the DCB surface is quickly reduced in height and most of the distinct high spots have been removed. Through the rest of the DCB's life a clear distinction is seen between the changing worn region and the constant unworn region of the DCB. The DCB used during wear test 9 exhibited the second-lowest initial runout of all the conducted wear tests ($r_{runout} = 2.71\,\mu m$). As a result of this, once past the wear-in phase, the wear of this DCB was seen to be uniform and consistent across the contact area, in Fig. 4.20(b – k). This period of stable wear relates to the DCB's phase II - steady-state. After 80 grinding passes, in Fig. 4.20(i), small regions of the contact region have worn below the mean surface, 0.65 mm. These small isolated regions of advanced wear, indicate a loss of abrasive grains in these areas, signifying the DCB is nearing wear phase III - wear-out. Over the next 20 passes these regions form into deeper surface craters with a 10 µm step height along the DCB's length. By grinding pass 110, Fig. 4.20(l), the surface crater has encompassed the tool's entire length and has started to expand around its circumference. Over the next 20 grinding passes, thin but deep bands of wear have formed around the entire DCB's circumference, in which the entire abrasive layer has been stripped, Fig. 4.20(n). Interestingly, the first band forms from the location of the first surface crater. Once formed, these wear bands quickly expand axially down the DCB, removing the majority of the plated surface, similarly to the effect of surface craters accelerating the wear rate seen in Section 4.1.1. The wear bands result in a large variation in grinding forces across a small area, dramatically increasing the wear rate of the DCB. This mechanism is what eventually caused complete tool failure, whereby the DCB snapped off, leaving only the unworn portion connected to the tool shank. The formation of small isolated craters with step heights, followed by the expansion into full wear bands lacking any abrasive grains, was present in all the "low" $r_{runout}$ wear tests conducted. So, whilst the timescale of each DCB's wear varies slightly, the mechanism and process of wear is repeatable when operating at a "low" level of $r_{runout}$.

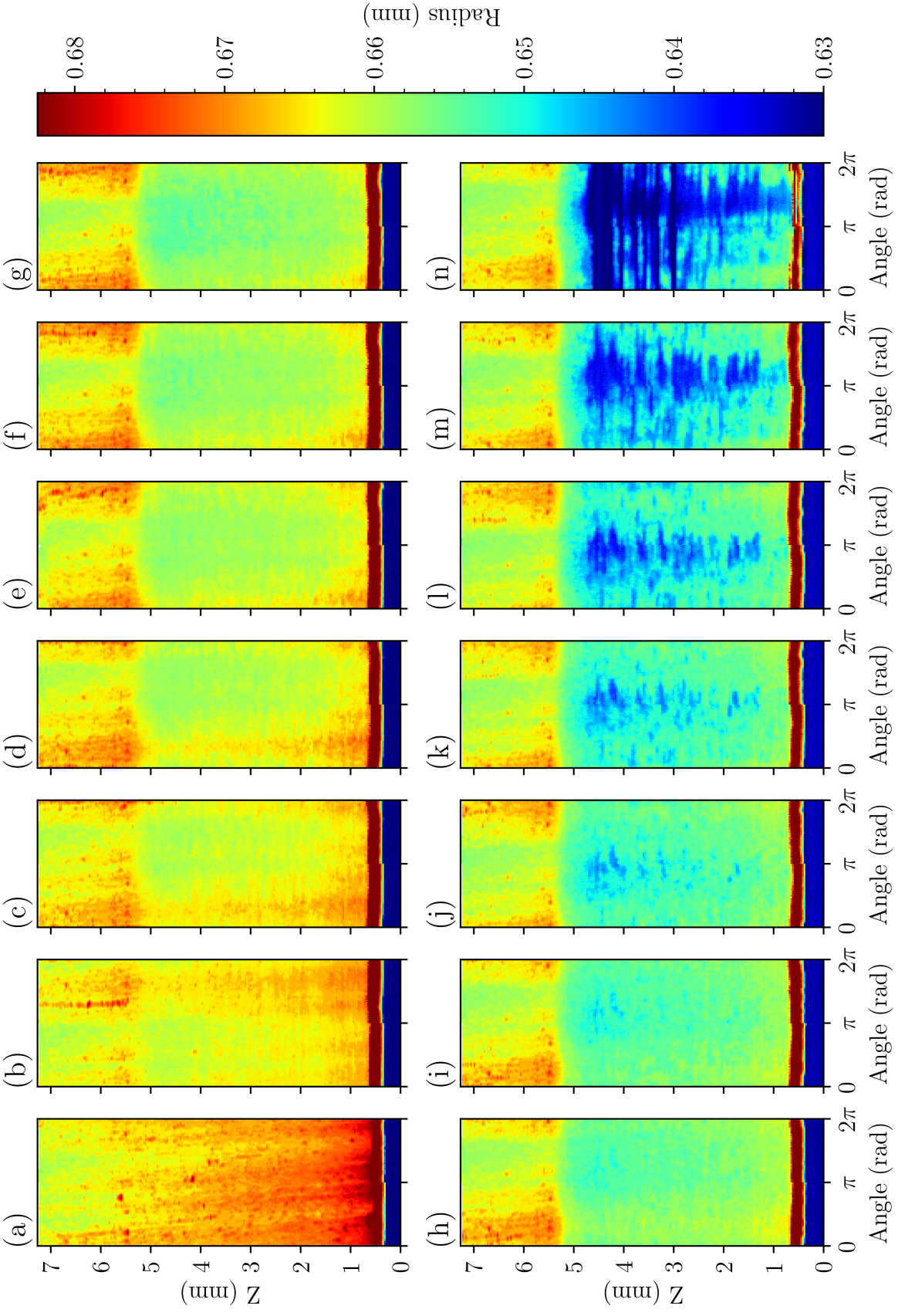


**Fig. 4.20:** NC4 spiral scans of the DCB during wear test 9 with 10 grinding passes between each figure (a – n).

As a comparison, Fig. 4.21 shows the wear progression of the DCB during wear test 12, which initially had a "medium" level of $r_{runout}$ at 36.49 µm. This higher level of $r_{runout}$ can clearly be seen through the large high spot in the middle of each subplot, spanning along the entire DCB's length. The initial scan, Fig. 4.21(a), also shows that the DCB's $r_{runout}$ has a component of axial tilt, seen by the increase in radius along the high point's midline. Similarly to the DCB used during test 9, the DCB in test 12 changes dramatically over the first 10 grinding passes, Fig. 4.21(a – b). Over the region of tool-workpiece contact, the localised high spots are removed, and the overall surface has been worn into a much more consistent surface, inline with the expected phase I - wear-in of a DCB's life cycle. Due to the runout of the DCB, after just 40 grinding passes in Fig. 4.21(e), a large portion of the high spot has worn significantly, having removed >10 µm of the abrasive layer near the top of the grinding region. This accelerated wear rate over the DCB's high spot is likely the result of increased grain penetration and therefore variation in grinding load around its circumference. After 70 grinding passes, in Fig. 4.21(h), significant surface craters have formed within the high spot producing a step height of 25 µm between the unworn and worn sections of the DCB. At the top of the grinding region where the wear initially started, the craters have expanded into a large flat spot removing a segement from the tool's cross-section, encompassing approximately half its circumference. After a further 10 passes, in Fig. 4.21(i), the central portion of the DCB has been completely stripped of the Ni-diamond abrasive layer, forming a surface crater along the DCB's length, leaving two isolated and prominent peaks on either side. Additionally, small bands of wear can be seen across the entire high spot where one or both the peaks have worn to the level of the crater. At this point in time, the portion of the DCB that was occupied by the high spot is clearly within phase III - wear-out, as it has been worn almost completely to the steel core. However, due to the limitation of NC4 spiral scans reaching a lower limit, as mentioned earlier, the state of the remaining abrasive surface is unknown, but likely wearing rapidly.

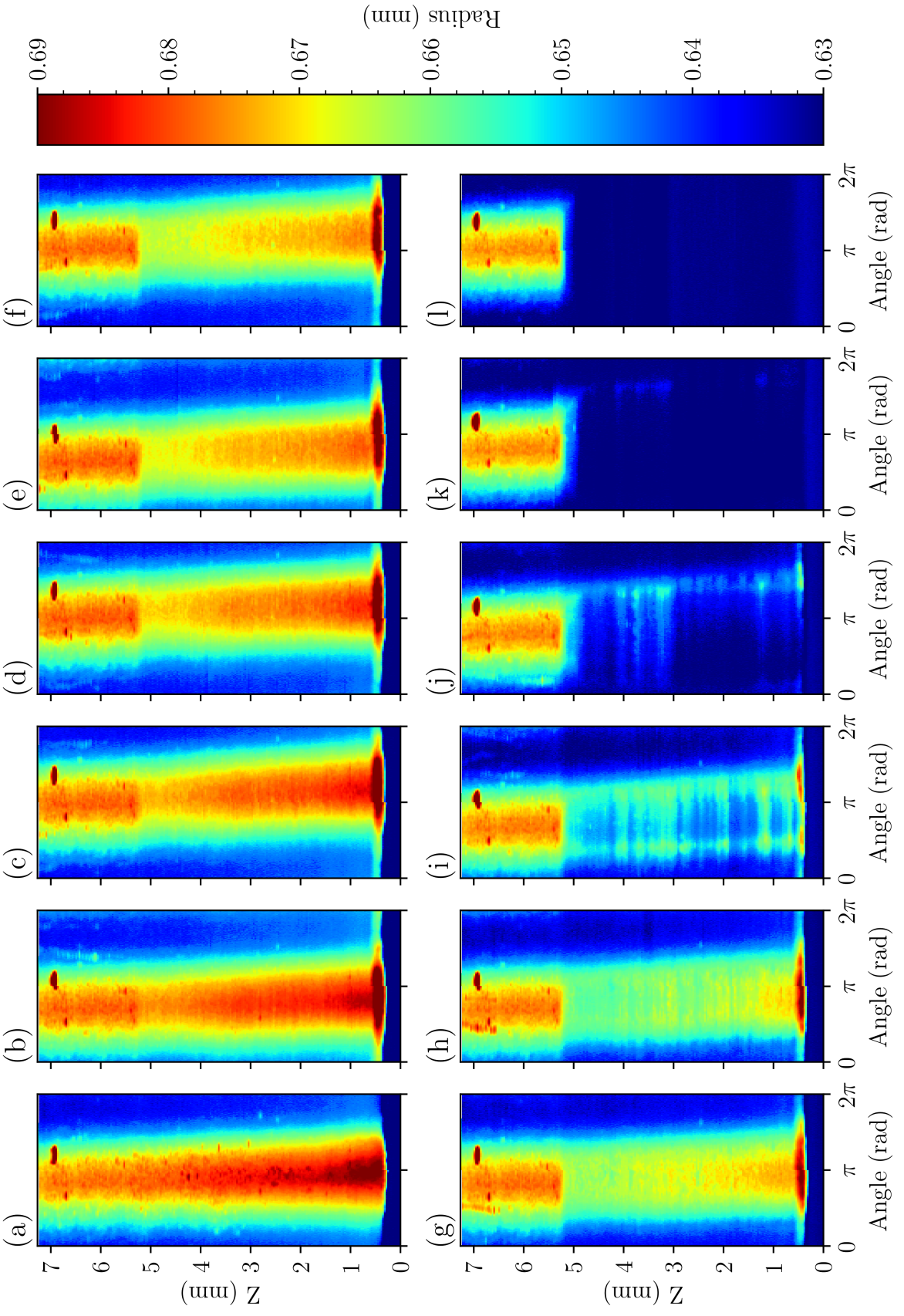


**Fig. 4.21:** NC4 spiral scans of the DCB during wear test 12 with 10 grinding passes between each figure (a – l).

Fig. 4.22 shows the wear of the DCB used during test 15, which was conducted at the "high" level of $r_{runout}$, with an initial value of 76.05 µm. Of interest, the DCB used in this test lasted the longest of all conducted tests within the runout variation series, completing 158 grinding passes until reaching the failure criteria. The extreme nature of $r_{runout}$ at the "high" level can be seen in Fig. 4.22(a), showing the scan of the initial DCB's state. The high spot is more pronounced and covers a smaller portion of the tool's circumference. Within the first 10 grinding passes, between Fig. 4.22(a – b), a larger amount of wear can be seen compared to the other DCBs presented above, but only across the small section of the high spot. The difference in contact area due to increasing $r_{runout}$ dramatically impacts the progression of wear across a DCB's surface. Throughout Fig. 4.22, the wear of the DCB is focused over the current high spot, occurring at an increased rate due to the reduced contact area. Similarly to the DCB in Fig. 4.21, significant wear stems from the top of the grinding region within the high spot. Between grinding passes 40 – 60, in Fig. 4.22(e – g), the wear forms a flat spot across the high spot, starting at the top of the grinding region gradually expanding down the DCB's axis. Additionally, in Fig. 4.22(g) a small wear band can be seen to form across the high spot, where the radius is $<$0.70 mm. After the wear flat has formed, a surface crater develops along the high spot due to the reduced number of abrasive grains in this region and the increased grinding forces. Fig. 4.22(h) shows an intermediate step whereby the DCB's high spot has nearly been stripped of the entire abrasive mono-layer. The formed crater then rapidly wears during the 10 passes between Fig. 4.22(h – i), as only the Ni-undercoat or steel core remain to resist wear from the workpiece. As a result of this accelerated wear, two very prominent peaks are again formed either side of the crater, which are now the highest points and subject to the greatest grinding loads. This effect was also seen by the DCB used in test 12 to a lesser extent as seen in test 15, where each peak has approximately 30 µm of drop-off on either side. After Fig. 4.22(i) in which the two peaks are formed around the surface crater, it begins expanding around the DCB's circumference, increasing the distance between the peaks whilst maintaining the large step height in between.

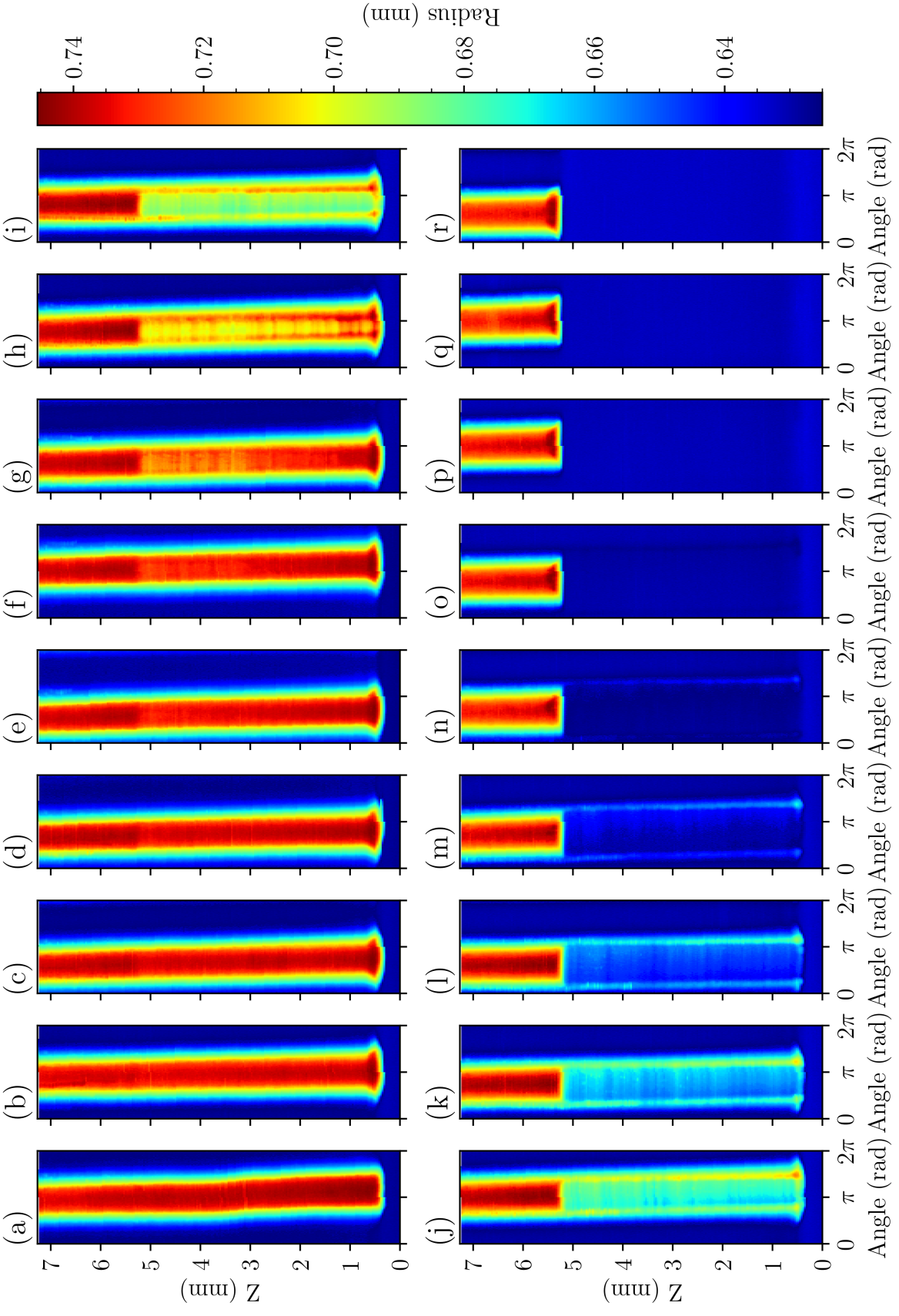


**Fig. 4.22:** NC4 spiral scans of the DCB during wear test 15 with 10 grinding passes between each figure (a – r).

The same mechanism of surface crater and band formation seen in the DCBs operated at a "low" level of $r_{runout}$, is present for DCBs operating at "high" $r_{runout}$ levels, however the random grain distribution plays a much larger role in determining the tool's overall life. The density of abrasive grains across the DCB's surface and the adhesive strength between the Ni bond material and diamond grains varies as a result of the electroplating process. This leads to regions of the DCB's surface being more or less resistant to the formation of surface craters. With increasing DCB $r_{runout}$ this variation in wear resistance becomes more critical, as it relies on a smaller region of the abrasive layer resisting an increased grinding load. Therefore, DCBs operating at higher runout levels have an increased variance in overall tool life, a result of their initial high spot's resistance to crater formation. Conversely, a DCB operating at a lower runout level, is capable of distributing the grinding load across a larger contact area, and therefore more abrasive grains. Allowing even weaker regions of the DCB's surface to resist the formation of wear bands until the majority of the abrasive layer has been worn. As once a wear band has formed, removing the whole electroplated layer from a small region of the tool, it quickly accelerates the wear of any DCB.

Another impact of increasing a DCB's level of $r_{runout}$, is the effect it has on a tool's progression through the wear cycle, as presented in Section 2.1.3. In Fig. 4.20 distinct transition points between each phase in the DCB's life can be identified as the majority of the grinding region experiences the same rate of wear. However, by comparison both Figs. 4.21 and 4.22 do not present such distinct transition points. According to the increased $r_{runout}$, there is a large variation in wear rate around each DCB's circumference, meaning that different sections around the DCB can be experiencing completely different phases of wear simultaneously. For example during wear test 15, as the $r_{runout}$ was set to 76.05 µm, the high spot will undergo phase I - wear-in very quickly, as this region of the DCB will try to remove roughly double the set $a_e$. But outside this thin high spot region, the remaining DCB surface is likely not making contact with the SiC workpiece. As a result, the side of the DCB opposite to the high spot, will not experience phase I - wear-in until the high spot is worn significantly to enable it to make contact. This

means that at any point in a DCB's life, when operating with an increased $r_{runout}$ level, it can be undergoing all three phases of wear concurrently in different regions around its circumference due to its variation in grain penetration and contact. Which in turn dramatically increases the difficulty in defining a distinct point of when to stop using any given DCB, as one region can be stripped of the entire electroplated abrasive layer whilst the other untouched.

Figs. 4.23, 4.26 and 4.29 show the NC4 2D surface scans of each DCB within the "low", "medium" and "high" ranges of $r_{runout}$, during the runout variation series. With Figs. 4.24, 4.27 and 4.30 showing the extracted attributes from the respective NC4 measurements, and Figs. 4.25, 4.28 and 4.31 showing the OMP600 measurements of $a'_e$ removed from the workpiece across each wear test in the runout variation testing series.

Each of the six DCBs worn at the "low" range of $r_{runout}$ behave very similarly to each other, wearing at a consistent rate around their entire circumference, until forming a surface crater near the end of each of their lives. Like the wear measurements seen in Fig. 4.3(c) of wear test 3, the only wear test during the feasibility series with an initial $r_{runout}$ of $<$10 µm, the $r_{mean}$ of each DCB clearly follows the typical three-phase wear trend. The three phases of wear can be identified through the observation of the gradients of both the $r_{mean}$ and $r_{peak}$ in Fig. 4.24. Unlike the wear tests conducted in the feasibility series, each DCB's phase I - wear-in, lasted over an increased number of grinding passes, resulting in a much smoother transition into phase II - steady-state, seen through the $r_{mean}$ plots of Fig. 4.24. This slowed wear-in phase is presumably the result of the consistent contact around the tool's circumference, allowing the entire grinding region to wear-in simultaneously. Also, whilst the $r_{runout}$ of each DCB was set to be $<$15 µm at the start of each wear test, the removal of weakly adhered diamonds or excess Ni bond during phase I, was seen to dramatically change the DCB's $r_{runout}$. The DCB used in test 6 increased in $r_{runout}$ by 10 µm across its first 10 grinding passes due to its wear, Fig. 4.24(a). Additionally, much like the four tests conducted in the feasibility series, a large increase in $r_{runout}$ during each of the DCBs' lives aligned with the formation of each DCB's surface crater. The phase II - steady-state of each of the six DCBs at "low"

$r_{runout}$ was very consistent, lasting the majority of each tool's life. This consistency in both rate and contact area, led the final portion of their RULs, phase III - wear-out, to occur suddenly when nearing the end of its steady-state phase.

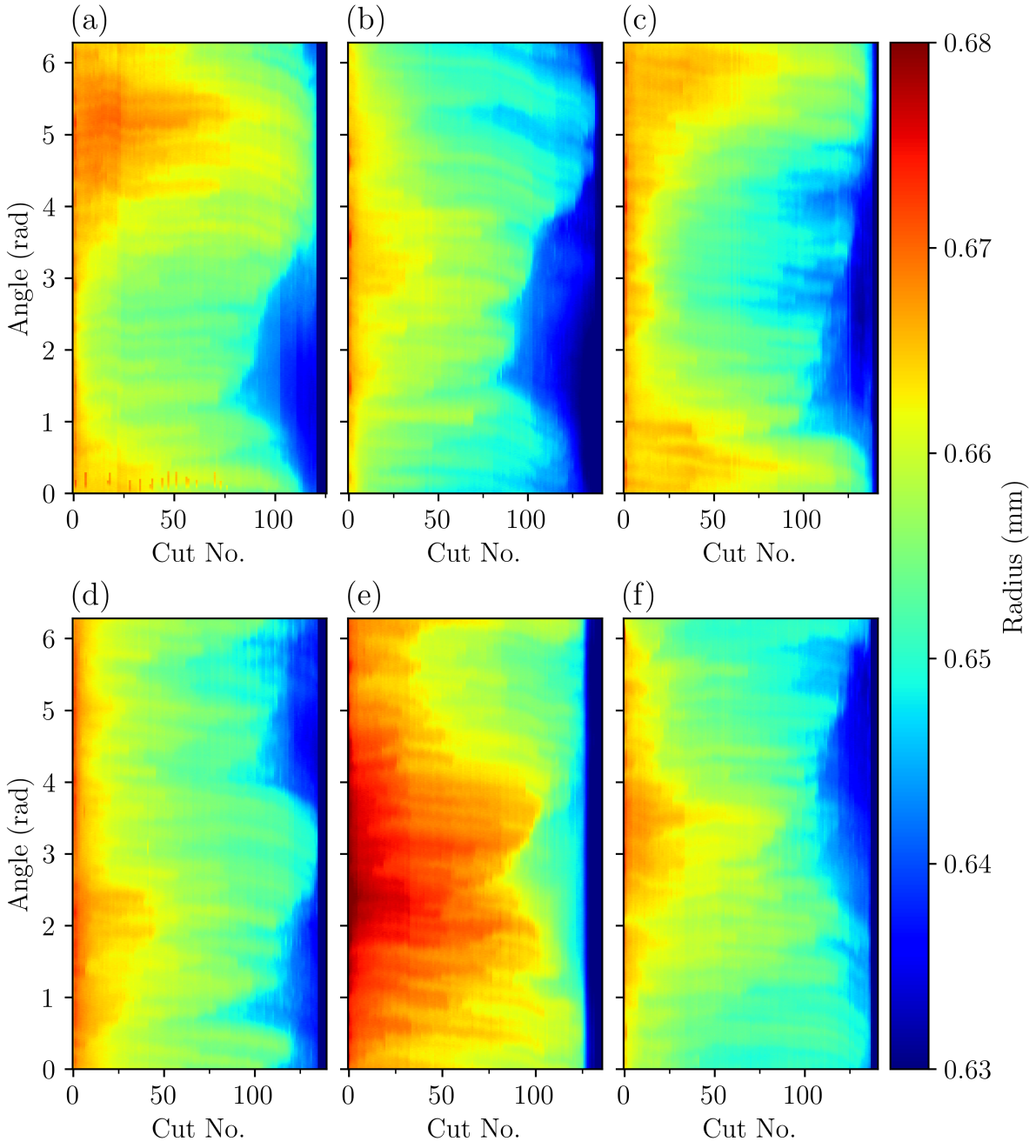


**Fig. 4.23:** NC4 circumferential surface scans during the six wear tests at "low" runout levels during the runout variation series, with tests 6 – 11 shown in (a – f).

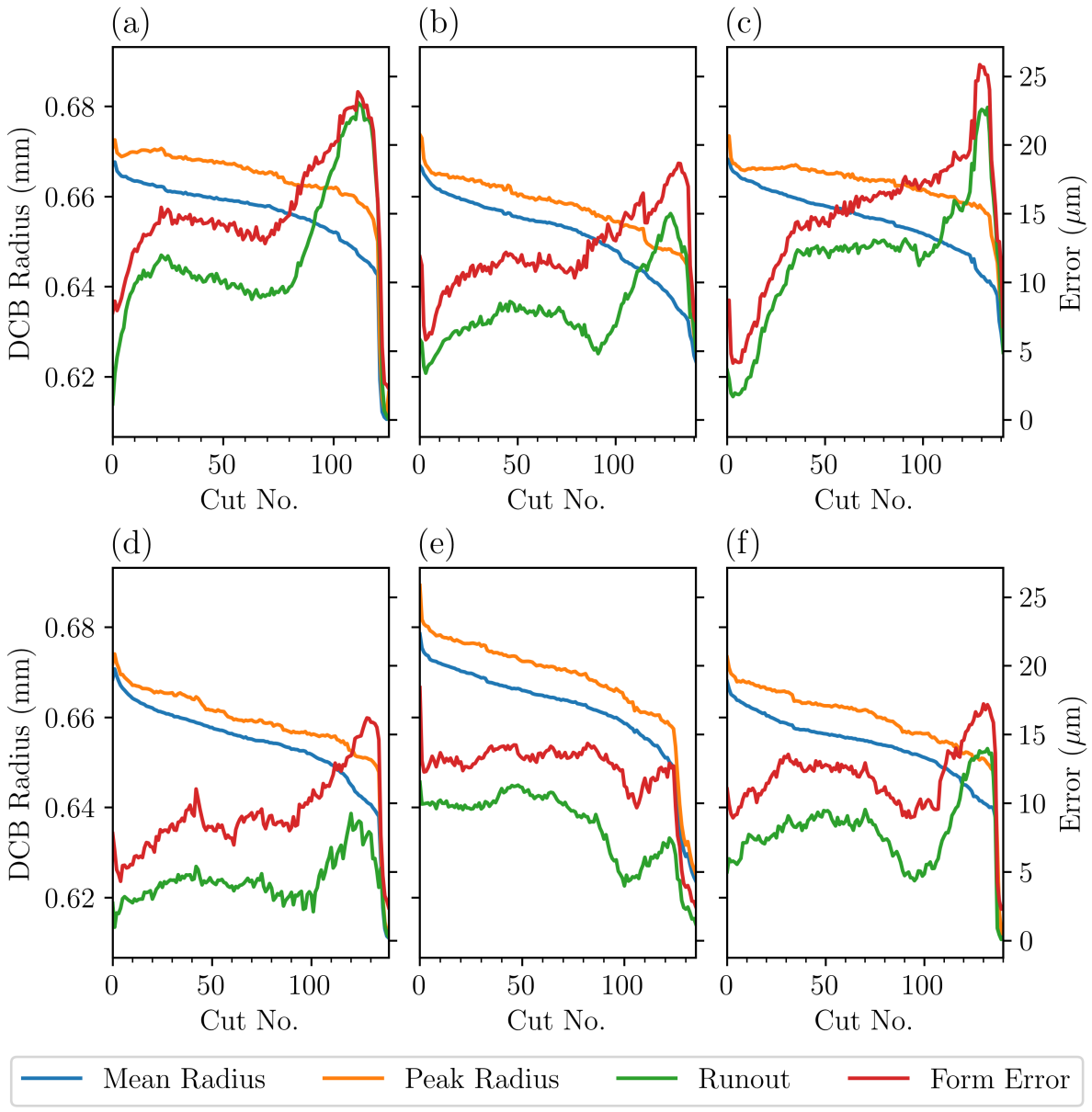


**Fig. 4.24:** NC4 attributes from the six wear tests conducted with "low" runout during the runout variation series, with tests 6 – 11 shown in (a – f).

Alongside the NC4 tool wear measurements, this testing series also introduced measurements of the workpiece surface with the OMP600, see Section 3.3.2. A worn DCB with a large surface crater was still capable of completing grinding passes, as seen through the 2D NC4 scans in Fig. 4.23, meaning that a DCB's level of wear should not be the sole component to base a TCM approach around. Fig. 4.25 shows the measurements of $a'_e$

across the six wear tests conducted at the "low" level of $r_{runout}$, in which each DCB's ability to remove workpiece material throughout its life can be observed. In an ideal grinding process whereby there is no machine deflection or grinding wheel wear, the $a_e'$ should equal the programmed radial depth of cut, $a_e$. As can be seen in each test in Fig. 4.25 this does not occur, instead the $a_e'$ follows an "n" shaped curve, which aligns with the DCB wearing through the three-phase cycle.

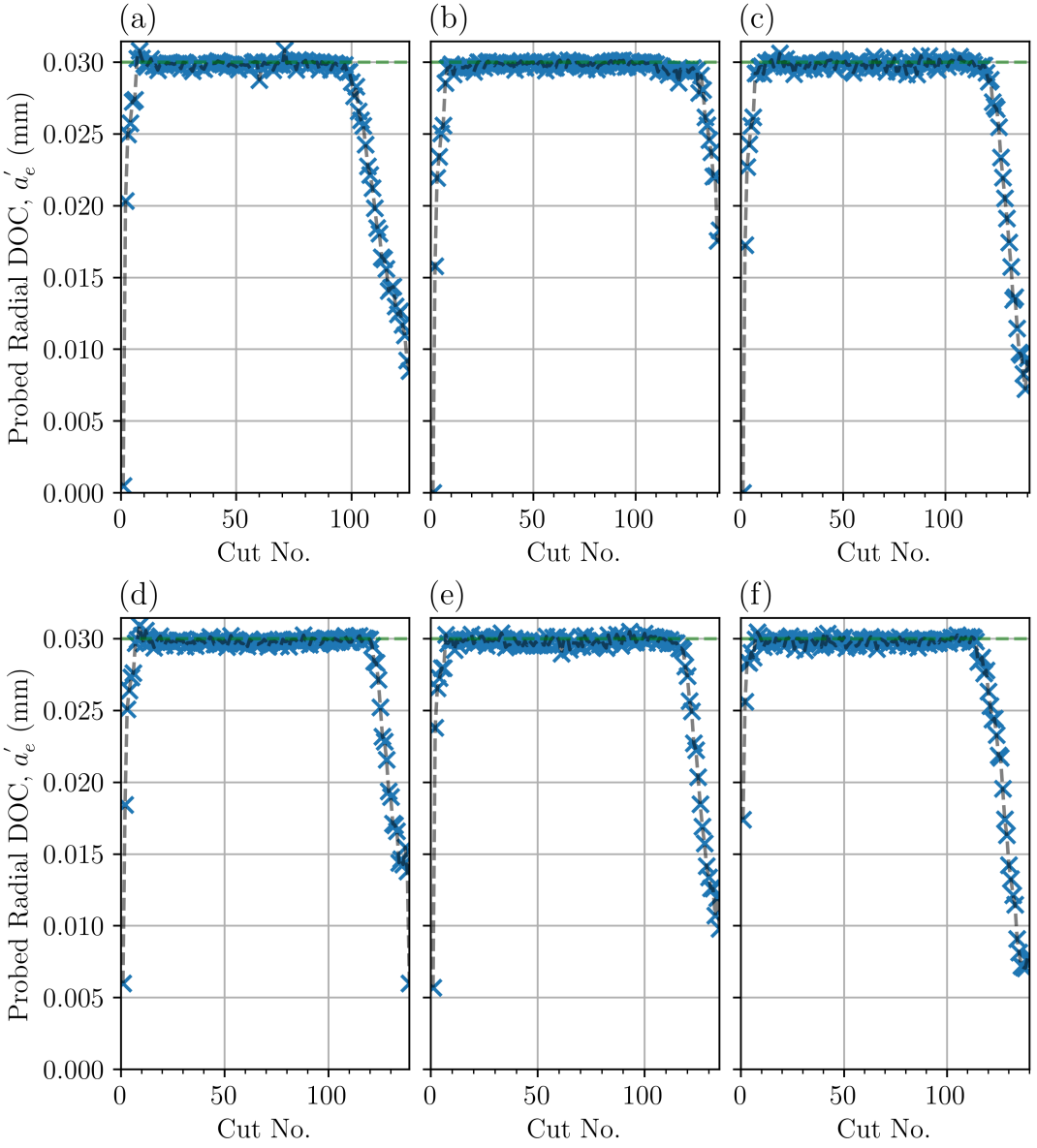


**Fig. 4.25:** True radial DOC, $a_e'$, measured throughout each wear test at the "low" runout level in the runout variation series, with tests 6 – 11 shown in (a – f).

At the start of each DCB's use, the first few grinding passes are removing significantly less material than programmed, shown by the measurements being significantly below the green dashed line at 0.03 mm denoting the wear test's $a_e$ in Fig. 4.25. But within at most 6 grinding passes, the $a'_e$ of each DCB rises up to match the $a_e$, where it then stabilises remaining close to the $a_e$ for the majority of their remaining life. This increase in $a'_e$ can be attributed to the DCB undergoing its wear-in phase, which as seen through the tool wear measurements in both Figs. 4.23 and 4.24, results in rapid initial wear, whereby the exposed abrasive grains of the DCB do not have the required strength to grind the workpiece. But as the weakly adhered grains and excess Ni bond material are removed, it exposes strongly bonded, sharp grains with adequate protrusion slowly enabling the DCB to remove the given $a_e$ from the SiC workpiece. Once past phase I - wear-in, the tools with a "low" runout level resulted in a consistent $a'_e$, inline with the expected behaviour of a DCB undergoing phase II - steady-state wear. As well as observing and validating the tool wear phase that the DCB is experiencing, the probe measurements also show each DCB's ability to grind precisely and repeatably within phase II of its life cycle. As the single abrasive layer is worn away, the DCB will start to wear rapidly when reaching the underlying Ni-undercoating and steel core, as they are of a much lower hardness than the workpiece. This rapid loss of the DCB's abrasive layer can also be seen in Fig. 4.25, through sharp reduction in $a'_e$ prior to each tool's failure point. The reduction in $a'_e$ occurs prior to the dramatic decrease in $r_{mean}$ in all the six tests conducted at the "low" level of $r_{runout}$. Compared with the NC4 tool wear measurements, the OMP600 probe measurements in Fig. 4.25 present much clearer transition points between each of the three wear phases. Furthermore, the measurements of $a'_e$ with the OMP600 probe tend to pre-empt changes in the DCB's state, likely the result of the probe averaging over a larger area than the NC4 2D measurements. As a result of this, the $a'_e$ measurements compliment the NC4 measurements to better determine the optimal stopping/changing point of a DCB.

As seen in the 3D NC4 spiral scans of wear test 12 shown in Fig. 4.21, each DCB used at the "medium" $r_{runout}$ range had a significant high spot along its length due to the

imparted offset runout, shown across Fig. 4.26. The effect of this high spot can then be seen through the very different trends presented by each of the DCB's $r_{mean}$ in Fig. 4.27. Observing Fig. 4.27, phase I - wear-in of each DCB occurred over a much shorter time period, with tests 12 and 14 presenting no discernable wear-in phase from their $r_{mean}$ data. More akin to the wear tests conducted within the feasibility series, rather than the six conducted at the "low" $r_{runout}$ range. This effect is also seen within the OMP600 $a_e'$ measurements of the three wear tests, in Fig. 4.28, whereby the first grinding passes remove significantly more material than seen by the DCBs with "low" $r_{runout}$. With the DCB used in wear test 12, Fig. 4.28(a), showing no wear-in phase, and removing an $a_e'$ of 28.8 µm in the first grinding pass. This shortened phase I - wear-in of the DCBs with a "medium" range of $r_{runout}$, is the result of the high spot reducing the initial contact area and increasing the grain penetration within said region. As a result, the contact area rapidly undergoes wear-in due to the increased grinding forces and is then required to remove a greater portion of the workpiece to meet the programmed $a_e$.

As well as indicating the very short phase I - wear-in of each DCB's life, both the $r_{mean}$ in Fig. 4.27 and the $a_e'$ in Fig. 4.28 show a simplified metric for the evolving wear state of each DCB, even when operating at the "medium" level of $r_{runout}$. Each DCB had a shortened phase II - steady-state in which the high spot underwent minimal wear, whilst being capable of removing the asked $a_e$, this presented as similar trends in both metrics as in wear tests 6-11 at the "low" range of $r_{runout}$. However, once the high spot starts to experience localised wear-out, a surface crater will form quickly in its place. Fig. 4.26(c) shows the forming of the surface crater during test 14, initially starting as a small channel worn into the high spot after ∼30 grinding passes, which with time deepened and widened into a large surface crater after pass 50. Once the high spot had worn, a clear reduction in gradient in both metrics can be seen as the crater expanded. However, as the crater expands the abrasive layer left on either side is still capable of removing material from the workpiece, albeit resulting in an accelerated rate of wear. After the surface crater has expanded to encompass the entire circumference and no abrasive layer remains around the DCB's steel core, each DCB experienced a shortened phase III - wear-out until failure. As

a result of the $r_{runout}$ being increased to the "medium" range, the DCB presents a much more ambiguous wear cycle, clouded by its limited contact and accelerated wear rate.

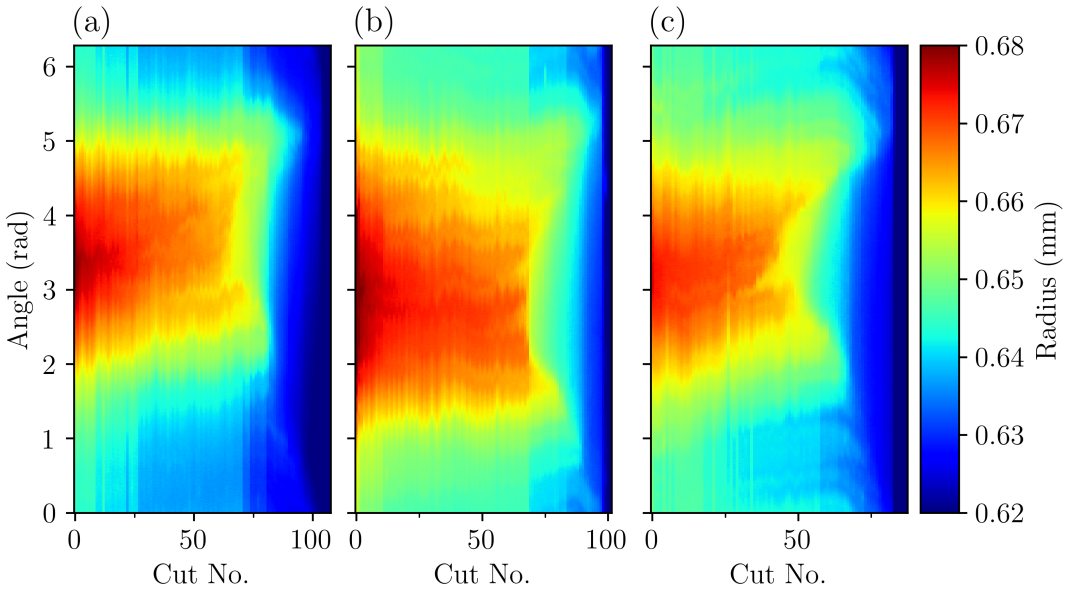


**Fig. 4.26:** NC4 circumferential surface scans during the three wear tests at "medium" runout levels during the runout variation series, with tests 12 – 14 shown in (a – c).

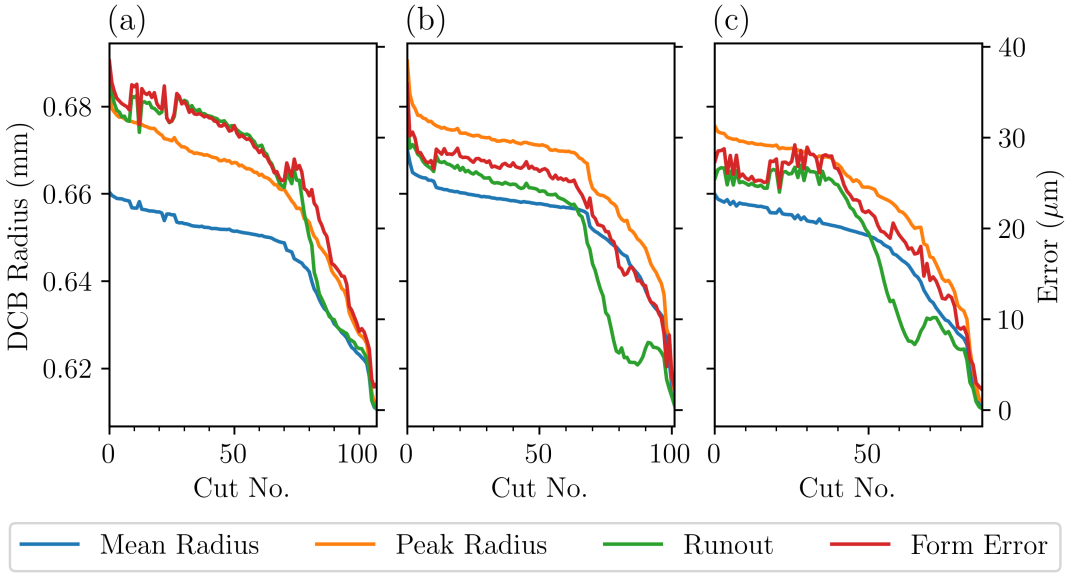


**Fig. 4.27:** NC4 attributes from the three wear tests conducted with "medium" runout during the runout variation series, with tests 12 – 14 shown in (a – c).

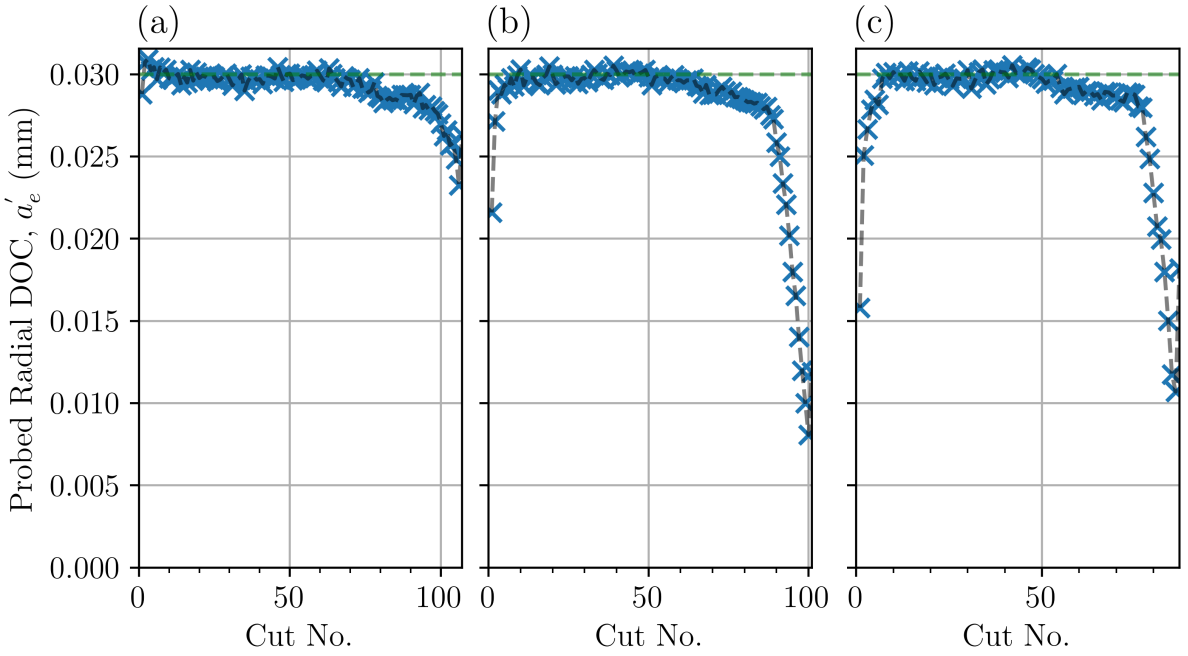


**Fig. 4.28:** True radial DOC, $a_e'$, measured throughout each wear test at the "medium" runout level in the runout variation series, with tests 12 – 14 shown in (a – c).

Much like the spiral scans of test 15 shown in Fig. 4.22, the 2D NC4 scans of the three "high" $r_{runout}$ wear tests, seen in Fig. 4.29, are similarly limited as a result of the laser beam's range of detection. Therefore, the scans and extracted attributes do not show a similar level of detail, that can be seen throughout the other $r_{runout}$ levels. Nonetheless, the data still provides useful information on the overall wear of the tool, which in conjunction with the $a_e'$ measurements, allowed a full picture of how each DCB was worn to be understood. The 2D NC4 measurements of the "high" $r_{runout}$ level DCBs presented a very similar pattern of wear to the three DCBs worn at the "medium" level, albeit to a more extreme level. With a more prominent and thinner high spot, and eventually a deeper and wider surface crater worn into their surface. From the NC4 attributes across each wear test, shown in Fig. 4.30, both the $r_{mean}$ and $r_{peak}$ start at a consistent level, during which there can be seen to be minimal wear over each DCB's high spot. During this period, the OMP600 probe's measurements of the $a_e'$, as shown in Fig. 4.31, are consistent in removing the desired $a_e$ during each grinding pass. But prior

to this period of consistency, the DCBs used during wear tests 16 an 17 both removed 5 µm more than the $a_e$ during their first pass, seen in Fig. 4.31(b – c). Whereas in test 15, the initial pass removed an $a'_e$ of 15 µm, akin to the wear tests conducted at lower $r_{runout}$ levels. This disparity between the initial $a'_e$ when using "high" runout DCBs is not understood fully, but likely a result of the initial tool radius setting operation. As it too was conducted with the NC4, it is possible the "high" level of runout combined with the system's laser beam size resulted in either under or over estimating the DCB's $r_{mean}$.

After a varying number of passes, each of the three DCBs' high spots started to experience noticeable wear, originating from their centreline, in Fig. 4.29. This localised wear developing into a surface crater, led to a clear change in trend of each DCB's $r_{runout}$ after the period of rapid radial wear, in Fig. 4.30. Of note, once each DCB reached this period of increased wear rate, they all wore with a very similar $r_{mean}$ gradient, wearing by approximately 2.5 µm after every grinding pass. And thus once within this period of increasing wear, due to the surface craters expansion, a steady decrease in the measured $a'_e$ can be seen in Fig. 4.31. Despite the similar wear rate over a large portion of each of the DCB's lives, it still resulted in a large variation in total completed passes prior to failure across the three wear tests, as a result of two factors. Firstly, the DCB used during wear test 16 failed unexpectedly when its surface crater encompassed half of its circumference. Comparing its wear state at failure through the $r_{mean}$ metrics of the other wear tests in Fig. 4.30, the DCB could be seen to have failed approximately three quarters of the way through its life. Secondly, the variation in wear resistance of each DCB's high spot can be seen through the differing number of passes till each tool started to form its flat spot; 60, 30 and 40 passes respectively. So whilst the DCBs wear at a similar rate after creating surface craters, they can still fail having removed vastly different amounts of material due to their "high" $r_{runout}$.

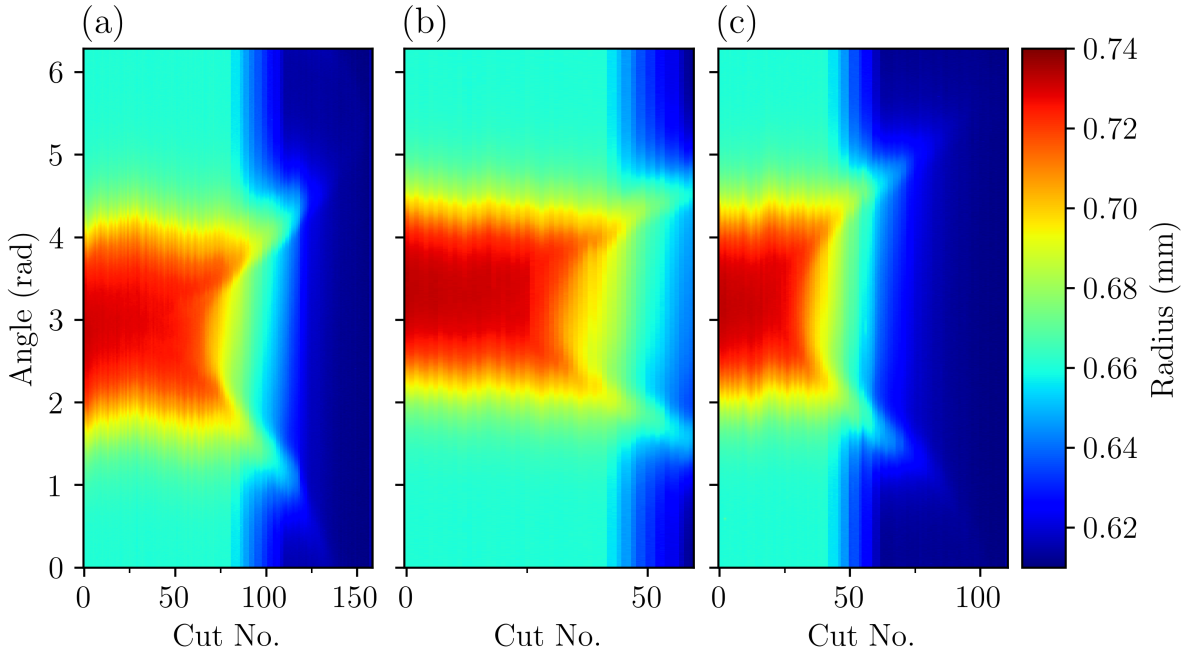


**Fig. 4.29:** NC4 circumferential surface scans during the three wear tests at "high" runout levels during the runout variation series, with tests 15 – 17 shown in (a – c).

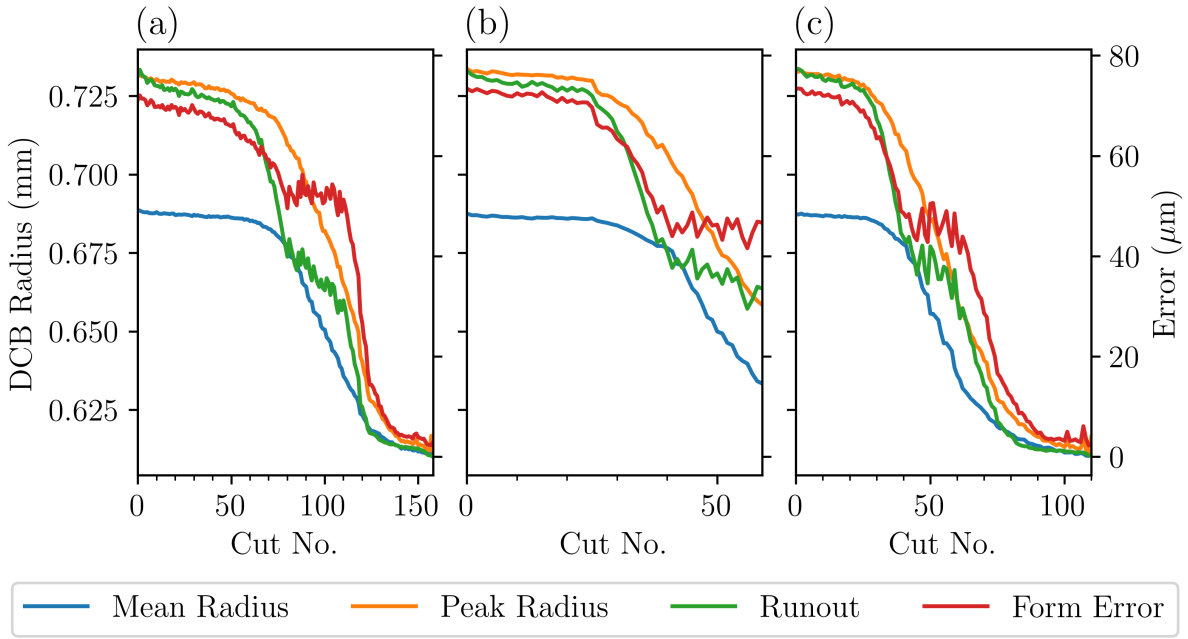


**Fig. 4.30:** NC4 attributes from the three wear tests conducted with "high" runout during the runout variation series, with tests 15 – 17 shown in (a – c).

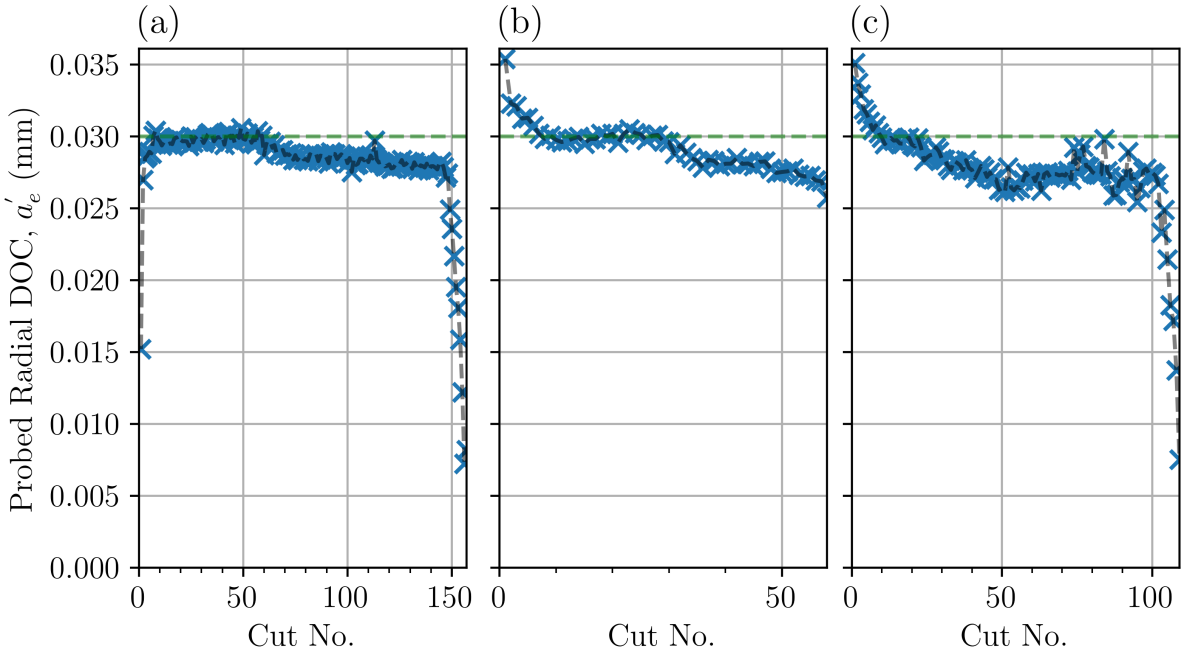


**Fig. 4.31:** True radial DOC, $a_e'$, measured throughout each wear test at the "high" runout level in the runout variation series, with tests 15 – 17 shown in (a – c).

Fig. 4.32 shows the OMP600 measurements of the reference bore during wear test 7, for tracking the machine tool's thermal drift. The results clearly show the effect of thermal drift, with the measured bore diameter reaching a max error of 2.5 µm. Additionally, Fig. 4.32(b) shows that the JD machine's X-axis is effected to a greater extent by thermal drift, with a maximum relative deviation of 10 µm to the Y-axis's 5.4 µm. This disparity between the two axes is likely due to the difference in size of each axis, as the bed dimensions are 830 × 400 mm, or a difference between the driving mechanics of each axis, due to space restrictions. Despite the thermal drift surmounting to 10 µm in the X axis, due to the OMP600 $a_e'$ probing cycle updating the grinding surface's position after every grinding pass, the effect was determined to be negligible across the wear test.

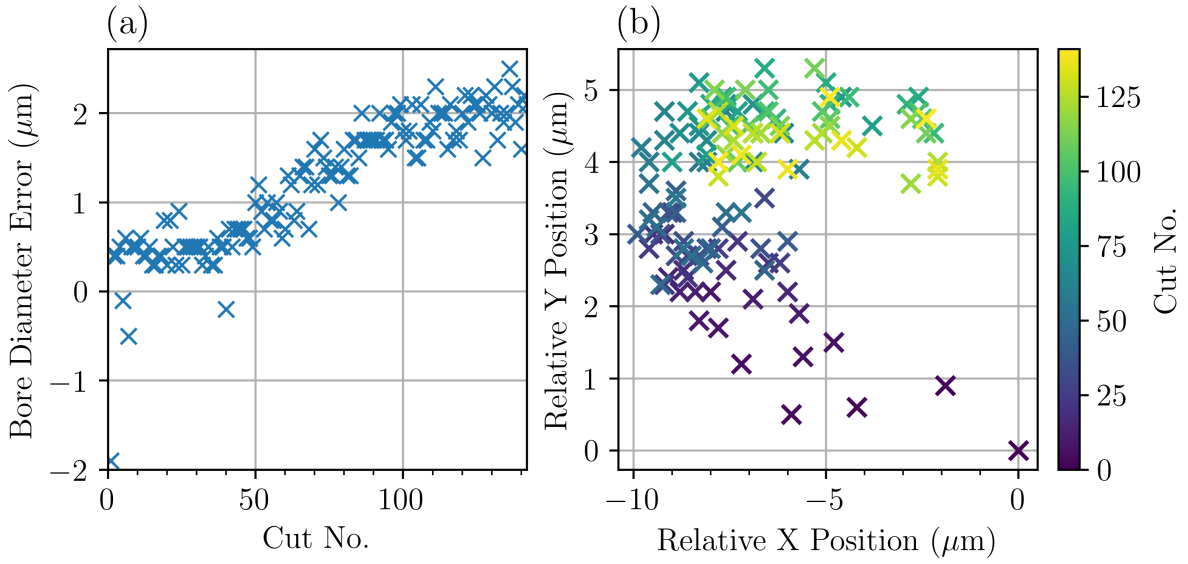


**Fig. 4.32:** OMP600 thermal drift measurements of a ⌀24.998 mm reference bore throughout wear test 7, (a) error of measured bore diameter, (b) relative X and Y positions of the bore.

The inspection cycle across the runout variation series showed clear difference in wear mechanisms between DCBs with increasing levels of $r_{runout}$, as well as its impact on material removal. Alongside the increased variability of a DCB's total useful life associated with increased $r_{runout}$, the $a'_e$ removed during each pass fluctuated more and resulted in larger geometric errors over time when compared to a DCB within the "low" $r_{runout}$ range. However, what is not clear from the inspection data is whether the DCB could recover and continue effectively, if the runout or tool offsets were adjusted once identified. As an example, the OMP600 measurements of wear test 15, in Fig. 4.31(a), indicate a large loss of abrasive grains within the DCB's contact area after grinding pass 60, by the $a'_e$ falling to 28 µm. The tool then continues to remove ∼28 µm for the following 90 passes, which through updating tool offsets could be compensated for. A complication of this potential solution is the added time and equipment to carry out tool offset during any process, and also more importantly, the impact $r_{runout}$ and the resultant surface craters have on the workpiece's surface quality. As detailed in Section 2.1.4, the effect of increased levels of $r_{runout}$ on surface quality is known to be detrimental and when using traditional wheels

and milling cutters, is a core reason to minimise $r_{runout}$.

Across the runout variation series of wear tests, 1443 AE signals were collected, each of which lasting >20 s. Much like the $AE_{raw}$ signal shown in Fig. 4.4, each acquired signal shows a clear increase in amplitude as the DCB comes into contact with the workpiece at the start of each pass. Within the $AE_{raw}$ signals of the feasibility series, it was indicated that each DCB's $r_{runout}$ and therefore level of contact could be seen through a change in AE across a single tool revolution, as seen in Fig. 4.5. The runout variation series allows a clearer observation of this principle, Fig. 4.33 shows a 10 ms section of $AE_{raw}$ from the $15^{\text{th}}$ grinding pass of wear tests (a) 9, (b) 12 and (c) 15. The three wear tests shown, cover a test from each of the $r_{runout}$ levels, indicated by their colour, with the associated DCB's $r_{runout}$ after each respective pass equal to 3.03 µm, 33.78 µm and 73.27 µm. The effect of increasing runout, and as a result decreasing the proportion of tool-workpiece contact per revolution, can be seen in Fig. 4.33. The $AE_{raw}$ generated by the DCB used in wear test 9, Fig. 4.33(a), resulted in a steady continuous signal with no discernable variation in amplitude across each DCB revolution. In direct contrast to this the $AE_{raw}$ from tests 12 and 15, in Fig. 4.33(b – c), show a clear periodic fluctuation in AE, inline with the spindle's rotational speed. Unlike the observation of this effect seen during the feasibility series, Fig. 4.5, the DCBs at "medium" and "high" $r_{runout}$ levels resulted in a larger loss of contact between the tool and workpiece, enabling the $AE_{raw}$ to ring down to the noise floor during each revolution. When the $AE_{raw}$ is at the noise floor it can be assumed that DCB is completely out of contact with the workpiece, and as such the bursts of AE can reveal a lot about the tool-workpiece contact. In Fig. 4.33(b), in which a "medium" $r_{runout}$ DCB was used, each burst lasts for ∼1.25 ms, half of the time taken for a single tool revolution, 2.5 ms. But in Fig. 4.33(c), where the DCB had a larger $r_{runout}$ by 39.49 µm, the bursts lasted for ∼1 ms. In addition to the difference in tool-workpiece contact being seen through the decreased time of each AE burst, the amplitude of the bursts was also greater during wear test 15 and resulted in a faster decay after each burst. All of these factors indicate the DCB's runout and contact between the grinding region and the workpiece surface, which could be utilised to indirectly infer a DCB's level of

$r_{runout}$.

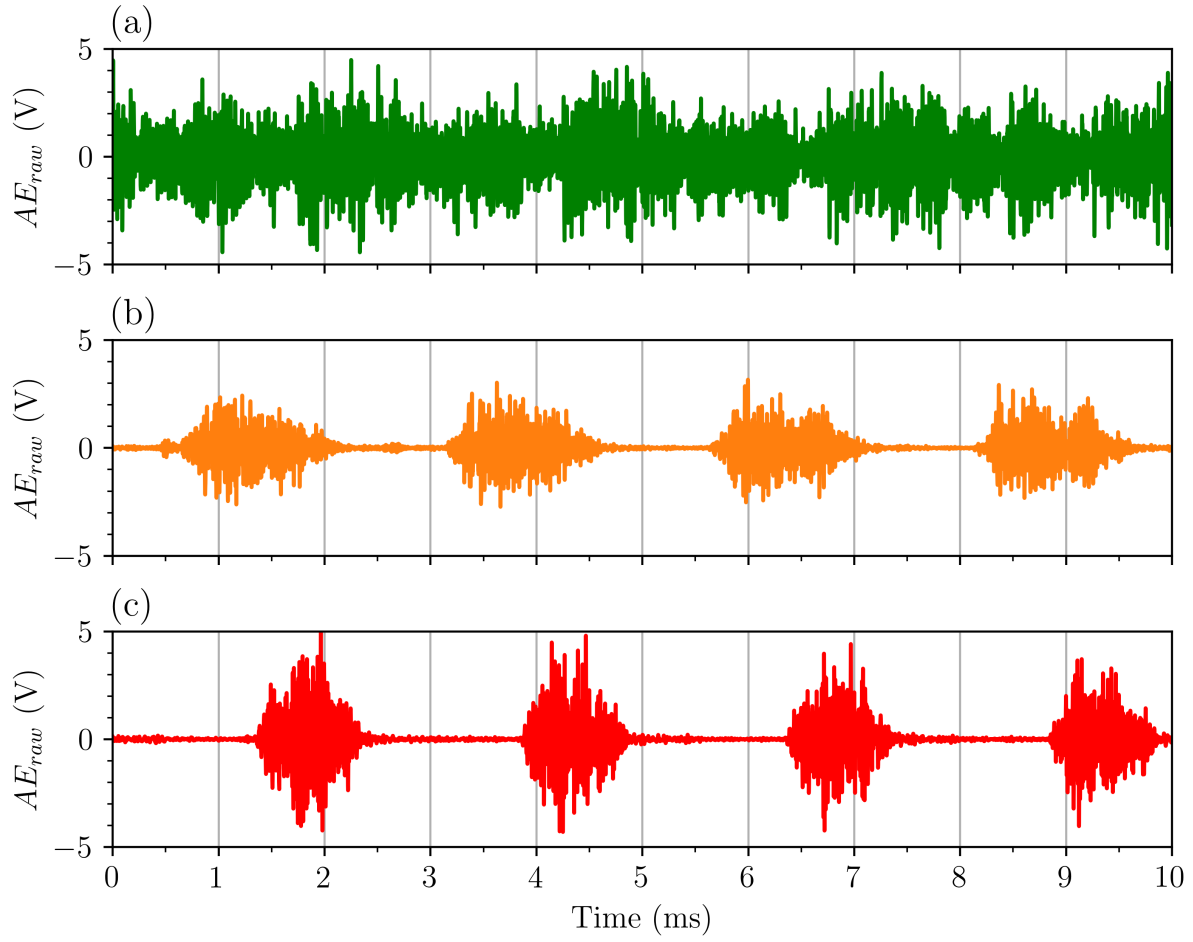


**Fig. 4.33:** Comparison of the generated $AE_{raw}$ between DCBs at different $r_{runout}$ levels; wear test (a) 9 - "low", (b) 12 - "med" and (c) 15 - "high".

To take advantage of this result from the $AE_{raw}$ signals, with the hope of tracking the wear progression of the DCBs, the DCB contact was monitored through the AE power envelope across each wear test. Figs. 4.34–4.36 show the AE power envelope from a single DCB revolution of each grinding pass of all the wear tests conducted during the runout variation series. Across all six of the "low" $r_{runout}$ wear tests, in Fig. 4.34, there is a consistent level of noise within the AE power envelope across each tool's life and around their circumference. As there is no distinct pattern aligned to the DCB's circumference, these figures indicate the tool has a low level of $r_{runout}$ and thus the grinding is consistent

in its aggressiveness. Both Figs. 4.35 and 4.36 show a markedly different result, with a distinct region of higher AE power as a result of the high spots on each DCB's surface from the increased level of runout. At the start of each wear test at the "medium" and "high" $r_{runout}$ levels, a clearly defined region around the DCB's circumference generates a large proportion of the AE power. Outside this region of high AE power, and therefore tool-workpiece contact, there is a clear drop-off in power to $<60\,\mathrm{dB_{AE}}$. Similar to the comparison seen in Fig. 4.33, the DCBs at the "high" level of $r_{runout}$ produce a more prominent power spike over a smaller region of each tool's circumference. Furthermore, the ability to monitor the flattening of each high spot and the subsequent expansion of surface craters is observable through the AE power within Figs. 4.35 and 4.36.

The clearest example of this is in Fig. 4.36(a), in which the region of high AE power splits into two distinct peaks after grinding pass 60, aligning with the point of initial high spot wear and flat spot formation, as observed in both Fig. 4.22(g) and Fig. 4.29(a). As the surface crater along the DCB's length expands around the tool's circumference, so too does the respective peaks within the AE power. Within most of the wear tests at the "medium" and "high" $r_{runout}$ levels the two AE power peaks, in Figs. 4.35 and 4.36, keep widening until eventually looping around and rejoining prior to failure. This indicates the craters have continued to expand around each tool's entire circumference, stripping the surface of its abrasive layer, before wearing the low point of the DCB and then failing as a result. This demonstrates a key advantage of an indirect AE-based approach for TCM, as this result was not seen in either NC4 surface measurements due to the laser's beam size limiting the measurement range.

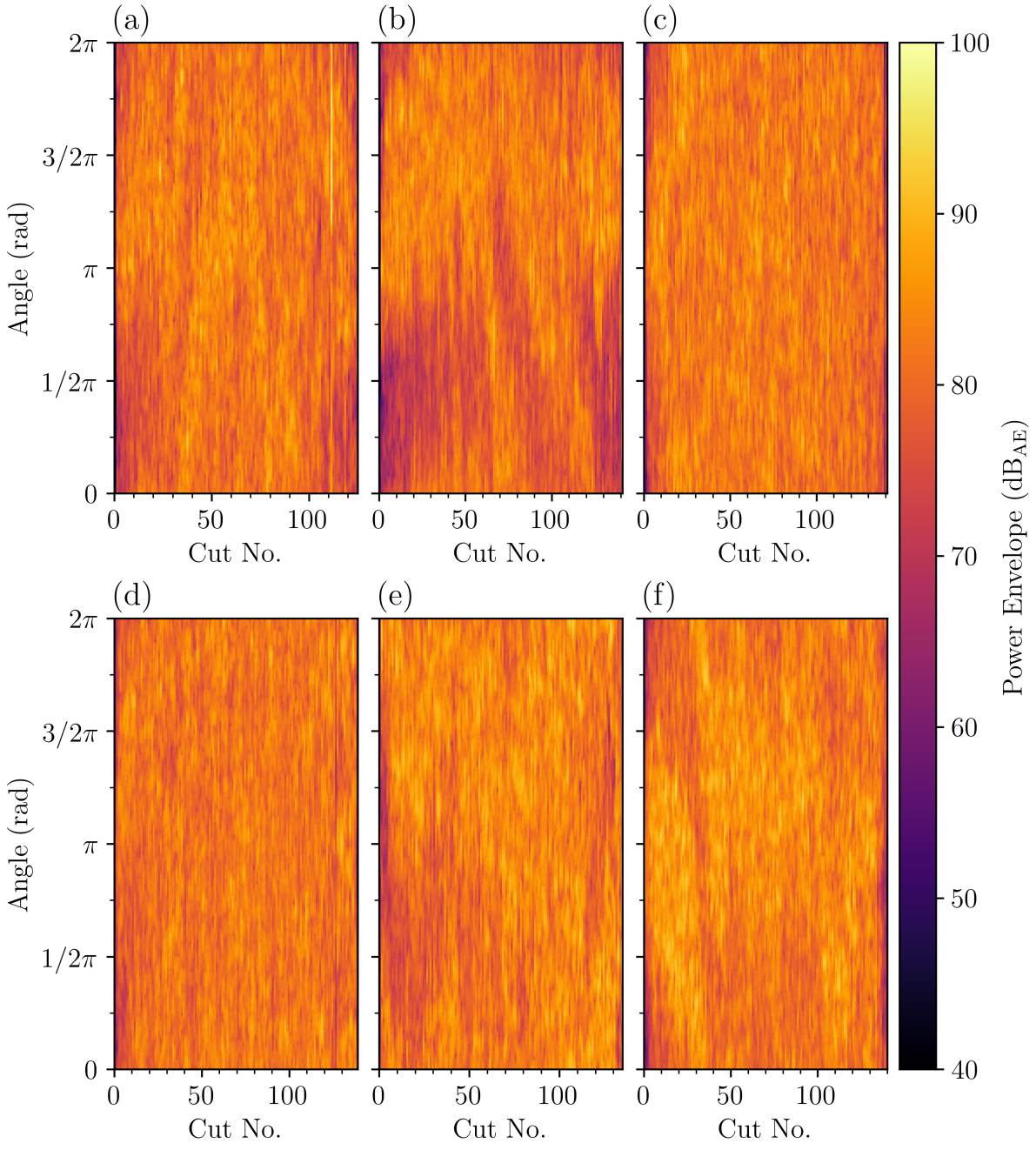


**Fig. 4.34:** AE power envelope over a single DCB revolution of each grinding pass from the "low" $r_{runout}$ level wear tests, with tests 6 – 11 shown in (a – f).

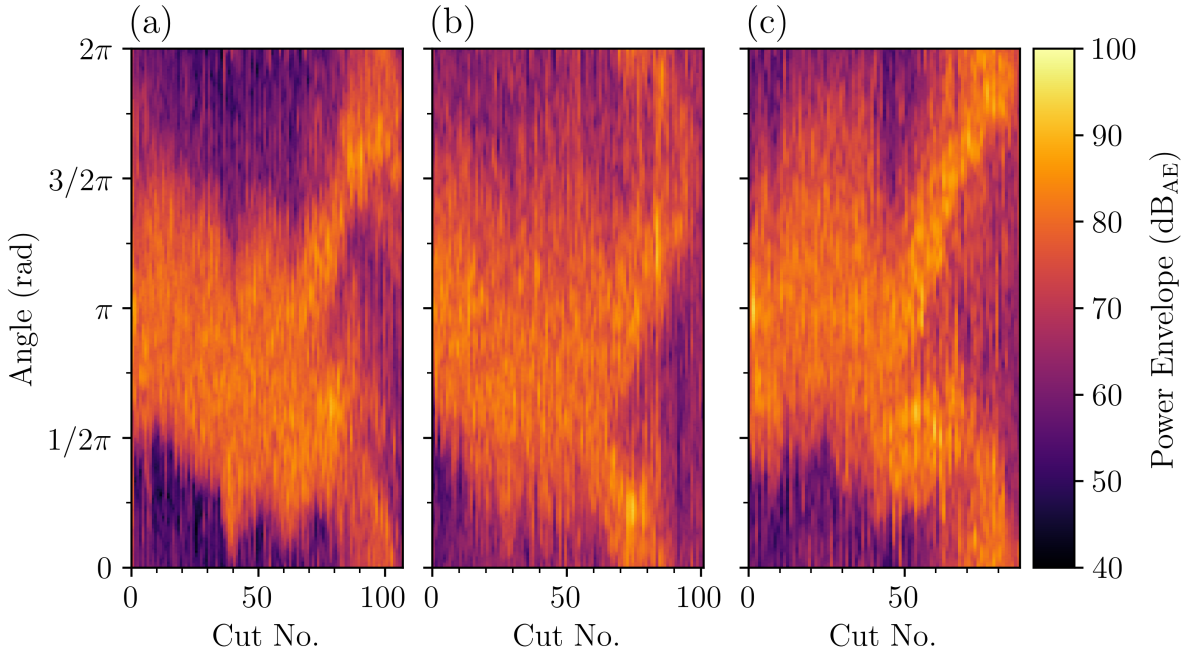


**Fig. 4.35:** AE power envelope over a single DCB revolution of each grinding pass from the "medium" $r_{runout}$ level wear tests, with tests 12 – 14 shown in (a – c).

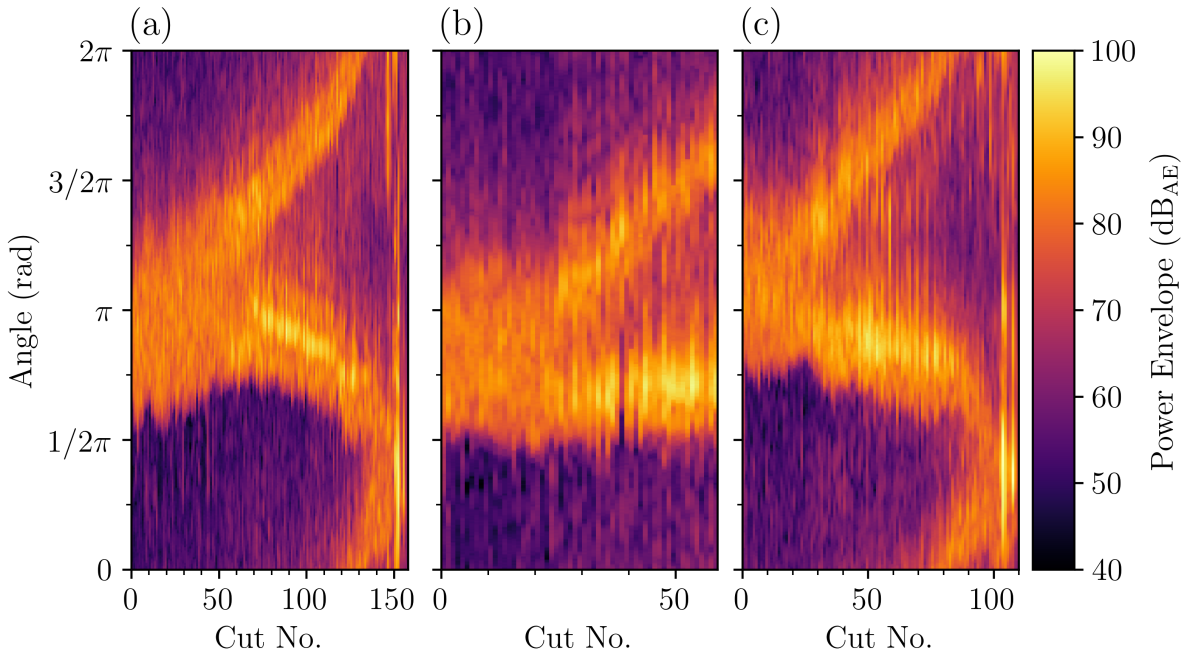


**Fig. 4.36:** AE power envelope over a single DCB revolution of each grinding pass from the "high" $r_{runout}$ level wear tests, with tests 15 – 17 shown in (a – c).

The raw time-domain AE signals are capable of identifying the contact period between the DCB and the SiC workpiece, indicating both a DCB's level of $r_{runout}$ and visualising the progression of wear around its circumference. However, due to the scale of the acquired data and the required computing power for processing, it is typically favoured to identify simplified features of the AE that best represent these $AE_{raw}$ results. Within the feasibility series, both $AE_{kurt}$ and $AE_{RMS}$ were seen to be useful metrics for determining the grinding condition and aggressiveness indirectly. Figs. 4.37–4.40 detail the capability of $AE_{kurt}$ across all wear tests within the runout variation series, with Fig. 4.41 showing the $AE_{RMS}$ of wear tests 9, 12 and 15.

The results of the four wear tests within the feasibility series highlighted $AE_{kurt}$ as a potential indicator for a DCB's $r_{runout}$, that is also capable of identifying the point of surface crater formation. As a measure of a distribution's "tailedness", the $AE_{kurt}$ of an idealised DCB should generate $AE_{raw}$ as a normal distribution, resulting in a $AE_{kurt} = 3$, which in the Figs. 4.37–4.40 is set to be the lower bound of the y-axis. Within Fig. 4.37, the DCB used during wear test 9, initially set to a "low" level of $r_{runout}$, resulted in a $AE_{kurt}$ slightly above three throughout its phase II - steady-state. The $AE_{kurt}$ therefore suggests that the DCB generating this AE, is near perfect, producing a continuous and steady $AE_{raw}$ signal throughout the majority of its life, as can be seen in Fig. 4.33(a–c). The $AE_{kurt}$ is validated by both the NC4 tool wear and OMP600 $a_e'$ measurements, which also indicate a near perfect DCB capable of removing the $a_e$ consistently within its steady-state phase of wear. By comparison, the increasing levels of $r_{runout}$ used in tests 12 and 15 resulted in clear and successive increases in the respective $AE_{kurt}$, a consequence of the decreasing level of tool-workpiece contact increasing the "tailedness" of the $AE_{raw}$ distribution.

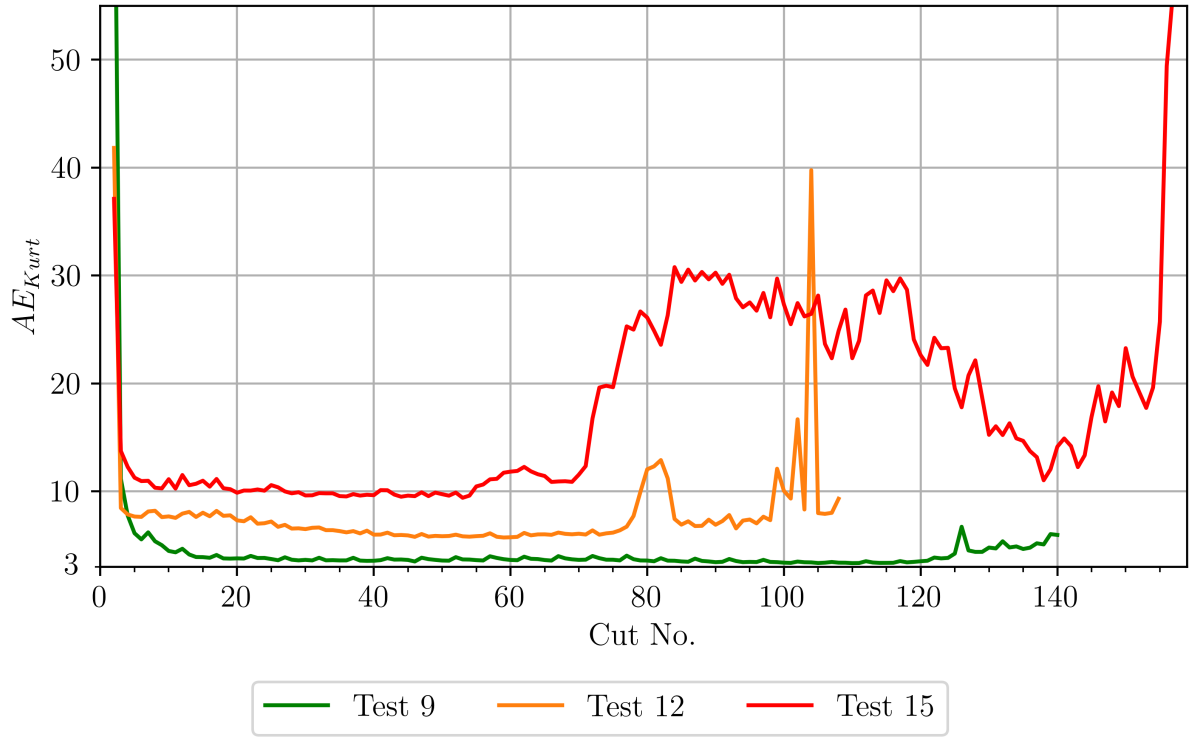


**Fig. 4.37:** $AE_{kurt}$ during wear tests 9, 12 and 15.

The $AE_{kurt}$ of each wear test in Fig. 4.37 also shows phase I - wear-in of each DCB, presented as an initial high that drops significantly over the first few passes to a baseline level. After reaching this baseline level, the $AE_{kurt}$ from each wear test slowly reduces as the DCB wears. This slight negative gradient indicates the $r_{runout}$ of each DCB is lowering as it wears into a more circular form, leading to more consistent tool-workpiece contact and AE generation. Whilst this is more apparent for the DCBs with higher $r_{runout}$, in tests 12 and 15, it is still observable for DCBs with "low" $r_{runout}$, such as in test 9, in Fig. 4.37. The minimum $AE_{kurt}$ occurs during grinding pass 109, 60 and 52 for tests 9, 12 and 15 respectively, after which the $AE_{kurt}$ starts to increase and eventually becomes more erratic in nature. These inflection points in the trends of the $AE_{kurt}$, indicate a large change in the tool's surface is imminent, seen through the large increase in $AE_{kurt}$ after passes 125, 75 and 70 of each test in Fig. 4.37. These increases all align with large wear bands or surface craters forming across the grinding region of each DCB in Figs. 4.20–4.22. The rise in $AE_{kurt}$ also scales with the DCB's level of $r_{runout}$, similarly to how the baseline

level is increased with the DCB's $r_{runout}$. Increases in $AE_{kurt}$ are compounded when the DCB has a high level of runout, as the generated $AE_{raw}$ bursts are of a greater amplitude across a shorter time period, as seen in Fig. 4.33. Both of which increase the "tailedness" of the $AE_{raw}$ distribution, in turn increasing the $AE_{kurt}$.

Figs. 4.38–4.40 show the $AE_{kurt}$ of each DCB used during the series, each showing a one of the three levels of $r_{runout}$ investigated. Within each $r_{runout}$ level, the $AE_{kurt}$ plots all follow a similar trend, with variance in timings and amplitudes as a result of each DCB's wear state. Across the "low" $r_{runout}$ wear tests in Fig. 4.38, all the DCBs resulted in low measurements of $AE_{kurt}$, mainly keeping below five, during each DCB's phase II - steady-state. In contrast, the $AE_{kurt}$ from the "medium" and "high" $r_{runout}$ wear tests stayed above 5 and 10 respectively. Throughout all the wear tests, the wear-in phase can be seen to be taking place through the $AE_{kurt}$, apart from in wear tests 16 and 17 in Fig. 4.40(b – c), whereby the $AE_{kurt}$ instead starts off at the baseline level. These two wear tests also happen to be the only tests with a $a'_e$ greater than the $a_e$ during their first grinding pass, seen in Fig. 4.31. And as such the DCBs' wear-in phase likely occurs very quickly, within a single grinding pass, preventing the $AE_{kurt}$ from detecting it.

In Figs. 4.38 and 4.39, showing the "low" and "medium" $r_{runout}$ wear tests, once a surface crater has formed the $AE_{kurt}$ increases up until the failure point. However, Fig. 4.40 shows a markedly different trend of the "high" $r_{runout}$ DCBs' $AE_{kurt}$. Instead of a constant increase to failure, the $AE_{kurt}$ first increases to a new high point and then falls back to the original baseline, and only then dramatically increases prior to the failure point. Fig. 4.40(b) can be seen to complete half of this trend, as the tool failed unexpectedly. This "hump" in the $AE_{kurt}$, between passes 70 – 140 of wear test 15 in Fig. 4.40(a) and passes 30 – 95 of wear test 17 in Fig. 4.40(c), directly aligns with the two peaks of the DCBs' surface crater expanding around the circumference and then rejoining on the opposite side. To explain this trend consider the expansion of said crater, as seen in Fig. 4.22. The $AE_{kurt}$ will continue to rise as the burst of $AE_{raw}$, from each peak's contact, increase in separation within a single revolution. Because a larger proportion of the $AE_{raw}$ generated during each revolution occurs at its maximum amplitude, due to the

two bursts, whilst the rest is at near zero due to the sharp ring down and complete loss of contact. This creates a more extreme and "tail-heavy" distribution, which therefore further increases the $AE_{kurt}$. However, as a surface crater expands around over half a DCB's circumference, the interval between AE bursts starts to decrease, inversing this effect and lowering the $AE_{kurt}$. Until the peaks rejoin, leaving a singular high spot of abrasive layer on the DCB surface, and returning the $AE_{kurt}$ back to a similar level prior to the original high spot wearing. The $AE_{kurt}$ then increases again as the DCB reaches its failure akin to the wear tests at lower levels of $r_{runout}$, in Figs. 4.38 and 4.39.

From the results of the runout variation series, $AE_{kurt}$ can be seen as a very useful AE feature for the TCM of a DCB. It is capable of indicating the end point of a DCB's phase I - wear-in, by falling from an initial high to a steady baseline. The baseline level then allows for a basic generalisation of the DCB's $r_{runout}$ level, through comparison with other wear tests. But perhaps most usefully, $AE_{kurt}$ also shows the wear state of a DCB regardless of its $r_{runout}$ level, through monitoring its slight downward trend and observing its inflection point. With a large increase during a DCB's steady-state phase of wear, scaled to its $r_{runout}$ level, indicating a significant change in tool-workpiece contact during the grinding pass.

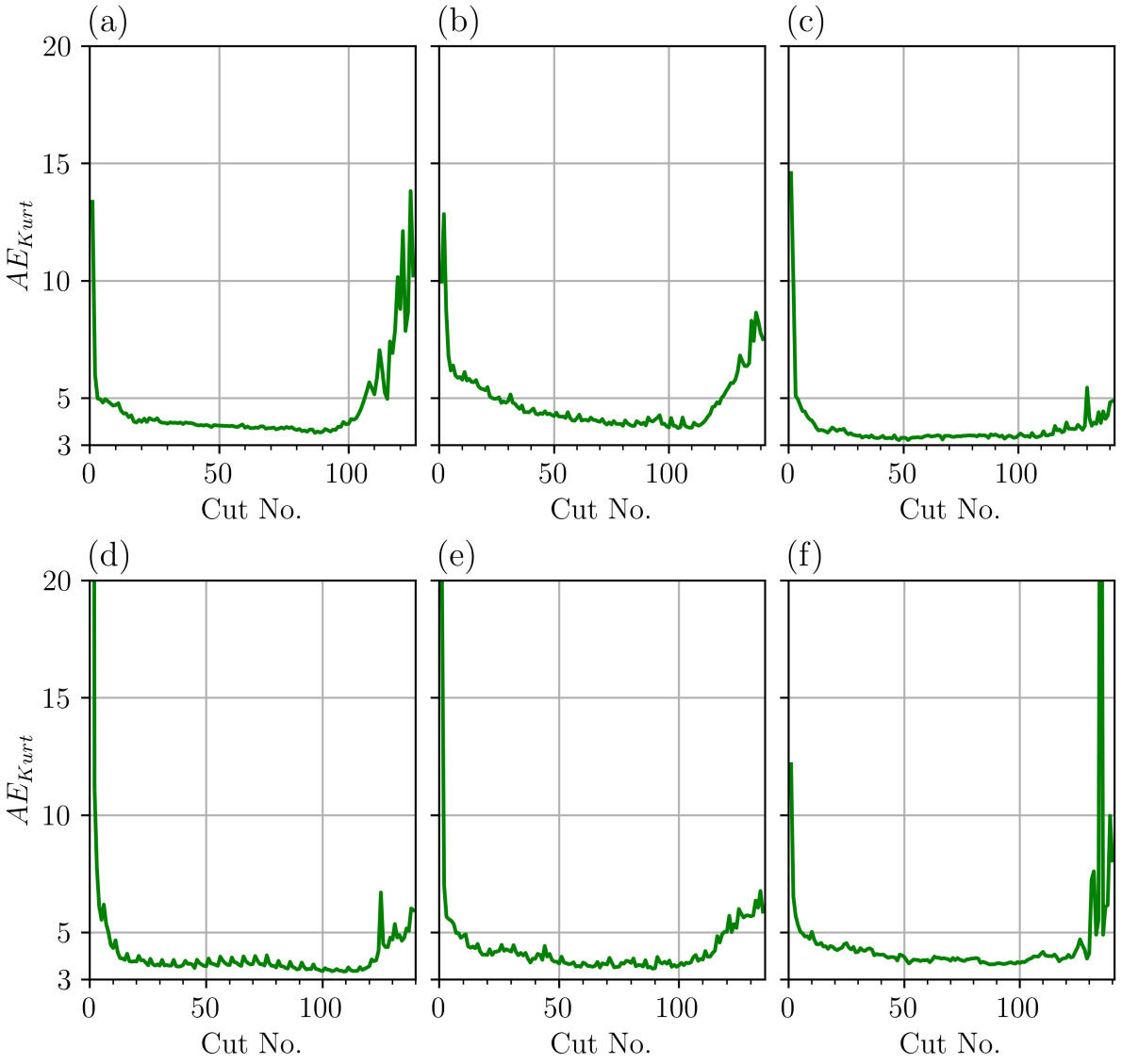


**Fig. 4.38:** $AE_{kurt}$ during the six wear tests conducted at the "low" level of $r_{runout}$, with tests 6 – 11 shown in (a – f).

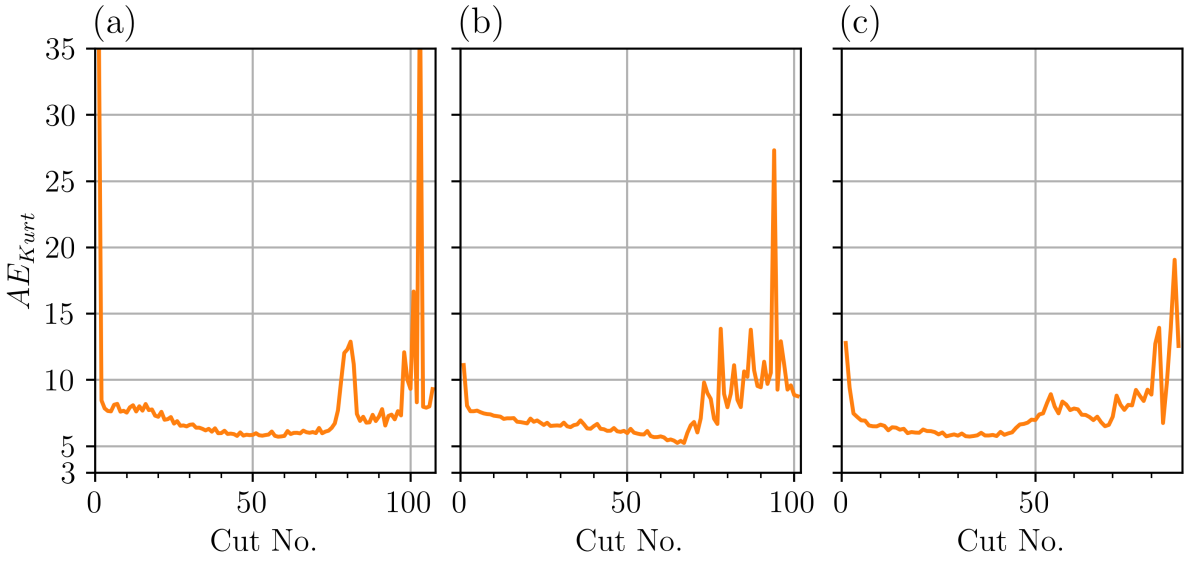


**Fig. 4.39:** $AE_{kurt}$ during the three wear tests conducted at the "medium" level of $r_{runout}$, with tests 12 – 14 shown in (a – c).

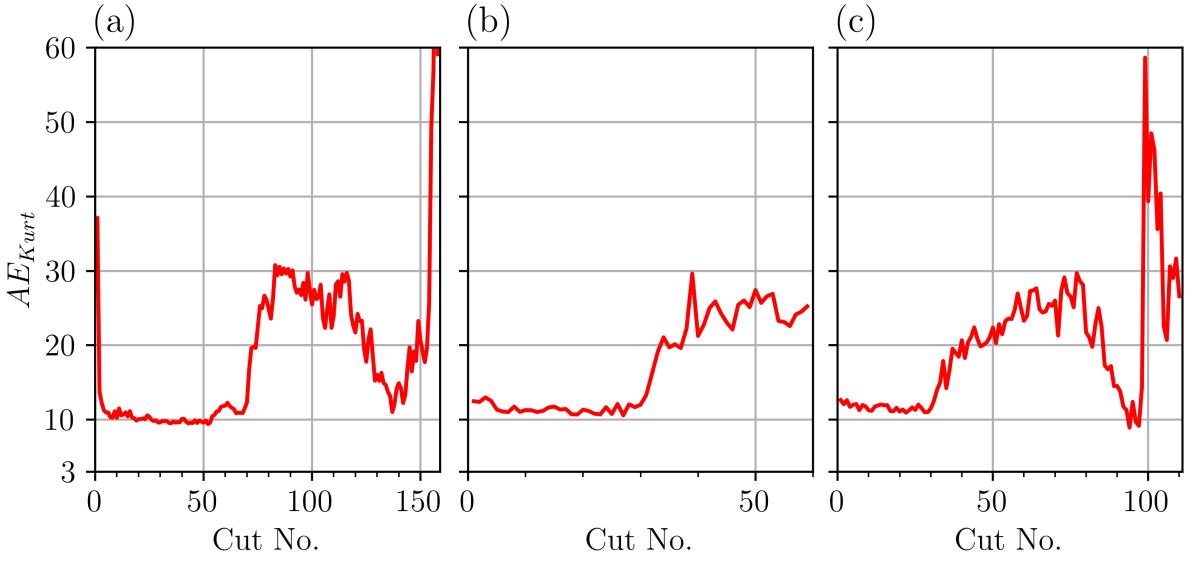


**Fig. 4.40:** $AE_{kurt}$ during the three wear tests conducted at the "high" level of $r_{runout}$, with tests 15 – 17 shown in (a – c).

The $AE_{RMS}$ represents the energy present within a continuous AE signal, making it a good indicator for the level of grinding contact between a wheel and workpiece.

Similarly to the $AE_{kurt}$ in Fig. 4.37, the wear-in phase of each tool can be identified through the initial variation in $AE_{RMS}$ prior to settling at a steady baseline shown in Fig. 4.41. Fig. 4.41 shows that once through the wear-in phase DCBs with "low" $r_{runout}$, such as in test 9, produce a consistent but high level of $AE_{RMS}$, until reaching phase III - wear-out. In contrast, the DCBs from tests 12 and 15 produced a lower level of $AE_{RMS}$ throughout their steady-state phases. In order for the $AE_{RMS}$ to increase, either the maximum amplitude or the duration held at that level must increase within the respective $AE_{raw}$ signal. Resulting in the more consistent grinding produced by "low" runout tools, yielding higher levels of $AE_{RMS}$. With the reduction in tool-workpiece contact, present during tests 12 and 15, therefore explaining the lowered level of $AE_{RMS}$ in comparison to test 9. Once the high spot of the DCBs seen in tests 12 and 15 have worn away, the $AE_{RMS}$ increases to a peak, the level of which indicating the scale/severity of the wear. The $AE_{RMS}$ plots seen in Fig. 4.41 allow for an understanding of the DCB's wear progression, similar to the aligned AE power envelopes in Figs. 4.34–4.36. Fig. 4.41 confirms that $AE_{RMS}$ is a capable indicator for the intensity of grinding over the entire workpiece's length. But without prior knowledge, it can be difficult to determine a given DCB's wear state based solely on its $AE_{RMS}$.

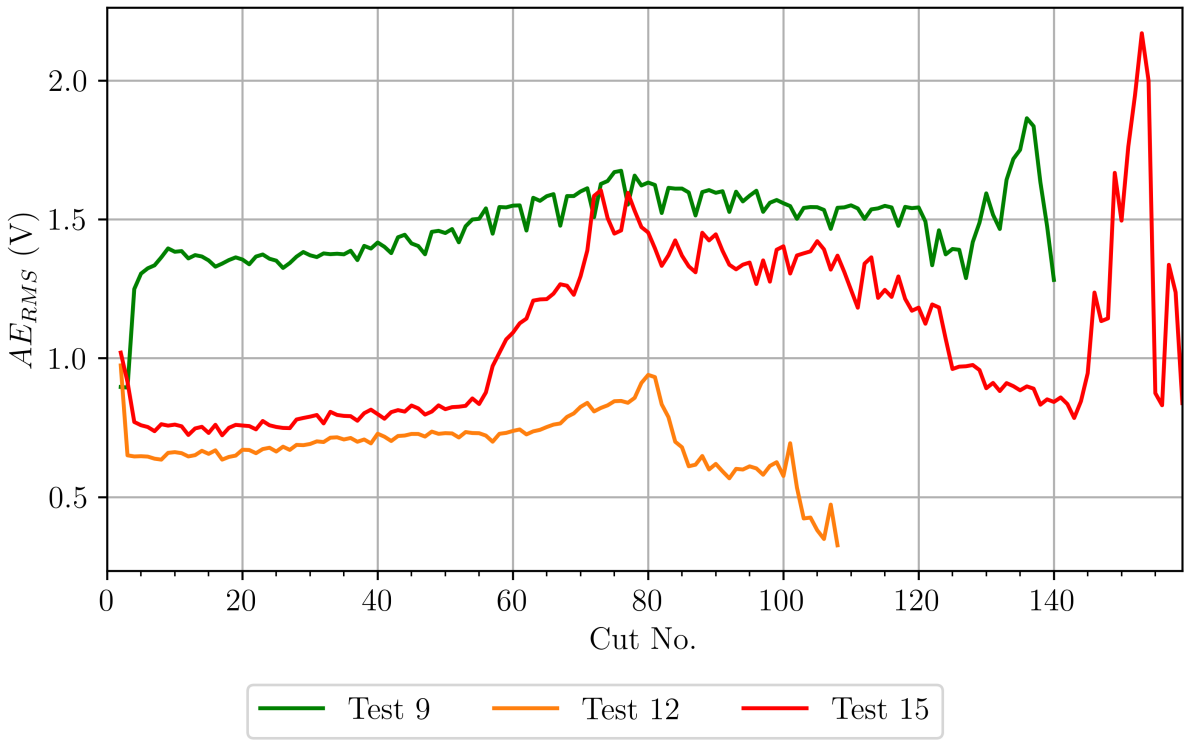


**Fig. 4.41:** $AE_{RMS}$ during wear tests 9, 12 and 15.

In conclusion, a successful series of twelve wear tests were conducted in which a NIKKEN adjustable tool-holder enabled the investigation of increasing levels of initial DCB $r_{runout}$. With the aim to both observe the subsequent effects on DCB wear and total tool life, and verify AE as an effective indirect monitoring technique regardless of $r_{runout}$.

The DCBs' $r_{runout}$ was varied between 1 – 77 µm, allowing observations across the feasible range of $r_{runout}$ for this specification of DCB. A distinct increase in the variability of a DCB's total useful life was found with increasing levels of initial $r_{runout}$, as well as a decrease to the total number of completed passes. The total number of grinding passes completed by DCBs at the "low" $r_{runout}$ level, resulted in a range of 16 grinding passes, whilst DCBs at the "high" level resulted in a range of 99 passes. Additionally, reducing a DCB's runout from "medium" to "low" levels yielded an increase in total life by 39 % on average.

The inspection phase of each wear test was advanced through the addition of two new

components: the 3D NC4 spiral scans and OMP600 probe workpiece measurements. These additions improved the previously limited inspection process by enabling monitoring wear over the entire tool's grinding surface and evaluating its grinding ability. 3D NC4 spiral scans, presented in Figs. 4.20–4.22, show the distinct effect of increasing $r_{runout}$. Through which consistently occurring wear mechanisms were identified, mainly the formation of wear bands around a DCB's circumference and larger surface craters spanning the DCB's length. The six "low" $r_{runout}$ DCBs all followed a similar process of wear, whereby a small band is worn through the abrasive layer which eventually expands along the tool's length, leading to failure. By contrast, the six DCBs at the "medium" and "high" $r_{runout}$ levels both initially wore flat spots along the axial high spot of the tool, resulting in a surface crater spanning the length of the DCB that slowly expanded around the circumference.

The use of an OMP600 spindle probe monitored the $a'_e$ removed by each DCB after every grinding pass, throughout their lives. The measurements shown in Figs. 4.25, 4.28 and 4.31, enabled an additional verification method to determine each DCB's wear state. The three-phase wear cycle of each DCB can be tracked through the characteristic "n" shaped curve the $a'_e$ measurements follow, presenting distinct transition points between each phase, unlike the NC4 wear measurements that present a more continuous trend. An increased variability in the $a'_e$ removed during each grinding pass was also seen through the probe measurements, with large scale wear resulting in a departure from the programmed $a_e$.

AE was capable of identifying a given DCB's $r_{runout}$ level by visualising the changing contact between workpiece and tool. As seen in Fig. 4.33, AE is clearly effected by a DCB's $r_{runout}$, impacting both its amplitude and overall signal characteristics. Through the sectioning and alignment of the $AE_{raw}$ signals, based on the rotational speed of the DCB, the severity of the high spot can be established, and its subsequent wear monitored, as seen in Figs. 4.34–4.36. Additionally, the use of simpler features such as $AE_{kurt}$ and $AE_{RMS}$ allowed the tracking of each DCB's wear state with reduced computational expense. Both features showing the transition points beteen each of the three wear phases, with $AE_{kurt}$ being more sensitive and useful to distinguish the DCB's $r_{runout}$ level. Fur-

thermore, AE presented a clear advantage over the NC4 system, as it captured the wear of DCBs, at the "high" level of $r_{runout}$, even when the NC4 had reached its measurement limit. This confirmed that the surface crater rejoined, having expanded around the entire tool circumference, a result that was only suggested through both the 2D and 3D NC4 measurements. Overall, When utilising a TCM approach based on AE, the signal changes stemming from a DCB's $r_{runout}$ could lead to premature tool replacement without the consideration of these effects, further increasing the existing tool-life wastage. However, with greater understanding of the process and the correct implementation of processing techniques it could also potentially allow for an on-machine, indirect and passive sensing methodology of determining a DCB's $r_{runout}$ and monitoring its wear simultaneously.

This series makes it evident that it is in an operator's best interest to reduce a DCB's $r_{runout}$, to not only increase its total life, but also ease any TCM system in identifying optimum tool change points, through the reduced variability of failure. But, even without measurement and reduction of a DCB's $r_{runout}$, AE allows the estimation of its severity and the ability to track wear progression even at the highest level of $r_{runout}$.

### 4.1.3 Control Series

After completing the runout variation series of wear tests, a further five tests were conducted within the control series. The aim of the series initially was to increase the dataset size of wear tests employing the full inspection cycle, tests including the 3D NC4 scans and OMP600 workpiece measurements. This would also allow further validation of the AE techniques seen across both Sections 4.1.1 and 4.1.2, on DCBs without any adjustment of $r_{runout}$. Table 4.4 shows a brief overview of the results from the five wear tests within this series.

**Table 4.4:** Control series overview.

| Test No. | DCB Initial Runout (µm) | DCB Mean Radius | | | Total No. Passes |
|---|---|---|---|---|---|
| | | Initial (mm) | Final (mm) | Wear (%) | |
| 18 | 7.88 | 0.657 | 0.611 | 7.022 | 71 |
| 19 | 3.67 | 0.647 | 0.611 | 5.560 | 68 |
| 20 | 9.29 | 0.661 | 0.611 | 7.625 | 74 |
| 21 | 1.85 | 0.652 | 0.610 | 6.349 | 64 |
| 22 | 8.61 | 0.663 | 0.611 | 7.895 | 72 |

After completing the first three wear tests, 18 – 20, in which the DCBs all completed less than 75 grinding passes, a concern was raised whether the methodology had changed, leading to this decrease in total life. By comparison, the "low" $r_{runout}$ DCBs of the runout variation series lasted between 125 – 141 grinding passes. The following two wear tests were then utilised to identify the cause of the consistent decrease in DCB life.

The machine g-code was unchanged between the two testing series, removing this as a potential cause. Additionally, the first three wear tests of the control series were conducted within a month of the last runout variation series test, during which time the machine tool was unused, significantly lowering the likelihood of the machine tool being the cause of the DCBs decrease in total life. Coolant evaporation was also ruled out through regular checking of the coolant additive concentration with a refractometer. At the start of the control series a new SiC workpiece of the same specification was set up for the following wear tests, therefore wear test 21 was conducted to eliminate this as a possible cause. Wear test 21 was completed with the same conditions as tests 18 – 20, except the DCB machined the previous SiC workpiece, used throughout the runout variation series. The DCB completed 64 total grinding passes prior to failure, falling within the range of inherent variation due to DCB manufacture, and therefore ruling out the new SiC as the cause. Finally, wear test 22 was then conducted with the NIKKEN adjustable tool-holder, without applying any adjustment to the DCB. This was done to rule out the chance that the normal BT30 tool-holder was responsible for the change in

life. Much like in wear test 21, the DCB in test 22 resulted in 72 total grinding passes, ruling out the tool-holder as the root of the decrease in tool life.

The remaining possible cause for the consistent but reduced level of DCB life across the five wear tests within the control series, is the DCB manufacture itself. The original order of DCBs from Genentech was fulfilled in early 2022, which were then used throughout both the feasibility and runout variation series. A further order of DCBs of the same specification was purchased from Genentech in June 2024, in anticipation of running out of DCB prior to completing all testing series. This new batch of DCBs was then used within the control series wear tests. Across the two batches of DCBs, it is possible that the manufacturing process was slightly modified by Genentech. Or even that a different grade of materials was utilised as a cost saving measure, leading to the decrease in total tool life. However, as Genentech are unwilling to provide any information about their DCB manufacturing processes. This hypothesis has not been confirmed beyond the reasoning laid out above.

Despite this change in each DCBs' total useful life, the five wear tests still provide valuable data for the training and validation of TCM approaches. The initial $r_{runout}$ of each DCB, seen in Table 4.4, was $<10\,\mu m$, inline with the "low" level of $r_{runout}$ used previously. Importantly, across the five wear tests, the DCBs resulted in a range of just 10 grinding passes between their failure points. This range is less than the range of 16 passes from the DCBs at the "low" level of $r_{runout}$ in the runout variation series, indicating the DCBs are still wearing through similar mechanisms as a result of constant grinding conditions within the series. Figs. 4.42 and 4.43 show the results from the 2D NC4 circumferential surface scans, and Fig. 4.44 shows the OMP600 $a'_e$ measurements during each of the five wear tests in the control series. The results from each wear test's inspection phase, show no distinct difference in their trends to the wear tests within the feasibility and runout variation series, other than the phase II - steady-state of each DCB lasting less passes.

Within the 2D NC4 measurements, seen in Fig. 4.42, the five DCBs can be seen to follow the standard three-phase wear cycle, with each DCB forming a surface crater within their steady-state wear phase. This is reflected in the $r_{mean}$ of each DCB, shown in

Fig. 4.43, presenting a similar trend to all the wear tests conducted at the "low" range of $r_{runout}$, in Fig. 4.24. The five control series tests also show a similar measurement trend for the $a'_e$ in Fig. 4.44, whereby each DCB follows an "n" shaped curve showing distinct transition points between each wear phase.

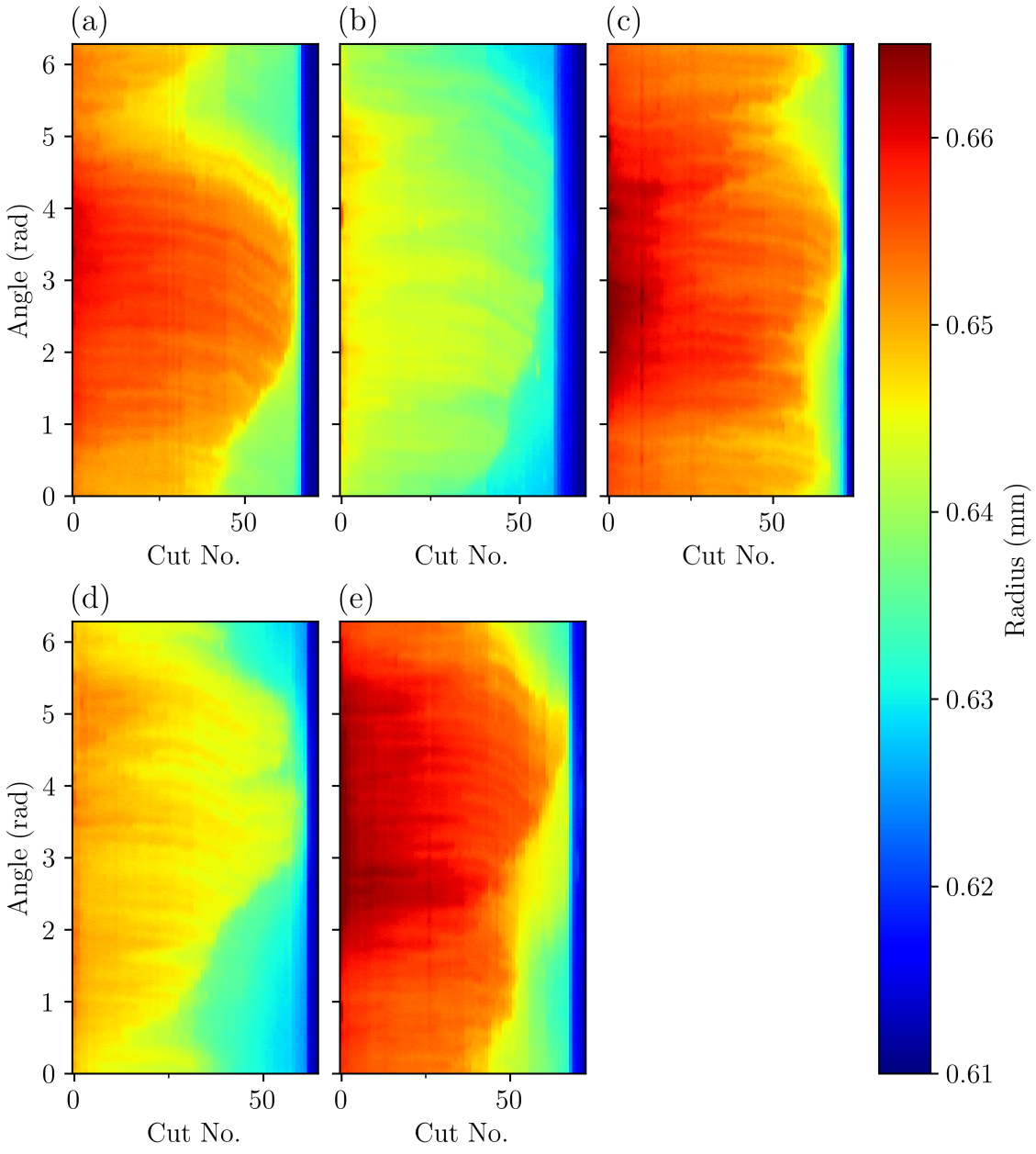


**Fig. 4.42:** NC4 circumferential surface scans during the five wear tests of the control series, with tests 18 – 22 shown in (a – e).

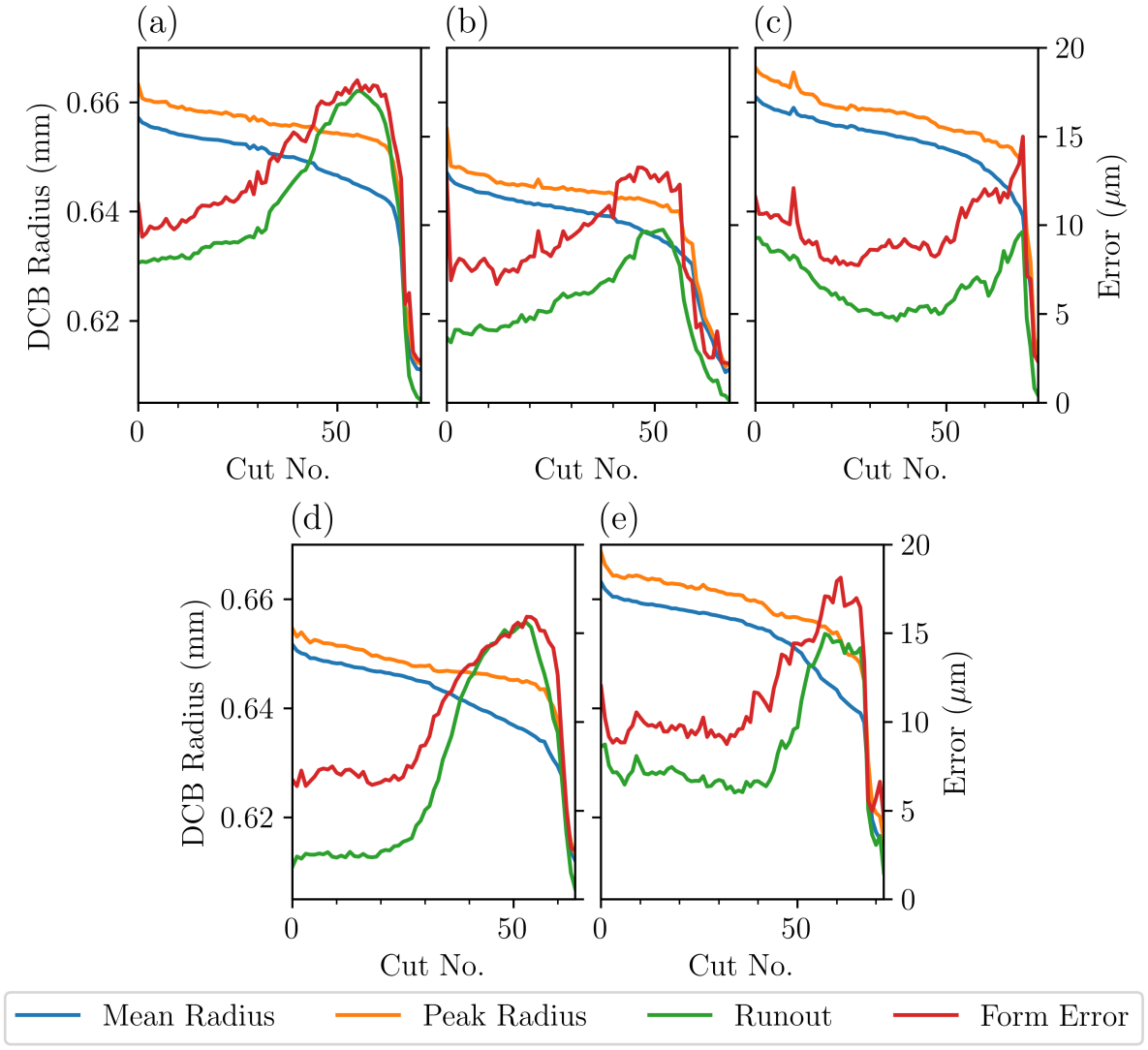


**Fig. 4.43:** NC4 attributes from the five wear tests conducted within the control series, with tests 18 – 22 shown in (a – e).

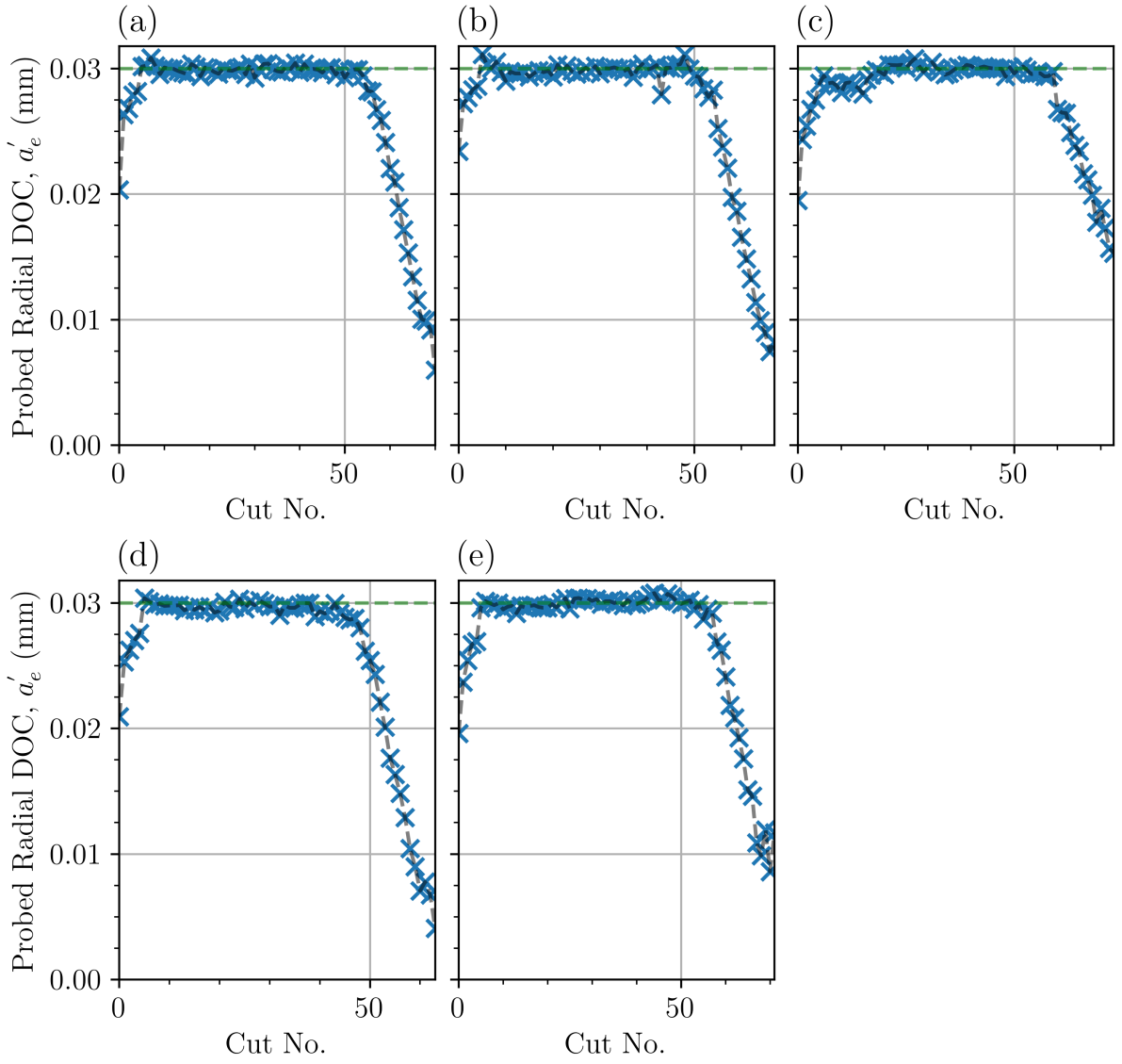


**Fig. 4.44:** True radial DOC, $a_e'$, measured throughout each wear test in the control series, with tests 18 – 22 shown in (a – e).

Figs. 4.45 and 4.46 show the NC4 spiral scans of the DCBs from wear tests 18 and 22 of the control series, with five grinding passes occurring between each sub-figure. Fig. 4.45(a) shows an anomaly at Z = 4.5 mm in the NC4 signal's acquisition, whereby the radius signal was corrupted for roughly half a tool rotation, causing a misalignment above this point in the scan. Within these figures, the wear mechanisms of both DCBs can be seen progressing through time. Akin to the other "low" $r_{runout}$ DCB 3D scans

seen in Fig. 4.20, both DCBs experienced wear bands around their circumference, which eventually led to tool failure. The presented DCBs in Figs. 4.45 and 4.46, had a larger initial $r_{runout}$ than the DCB in Fig. 4.20, and as such the a larger variation in tool radius can be seen around each tool's circumference and along its length. Additionally, the severity of each DCBs' phase I - wear-in can be seen over the first five grinding passes of each wear test.

The results from the inspection cycle, shown in Figs. 4.42–4.46, reinforce that the five control wear tests are still valuable for dataset expansion. Whilst the DCBs resulted in shorter wear tests under the same conditions, the underlying wear mechanisms are the same as previous wear tests. Furthermore, the DCBs resulted in a lower range across their total grinding passes than previously seen within the feasibility series and "low" $r_{runout}$ wear tests. Therefore, whilst concerning that DCBs of the same specification can have this large of a variance in life between batches, it is a net positive with regard to developing potential TCM approaches. As it exposes further unexpected scenarios for model training, in which a non-generalising model may fall short.

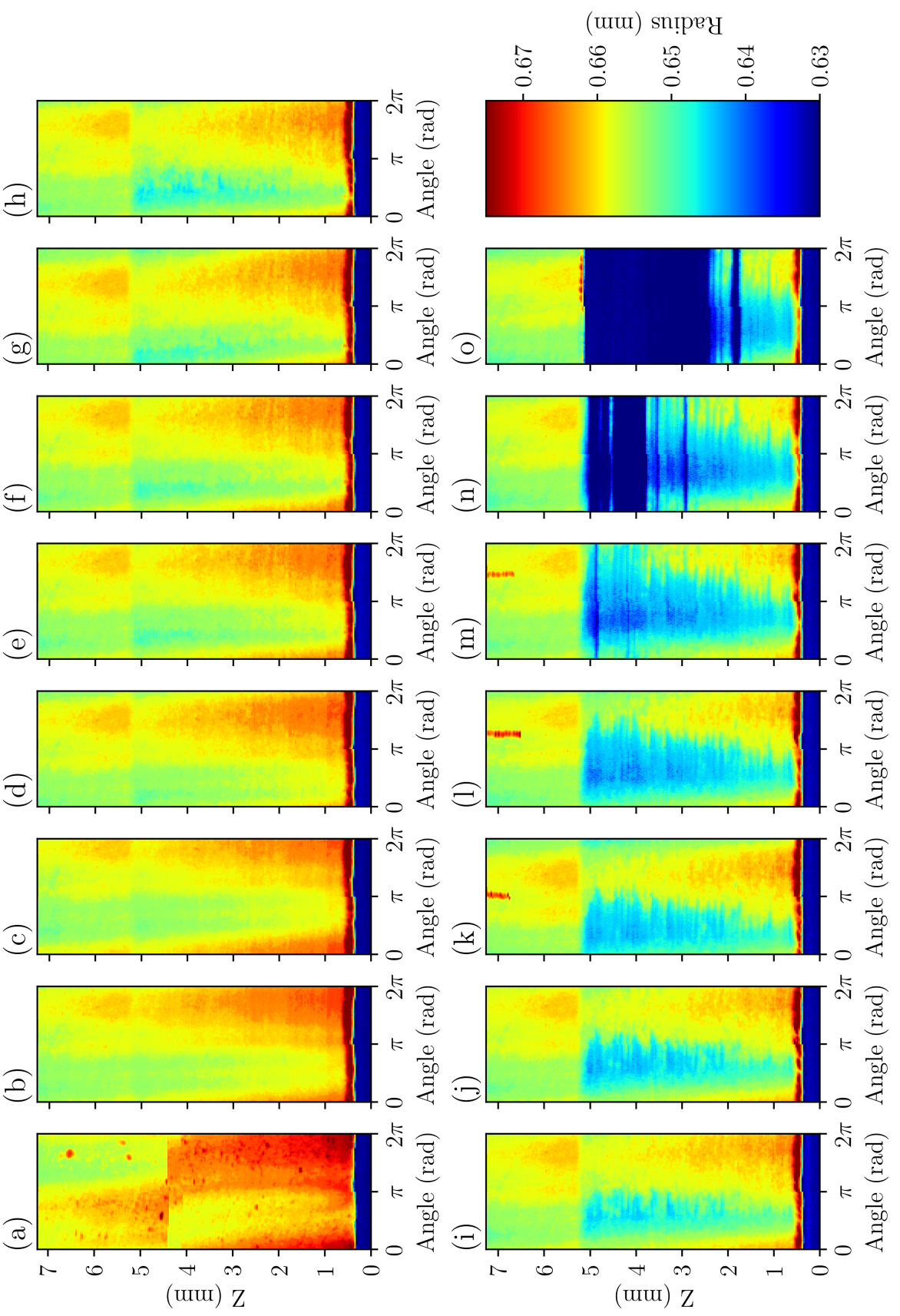


**Fig. 4.45:** NC4 spiral scans of the DCB during wear test 18 with 5 grinding passes between each sub-figure (a – o).

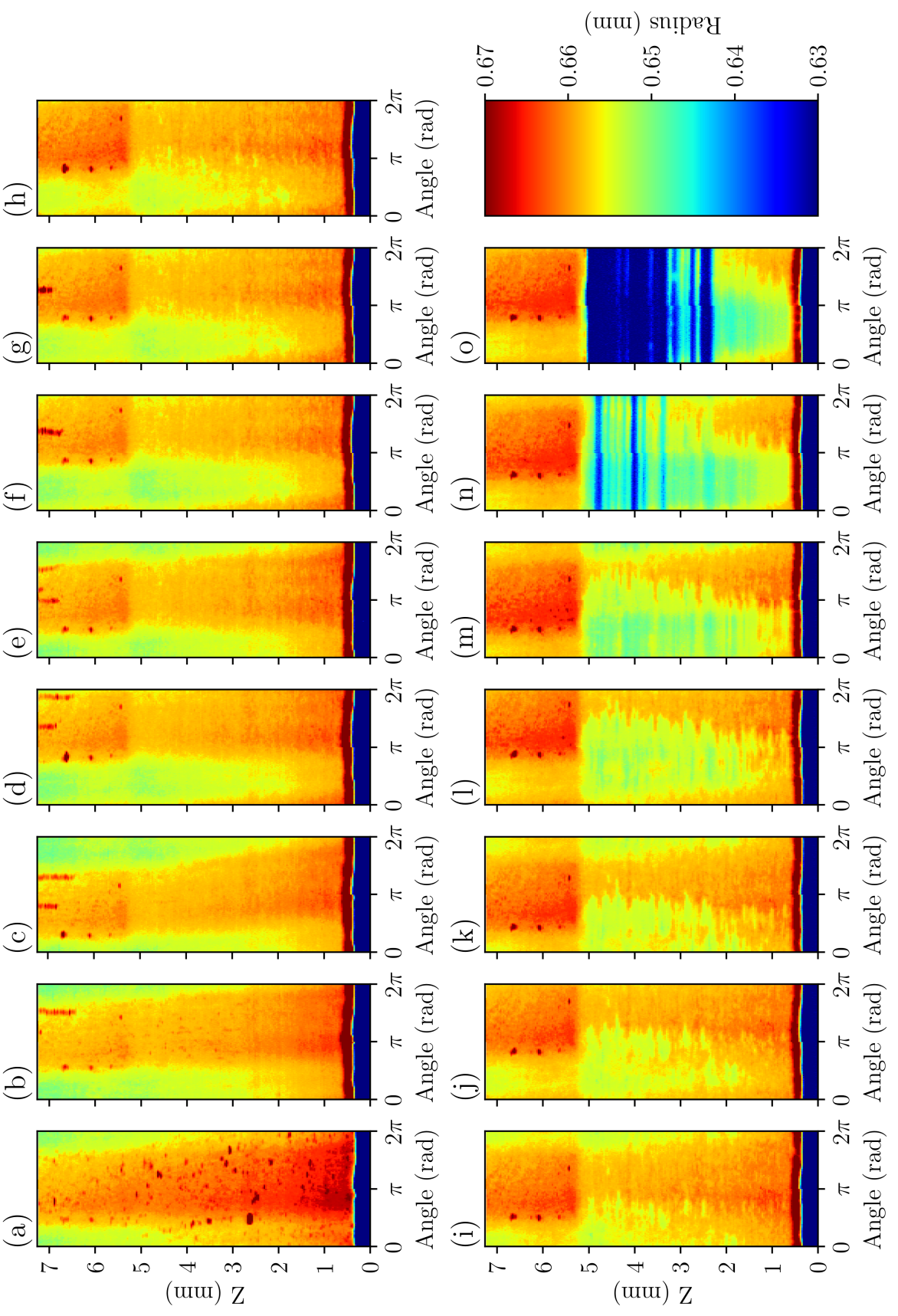


**Fig. 4.46:** NC4 spiral scans of the DCB during wear test 22 with 5 grinding passes between each sub-figure (a – o).

Similarly to the inspection phase measurements of the five control series wear tests, the AE also follows similar trends to the tests seen within the feasibility and runout variation series. Fig. 4.47 shows the aligned AE power envelope over a single tool revolution of each wear test in the control series. Much like the results from the "low" $r_{runout}$ wear tests, in Fig. 4.34, the aligned AE power plots in Fig. 4.47 show no distinct pattern associated with high levels of $r_{runout}$. Instead, each wear test presents as a consistent level of random noise, as expected of a grinding tool with a random distribution of abrasive grains around its circumference and minimal $r_{runout}$. Therefore, seeing no discernable pattern within the sub-figures of Fig. 4.47, indicates each DCB was operating with a "low" level of $r_{runout}$

Within the AE time domain features, both $AE_{kurt}$ and $AE_{RMS}$, shown in Figs. 4.48 and 4.49 respectively, also follow a similar trend to the previously presented data. Apart from wear test 19 that fluctuated within its first 40 grinding passes, all the DCBs produced consistent and very low $AE_{kurt}$, until the end of their steady-state wear phase. At the end of each DCBs' steady-state phase, the $AE_{kurt}$ increases up to the point of failure. Whilst each wear test's baseline is approximately the same level, the amount of increase prior to failure is not consistent across each wear test.

Fig. 4.49 of each wear tests $AE_{RMS}$ measurements, shows a much larger amount of variation within each DCBs' life. However, each phase within the DCB's three-phase wear cycle can be identified visually. Phase I - wear-in of each of the five wear tests, is seen through a sharp increase in the $AE_{RMS}$ over the first few grinding passes, similarly to the "low" $r_{runout}$ DCBs within the runout variation series, in Fig. 4.41. Followed by a period of consistent $AE_{RMS}$ leading into a more erratic and unpredictable period, inline with the DCBs' phase II - steady-state and III - wear-out.

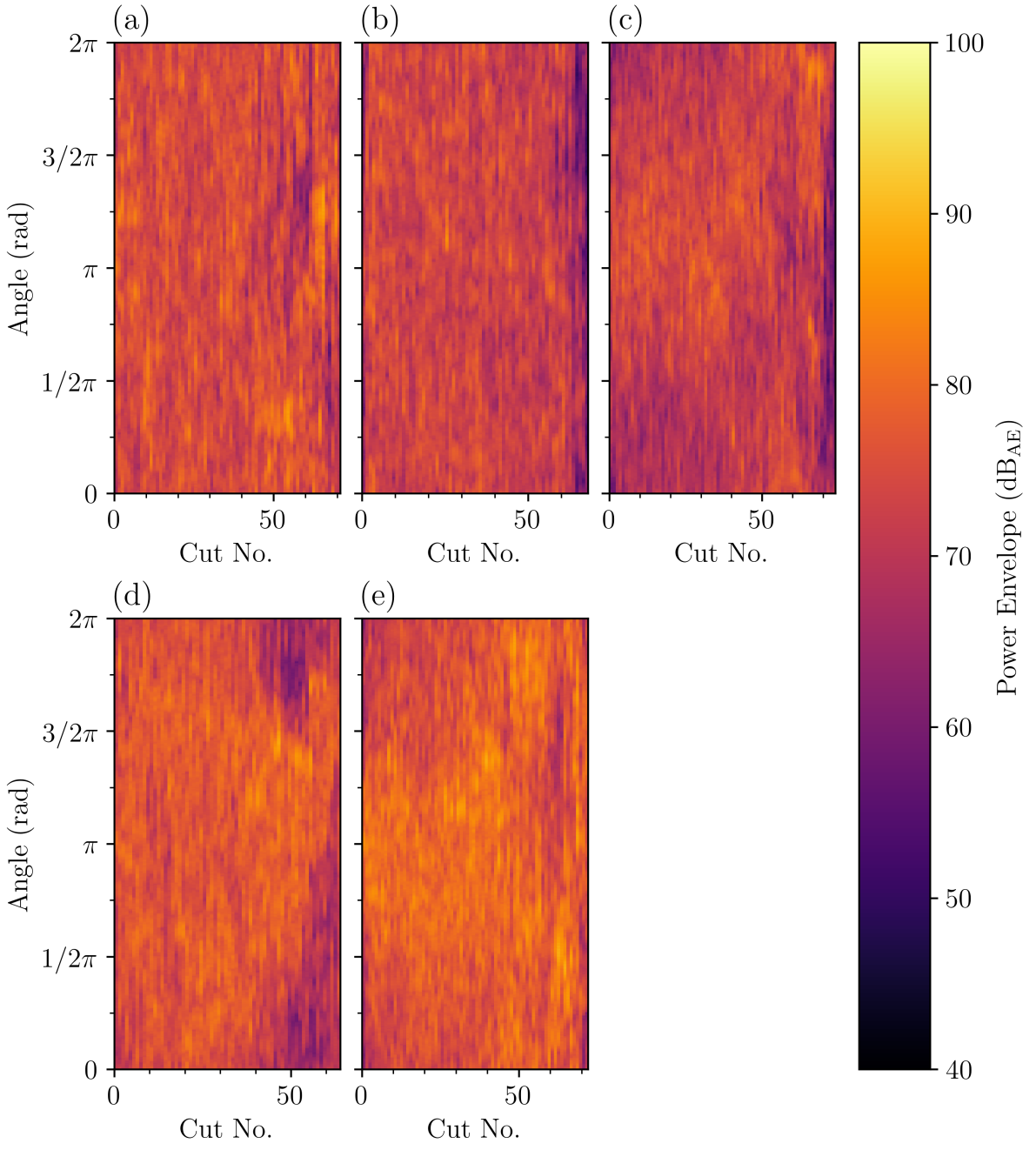


**Fig. 4.47:** AE power envelope over a single DCB revolution of each grinding pass of the five control series wear tests, with tests 18 – 22 shown in (a – e).

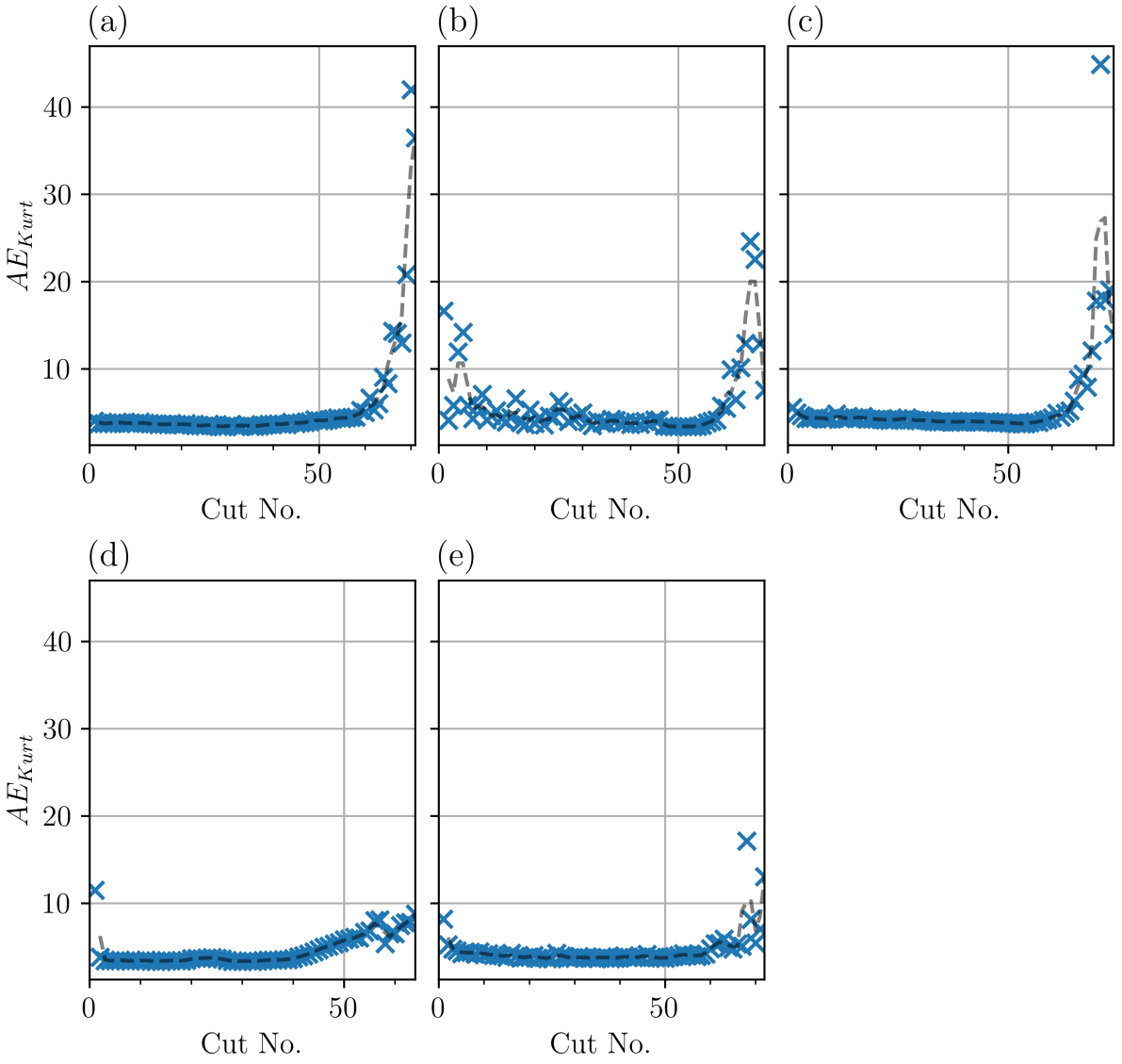


**Fig. 4.48:** $AE_{kurt}$ during each wear test of the control series, with tests 18 – 22 shown in (a – e).

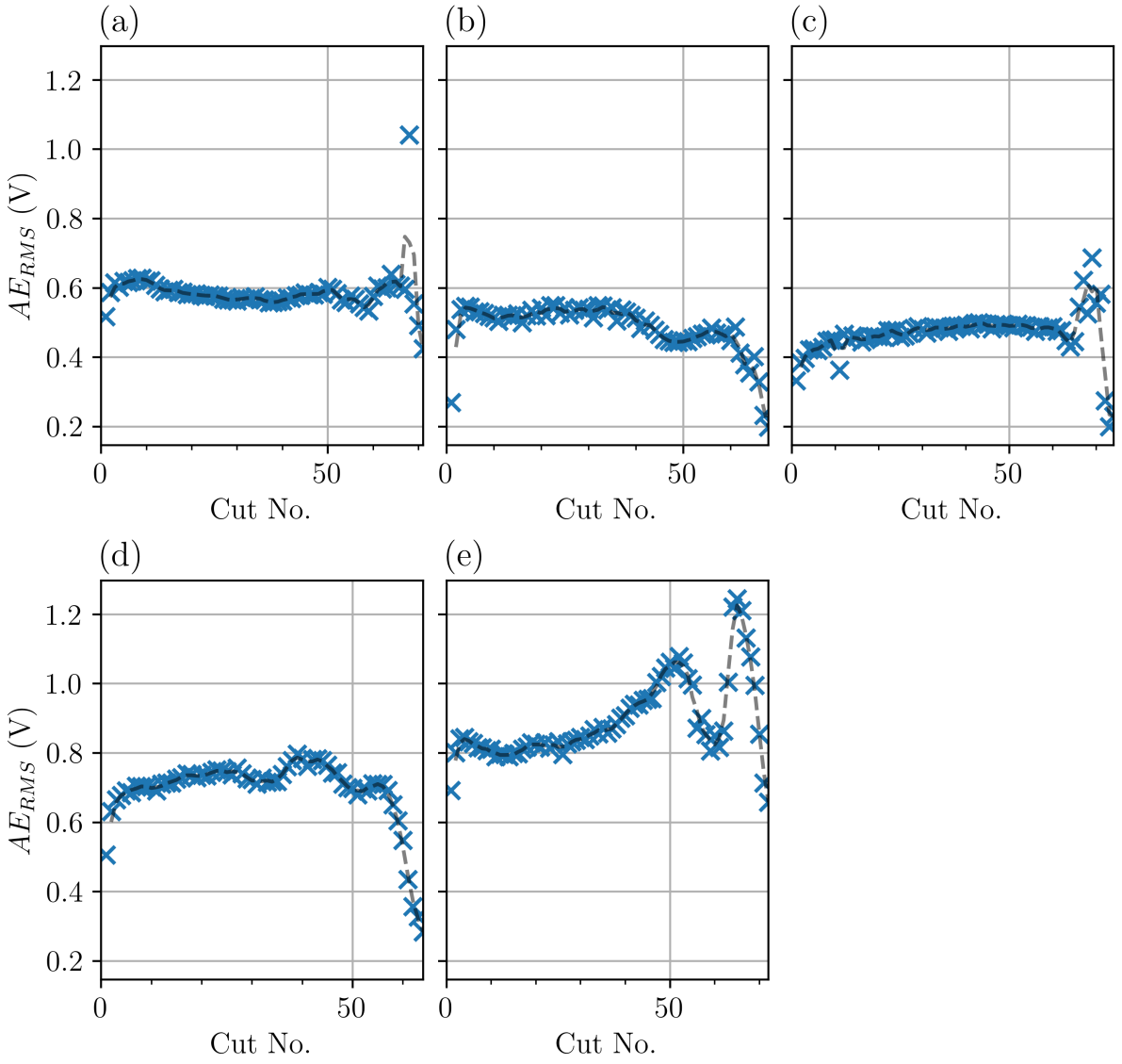


**Fig. 4.49:** $AE_{RMS}$ during each wear test of the control series, with tests 18 – 22 shown in (a – e).

The PSD of the 30$^{\text{th}}$ grinding pass of each wear test in the control series can be seen in Fig. 4.50. The AE from each of the five wear tests, produced a consistent spectrum with peaks and troughs aligned between each of the PSDs. A different AE sensor of the same specification, a MISTRAS WD, was used for the runout variation and control series, due to availability, explaining the slight differences in spectral shape between Fig. 4.50 and Fig. 4.11. However, the same key peaks are consistent across both sensors and all

wear tests. Within Fig. 4.50, the PSDs from wear tests 21 and 22 can be seen to attenuate less at the higher frequency ranges than in tests 18 – 20. This difference in attenuation is the result of wear tests 21 and 22 using the old SiC workpiece rather than the new workpiece used for the previous three tests. Whilst of the same specification, the old workpiece had been used for all the runout variation wear tests, leading its grinding surface to be significantly closer, by approximately 30 mm, to the sensor than on the new SiC workpiece. This difference in distance has a minimal effect on any AE features other than high frequency $PP$, as seen in Fig. 4.50.

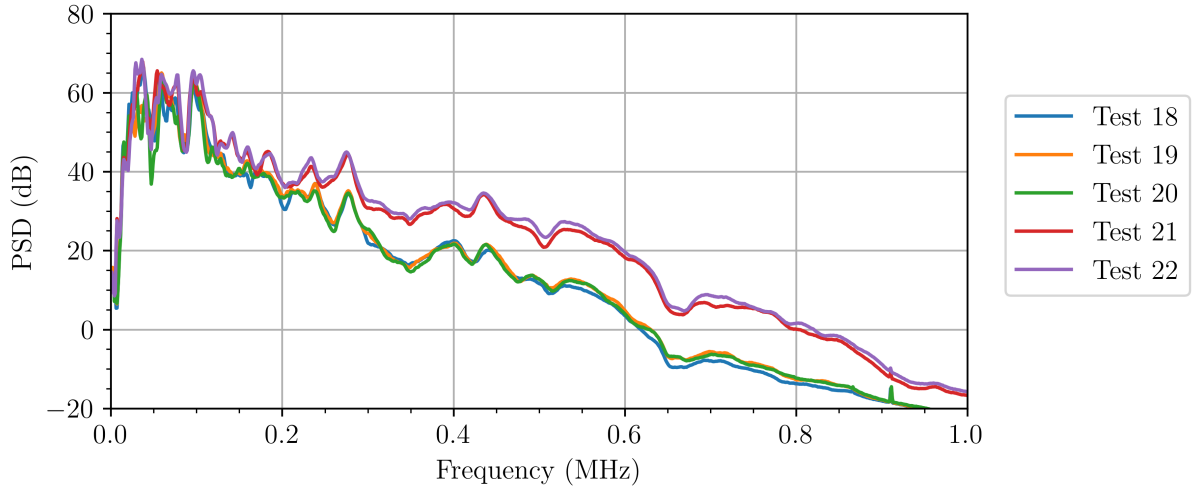


**Fig. 4.50:** PSD from the 30$^{\text{th}}$ grinding pass of each wear test during the control series.

Fig. 4.51 shows the $PP_{350}$ during each grinding pass of the five control series wear tests, having been identified manually as a highly correlated feature. The aforementioned decreased level of attenuation can be seen in Fig. 4.51(d – e), in which the $PP_{350}$ values are on average ∼15 dB larger. Despite this difference in power level, the trend of every DCBs' $PP_{350}$ is not only consistent, but also correlates very well to the $a'_e$ measurements during each test, seen in Fig. 4.44. Similarly to OMP600 $a'_e$, in Fig. 4.44, the $PP_{350}$ show a period of relatively constant levels during the DCBs' phase II - steady-state. Then followed by a slow decrease in $PP_{350}$ inline with the DCB' loss of tool-workpiece contact, during their phase III - wear-out. This result opens an avenue of utilising a single $PP$ feature as a measure of radial wear, alongside a form of attenuation compensation method, to correct

for changing source distances.

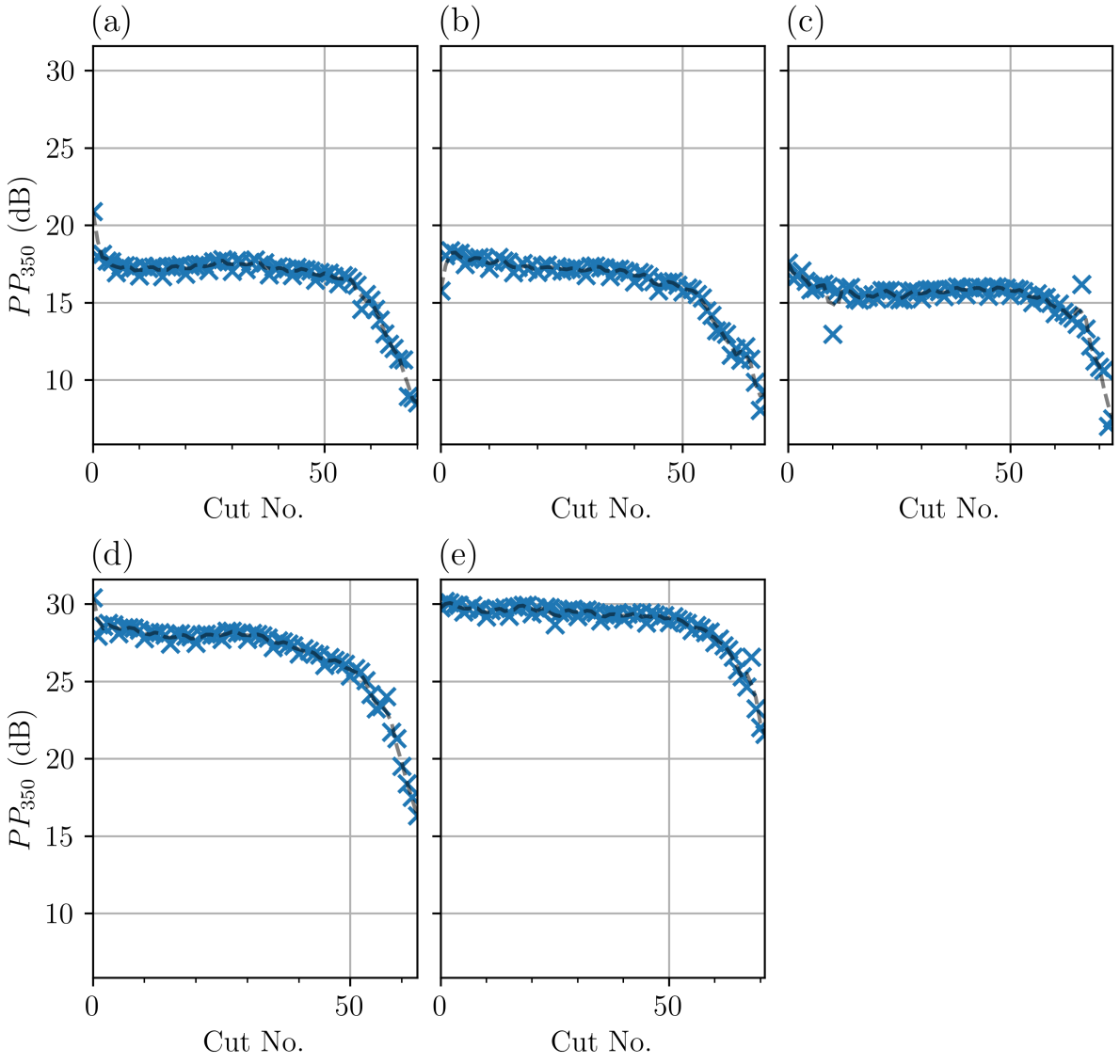


**Fig. 4.51:** $PP_{350}$ during each wear test of the control series, with tests 18 – 22 shown in (a – e).

To summarise, five additional DCB wear tests were conducted with the premise of expanding the existing TCM dataset. Each DCBs' $r_{runout}$ level was not adjusted and the five wear tests were conducted under the same specifications and methodology as prior testing series, yet resulted in a consistent but premature failure of each DCB. A 50 % reduction in the number of grinding passes completed by each DCB, was deemed to be

the result of differences in manufacture of a new batch of DCBs used for the control series.

Despite this, results from the five wear tests coincided with the expected wear mechanisms and AE feature trends seen in both the feasibility and runout variation testing series. The inspection cycle, conducted throughout each wear test, proved that in spite of their reduced overall tool life, each DCB still followed the three-phase wear cycle and was worn as a result of the identified mechanisms in prior testing series. Additionally, the OMP600 $a'_e$ measurements in Fig. 4.44, confirmed that the DCBs were still capable of carrying out the programmed grinding pass. Measurements from both the NC4 and OMP600, proved that the five control series wear tests are still valid for inclusion in the larger wear test dataset.

The collected AE showed no clear anomalies as a result of the difference in DCB quality. Furthermore, the five wear tests further confirmed the efficacy of AE in monitoring the wear progression of a DCB. Through the aligned AE power envelope of each DCB, in Fig. 4.47, the DCBs could be seen to be at a "low" $r_{runout}$ level. Both the $AE_{kurt}$ and $AE_{RMS}$ presented as clear indicators of DCB surface wear through their changing levels and trends. Additionally, the AE frequency domain showed a clear correlation with the OMP600 $a'_e$ measurements. The $PP_{350}$ of each wear test, in Fig. 4.51, enabled clear tracking of the DCBs' tool-workpiece contact, detailing the decline in material removal due to radial tool wear.

## 4.2 Grinding Parameter Variation Study

To prove that these AE techniques and ML approaches are suitable for real-world applications, there is still a large amount of verification to be conducted. Other studies [119, 120, 181] have comprehensively covered the matter of AE sensor location, therefore it was decided to instead investigate changing process parameters and the effect it has on acquired AE signals. A short initial study was conducted to observe the effects of changing feedrate, $V_f$ and spindle speed, $n$.

Across the study, 17 grinding passes were completed with a new DCB. Table 4.5 shows an overview of how the grinding parameters changed for each grinding pass. Feedrate and spindle speed were the only two grinding parameters varied from the previously used methodology, presented in Section 3.2. Prior to varying the grinding parameters, five grinding passes were completed with unchanged parameters, acting both as control data points for any comparisons and to ensure the DCB has completed phase I - wear-in. After which, three grinding passes were completed at both 80 % and 60 % of the control feedrate and spindle speed. These changed parameter values were chosen arbitarily, whilst still ensuring the specified grinding pass in Table 3.1 was capable of being completed.

**Table 4.5:** Grinding parameter variation study overview.

| Cut No. | Spindle Speed (rpm) | Feedrate (mm/min) | Description |
|---|---|---|---|
| 1-5 | 24,000 | 60 | Control |
| 6-8 | 24,000 | 48 | 80 % Feedrate |
| 9-11 | 24,000 | 36 | 60 % Feedrate |
| 12-14 | 19,200 | 60 | 80 % Spindle Speed |
| 15-17 | 14,000 | 60 | 60 % Spindle Speed |

Figs. 4.52 and 4.53 show the NC4 attributes and OMP600 $a'_e$ measurements after each of the 17 grinding passes. The NC4 $r_{mean}$ and $r_{peak}$ attributes show minimal radial wear occurring over the first few passes, as would be expected of a DCB undergoing phase I - wear-in. However, Fig. 4.53 shows a clear wear-in phase over the first two grinding passes, in which the DCB removes $<25\,\mu m$, prior to the DCB reaching phase II - steady-state and removing a consistent level of $a'_e$ near the programmed $a_e$. As such, the first two grinding passes have been removed from any of the following comparisons, as the AE data over the two passes present as clear anomalies.

Other than the DCB's wear-in phase, Figs. 4.52 and 4.53 show the DCB is grinding within phase II - steady-state, an important consideration when making comparisons between the generated AE. Also, the DCB can be seen to have a "medium" level of

$r_{runout}$, >15 µm, across all the completed grinding passes.

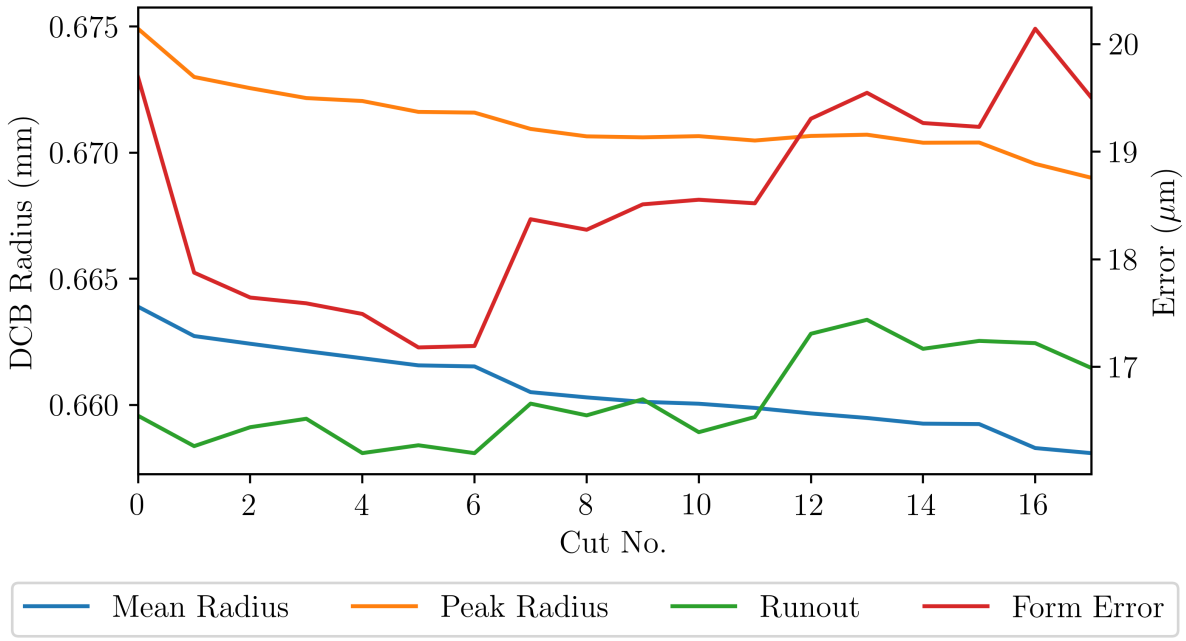


**Fig. 4.52:** NC4 attributes after each grinding pass of the parameter variation study.

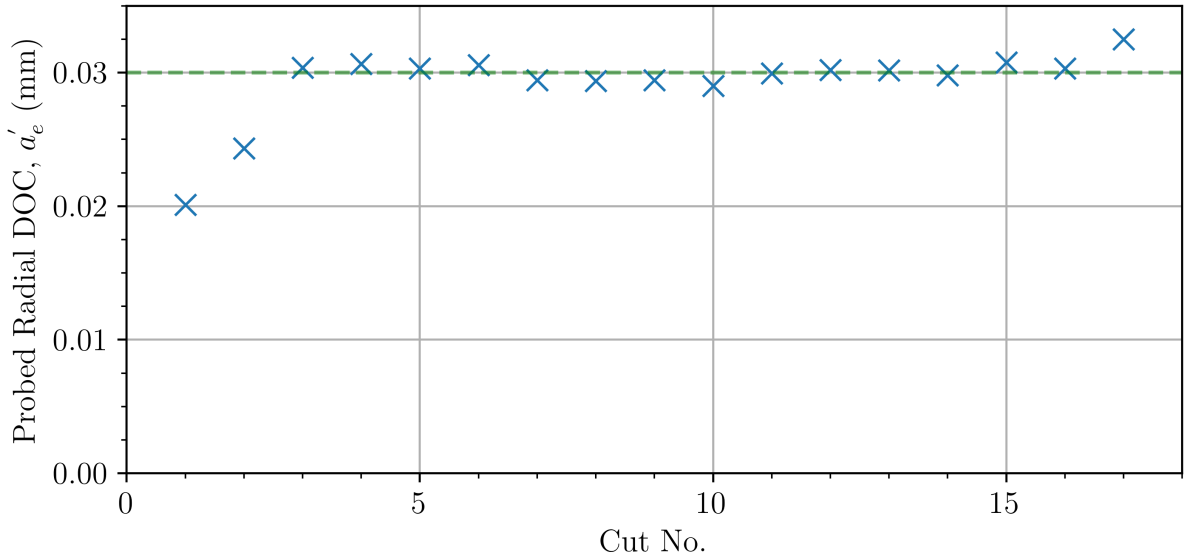


**Fig. 4.53:** OMP600 $a_e'$ measurements after each grinding pass of the parameter variation study.

Fig. 4.54 shows a 10 ms section of $AE_{raw}$ from grinding pass 4 (a), pass 7 (b) and pass

10 (c), to compare the effect of decreasing feedrates. Across the three subplots, minimal differences can be seen within the $AE_{raw}$, aside from the inherent variation associated with AE signals. One slight difference is that the DCB's $r_{runout}$ level is less pronounced in the $AE_{raw}$ at lower feedrates, despite the $r_{runout}$ increasing. Also, as the feedrate decreases the $AE_{raw}$ after each burst does not reduce as significantly.

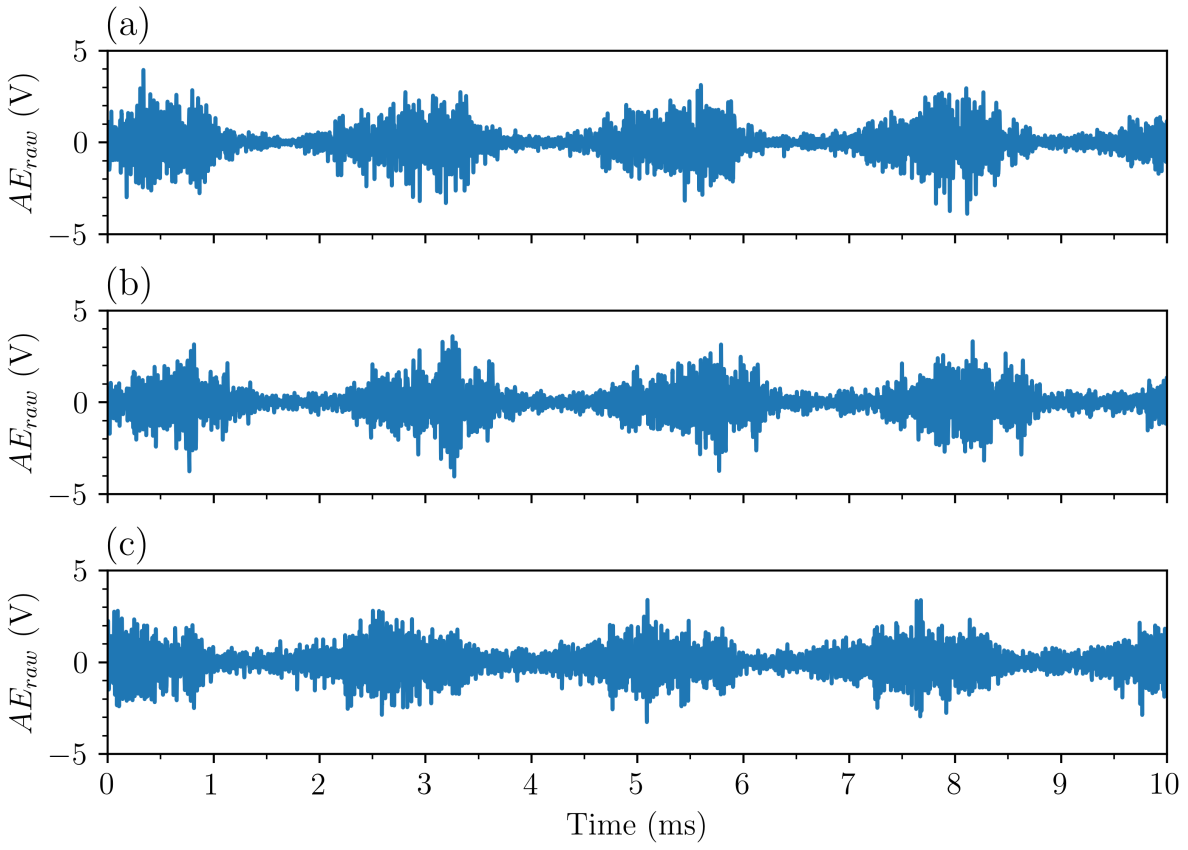


**Fig. 4.54:** A 10 ms $AE_{raw}$ section from three grinding passes with decreasing feedrates; (a) pass 4 - 60 mm/min, (b) pass 7 - 48 mm/min and (c) pass 10 - 36 mm/min.

Fig. 4.55 shows a comparison of the $AE_{raw}$ generated during grinding passes with decreasing DCB spindle speed. With each of the three subplots showing a 10 ms section of $AE_{raw}$ from different grinding passes; (a) pass 4, (b) pass 13 and (c) pass 16. An observable difference between the three $AE_{raw}$ signals, is the stretching out of the AE bursts, as a result of the increased time for a single DCB revolution. The vertical dashed black lines in each subplot show the theoretical time period for a single rotation at each spindle speed.

Additionally, the amplitude of each burst of $AE_{raw}$ in Fig. 4.55(c) is reduced, compared to the other two scenarios.

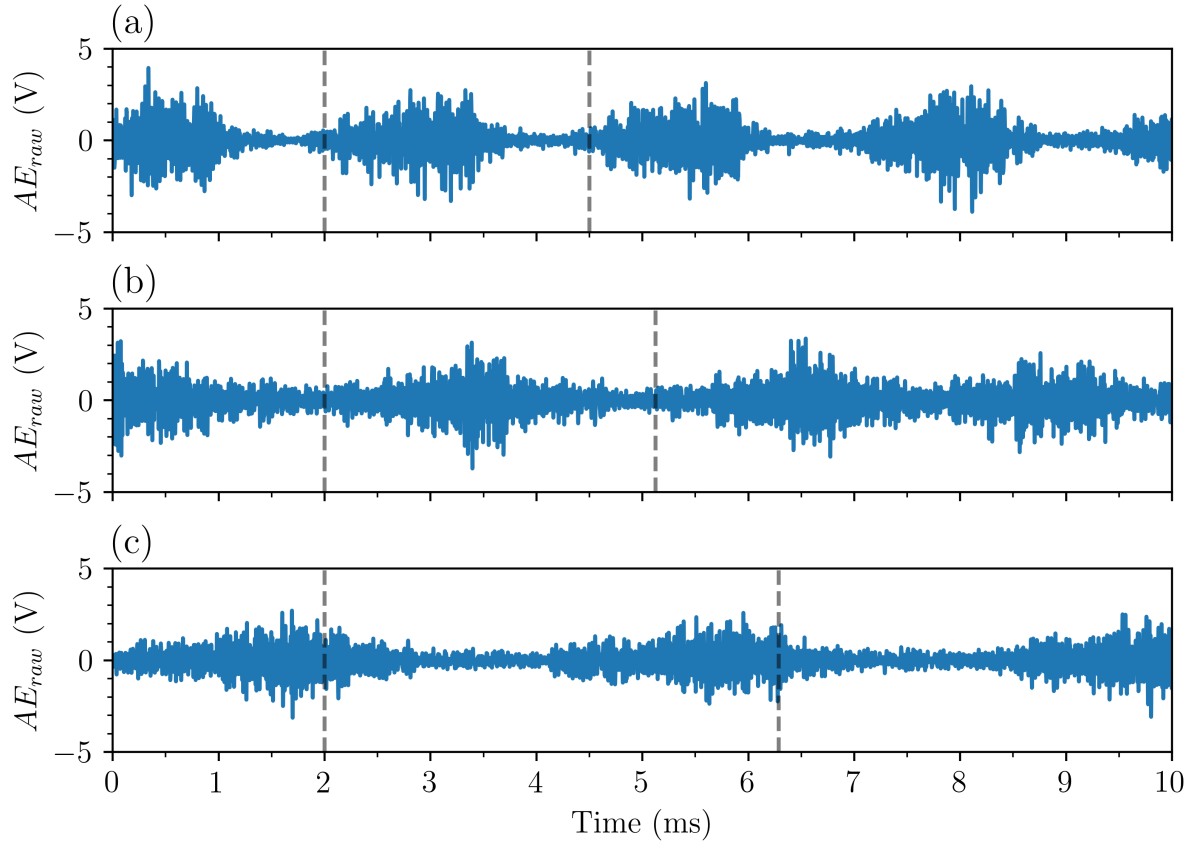


**Fig. 4.55:** A 10 ms $AE_{raw}$ section from three grinding passes with decreasing spindle speeds, with vertical dashed line denoting one DCB revolution; (a) pass 4 - 24.000 rpm, (b) pass 13 - 19.200 rpm and (c) pass 16 - 14.000 rpm.

Fig. 4.56 presents the $AE_{RMS}$ of each grinding pass within this parameter variation study. The first two passes have been excluded from the figure, as they were clear anomalies due to the DCB's wear-in phase. From the $AE_{RMS}$ an indication of a grinding pass' aggressiveness can be established. A grinding pass' aggressiveness will increase with decreasing spindle speed, and increasing feedrate. Therefore, it would be hypothesised that the $AE_{RMS}$ also follows this theory. However, from Fig. 4.56 it is clear this is not the case. A slight decrease in $AE_{RMS}$ can be seen by lowering the feedrate of a pass to 80 % of the control, but a further decrease to 60 % does not further lower the $AE_{RMS}$. Decreasing

the tool's spindle speed however has a much more pronounced effect on $AE_{RMS}$, but it too decreases the generated $AE_{RMS}$. With significant decreases to the $AE_{RMS}$ occurring with each decrease in spindle speed, whereas the grinding forces should theoretically be increasing.

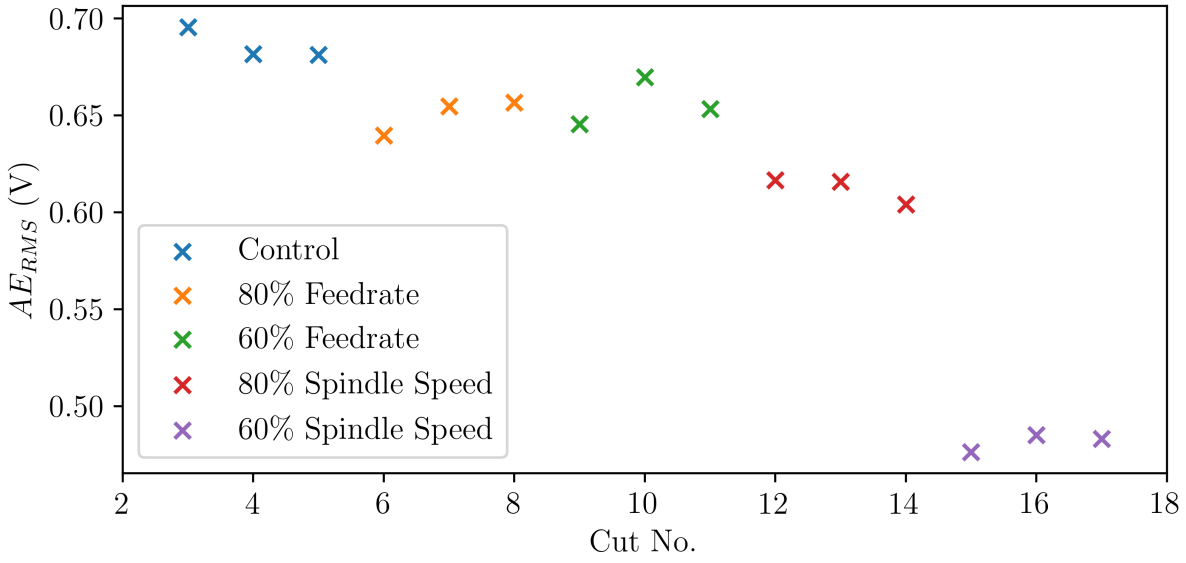


**Fig. 4.56:** $AE_{RMS}$ of each grinding pass across the parameter variation study, excluding the first two passes due to DCB wear-in.

The same effects can be seen through a comparison of an averaged PSD of each parameter variation stage, in Fig. 4.57. A very slight decrease in power across the frequency spectrum can be seen by reducing the feedrate in Fig. 4.57(a). Whilst, a more significant decrease can be observed by decreasing the spindle speed in Fig. 4.57(b). This is easier to observe by focusing on a single frequency band, as in Fig. 4.58, in which the $PP_{35}$ of each pass is shown. The decrease in grinding aggressiveness due to decreasing feedrates can be clearly seen through its $PP_{35}$. And whilst the trend of decreasing the DCB's spindle speed is inverse to the theoretical changes, the decreases are significantly larger than that of the decreases in feedrate. An important distinction, as the tool's cutting speed is three order of magnitudes greater than that of the feedrate.

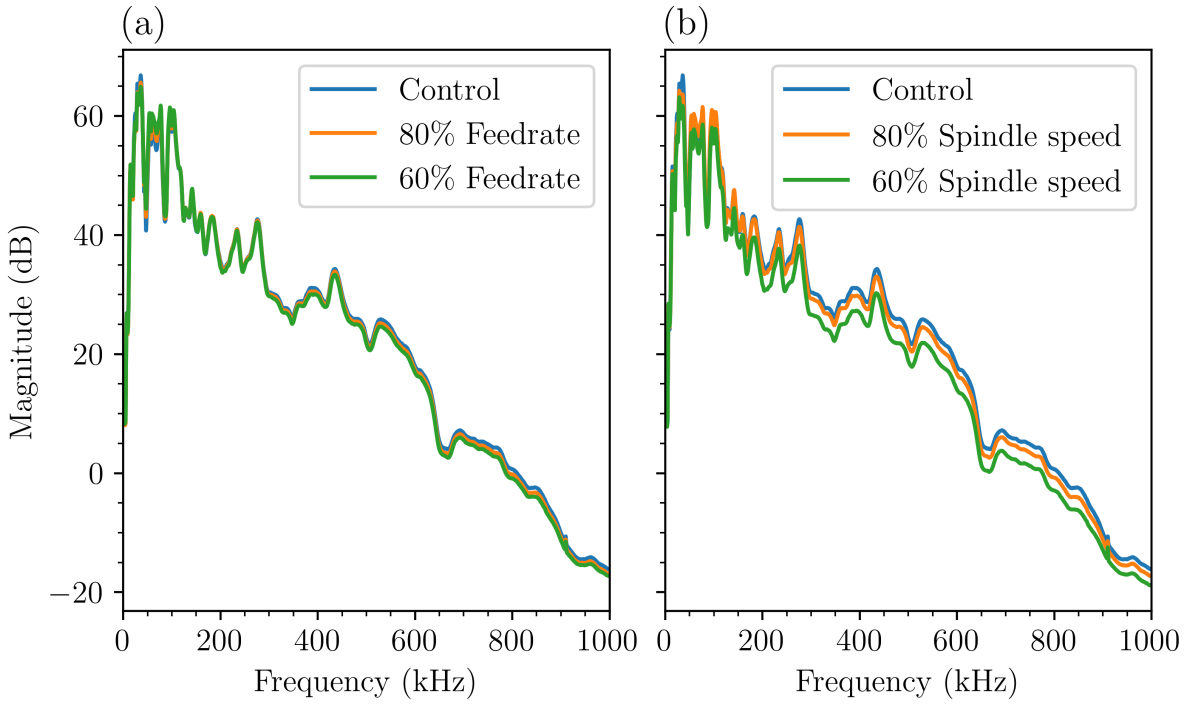


**Fig. 4.57:** Averaged PSD over the three grinding passes at each point of parameter variation for (a) feedrate and (b) spindle speed.

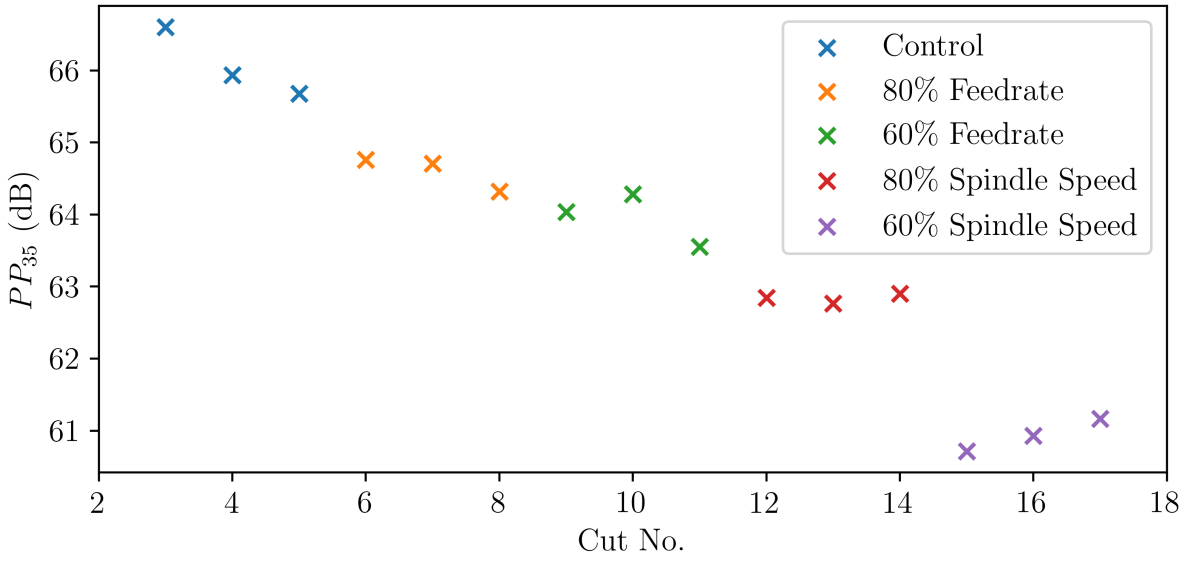


**Fig. 4.58:** $PP_{35}$ of each grinding pass across the parameter variation study, excluding the first two passes due to DCB wear-in.

From this short study, the effect of varying both a DCB's feedrate and spindle speed, for a given grinding pass, on its generated AE was investigated. 17 grinding passes were conducted covering four different parameter scenarios and a control. Across which a noticeable effect was observed in both the AE signals and extracted features. Decreases in both $AE_{RMS}$ and $PP_{35}$ were observed with decreases in feedrate, aligning with the theoretical decrease in grinding forces. However, decreases in both features were also seen when the spindle speed was reduced, opposing the hypothesis that $AE_{RMS}$ is linked to the grinding aggressiveness. This result could be because of a build-up of workpiece particulate/swarf, that higher spindle speeds are capable of removing from the tool/workpiece contact region. Adhesive wear of the DCB due to workpiece debris, would effectively lower grain protrusion and therefore dullen the grinding tool, explaining a reduced grinding aggressivenss. Nevertheless, without further investigation, the reason for this observed decrease in $AE_{RMS}$ as a result of a decrease in spindle speed, remains unclear.

As an initial study, these results are not conclusive, and as such a larger sample size is needed to validate these findings. Further investigations on this topic, should ensure that the DCB has a "low" level of $r_{runout}$, instead of the "medium" level this DCB had, to remove the influence of periodic AE bursts on the extracted features and reduce unpredictable tool wear. 3D NC4 tool scans were not conducted during this study due to the small number of passes conducted. But, a larger wear study in which more grinding passes are conducted at each scenario would be better suited to 3D NC4 scans due to their added cycle time. Additionally, starting the variation scenarios after a larger portion of steady-state wear may further reduce variation in AE as a result of large scale tool wear.

# 5 Tool Condition Monitoring Approaches

Throughout Chapter 4, results from the acquired AE, across all the testing series, have identified potentially useful features for inferring a DCB's wear state. However, using solely these AE features as a robust TCM system, to decide when to stop using a DCB, presents multiple problems. The following chapter utilises the collected wear test dataset, from all three testing series presented in Chapter 4, to investigate multiple avenues for an AE-based TCM system. Initially, a method is presented using transformations of previously presented AE features to enable a threshold-based criterion approach. As presented in Section 2.3.2, ANNs have shown significant promise for TCM in similar applications in the current literature, and as such have been used in combination with the more classical threshold-based criterion approach. Therefore, the use of ANNs for both a regression and classification application have been investigated, potentially making better use of the large amount of available data.

## 5.1 Threshold-based Criterion

The simplest method of developing a robust TCM system is to use a threshold-based criterion, which is often used in the AE testing of mechanical structures [109, 182]. In this approach, user defined thresholds are set for multiple AE features, which then alert the user as to when the threshold has been exceeded, often signalling damage or failure. For this approach to work effectively, a correlated feature must first be established from the AE to a relevant target metric. The threshold for said feature, is then typically

manually chosen based on operator knowledge gained from multiple testing repeats. Or with sufficient data, a statistical approach can be utilised to pick the threshold. A robust and effective threshold-based criterion approach is often costly to develop, as it requires finding both optimal features and thresholds, but simple to implement and utilise once developed.

A limitation of the AE features previously presented in Chapter 4, for use in a threshold-based approach, is the inconsistent nature of their baseline levels. Fig. 4.41 shows how a DCB's $r_{runout}$ level effects the $AE_{RMS}$ measurement's overall amplitude, making it impossible to choose a threshold to cover all scenarios reliably. This variation in baseline level across all the identified AE features drastically limits the effectiveness of a constant threshold-based approach. To circumvent this problem, a dynamic threshold could be developed to automatically adjust the threshold based on initial measurements and past knowledge. Or instead the features can be transformed or combined, to enable the use of a constant threshold.

From the three testing series, $AE_{kurt}$, $AE_{RMS}$ and $PP_{350}$, were seen to be most beneficial AE features for inferring a given DCB's tool state, and as such were focused on for this approach. The information of each feature stems mainly around changes in their gradient, rather than their baseline level or amplitude. Examples of this can be seen in Fig. 4.37, whereby deviations from the baseline level of $AE_{kurt}$, indicate DCB surface crater formation. Therefore, by using each AE features' gradient, the limitation of varying baseline levels can be overcome whilst maintaining the features' information.

Figs. 5.1–5.4 show the absolute gradient of a DCB's $PP_{350}$, $|\nabla PP_{350}|$, across all wear tests of the runout variation and control series. The resulting transformation presents a much more stable and amplitude independent period during each DCBs' phase II - steady-state. And phases I - wear-in and III - wear-out of each DCB are easily distinguished by large increases away from the baseline. The five control series wear tests, shown in Fig. 5.5, were then used to manually pick a threshold to best identify the transition point between phases II and III, without inducing false positives. The threshold was based on the OMP600 $a_e'$ measurements during each of the wear test, shown in Fig. 4.44. However,

in order for this approach to work, threshold crossing within each DCB's wear-in phase were ignored.

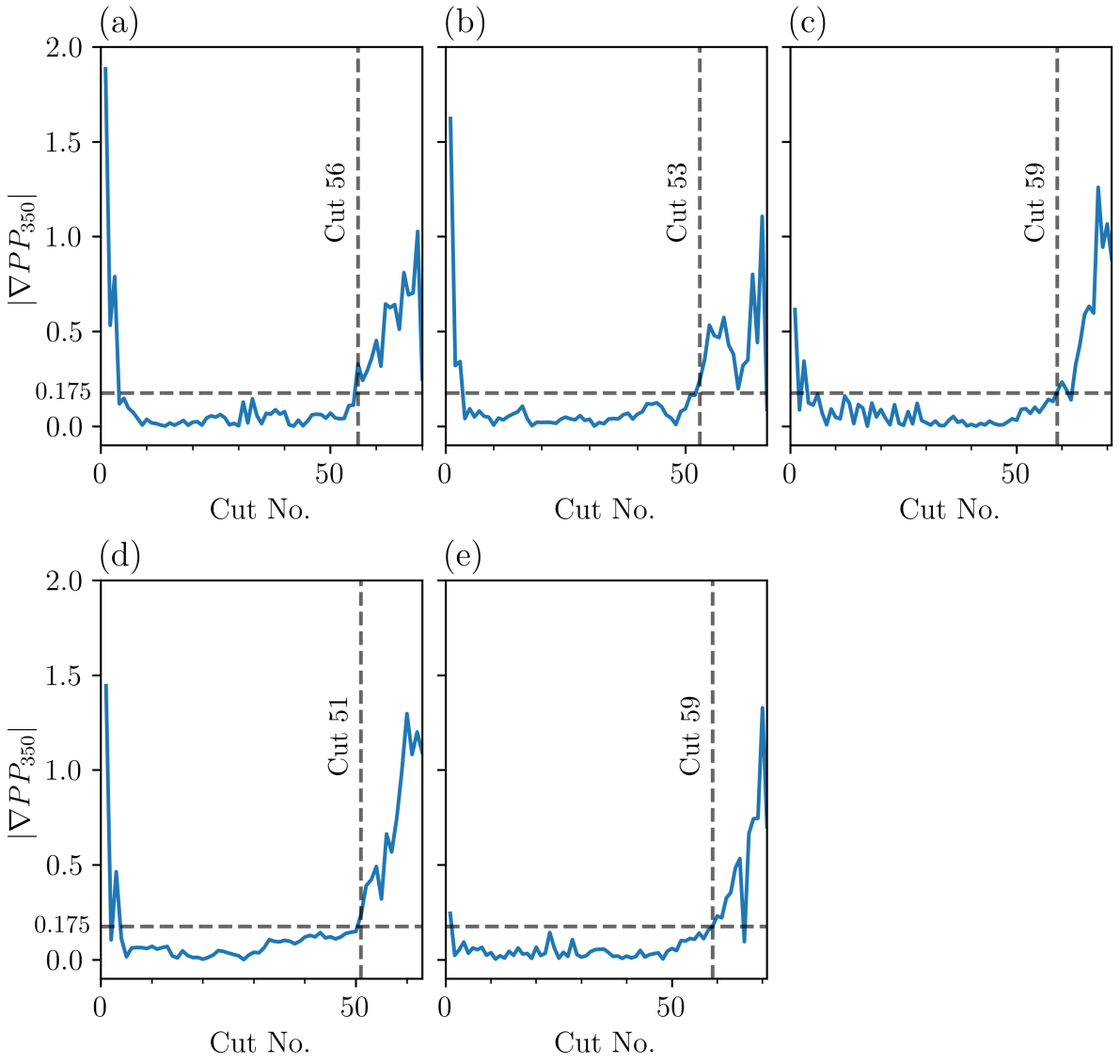


**Fig. 5.1:** $|\nabla PP_{350}|$ for each wear test of the control series, with tests 18 – 22 shown in (a – e). The cut-off thresholds are shown by black dashed lines with labels.

With the threshold set at 0.175, the picked transition point between phases II and III of each "low" $r_{runout}$ DCB, shown by the vertical black dashed line in Fig. 5.2, all occurred with 3 grinding passes of the true point seen through the $a'_e$ measurements. Furthermore, due to the increased consistency at this "low" $r_{runout}$ level, the threshold could be lowered

further to potentially increase the precision of the picked transition points.

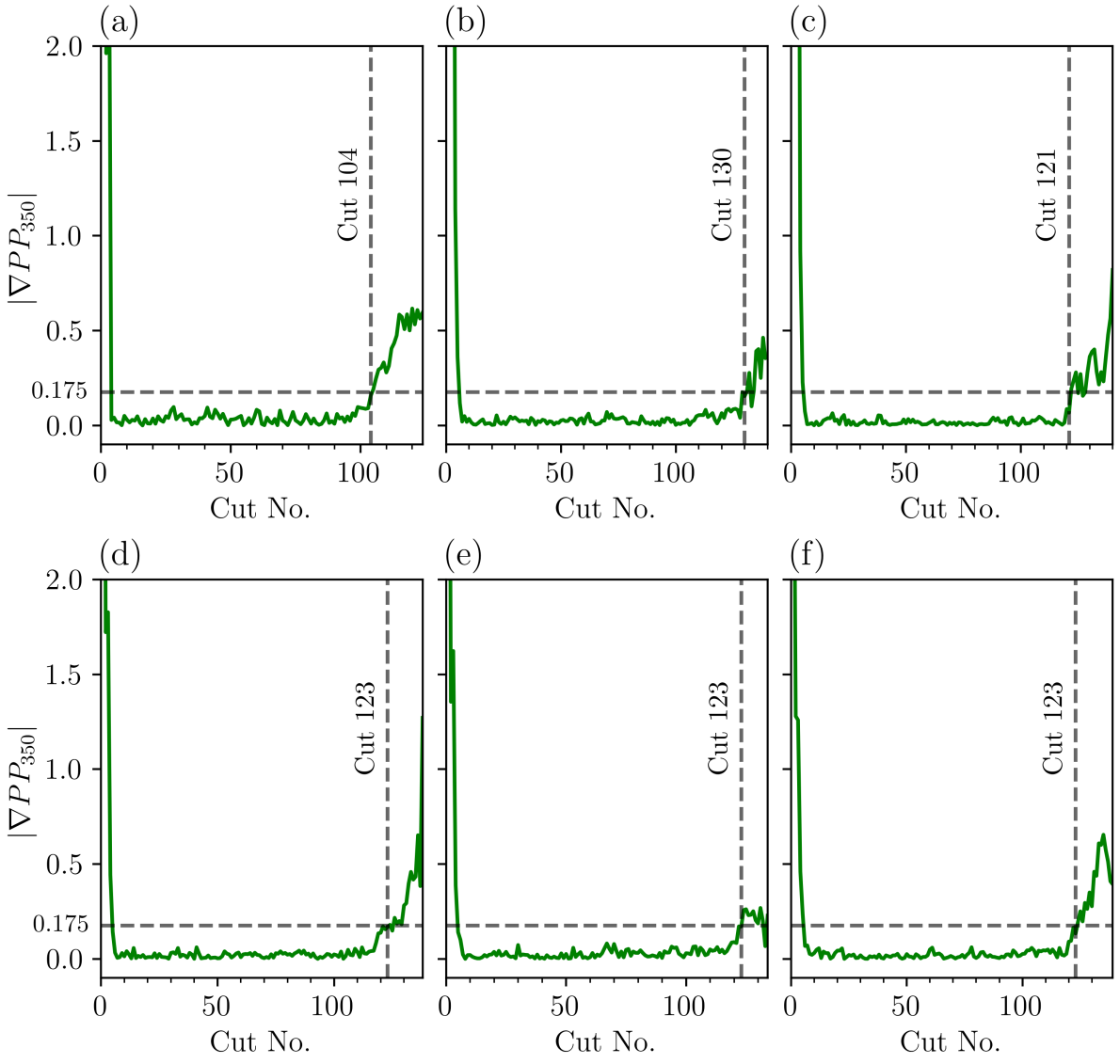


**Fig. 5.2:** $|\nabla PP_{350}|$ for each "low" $r_{runout}$ wear test of the runout variation series, with tests 6 – 11 shown in (a – f). The cut-off thresholds are shown by black dashed lines with labels.

The approach did not work as well for DCBs with a higher level of $r_{runout}$, with the picked transition point of wear test 12, in Fig. 5.3(a), occurring at grinding pass 18 rather than the true value of 100. A similar result occurs in Fig. 5.4(b), whereby the approach picks a transition point of pass 23 in wear test 16. Optimistically, it could be theorised

that this approach has picked the point at which the DCB's high spot initially forms a flat spot, seen to occur at pass 24 in Fig. 4.29(b). However, it is more likely an erroneous prediction as a result of a noisier $|\nabla PP_{350}|$ feature, similarly to the one seen in Fig. 5.3(a).

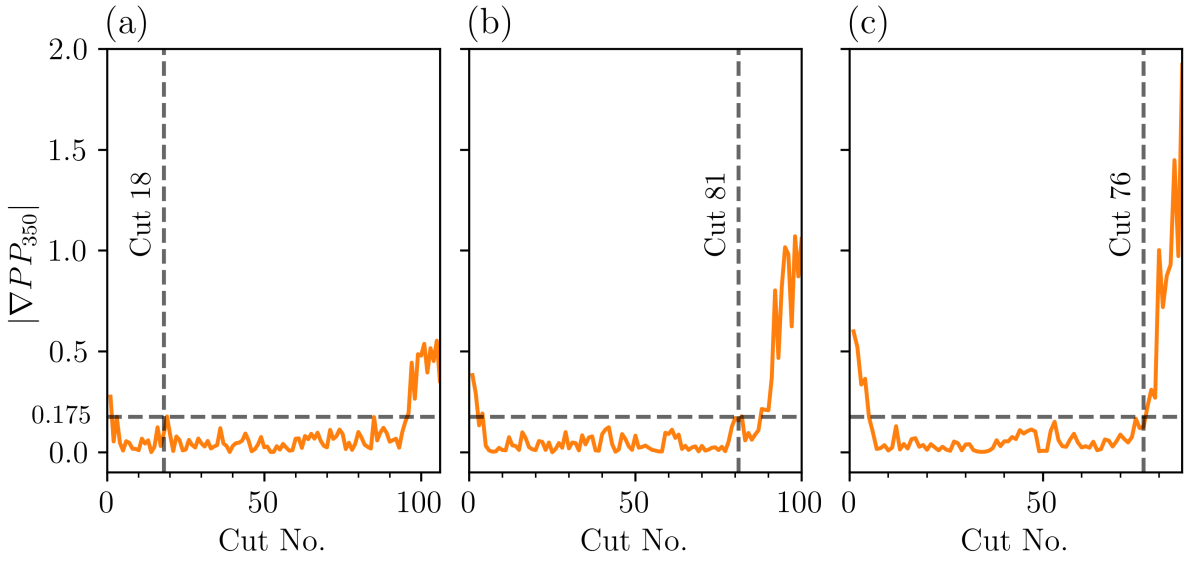


**Fig. 5.3:** $|\nabla PP_{350}|$ for each "medium" $r_{runout}$ wear test of the runout variation series, with tests 12 – 14 shown in (a – c). The cut-off thresholds are shown by black dashed lines with labels.

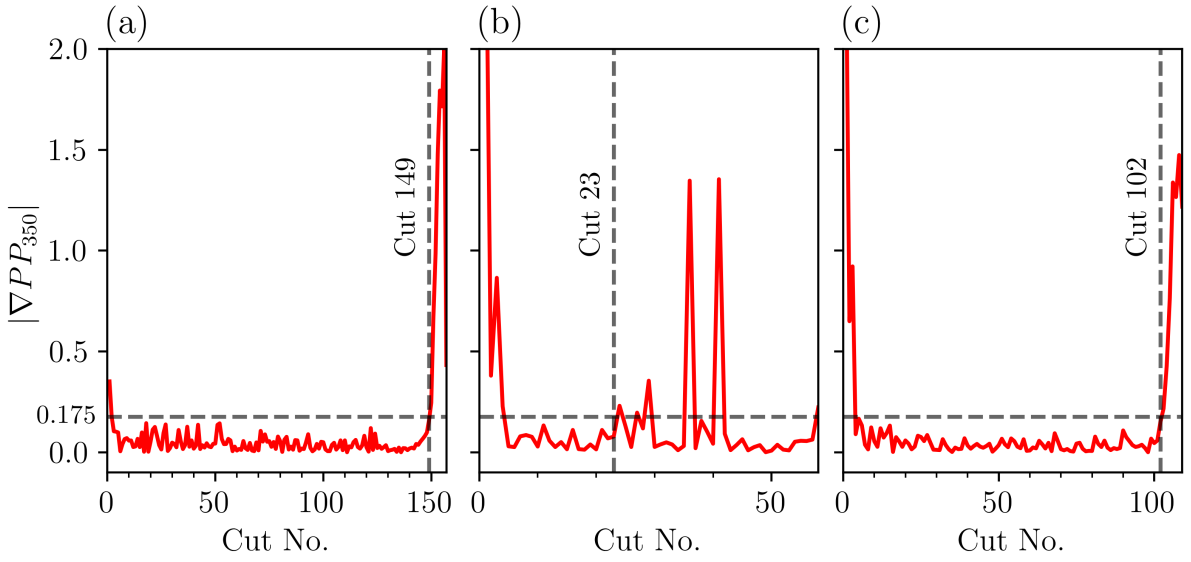


**Fig. 5.4:** $|\nabla PP_{350}|$ for each "high" $r_{runout}$ wear test of the runout variation series, with tests 15 – 17 shown in (a – c). The cut-off thresholds are shown by black dashed lines with labels.

Figs. 5.5–5.8 show the absolute gradient of the product of a DCB's $AE_{kurt}$ and $AE_{RMS}$, multiplied by $n$, the number of grinding passes completed at that point, $|\nabla(AE_{RMS} \cdot AE_{kurt})| \cdot n$, across all wear tests of the control and runout variation series. The combination of $AE_{RMS}$ and $AE_{kurt}$ allowed for a good middle ground, improving on results achieved by each individual feature. Whilst $AE_{kurt}$ is consistently precise in showing the point of large scale wear, it also increases immensely at high $r_{runout}$ levels. $AE_{RMS}$ reduced the scale of this increase, allowing a steady baseline to form prior to initial surface crater formation. Additionally, the addition of $n$ into the features transform, aimed to restrict the large increase seen over the DCBs' phase I - wear-in. Potentially removing the requirement of ignoring the tool's wear-in phase required using the $|\nabla PP_{350}|$ feature. As seen in Fig. 5.5 this was successful, and a threshold could be manually picked without ignoring initial measurements. A further improvement of this feature was the reduced noise during phases I and II of a tool's wear cycle, which enabled a more precise threshold to be chosen without inciting false positives. But crucially for this approach, a sharp increase in the feature was still seen once reaching phase III - wear-out of each DCB.

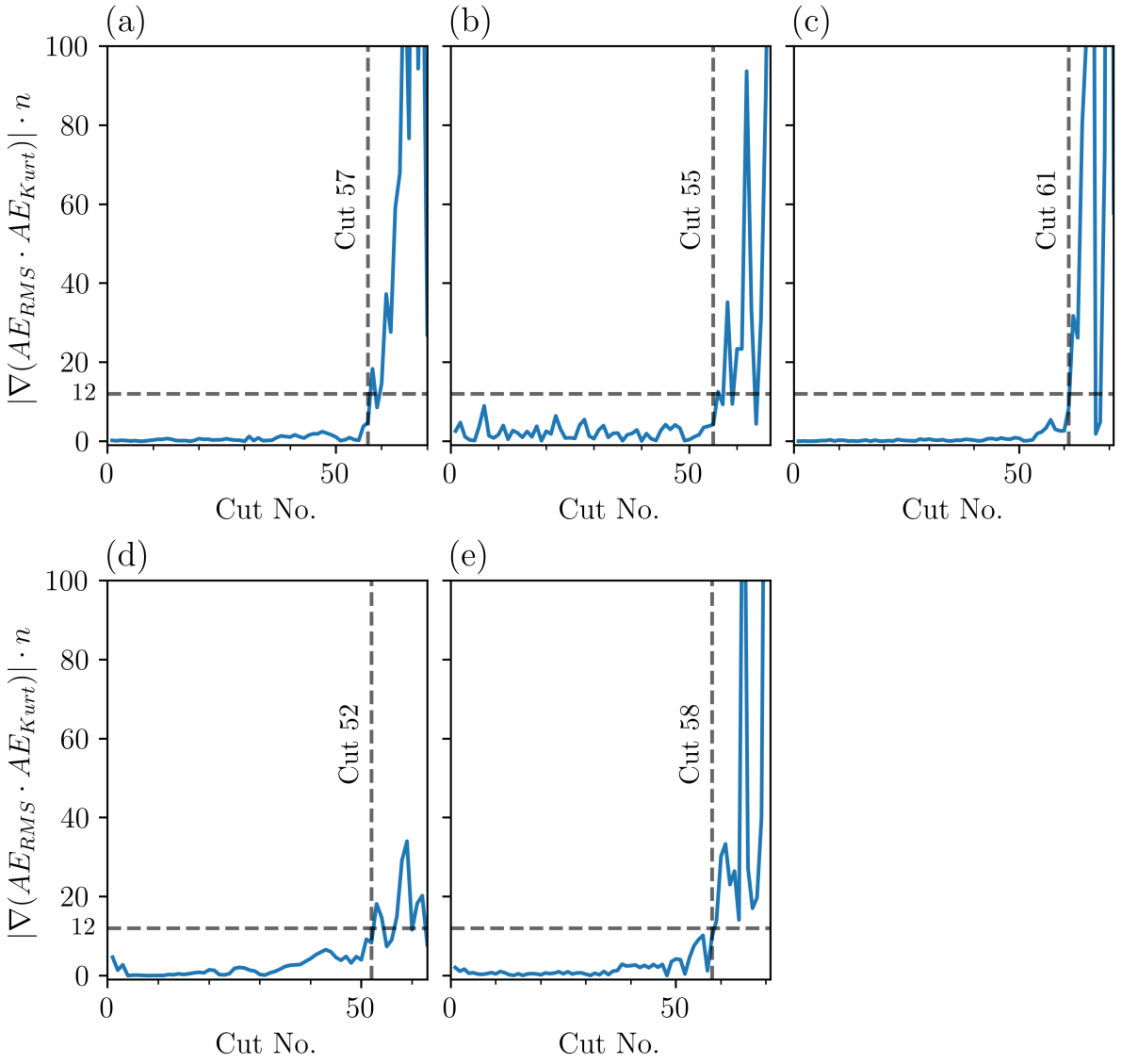


**Fig. 5.5:** $|\nabla(AE_{RMS} \cdot AE_{kurt}) \cdot n|$ for each wear test of the control series, with tests 18 – 22 shown in (a – e). The cut-off thresholds are shown by black dashed lines with labels.

With a manually chosen threshold of 12, for the $|\nabla(AE_{RMS} \cdot AE_{kurt})| \cdot n$ feature, a similarly accurate picking of the phase II to III transition point can be seen in Fig. 5.6. Also, the addition of $n$ to the feature has still limited the effect of each DCB's phase I, therefore only wear test 12 required the initial passes to be ignored for a reasonable prediction.

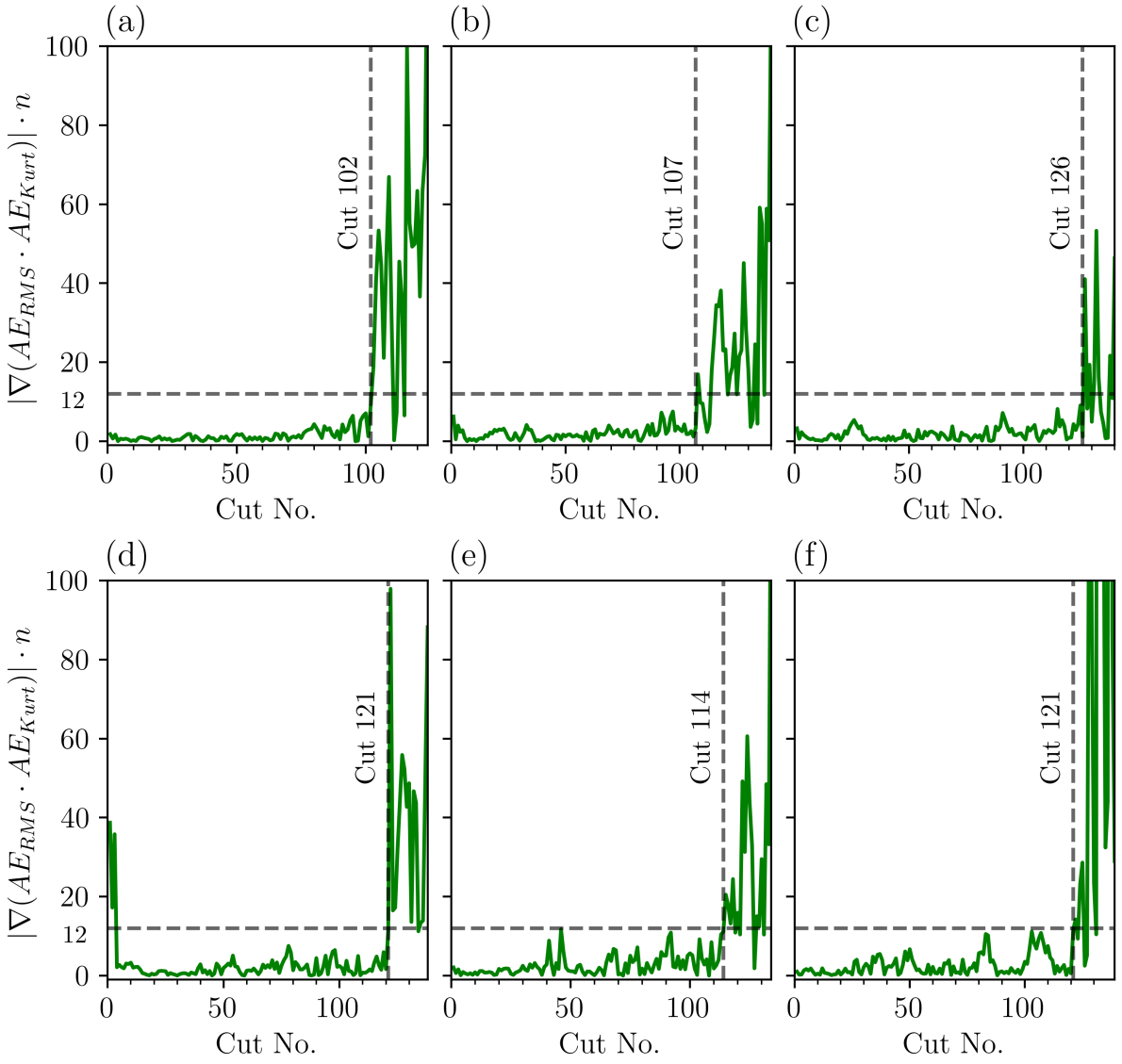


**Fig. 5.6:** $|\nabla(AE_{RMS} \cdot AE_{kurt})| \cdot n$ for each "low" $r_{runout}$ wear test of the runout variation series, with tests 6 – 11 shown in (a – f). The cut-off thresholds are shown by black dashed lines with labels.

Compared to the results from the $|\nabla PP_{350}|$ feature for the "medium" and "high" $r_{runout}$ DCBs, in Figs. 5.3 and 5.4, utilising the $|\nabla(AE_{RMS} \cdot AE_{kurt})| \cdot n$ feature, in Figs. 5.7 and 5.8, showed more reliable results. As a result, this method did not prematurely pick the transition points for any of the runout variation series wear tests, unlike in Fig. 5.3(a). The use of the $|\nabla PP_{350}|$ feature tended to result in the threshold crossing happening much

later in the DCBs' life, typically within 20 passes of failure despite the large scale wear of the tool is experiencing. Figs. 5.7 and 5.8 show a different result, instead through using the $|\nabla(AE_{RMS} \cdot AE_{kurt})| \cdot n$ feature, the picked point of each wear test corresponds with the DCB high spot flattening. Therefore, both the reduction in the measured $a'_e$, seen in Figs. 4.28 and 4.31, and changes in tool-workpiece contact, seen in Figs. 4.26 and 4.29, are identified through this threshold-based criterion approach.

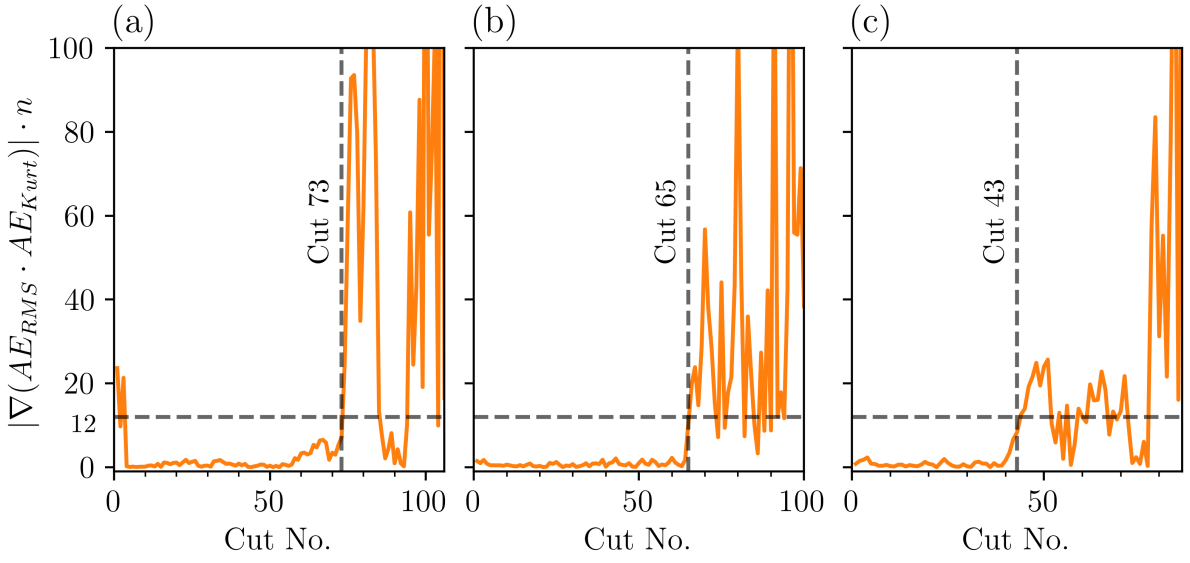


**Fig. 5.7:** $|\nabla(AE_{RMS} \cdot AE_{kurt})| \cdot n$ for each "medium" $r_{runout}$ wear test of the runout variation series, with tests 12 – 14 shown in (a – c). The cut-off thresholds are shown by black dashed lines with labels.

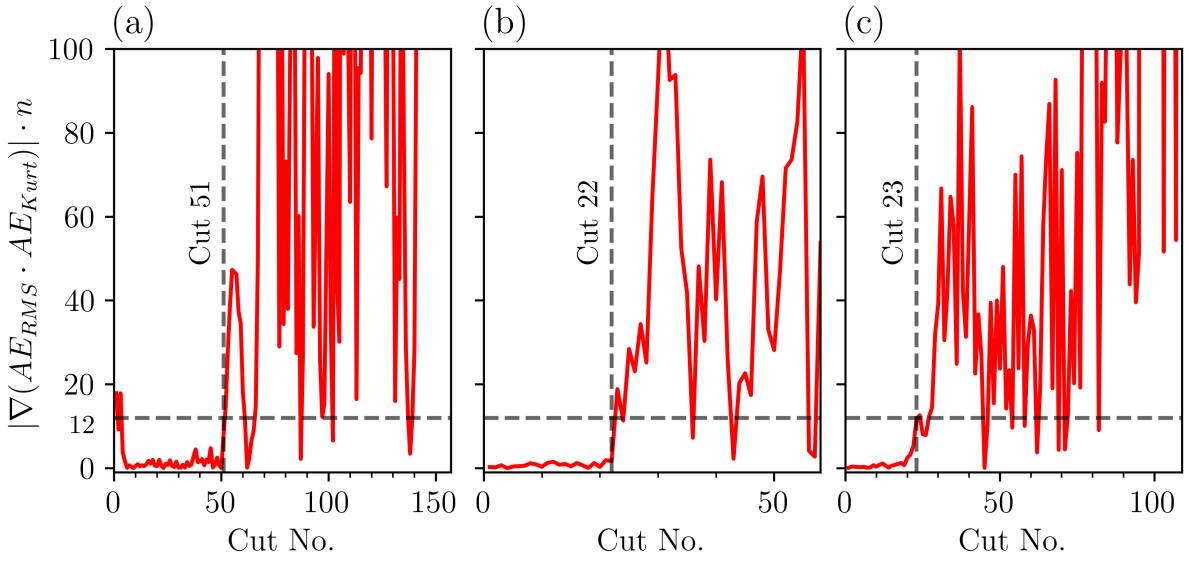


**Fig. 5.8:** $|\nabla(AE_{RMS} \cdot AE_{kurt})| \cdot n$ for each "high" $r_{runout}$ wear test of the runout variation series, with tests 15 – 17 shown in (a – c). The cut-off thresholds are shown by black dashed lines with labels.

In summary, a threshold-based criterion approach is surprisingly effective at reliably identifying the transition point between a DCB's phase II and III. Utilising the absolute gradient of highly correlated AE features, transforms the difficult to use features into suitable metrics for a constant threshold approach. Two such metrics were presented, $|\nabla PP_{350}|$ and $|\nabla(AE_{RMS} \cdot AE_{kurt})| \cdot n$. Both metrics produced a near zero baseline during each DCB's steady-state wear phase, independently of its level of $r_{runout}$. Followed by distinct increases in the metrics aligned to the DCBs reaching phase III - wear-out, or having formed a large surface crater on its surface, whichever arrived first. Additionally, to reduce the effect of a tool's wear-in phase on the transformed metric, the inclusion of $n$, the number of completed grinding passes, was investigated. This addition represented the amount of workpiece material a DCB had removed throughout its life.

By manually selecting the threshold criterion for each metric, based on the five control series wear tests, validation of this approach can be seen through its application to the 12 runout variation wear tests. On average, the $|\nabla PP_{350}|$ feature resulted in the approach picking transition points within ∼5 grinding passes of the true values, represented by the

OMP600 $a'_e$ measurements, with two false positives occurring for DCBs with "medium" and "high" $r_{runout}$ levels. The $|\nabla(AE_{RMS} \cdot AE_{kurt})| \cdot n$ feature, displayed a much lower baseline level of noise during phase II - steady-state of each DCB. Which then allowed a more precise threshold to be picked to best match the transition point of each DCB in the control series. Across the runout variation series wear tests, no false positives were triggered and the metric reliably picked the point of surface crater formation over all $r_{runout}$ levels.

However, this threshold-based approach is not without downsides and limitations. The main downside is the manual aspect of the approach to obtain a useable feature and threshold. Significant operator knowledge and time is required to develop an effective transformed AE feature, and then a large amount of data, five wear tests in this case, is then required to allow for an adequate threshold to be chosen. Additionally, a limitation of the two presented features is the requirement to ignore most of the DCBs' phase I - wear-in, to prevent false positives occurring within the tool's first five grinding passes. Finally, the effect of increasing $r_{runout}$ levels and changing grinding parameters can have pronounced effects on the acquired AE features, as seen in Sections 4.1.2 and 4.2. As a result, these variations can lead to false positives with a constant threshold approach, as seen in Fig. 5.3(a) and Fig. 5.4(b). However, requiring little computational power and capable of being deployed in real-time, this threshold-based criterion approach is a useful TCM strategy capable of being both precise and reliable. The impact of manual feature and threshold selection is also limited if more computationally expensive ML models are also being developed, requiring large amounts of data themselves. Overall, this approach of utilising a constant threshold and a highly correlated AE feature can most effectively be used as an indirect method to indicate that direct tool wear or workpiece measurements should be conducted. This could therefore remove the requirement for time-consuming direct measurements to be conducted periodically, and instead be conducted when required to better assess a DCB's wear state.

## 5.2 Artificial Neural Networks

To combat limitations of the previously presented threshold-based criterion approach, in Section 5.1, and due to the suitability of the methodology developed in Chapter 3, it was decided to utilise ANNs to investigate different TCM approaches. Section 2.3.2 detailed the effectiveness of ANNs to interpret indirect AE signals and features for the application to a TCM system. Therefore, the following section covers both the approach and results of the application of ANNs framed as both a regression and classification TCM problem.

### 5.2.1 Approach for ANNs

Across this thesis 22 DCB wear tests were conducted, and throughout all of them continuous AE was recorded during each grinding pass, as detailed in Section 3.2. Alongside this, each wear test's inspection phase methodology, laid out in Section 3.3, captured the DCB's wear state after every grinding pass during its life. Depending on the development stage of the methodology at the time each testing series was conducted, the inspection phase could either be comprised of only NC4 2D DCB surface scans, or additionally included OMP600 $a'_e$ workpiece removal measurements. This methodology and dataset size enabled a large variety of different ANN model architectures to be potentially used with success, each by framing the TCM problem slightly differently. Therefore, prior to choosing an architecture, it was important to determine both the model inputs and objectives to best inform the approach going forward.

AE features from both the time and frequency domains were utilised as inputs into the ANNs, all of which have been presented throughout Chapter 4. By using AE features in place of the raw AE signals, a significant computational overhead can be avoided, with a potential downside of losing some hidden but relevant information. With regard to the target objective, the two inspection methods present two different, but equally useful approaches to monitor a DCB's wear state. Utilising the 2D NC4 tool scans, a DCB's $r_{mean}$ can be seen to follow each tool's three-phase life cycle. As the $r_{mean}$ presents as

a continuous function, and as each wear test has a high resolution of measurements, a regression ANN aiming to predict the current $r_{mean}$ from inputted AE features was highly suited to this problem. The second approach, utilises the OMP600 $a'_e$ measurements and its clear transition points between wear phases. From which a classification model was developed, aiming instead to output the DCB's current wear phase. Due to the timeline of this thesis' undertaking, the classification model was only capable of being trained on wear tests within the runout variation and control testing series, as the OMP600 was only employed after the feasibility series.

The choice of ANN architecture is important as it defines the capabilities of a model for a given application. But the choice is also dependent on other factors, such as the dataset size, available computational power, required precision, and developer capability. For the supervised regression ANN looking to predict the DCB $r_{mean}$, three different architectures were selected: MLP, MLP with sliding window (MLP-WIN), and LSTM. Whilst for the supervised classification ANN trained to predict the DCB's wear phase, only a MLP architecture was investigated, due to time constraints.

MLP models are a simple and well researched form of ANN, and as such are the ideal baseline for comparison to other architectures or novel processing techniques. MLPs are feed-forward networks consisting of at least three layers of perceptrons/neurons; the input layer, the hidden layer/s and the output layer. Fig. 5.9 shows a diagrammatic representation of the MLP architecture, displaying each layer and neuron connections. For a given neuron in layer $k$ it is connected to each neuron in the previous layer, $k-1$, forming a fully-connected or "dense" layer, as seen in Fig. 5.9. Each input to every neuron is separately weighted, before the sum is added to a bias term and passed through an activation function, $\phi$. The activation function allows for the introduction of non-linearity into the model, a vital component of all ANNs success. The computation to determine a fully connected layer's output, $\boldsymbol{h}$, is shown in Eq. (5.1). In which $\boldsymbol{X}$ represents the matrix of inputs to the layer, $\boldsymbol{W}$ the matrix of trainable weights and $\boldsymbol{b}$ the bias vector [183]. Through the optimisation of both $\boldsymbol{W}$ and $\boldsymbol{b}$ of each layer with a backpropagation gradient descent algorithm, aiming to minimise the selected loss function, MLP models

can approximate almost all continuous functions if sufficiently complex [184].

$$\boldsymbol{h}_{W,b}(\boldsymbol{X}) = \phi(\boldsymbol{X}\boldsymbol{W} + \boldsymbol{b}) \tag{5.1}$$

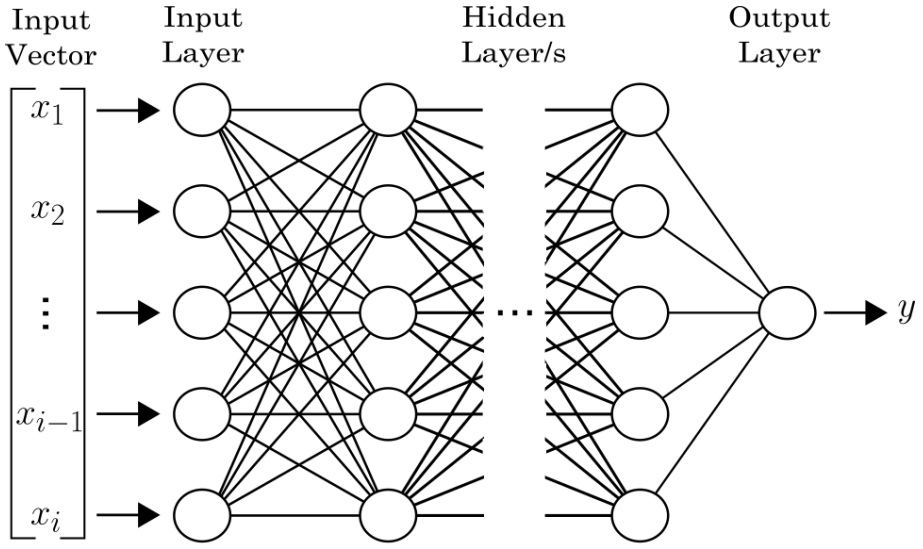


**Fig. 5.9:** MLP diagram showing layers and connections.

The choice of activation function, $\phi$, in Eq. (5.1), has a large impact on a hidden layer's capability to generalise from the inputted data. There are a wide range of common functions, most notably the logistic sigmoid, $\sigma$, the hyperbolic tangent function, tanh, and the Rectified Linear Unit (ReLU) function [185]. Also, the choice of activation function for any ANN's output layer determines the type of output the ANN produces. A linear activation function maps the output from a single neuron to a continuous spectrum, and as such is best suited to regression problems in which the target data is also a continuous function. To obtain a relevant output for a classification approach, a softmax function is commonly employed, outputting a probability distribution from each neuron of the ANN's output layer, in respect to each class label of the approach.

Within MLP models there are no feed-back connections, in which the outputs of layers or neurons are fed back into itself. RNNs utilise this idea of sharing parameters across the model to better work with sequential data. This small inclusion of cyclic

connections can allow RNNs to map the whole history of previous inputs to each output, vastly improving results for time-series inputs [186]. Currently, the most effective and utilised RNN architecture for working with sequenced data are LSTM models. Developed by Hochreiter and Schmidhuber [161] to remedy the vanishing gradient problem [187], the ability of LSTM models to generalise over large time windows allow them to represent both short and long term dependencies, a significant improvement from classic RNNs.

LSTMs differ from MLPs by using LSTM cells in place of the classical ANN neurons. LSTM cells are comprised of two memory states: a short-term hidden state, $\boldsymbol{h}$, and a long-term cell state, $\boldsymbol{c}$, three $\sigma$ decision gates (forget, input, and output gates) and an additional single layer ANN. An LSTM model can contain multiple layers of many cells, in which every cell recursively loops over each input sequence. Fig. 5.10 shows the internal architecture of an LSTM cell and the recursive process of training.

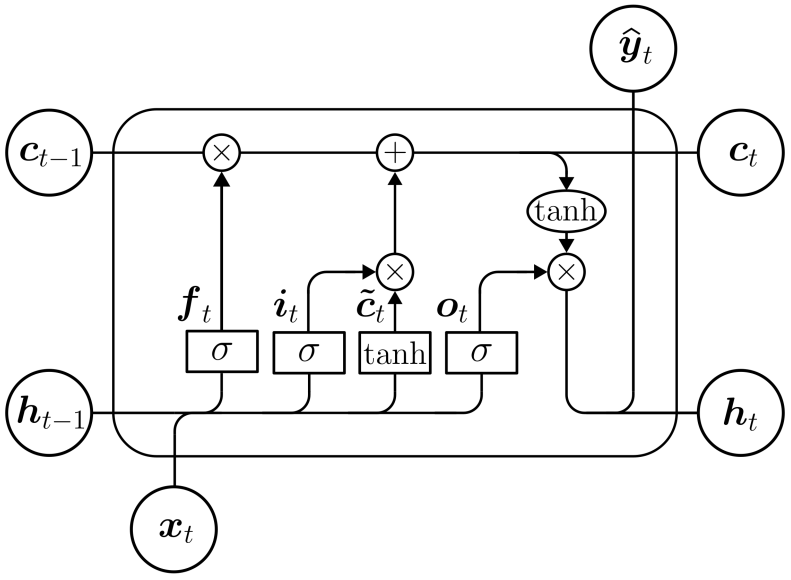


**Fig. 5.10:** LSTM cell schematic.

An LSTM layer's long-term state, $\boldsymbol{c}$, is the foundation of its capacity to operate with historical data. By selectively storing data within $\boldsymbol{c}$, relevant outputs, $\hat{\boldsymbol{y}}_{\mathrm{t}}$, can be formed over large input sequences without modifications to the cell's built-up memory. The cell's

history and outputs are tuned by each of the three decision gates, which combine both the longer term memory from $\boldsymbol{c}$ with the recent outputs stored within $\boldsymbol{h}$. The three decision gates within an LSTM cell decide what information within the sequence should be stored, thrown away or used. All three gates are a single fully-connected layer, with a sigmoid activation function, shown in Fig. 5.10 by the $\sigma$ labelled boxes. Based on the previous time steps' hidden state, $\boldsymbol{h}_{\text{t-1}}$, and the current input features vector, $\boldsymbol{x}_{\text{t}}$, each gate outputs a vector with values between $0-1$, indicating the irrelevance or relevance of the corresponding values. These gate vectors are then used to scale their respective sequences, resulting in either the removal or persistence of values within the sequence. The forget gate vector, $\boldsymbol{f}$, input gate vector, $\boldsymbol{i}$, and output gate vector, $\boldsymbol{o}$, are calculated with Eqs. (5.2)–(5.4).

$$\boldsymbol{f}_t = \sigma(\boldsymbol{W}_f \cdot [\boldsymbol{h}_{t-1}, \boldsymbol{x}_t] + \boldsymbol{b}_f) \tag{5.2}$$

$$\boldsymbol{i}_t = \sigma(\boldsymbol{W}_i \cdot [\boldsymbol{h}_{t-1}, \boldsymbol{x}_t] + \boldsymbol{b}_i) \tag{5.3}$$

$$\boldsymbol{o}_t = \sigma(\boldsymbol{W}_o \cdot [\boldsymbol{h}_{t-1}, \boldsymbol{x}_t] + \boldsymbol{b}_o) \tag{5.4}$$

Following through the recursive flow of sequences within an LSTM cell, shown in Fig. 5.10. At each time step, $t$, the previous time steps' cell state, $\boldsymbol{c}_{\text{t-1}}$, is first scaled by $\boldsymbol{f}_{\text{t}}$. This step controls the cell's long-term memory up to the previous time step, allowing the meaning and importance of the long-term dependency to be modified prior to additional information being added.

Next, $\boldsymbol{i}_{\text{t}}$ is used to evaluate which values should be stored in the cell state. The additional single dense layer, utilising a tanh activation function, is used to analyse both $\boldsymbol{x}_{\text{t}}$ and $\boldsymbol{h}_{\text{t-1}}$ and output the current time steps' temporary cell state, $\tilde{\boldsymbol{c}}_{\text{t}}$. From which, $\tilde{\boldsymbol{c}}_{\text{t}}$ is then scaled via $\boldsymbol{i}_{\text{t}}$ and added to $\boldsymbol{c}_{\text{t-1}}$, to create the current updated cell state, $\boldsymbol{c}_{\text{t}}$, both are shown through Eqs. (5.5) and (5.6).

$$\tilde{\boldsymbol{c}}_t = \tanh(\boldsymbol{W}_{\tilde{c}} \cdot [\boldsymbol{h}_{t-1}, \boldsymbol{x}_t] + \boldsymbol{b}_{\tilde{c}}) \tag{5.5}$$

$$\boldsymbol{c}_t = \boldsymbol{c}_{t-1} \cdot \boldsymbol{f}_t + \tilde{\boldsymbol{c}}_t \cdot \boldsymbol{i}_t \tag{5.6}$$

These two operations are key as they control the addition of information to the long term memory of the LSTM cell, through both the input gate filtering and the temporary cell state computation. Finally, $\boldsymbol{o}_\mathrm{t}$ is used to determine which parts of $\boldsymbol{c}_\mathrm{t}$ should be filtered out to create this time steps' main output, $\hat{\boldsymbol{y}}_\mathrm{t}$, and short-term memory, $\boldsymbol{h}_\mathrm{t}$. Prior to filtering with $\boldsymbol{o}_\mathrm{t}$, $\boldsymbol{c}_\mathrm{t}$ is passed through an additional tanh function to scale the data between -1 and 1, shown in Eq. (5.7).

$$\hat{\boldsymbol{y}}_t = \boldsymbol{h}_t = \tanh(\boldsymbol{c}_t) \cdot \boldsymbol{o}_t \tag{5.7}$$

To accommodate this recurrent nature of LSTMs, its input data must be sequenced and reshaped to provide a history of previous data points for every input. Therefore, the data inputted into LSTM models is formatted as a 3D matrix of shape: (batch size, number of time steps, number of input features). Where batch size relates to the number of input sequences to train over prior to updating neuron weights. The number of time steps, is the length of each inputted feature sequence, which can be seen as the amount of history the model has available for each input. And finally, the number of input features are in this case the number of AE data features used for model training. Of these three parameters, the number of included time steps is the most important when optimising LSTM models, as it effects the amount of history the LSTM has to generalise over [188]. Increasing the length of each individual sequence available to the LSTM allows it to generalise longer term dependencies, with the impact of increasing the number of internal iterations of each LSTM cell [189, 190].

Both MLP and LSTM model architectures have distinct benefits and drawbacks. MLP models are highly capable and due to their relative simplicity are quick to train. But MLPs lack the ability of LSTMs to generalise across previous inputs, limiting their capability when working with sequenced data. With the hope of combining the benefits

of each architecture, the capability of an MLP-WIN [191, 192] was also investigated. By applying a sliding time window to the input data, the same level of history present in each LSTM input can be inputted into an MLP model. Comparing to the 3D input data of LSTMs, the MLP-WIN input matrix is reshaped to a 2D shape of (batch size, number of time steps $\times$ number of input data features) [193]. The squeezed dataset is then used as the input to an MLP model, which due to the increased amount of available information typically requires a more complex or deep architecture.

Prior to any ANNs being trained, the inputted data must first be selected and then pre-processed to be suitable for working with ANNs. For the AE data, this comprised of selecting the relevant features to be used as ANN inputs. Chapter 4 presents multiple AE features, all of which can be seen to be well correlated and unique in nature, therefore no further feature selection was undertaken. To verify no two features were overly similar and therefore superfluous, the Pearson Correlation Coefficient (PCC) was calculated between each wear tests AE features and objective function. Fig. 5.11 shows the PCC against (a) the $r_{mean}$ and (b) the $a'_e$ of the respective wear tests. PCC is a measure of the linear correlation between two variables; in this application an AE feature and the respective target value. Outputting a value between -1 and 1, indicating a perfect negative or positive correlation. An absolute PCC value of $>$0.7 can be interpreted as a strong correlation between the two variables [194]. The PCC of each AE feature can be seen to vary significantly across the wear tests, but despite this both $AE_{kurt}$ and $PP_{350}$ are the most consistently high correlating AE features. In total, all nine of the AE features shown in Fig. 5.11, four time-domain features and five frequency partial powers, were used as inputs to both the regression and classification ANNs.

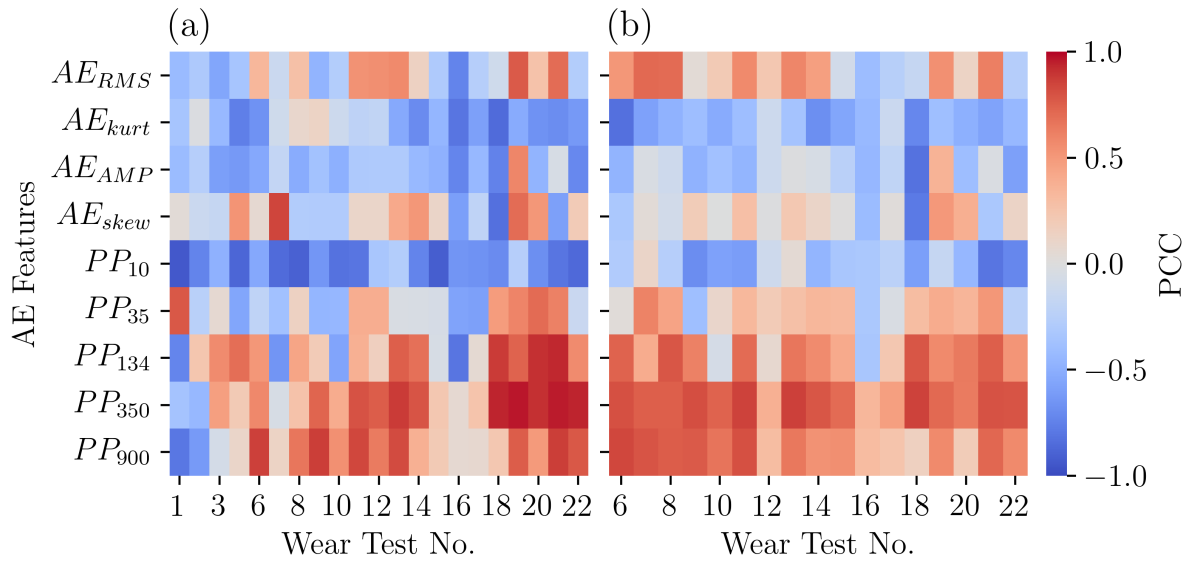


**Fig. 5.11:** PCC between the extracted AE features and (a) $r_{mean}$, and (b) $a'_e$.

When training any ML model, it is crucial to avoid contamination between the data used to train the model, and the data used to score the model [195]. In the worst case, whereby the same data is used to both train and score the model, a ML model will not be incentivised to generalise and learn from the data. Instead, the model will simply act as a "parrot" and repeat exactly the input data when being evaluated. This data contamination can severely misrepresent a ML model's ability, or lead to incorrect hyperparameter tuning. Therefore, to get a true evaluation of the ANNs, the dataset was randomly split into a training and test datasets, denoted by $_{\text{tr}}$ and $_{\text{te}}$ respectively, and kept separate throughout training and evaluation phases. Due to the size of the dataset collected across the wear tests, a 70:30 training to test dataset split was used. Meaning that 30 % of the entire dataset is reserved only for the final validation of any trained ANN. This train-test split ratio, can also be an additional hyperparameter to optimise for a given datasets size and model performance, owing to the idea that typically a larger training dataset produces higher accuracy models [196].

In addition to randomly splitting a dataset to prevent data contamination, a further consideration is required when splitting classification datasets relating to the proportion

of each class in the dataset. When splitting a classification dataset, there is a chance that all inputs from one class are omitted from either the training or test sets. Instead, a statistical stratified sampling method can be used, ensuring that a consistent proportion of each class, inline with the overall dataset composition, is represented in both the training and test sets [197]. This problem is exacerbated when training an ANN on imbalanced datasets, in which case a single class can be spread too thin, severely limiting a model's performance over said class.

When using any ANN it is best practice to normalise each feature with the input data matrix, $\boldsymbol{X}$, prior to training. Normalisation improves model performance by both increasing convergence rate, and preventing a model from focussing too heavily on features with larger ranges and scales during its initial learning [198]. Therefore, each AE feature was normalised between a range of $0-1$ using Eq. (5.8). Importantly, the normalisation is based solely on the training data's minimum, $\boldsymbol{X}_{tr\,\min}$, and maximum, $\boldsymbol{X}_{tr\,\max}$, values. If the maximum and minimum values are taken over the whole input dataset, data contamination will occur, whereby data within the test set that should be unseen to the model during its training phase is influencing the model's inputs.

$$\boldsymbol{X}' = \frac{\boldsymbol{X} - \boldsymbol{X}_{tr\,\min}}{\boldsymbol{X}_{tr\,\max} - \boldsymbol{X}_{tr\,\min}} \tag{5.8}$$

When developing a regression model the target feature, the DCB's $r_{mean}$ in this work, requires no pre-processing as the final output layer of each ANN is capable of outputting any numeric value, due to its linear activation function. However, in order to train the MLP classification model, pre-processing is first required to label the OMP600 $a'_e$ measurements into classes useful for a TCM system. Multiple different avenues can therefore be followed to label the DCB wear test dataset.

One such method is multi-class labelling, whereby each phase within the wear cycle, Fig. 2.7, is a unique label. Each model input can then be assigned a single label depending on its $a'_e$, i.e. grinding pass five is labelled as zero, representing phase I - wear-in. Fig. 5.12(a) shows an example of this labelling methodology, for the $a'_e$ measurements of

wear test 7. The transition points between each wear phase have been manually picked, and then the dataset labelled accordingly. Everything preceding the first transition point is receives a label of zero, signifying phase I - wear-in, data points after the second transition point is labelled as two, representing phase III - wear-out, and all other data is labelled one for phase II - steady-state. Appendix G shows the manually picked transition points for the multi-class labelling of wear tests $6-22$.

An additional binary labelling method can be produced by applying a $\pm 1.5\,\mu m$ tolerance to the OMP600 $a_e'$ measurements. From which, each grinding pass can be labelled as in or out of tolerance, depending on whether the $a_e'$ falls within the tolerance band of $30 \pm 1.5\,\mu m$. The value $1.5\,\mu m$ of was recommended by the Renishaw Machine Tool Team, as a reasonable tolerance for a single surface grinding pass with this DCB specification. Fig. 5.12(b) shows the output of this labelling methodology, for the $a_e'$ measurements of wear test 7. Samples in tolerance are labelled as 0 and samples out of tolerance labelled as 1, creating a binary classification dataset instead of the previous multi-class labelling method. Unlike the multi-class labelling method, this binary approach is automatic and requires no manual input or picking of transition points. The target data labels from both labelling methods are then passed through a one-hot encoder to output the final data targets for model training.

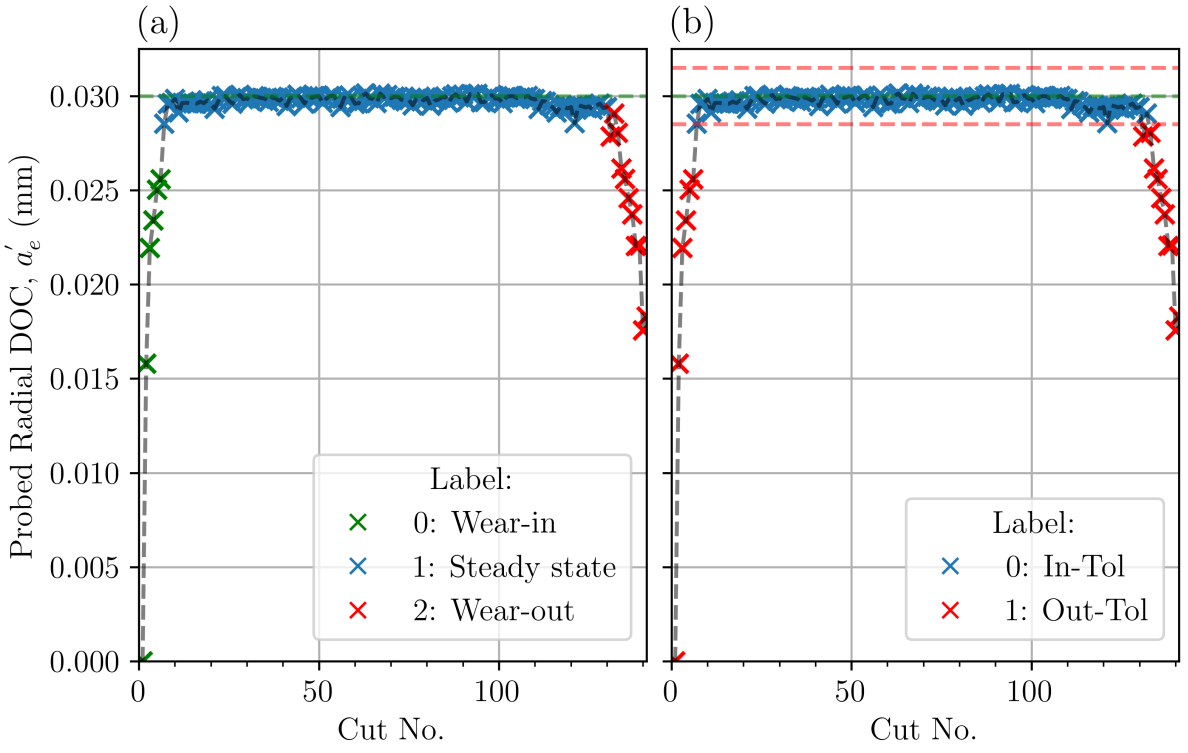


**Fig. 5.12:** Outputs of both classification labelling methods for the OMP600 $a_e'$ measurements of wear test 7; (a) multi-class: DCB wear phase and (b) binary: $a_e'$ tolerance.

Once trained, an ANN's performance must be evaluated to determine its capability and usefulness. For this, a range of evaluation metrics are employed relating a model's predictions, $\hat{\boldsymbol{y}}$, to the target values, $\boldsymbol{y}$. As a result of the different desired outcomes and output types, different evaluation metrics are used for regression and classification models. The resulting evaluation metric scores allow for comparison between different iterations of a model, or between architectures, and as such the choice of metrics is important. However, the process of obtaining the chosen scoring metrics is as critical as the choice of metrics themselves.

To evaluate the performance of all regression ANNs, three metrics were utilised; RMSE, MAE and $R^2$. MAE gives an average difference between the actual and predicted values, and acts as a good representation of a model's general prediction capabilities.

Additionally, the unit of MAE matches the units of the target value to be predicted. Eq. (5.9) is used to calculate MAE, where $\boldsymbol{y}$ is the true target value, $\hat{\boldsymbol{y}}$ is the predicted value and $n$ is the observation sample size.

$$MAE = \frac{1}{n}\sum_{i=1}^{n} \|\boldsymbol{y}_i - \hat{\boldsymbol{y}}_i\| \tag{5.9}$$

However, MAE is not effective at identifying models producing large predictive errors or outliers, especially when the number of samples, $n$, is large, as the metric linearly increases with increasing error. Therefore, RMSE was also employed as a metric, which instead heavily penalises larger prediction errors. As an extension of the common Mean Square Error (MSE) metric and loss function [199], RMSE is very useful when used in conjunction with the MAE metric. RMSE was selected over MSE for a scoring metric as it too uses matching units to the target values. Eq. (5.10) is used to calculate the RMSE metric. A superior ANN will result in lower values of both MAE and RMSE, with a value of zero representing perfect model performance.

$$RMSE = \sqrt{\frac{1}{n}\sum_{i=1}^{n} (\boldsymbol{y}_i - \hat{\boldsymbol{y}}_i)^2} \tag{5.10}$$

The $R^2$ score represents the proportion of variance resulting from the model's prediction. Therefore, indicating how well the model will predict over unseen sample data. Eq. (5.11) is used to calculate $R^2$, in which $\bar{\boldsymbol{y}}$ denotes the mean value of $\boldsymbol{y}$. The $R^2$ metric will result in a score of zero for a model constantly outputting $\bar{\boldsymbol{y}}$ regardless of the inputted features, with a $R^2$ score of one indicating perfect predictions.

$$\begin{aligned} R^2 &= \frac{\text{Residual Sum of Squares}}{\text{Total Sum of Squares}} \\ R^2 &= \frac{\sum_{i=1}^{n} (\boldsymbol{y}_i - \hat{\boldsymbol{y}}_i)^2}{\sum_{i=1}^{n} (\boldsymbol{y}_i - \bar{\boldsymbol{y}})^2} \end{aligned} \tag{5.11}$$

Evaluating a classification model is more complex and first requires converting the outputted likelihoods of the output layer's softmax neurons to a class prediction. A classification MLP model will output a vector, $\hat{\boldsymbol{y}}$, of length $n_{classes}$ summing to one, from its softmax activated neurons. To determine the predicted class from $\hat{\boldsymbol{y}}$, two common classification rules are used:

- argmax: The predicted class is based on the maximum value of $\hat{\boldsymbol{y}}$, i.e. $\texttt{argmax}(\hat{\boldsymbol{y}})$.
- threshold: The predicted class is chosen based on the value of $\hat{\boldsymbol{y}}$ that exceeds a set threshold.

These classification rules are utilised for different approaches, the "threshold" approach particularly for imbalanced binary classification tasks. The "threshold" method is particularly beneficial if accuracy of a single class is a much higher importance, as the threshold can be adjusted after training to optimise for a particular application. Threshold moving [200, 201] therefore can be a very useful optimisation technique for imbalanced binary classification. For a multi-class classification problem, the "argmax" approach is much simpler to utilise, as it avoids potential conflicts whereby no value in $\hat{\boldsymbol{y}}$ is greater than the set threshold, leading to a "no prediction" result. Therefore, the "argmax" method was used as the classification rule for all multi-class classification approaches, to convert the softmax neuron outputs to useful class predictions. Whilst for binary classifications training results were scored with the "argmax" method, i.e. a threshold of 0.5, which could then be optimised across the test dataset by utilising a "threshold" based classification rule instead.

A confusion matrix simply visualises a classification model's predictions, by showing the number of samples classified into each class and their true labels. Fig. 5.13 shows an example confusion matrix for a binary classification problem, in which the outputs have been binned into four cells. The predictions, falling into the green main diagonal of the confusion matrix, are those that have been correctly classified and thus designated True Positives (TPs) or True Negatives (TNs). Whereas those in the red boxes have been incorrectly classified, and thus being False Positives (FPs) or False Negatives (FNs).

Additionally, confusion matrices can be expanded to convey results from multi-class classification approaches. Most classification metrics are formulated to better convey the information present within a model's confusion matrix.

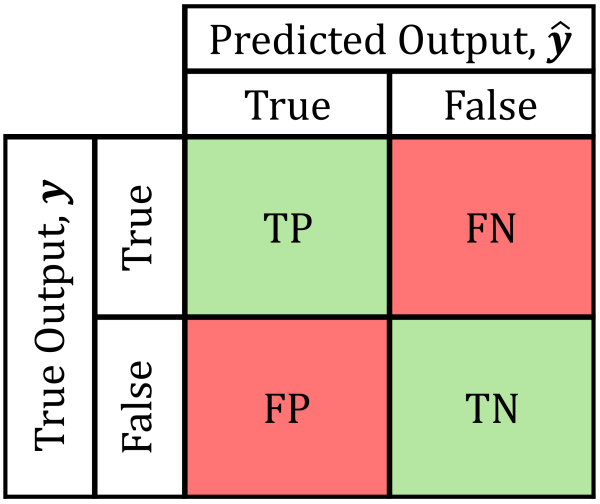


**Fig. 5.13:** Schematic of a confusion matrix for a binary classification problem.

To complement each model's confusion matrix, six metrics have been included; accuracy, balanced accuracy, recall, precision, $F_1$ score and Matthews Correlation Coefficient (MCC). Unlike the regression metrics, these classification metrics are not intuitive and as such are explained below [202, 203].

The precision of a binary classification model, resulting in a confusion matrix as seen in Fig. 5.13, is the ratio between the number of TP samples and the total number of samples predicted as positive, seen in Eq. (5.12). In simpler terms, precision is a measure of how trustworthy a model's true predictions are. Recall however is the proportion of TP samples within the total number of samples labelled as true, seen in Eq. (5.13). And therefore acts as a measure of a model's reliability in finding all true labelled samples.

$$Precision = \frac{TP}{TP + FP} \tag{5.12}$$

$$Recall = \frac{TP}{TP + FN} \tag{5.13}$$

This also expands to multi-class problems, where a more generalised description of both metrics can be stated as follows. Precision is the probability that a sample is labelled as

class X, given it was classified as class X. And recall is the probability that a sample will be classified as class X, given it is labelled as class X.

A classification model's accuracy is the probability that the model prediction is correct, and as such is simply the number of ratio of correctly classified inputs against the total number of inputs classified, as such it ranges between $0-1$. Eq. (5.14) shows the calculation of accuracy from a model's confusion matrix.

$$Accuracy = \frac{TP + TN}{TP + TN + FP + FN} \tag{5.14}$$

Whilst accuracy is probably the most intuitive and widely used classification metric, it can be misleading and even inappropriate in situations of a large imbalanced dataset. In this case, accuracy can hide large errors within classes of a smaller size, as the size of each class is not taken into account. To counteract this balanced accuracy is also employed, as it is insensitive to an imbalanced dataset, equally weighting classes based on their proportion over the whole dataset. Eq. (5.15) shows the formula for a model's balanced accuracy score, from which it can be seen to be an average of the recalls for each dataset class.

$$BalancedAccuracy = \frac{\frac{TP}{TP+FN} + \frac{TN}{TN+FP}}{n_{classes}} \tag{5.15}$$

The $F_1$ score for a binary classifier is the harmonic mean of its precision and recall, which is useful for a metric as model selection often depends on a trade-off between recall and precision. Eq. (5.16) shows how to calculate the $F_1$ score for a binary classification model's output An important note however, is that equal weight is given to both a model's precision and recall in Eq. (5.16), which may not be an optimal strategy for the given application [204].

$$F_1 = \left( \frac{2}{precision^{-1} + recall^{-1}} \right) = 2 \cdot \frac{precision \cdot recall}{precision + recall} \tag{5.16}$$

In order to expand the $F_1$ score to a multi-class case, an $F_1$ score is computed for each of the $n_{classes}$ based on each classes' individual recall and precision scores. These values

themselves are useful, but an additional "averaging" step is commonly applied to generate a single value. Depending on the "averaging" step utilised, three different versions of $F_1$ score are produced; $F_{1\,micro}$, $F_{1\,macro}$ and $F_{1\,weighted}$. Taking the arithmetic mean of each of the classes $F_1$ scores yields $F_{1\,macro}$, as seen in Eq. (5.17).

$$F_{1\,macro} = \sum_{i=1}^{n_{classes}} F_{1\,i} \tag{5.17}$$

The $F_{1\,weighted}$ score is an adjusted version of $F_{1\,macro}$, in which each classes $F_1$ is weighted based on its proportion within the dataset, $W$.

$$F_{1\,weighted} = \sum_{i=1}^{n_{classes}} F_{1\,i} \times W_i \tag{5.18}$$

$F_{1\,micro}$ aggregates the values across all classes, which in the case of a multi-class approach equates to the model's accuracy score adjusted for multiple classes.

Finally, the MCC metric which includes all entries within the confusion matrix for its calculation, in both its numerator and denominator, as seen in Eq. (5.19), making it a very well-balanced metric.

$$MCC = \frac{TP \times TN - FP \times FN}{\sqrt{(TP + FN)(TP + FP)(TN + FN)(TN + FP)}} \tag{5.19}$$

Unlike both accuracy and the $F_1$ score, to produce a high MCC score the classifier must make good predictions of both the true and false classes, irrespective of their dataset proportions [205]. As such, MCC is an ideal metric when evaluating any imbalanced dataset.

An ML model has two types of error, a training, and a test error. Test error is the model's capability when predicting from unseen/new samples. This can arise in two forms either from using data not employed in the training process, i.e. the test dataset, or through a model's deployment and use once trained. Training error is determined by evaluating a model over the dataset used for its training. The training and test error of an ML model is often very different, and comparison between both types of evaluations can help determine a model's capability and suitability for given applications [206]. Generalisation is the desired outcome of any ML model, requiring the model to

develop an understanding of the underlying data patterns and as a result allowing it to yield good prediction scores no matter the inputted data. Therefore, by evaluating both a model's training and test errors, a measure of its ability to generalise can be inferred. As mentioned previously, each ANNs datasets are split 70:30 into train and test sets for this purpose.

There is an element of variability and randomness in the training of any ML-based model, and as such, resampling methods are utilised to obtain a more accurate measure of a model's training error. Resampling involves training multiple permutations of the same model with different samples of the training data, to then examine the distribution of scores [206]. Repeated $k$-fold CV was used throughout this thesis as the resampling method [197, 202]. $k$-fold CV involves the process of randomly splitting the data into $k$ splits of approximately equal size, from which a model is trained on $k-1$ of the splits, with one split used for evaluating the model. The process is then repeated, rotating which split is used for evaluation, until all the data has been used. This process can be seen in Table 5.1, whereby the data pipeline for model's evaluation is shown, using a $k$-fold CV process, with $k = 5$, to obtain the training errors. Much like the stratified splitting of the dataset for a classification approach, each fold within the CV is also stratified to maintain class distributions when training and scoring. Repeated $k$-fold CV involves repeating this process $n_{repeats}$ times, leading to different splits to be created during each repetition. The required number of splits, $k$, and repeats, $n_{repeats}$, is a trade-off between computational time/expense and scoring accuracy. Current literature agrees on minimum values of $k = 10$ and $n_{repeats} = 10$ for repeated $k$-fold CV, to avoid the requirement of bias correction [202, 207]. This CV process results in a distribution of scores, from which the mean and standard deviation can be used as measures of the model's true training error.

**Table 5.1:** Evaluation process of an ML model, showing the dataset pipeline.

| Operation: | | | | | | | |
|---|---|---|---|---|---|---|---|
| Pre-process | | Dataset | | | | | |
| Train:Test Split | | Training Data | | | | | Test Data |
| k-Fold CV (k=5) | | Fold 1 | Fold 2 | Fold 3 | Fold 4 | Fold 5 | |
| | Split 1 | Test | Train | Train | Train | Train | |
| | Split 2 | Train | Test | Train | Train | Train | |
| | Split 3 | Train | Train | Test | Train | Train | |
| | Split 4 | Train | Train | Train | Test | Train | |
| | Split 5 | Train | Train | Train | Train | Test | |
| Final Evaluation | | | | | | | Test Data |

Optimisation of the model's architecture and hyperparameters is often conducted to improve a model's capability. To do this a model's CV scores are typically used as benchmarks to compare the different variations in parameters. The optimal choice of each parameter are then usually selected to improve scoring metrics whilst not incurring a large penalty, such as over/underfitting, increased training time or inconsistent training scores.

A common problem for ANNs is overfitting, in which a model performs well over its training data but is not able to generalise sufficiently to perform as well over the test dataset [195]. Overfitting occurs when the model is too complex relative to the quantity and noisiness of the training data. To avoid overfitting three options can be implemented; simplify the model, use a larger training dataset, or reduce the noise level within the training dataset [183]. Overfitting is usually diagnosed through a comparison between the model's training and test errors, and as such optimisation can result in limiting a model's complexity to prevent overfitting. Alternatively, the inverse can also be true and the model can underfit, because the model is insufficiently complex to learn from the input data.

When conducted in this thesis, the hyperparameter optimisation was conducted using a grid-search methodology. Grid-search is an exhaustive search across a manually defined set of hyperparameters, from which the optimal choice can be determined.

Fig. 5.14 shows the optimisation process, in which the training data is used to determine the optimal hyperparameters during the CV process. After being determined, the best parameters can then be used to build a new model which is trained on all the training data. Final evaluation of the model can then be conducted with the test dataset data, as well as repeating the CV process with the training data.

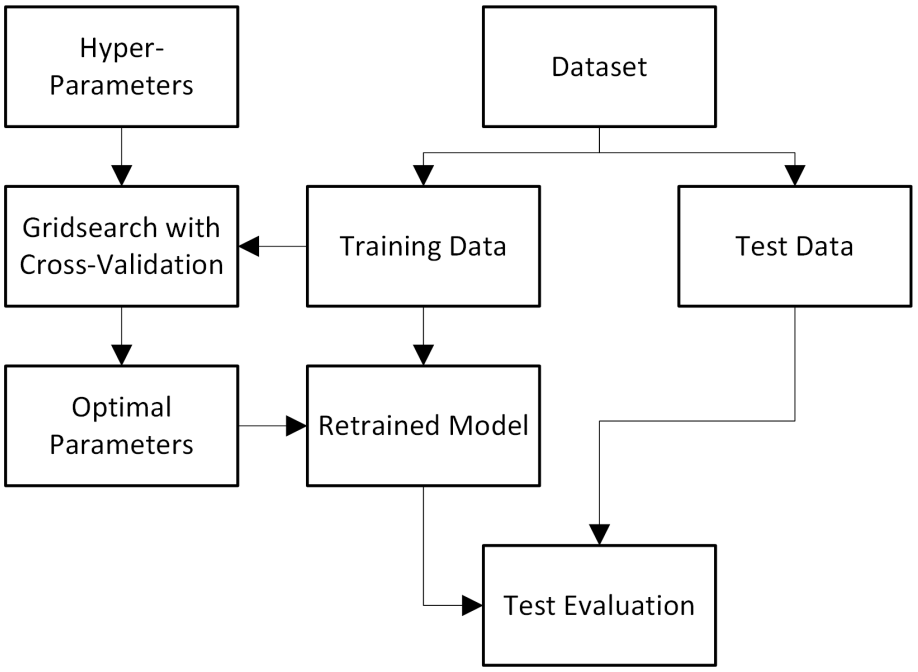


**Fig. 5.14:** Optimisation process diagram for any ANN.

### 5.2.2 Regression: Tool Radius Prediction

Utilising the approach presented in Section 5.2.1, the three different regression ANNs architectures were each trained, optimised and evaluated, based on the data presented within Chapter 4. The three architectures investigated were MLPs, MLP-WINs and LSTMs. Each of which are aiming to predict a DCB's $r_{mean}$ utilising only AE features for inputs. The following section details the results from these models and compares their performance, whilst also highlighting their potential advantages and use cases.

Once pre-processed, the regression dataset contained 2499 samples, each of which containing nine AE features, $\boldsymbol{X}$, and the respective target value of $r_{mean}$, $\boldsymbol{y}$. With an

70:30 train:test data split, 1749 samples were used for model training, and the remaining 750 samples were held for each test dataset. From initial training results, all three model architectures were seen to be capable of generalising across the dataset and therefore outputting good results. This initial check signified that model optimisation was worthwhile prior to conducting the computationally expensive grid-search method. The hyperparameter space investigated within the grid search method is shown in Table 5.2. Due to the available computational power at the time, the four hyperparameters were chosen for investigation were those will largest effect on model score across initial testing. Repeated $k$-fold CV was utilised with $k = 10$ and $n_{repeats} = 10$ was used throughout, with Table 5.3 showing the constant parameters across the three architectures, in relation to the compilation and fitting of each ANN.

**Table 5.2:** Hyperparameters evaluated with the grid-search method for each regression ANN architecture.

| Hyperparameter | Values |
|---|---|
| No of Layers | [1, 2, 3, 4] |
| No of Neurons | [32, 64, 128] |
| Dropout Rate | [0.001, 0.01, 0.1] |
| Sequence Length | [5, 10, 15] |

**Table 5.3:** Fit and compile parameters for all three regression architectures.

| Epochs | Batch Size | Loss | Optimiser |
|---|---|---|---|
| 3000 | 128 | MSE | Adam |

As a result of the optimisation process, the hyperparameters that yielded the highest scoring and most consistent predictions for each model are detailed in Table 5.4. Consistency in scores during CV was prioritised over small average performance gains, as repeatability is a crucial factor within large scale applications. Interestingly, the MLP-WIN's performance worsened with increasing sequence length, unlike the LSTM which improved

significantly with small increases in sequence length. This observation could signify that the MLP-WIN was unable to take advantage of the increased history, associated with a higher sequence length, or that increases in sequence length required significant increases in model depth/complexity. Additionally, a significant improvement in the LSTM model's scores stemmed from the inclusion of two dense layers after the LSTM layers, a common technique to allow the model to better make use of the LSTM cells outputs.

Comparing each model's complexity is also of interest; as expected due to its RNN basis, the LSTM model is the most complex, being comprised of five layers (three LSTM followed by two dense). As a result of this, the LSTM architecture required a higher level of dropout, 0.1, compared to the 0.01 dropout used by both MLP and MLP-WIN. Dropout is a regularisation technique which aims to prevent overfitting by randomly setting a fraction, the dropout parameter, of the layer's inputs to zero on each training epoch [208, 209]. By removing this small percentage of inputs during training, it forces the ANN to generalise more efficiently and prevents static predictions, a particular concern with more complex model architectures. Utilising dropout as a regularisation method does have a downside however, mainly stemming from its stochastic nature. Dropout can increase the time required for a model to converge during training, which can be further compounded when training over smaller datasets. Also of interest in regard to model complexity, is the difference between the MLP and MLP-WIN architectures. The MLP performed best when utilising four 128 neuron dense layers, whilst the MLP-WIN model, with a more complex input $\boldsymbol{X}$, utilised only three 128 neuron layers. This difference potentially suggests that sequencing the input data, $\boldsymbol{X}$, allowed for improved model generalisation without increased complexity.

**Table 5.4:** Optimised model hyperparameters for the three regression architectures.

| Model | Layers (D-Dense, L-LSTM) | Sequence Length | Dropout | Activation Function |
|---|---|---|---|---|
| MLP | [D128, D128, D128, D128] | - | 0.01 | ReLU |
| MLP-WIN | [D128, D128, D128] | 5 | 0.01 | ReLU |
| LSTM | [L64, L64, L64, D64, D64] | 15 | 0.1 | ReLU |

The optimised hyperparameters from the grid-search process were then used to train a final ANN for each architecture. Fig. 5.15 shows each model's loss throughout its training, over its training and validation data. Evaluation of each model was then conducted over CV and the corresponding test dataset, Table 5.5 shows the scores of all three optimised regression ANNs. Both the convergence of each model's loss in Fig. 5.15 and all architectures scoring $<$3.41 µm RMSE over the test datasets in Table 5.5, prove that all three model architectures are capable of generalising over and predicting a DCB's $r_{mean}$ when trained solely on AE features.

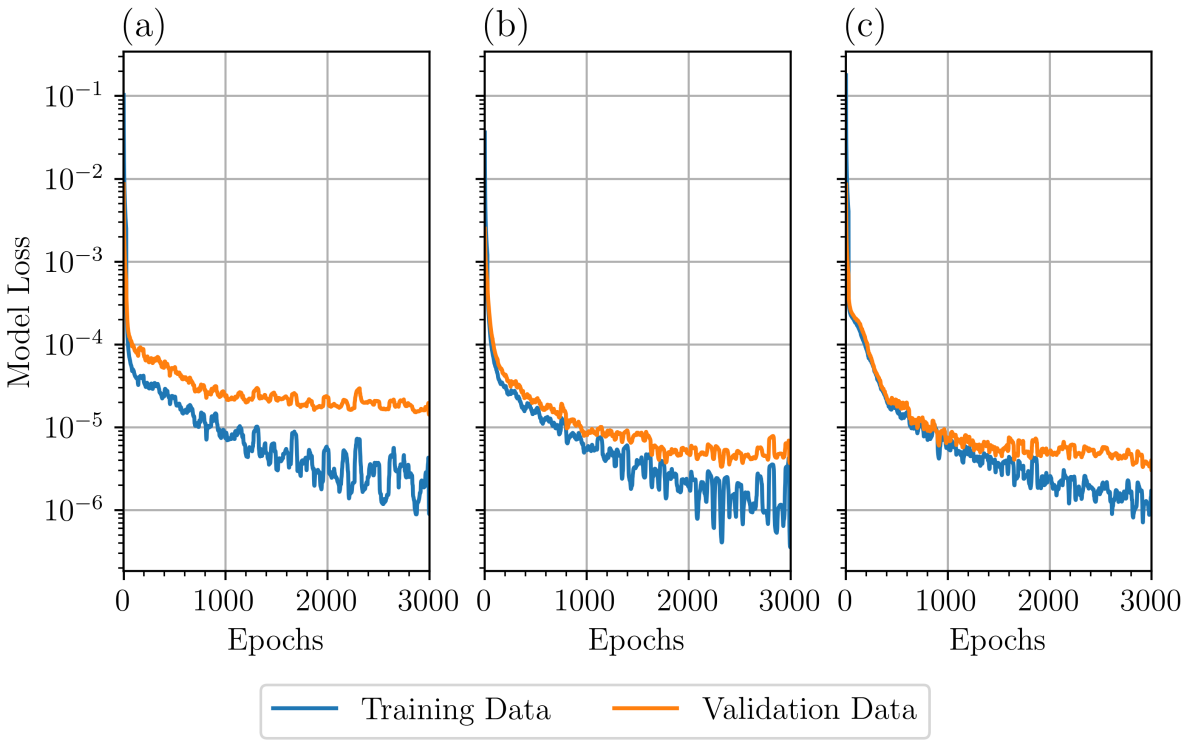


**Fig. 5.15:** Loss plots of each optimised regression model architecture over the training and validation datasets: (a) MLP, (b) MLP-WIN and (c) LSTM.

**Table 5.5:** Evaluation scores of each optimised ANN architecture during the CV, using the training dataset, and the test dataset scores.

| Model | CV Scores | | | Test Scores | | |
|---|---|---|---|---|---|---|
| | RMSE (µm) | MAE (µm) | $R^2$ | RMSE (µm) | MAE (µm) | $R^2$ |
| MLP | 4.346 (±0.959) | 1.870 (±0.443) | 0.918 (±0.036) | 3.408 | 1.487 | 0.948 |
| MLP-WIN | 3.501 (±0.756) | 1.689 (±0.511) | 0.944 (±0.023) | 3.212 | 1.272 | 0.957 |
| LSTM | 2.207 (±0.769) | 1.431 (±0.780) | 0.976 (±0.018) | 1.407 | 0.656 | 0.992 |

The MLP architecture scored the worst of the three models across all scoring met-

rics, both in CV and test. Through comparing the MLP model's RMSE and MAE scores, it can be inferred that the model performs well on average with a few predictions resulting in larger errors, thus increasing its RMSE scores. Fig. 5.16 compares the true and predicted value of each sample across each architecture's test dataset. The reduced predictive capability of the MLP, in Fig. 5.16(a), can be seen visually when predicting over the lower and higher end of true DCB $r_{mean}$ values. The MLP-WIN by comparison, with one less dense layer but a greater level of history per sample input, performed markedly better, improving on every scoring metric. Of particular interest is the standard deviation across the RMSE CV scores of $\pm 0.756\,\mu m$, the lowest across all model architectures. This stability during training is crucial, indicating the MLP-WIN architecture significantly better at learning from the $r_{mean}$ dataset, no matter the splitting of data within each fold during CV. And as such in Fig. 5.16(b) lower error can be seen when predicting samples where the true DCB $r_{mean}$ is $>0.67\,mm$.

A similar increase in model capability can be seen with the LSTM architecture, when compared to the MLP-WIN. With a significant increase in predictive capability across its test dataset, leading to a MAE of $0.656\,\mu m$ on unseen data. Fig. 5.16(c) shows a clear difference in the errors of the LSTM in comparison to both the MLP and MLP-WIN models. Due to its recurrent nature, the LSTM is more precise than both other architectures across the entire range of $r_{mean}$, with a sole outlier as the only poor prediction. Furthermore, by comparing the loss plots of each architecture in Fig. 5.15, the LSTM is the sole model that has not fully converged with both its training and validation losses still decreasing after 3000 epochs. Potentially, suggesting further improvements could be made with increased training time. However, a limitation of the LSTM model is its significantly slower training time, $2.06\,\text{epochs}\,s^{-1}$, whereby it was three times slower to train than both the MLP and MLP-WIN models, at 6.0 and $6.5\,\text{epochs}\,s^{-1}$ respectively.

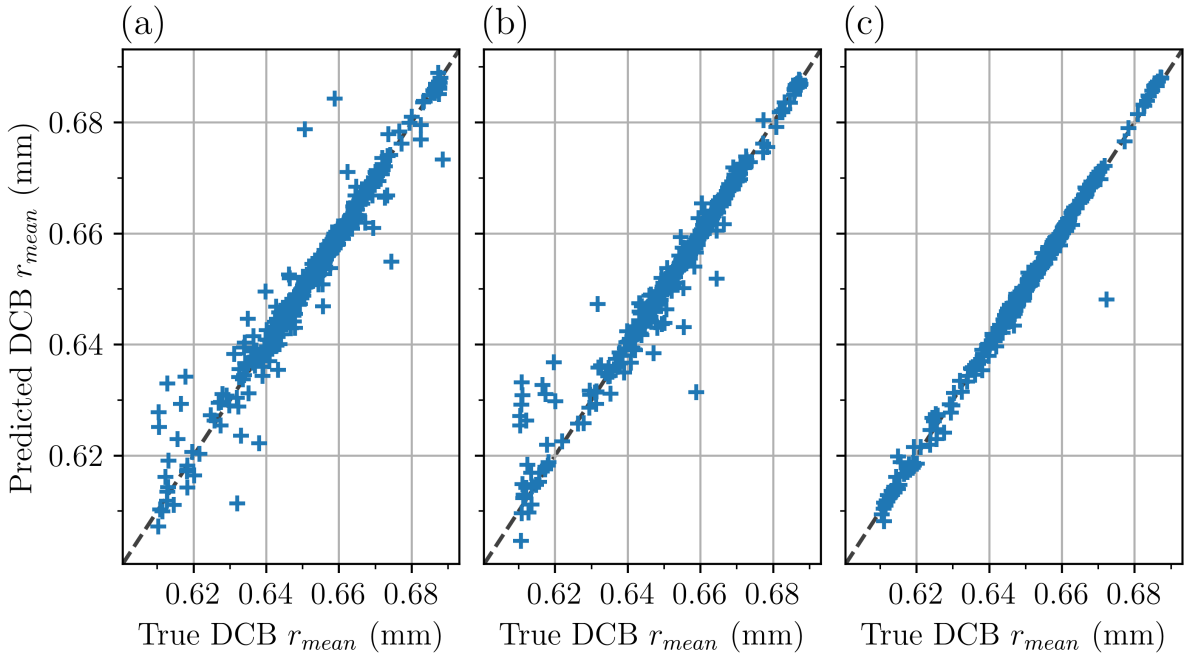


**Fig. 5.16:** Comparison of actual and predicted DCB $r_{mean}$ values within each model's test dataset: (a) MLP, (b) MLP-WIN and (c) LSTM.

Three ANN architectures were trained, optimised and evaluated as regression models utilising AE features to predict the DCB $r_{mean}$, a representation of a tool's RUL. All three architectures; MLP, MLP-WIN and LSTM, were able to learn from, and generalise the AE inputs sufficiently to predict both precise and accurate values. Across both the training data during CV and the test data, the LSTM ANN performed the best with a test RMSE of 1.407 µm and an MAE of 0.656 µm.

An exhaustive grid-search was utilised to determine the optimal hyperparameters for each architecture, utilising repeated $k$-fold CV ($k = 10$ and $n_{repeats} = 10$). The inclusion of past input samples as a sequence forming the MLP-WIN architecture outperformed the more common MLP. But, the LSTM architecture, purpose built for time-series data, resulted in a halving of the RMSE and MAE on unseen test data compared to the MLP-WIN model. Furthermore, the LSTM model was capable of predicting with low error across the whole range of $r_{mean}$ values, whilst both the MLP and MLP-WIN models performed worse over the lower end of the range. Whilst the LSTM outscored both other

models, it took approximately three times longer to train, at 2.06 epochs $s^{-1}$, significantly increasing its expense to develop.

Despite this, all three model architectures are successful predictors of a DCB's $r_{mean}$, and as such, all could be employed within a TCM system. The MLP-WIN architecture presents all the benefits of the MLP architecture, faster training time and less computational overhead, with improved prediction scores therefore removing the use case for an MLP architecture. The choice between the LSTM and MLP-WIN architectures, is a trade-off between prediction accuracy and computational expense. An MLP-WIN model could be deployed and even re-trained on an edge device or within the machine tool controller, whereby its output could be combined with other information to compensate for its worse predictive ability. The LSTM model however, is more reliable and precise across the whole range of DCB $r_{mean}$, potentially enabling it to be a main component for a larger scale TCM system, in which its computational expense is worthwhile.

Overall, these regression ANNs are extremely promising, allowing an indirect measurement of the DCB's $r_{mean}$. Due to the extremely low prediction errors seen when utilising an LSTM architecture, this methodology could be used to enable an indirect radius compensation method. Radius compensation updates the tool radius within the g-code to counteract the effect of radial wear, typically this requires direct measurements such as those seen in Chapter 4 with the NC4. Significant cycle time can therefore be saved through the removal or reduction of direct measurements, whilst also enabling a process to extend the life of a DCB. Furthermore, once developed, the computational expense to process the AE and predict with the regression model is minimal and could be deployed to an edge device.

### 5.2.3 Classification: Tool State Prediction

As a result of the two different dataset labelling approaches for a classification ANN; multi-class: wear phases and binary: $a'_e$ tolerance, different class distributions were produced across the two datasets. The distribution of class labels within the dataset is

an important consideration when evaluating a classification model's capability, especially when training on an imbalanced dataset. Table 5.6 shows the resultant class distribution from each labelling method, in which both show clear imbalanced datasets. The multi-class approach results in just 63 samples falling into its class 0: phase I, equating to 3.52 % of the entire dataset. As a result, it is likely that the model's predictions will be significantly worse over this class, as it will not have adequate training inputs to generalise successfully. The binary approach leads to a less extreme imbalance, but nonetheless with only 26.79 % of the dataset falling into class 1: out-tolerance, predictions may also be limited.

**Table 5.6:** Class distribution within the classification dataset of each labelling method.

| Labelling Method | Class Label | No. Samples in Class | Proportion (%) |
|---|---|---|---|
| Multi-class: Wear Phase | 0: Phase I - Wear-in | 63 | 3.52 |
| | 1: Phase II - Steady-state | 1483 | 82.76 |
| | 2: Phase III - Wear-out | 246 | 13.73 |
| Binary: $a'_e$ tolerance | 0: In-tolerance | 1312 | 73.21 |
| | 1: Out-tolerance | 480 | 26.79 |
| | Total | 1792 | 100 |

With these distributions in mind, stratified splitting of the dataset with a 70:30 train:test ratio was done after pre-processing and labelling. Leading to the training dataset being comprised of 1254 samples with 538 samples separated for each test dataset, each of which maintaining the class distributions seen across the whole dataset. Grid-search hyperparameter optimisation of the MLP classification models was not conducted, and instead a manually adjusted set of hyperparameters were used for both labelling methods. Table 5.7 shows the hyperparameters used for both the MLPs architectures, with Table 5.8 showing the compilation and fitting parameters of each model. As a result, the only difference prior to training between the two classification MLPs was the number of softmax activated neurons in each model's final output layer, with the multi-class

approach requiring three and the binary requiring only two.

**Table 5.7:** Hyperparameters used for MLP classification model architecture.

| Model | Layers (D-Dense, L-LSTM) | Kernel Regularisation | Dropout | Activation Function |
|---|---|---|---|---|
| MLP Classification | [D64, D64, D64] | L2: 0.001 | 0.01 | ReLU |

**Table 5.8:** Fit and compile parameters for MLP classification models.

| Epochs | Batch Size | Loss | Optimiser |
|---|---|---|---|
| 3000 | 128 | categorical cross-entropy | Adam |

A total of two MLP models were then trained, one for each labelling approach, with Fig. 5.17 showing the convergence of each model's loss over both the training and test datasets. Evaluation of the MLPs were conducted over the training dataset with CV and the test dataset, obtaining measures of both the training and test errors for these approaches. Tables 5.9 and 5.10 show both the CV and test classification metrics of both MLPs. Both the loss plots in Fig. 5.17 and the model scores shown in Tables 5.9 and 5.10 clearly show that a MLP architecture is capable of learning from the inputted AE features to produce a successful classification model, with both labelling approaches.

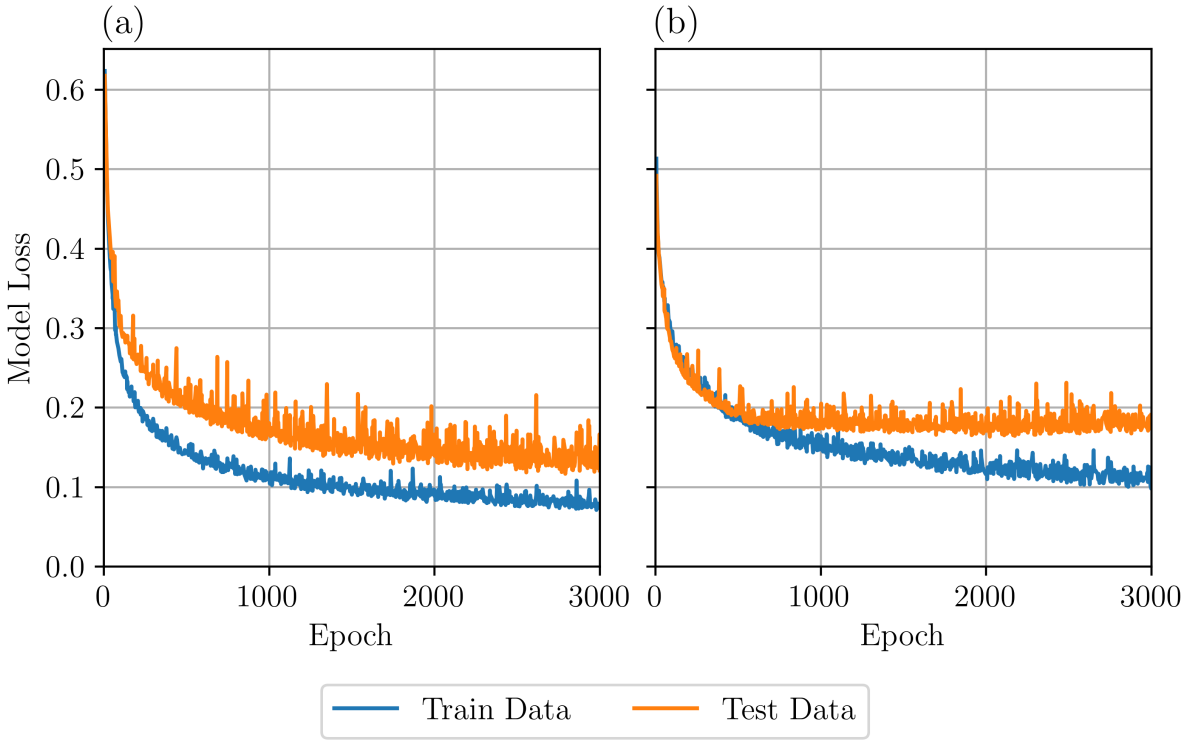


**Fig. 5.17:** Loss plots of the final MLP classification model over the training and validation datasets; (a) Multi-class and (b) Binary labelling approaches.

**Table 5.9:** CV scores of the MLP classification models.

| Labelling Method | CV Scores | | | | | |
|---|---|---|---|---|---|---|
| | Accuracy | Balanced Accuracy | Recall $_{macro}$ | Precision $_{macro}$ | $F_{1\,macro}$ | MCC |
| Multi-class: Wear Phase | 0.959 (±0.013) | 0.845 (±0.067) | 0.845 (±0.067) | 0.910 (±0.049) | 0.868 (±0.054) | 0.857 (±0.048) |
| Binary: $a'_e$ tolerance | 0.944 (±0.016) | 0.925 (±0.023) | 0.925 (±0.023) | 0.934 (±0.021) | 0.929 (±0.020) | 0.859 (±0.040) |

**Table 5.10:** Test scores of the MLP classification models.

| Labelling Method | Test Scores | | | | | |
|---|---|---|---|---|---|---|
| | Accuracy | Balanced Accuracy | Recall | Precision | $F_1$ | MCC |
| Multi-class: Wear Phase | 0.974 | 0.896 | [0.789, 0.993, 0.905] | [1.000, 0.976, 0.957] | [0.882, 0.984, 0.930] | 0.910 |
| Binary: $a'_e$ tolerance | 0.952 | 0.938 | [0.967, 0.910] | [0.967, 0.910] | [0.967, 0.910] | 0.877 |

The accuracy of each MLP is shown to be >0.944 across both the CV and test scores, indicating a highly capable classification model has been developed for both labelling approaches. However, as mentioned in Section 5.2.1 the accuracy metric of classification models can be misleading when utilised on imbalanced datasets. As a result, a better view of each model's capability can be seen through the other scoring metrics and through both model's confusion matrices, in Figs. 5.18 and 5.19.

The balanced accuracy of both MLPs, across CV and test data, were reduced in comparison to their accuracy scores. This reduction stems from each dataset's imbalanced class distribution and the limiting effect this has on each model's predictive capability. Fig. 5.18 shows the multi-class classification MLP's confusion matrices over the CV and test dataset, in which this effect can clearly be seen by observing the model's misclassification across class 0: phase I - wear-in. Due to the large difference in sample size between classes 0 and 1 of the multi-class dataset, seen in Table 5.6, the trained multi-class MLP incorrectly classifies 21 % of the samples labelled as class 0: phase I in its test dataset as class 1: phase II, seen in Fig. 5.18(b). This poor performance, results in the test recall for class 0 equalling 0.789 in Table 5.10. A similar but lessened effect can also be seen where the model misclassified 10 % of the samples from class 2 as class 1, in Fig. 5.18(b). The binary MLP also shows a worse predictive capability over samples labelled as class 1: Out-tolerance in Fig. 5.19, however due to the less severe dataset imbalance the model's

recall is much better than the multi-class MLP produces.

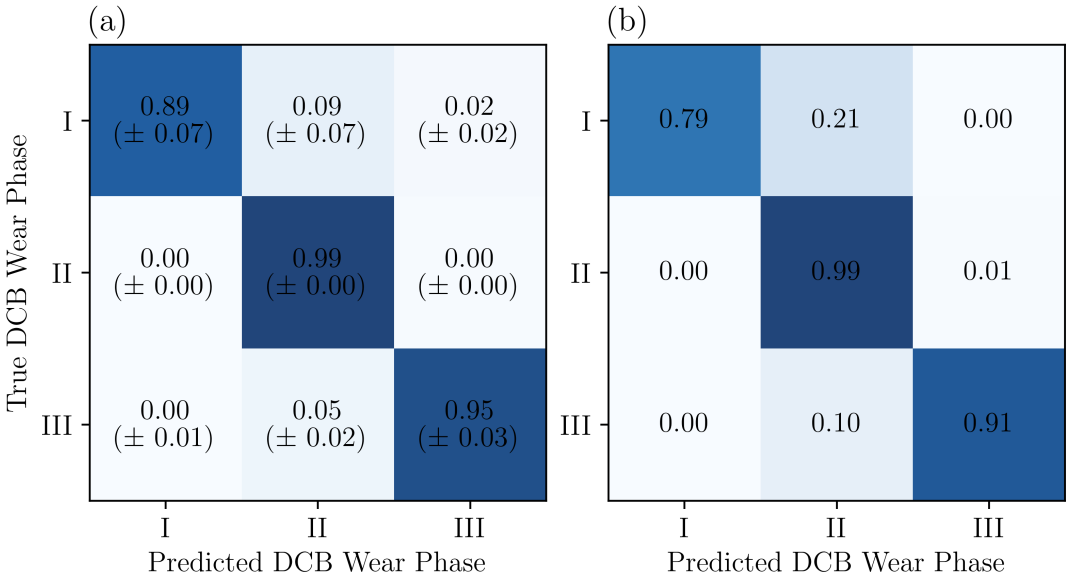


**Fig. 5.18:** Normalised Confusion matrices of the multi-class MLP classification model over the (a) training data during CV and the (b) test dataset.

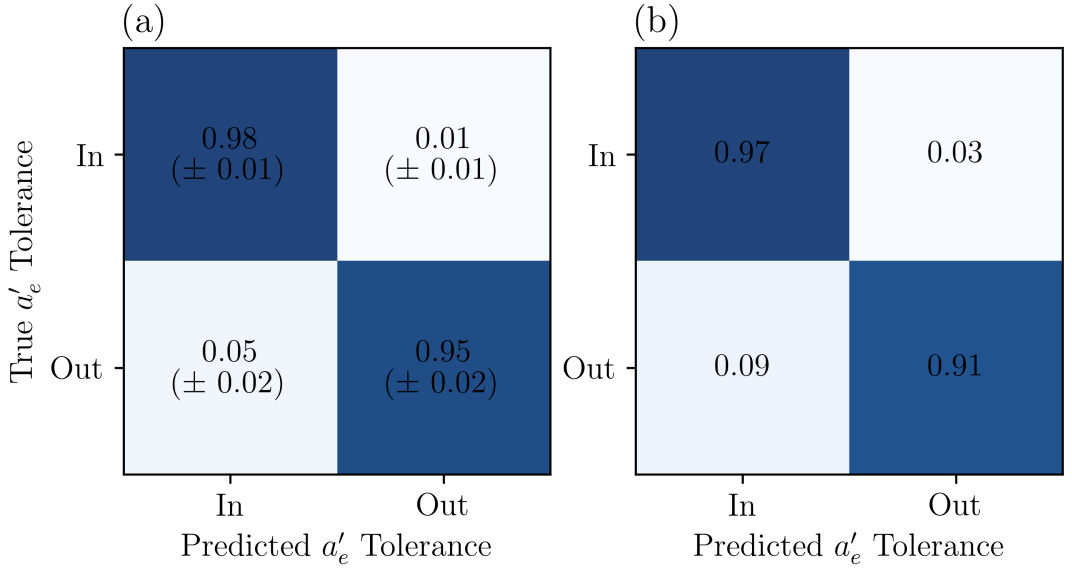


**Fig. 5.19:** Normalised confusion matrices of the binary MLP classification model over the (a) training data during CV and the (b) test dataset.

Additionally, the CV scores show small standard deviations across all the metrics of both models in Table 5.9, with the largest variability stemming from the multi-class MLP. Therefore, not only is the balanced accuracy and $F_1$ score higher with the binary labelling approach, but the MLP is more consistently producing a model to that standard when compared to the multi-class approach. Whilst reduced model capability and repeatability of the multi-class approach is observed, the multi-class MLP is still capable of generalising over its dataset. Suggesting that further data within classes 0 and 2, associated with the wear-in and out of the DCB, or utilising other techniques to combat the datasets imbalanced nature could yield significantly better results.

Depending on the application of the binary MLP classification model, incremental improvements can still be made through adjusting the classification rule's threshold. By investigating the models Receiver Operating Characteristic (ROC) curve and variation in MCC scores with threshold variation, other optimal thresholds can be found for different applications. Fig. 5.20(a) shows how the model's test dataset MCC score varies with changes to the classification threshold. The red dot on the figure shows the highest value of MCC is obtained with a threshold of 0.528, slightly above the standard threshold of 0.5. Fig. 5.20(b) instead shows the ROC curve of the model, that evaluates the trade-off between a model's true positive rate (recall) against its false positive rate over class 1: Out-tolerance. An optimal threshold can then be found from the ROC curve by determining the threshold yielding the largest geometric mean between the true and false positive rates Which, as shown by the red dot in Fig. 5.20(b), is the point on the ROC curve closest to the top left of the graph, equalling a threshold of 0.882 in this case. An additional two thresholds aimed at improving different model aspects have therefore been found; overall classification improvement by optimising the MCC score, and improvement to the recall achieved over the minority classes through the ROC curve. The MLP's scoring can then be recalculated, utilising the new classification rule thresholds, allowing comparison between the difference in outputs.

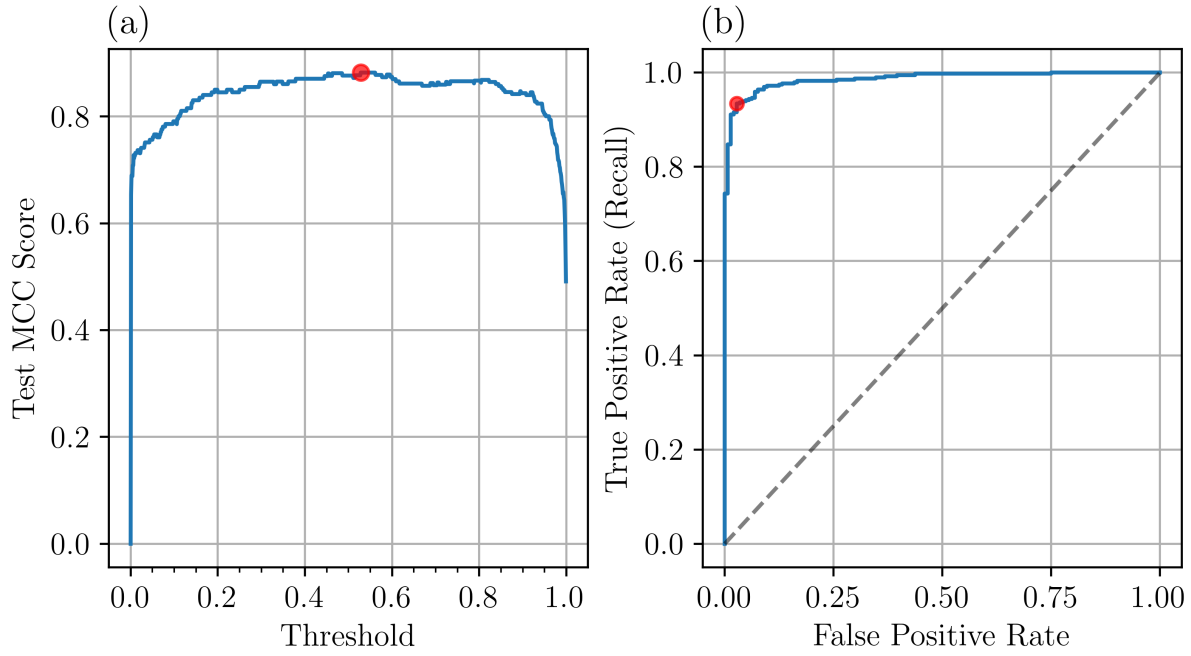


**Fig. 5.20:** Binary MLP threshold moving approaches; (a) MCC against threshold and (b) the ROC curve. Whereby the optimal point is shown by the red dot in each subplot.

Fig. 5.21 and Table 5.11 shows how changing between the three classification rule thresholds varies the test datasets confusion matrix and evaluation scores of the binary classification MLP. By changing from the standard "argmax" threshold of 0.5, to either of the other thresholds, resulted in the model's balanced accuracy increasing by 0.006. Using a threshold of 0.528, associated with obtaining the maximum MCC score, led to a slightly more even predictive capability across both classes. And as expected, utilising the threshold determined from the ROC curve of 0.882, improved the model's recall over class 1: Out-tolerance, increasing by 0.62, to the detriment of class 0: In-tolerance. As class 0: In-tolerance comprising a larger proportion of the binary dataset, the other generic metrics (accuracy, $F_1$ and MCC) all decrease as a result of favouring the recall of class 1.

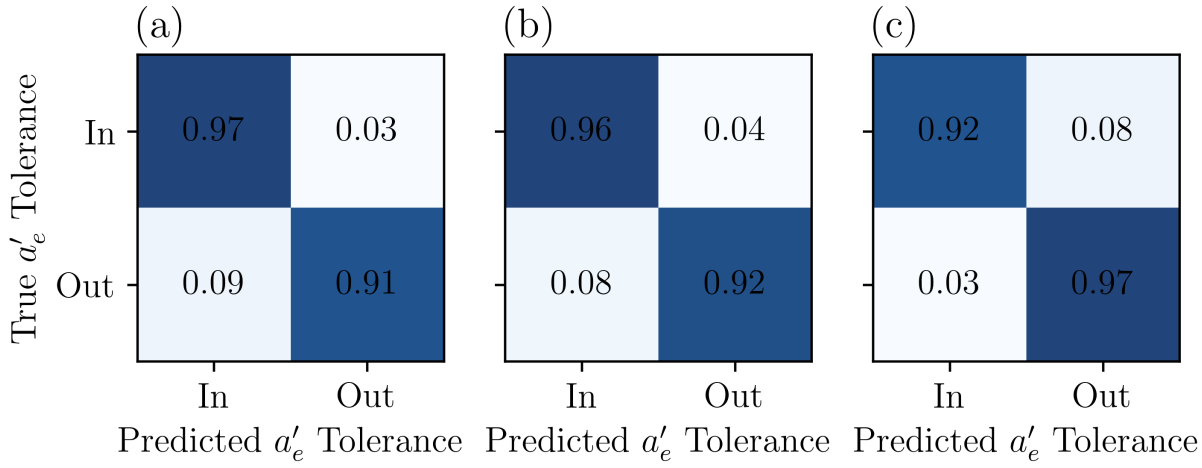


**Fig. 5.21:** Confusion matrix of the binary classification MLP when utilising different classification rule thresholds; (a) 0.5 - "argmax", (b) 0.528 - maximum MCC score and (c) 0.882 - optimal ROC point.

**Table 5.11:** Threshold moving of binary classification MLP model, showing test scores comparison.

| Threshold (Decision method) | Test Scores | | | | | |
|---|---|---|---|---|---|---|
| | Accuracy | Balanced Accuracy | Recall | Precision | $F_1$ | MCC |
| 0.5 ("argmax") | 0.952 | 0.938 | [0.967, 0.910] | [0.967, 0.910] | [0.967, 0.910] | 0.877 |
| 0.528 (max MCC) | 0.954 | 0.944 | [0.964, 0.924] | [0.972, 0.905] | [0.968, 0.914] | 0.882 |
| 0.882 (max ROC) | 0.931 | 0.944 | [0.916, 0.972] | [0.989, 0.809] | [0.951, 0.883] | 0.842 |

The frequent OMP600 $a'_e$ measurements enabled two simple methods to label each grinding pass completed throughout a DCB's life. The first of which is a multi-class approach, assigning a label to each of the three tool wear phases. And the second approach uses a $\pm 1.5\,\mu m$ tolerance from the programmed $a_e$, to determine a binary label as either in

or out of tolerance. From which an MLP classification ANN was trained for both labelling methods. However, due to the trend associated with the wear cycle, seen in Fig. 2.7, a majority of each DCB's total life is spent within wear phase II - steady-state. Leaving each classification dataset to be imbalanced, with the worst case being class 0: phase I - wear-in of the multi-class dataset comprising just 3.52 % of the total.

Despite this, the trained MLPs resulted in a balanced accuracy of 0.896 and 0.938 over each test dataset. Due to the large disparity in class size, the multi-class MLP scored notably lower when predicting samples from class 0: wear-in, but improved across both other classes, resulting in an MCC test score of 0.910. The binary MLP consistently scored higher on average over the stratified $k$-fold CV process ($k = 10$ and $n_{repeats} = 10$), and also resulted in lower standard deviations. Additionally, optimisation of the classification threshold for the binary MLP demonstrated the ability of tailoring the classifier for a particular application. Predicting the pass to have been out of tolerance incorrectly could prompt at worst a direct tool and workpiece measurement to be carried out, but misclassifying an out of tolerance sample could result in tool failure or damage. Therefore, in this use case where increased cycle time is less costly than damaged or unsalvageable workpieces due to failure, the model's recall over class 1: out-tolerance is critical. Threshold moving based on the model's ROC curve not only enabled a slight increase in balanced accuracy, but also a significant increase in recall over class 1, from 0.910 to 0.972. Resulting in an additional 6 % of the class 1 samples in the test dataset being correctly classified.

Similarly to the regression ANN, this approach enables indirect prediction of the DCB's wear phase, when employing the multi-class: wear phase approach. As such a clear use case for the multi-class classification MLP, could be to enable a DCB's wear-in phase to be monitored whilst grinding on a sacrificial workpiece. Therefore, allowing each DCB's steady-state to be used solely for machining components, and then indicating its transition into phase III - wear-out. Moreover, the binary $a'_e$ approach, relating the DCB's wear to the grinding output, could be utilised to decrease the required frequency of direct workpiece measurements. The MLP classification models, whilst manually adjusted, were not robustly optimised, potentially missing further improvements. Despite this, the simple

nature of the MLP architecture is a considerable benefit to this approach over the complex LSTM regression model architecture. Further expansion of the existing dataset to obtain more samples in the lower occurring classes could yield a more reliable classifier still.

# 6 Discussion

The efficacy of AE as an indirect and on-machine monitoring technique to optimise the usage of DCBs has been thoroughly investigated. This thesis details the reasoning for this research as well as, relevant background information, a developed wear test methodology, three series of wear tests, and the subsequent data analysis and applied TCM approaches. This chapter provides a summary of the work as a whole, presenting the main outcomes and limitations encountered through the development and fulfilment of this research, as well as setting out avenues for future work.

## 6.1 DCB Wear Test Methodology

In order to develop a reliable TCM approach, based on the AE generated as a DCB wears, a methodology to systematically wear a DCB was first developed. The wear test methodology was formed around a repetitive cycle consisting of two phases; grinding, and inspection, shown in Fig. 3.1. The grinding phase consisted of a grinding pass, with constant parameters to progressively wear a DCB, whilst simultaneously acquiring continuous AE throughout the period of tool-workpiece contact. After every grinding phase, an inspection routine, consisting of both direct tool and workpiece measurements, was conducted to obtain relevant metrics of the DCB's wear state. Acquisition of the direct wear measurements enabled the extraction, correlation, and validation of pertinent AE features to monitor a DCB's wear progression.

The use of an NC4 laser tool setter and an OMP600 contact spindle probe allowed direct measurements of both the tool and workpiece to be obtained from within the machine tool environment. These collected measurements, as a result of utilising the two

systems, allowed control of the wear test to be automated, alongside their primary role of monitoring a DCB's wear. Within any study utilising wear tests, a trade-off has to be made between the temporal resolution of the acquired wear measurements and the expense of both cycle and operator time to conduct the measurements. As such, the number of direct tool measurements conducted during wear studies often limits the predictive capability of any developed TCM approach. Therefore, an aim of the developed wear test methodology was to enable a high number of direct wear measurements to be obtained over the course of a tool's lifetime, allowing more accurate TCM approaches to be achieved and validated. Due to the inspection phase consuming over 83 % of each cycle of a wear test, automating process control was essential to ensure wear tests could continue uninterrupted outside working hours of the machine shop.

Wear test automation also required the implementation of a stopping criterion, to prevent erroneous measurements or damage to the JD machine, after the DCB had failed. A reduction in DCB length of $\geq$0.5 mm, measured during the NC4 inspection cycle, was determined to be appropriate for an automated stopping criterion. Crucially, this criterion was dependent on a DCB's length not radius, ensuring the maximal amount of data was captured relating to the radial wear of each DCB. Thus, ensuring the DCB's final passes prior to failure were captured within the AE dataset. A downside of this approach, however, was that each wear test typically ended destructively after the DCB had failed, leaving no DCB to analyse after the test.

Through all wear tests, AE was acquired continuously at a 2 MHz sampling rate, triggered through the g-code, to capture the entire grinding pass. A MISTRAS WD sensor was bonded to the top face of the SiC workpiece throughout each wear test, minimising signal attenuation whilst still enabling easy installation. Importantly, prior to each wear test the AE sensor's response was verified through PLBs, as well as also re-surfacing the SiC workpiece with a sacrificial DCB. Furthermore, the impact of background noise from a variety of environmental and machine related sources was also quantified, the results of which are presented fully in Section 3.5.2. Across all the noise scenarios, the machine's coolant was seen to generate the most significant noise, resulting in an $AE_{AMP} = 60\,\mathrm{dB_{AE}}$,

but is still seen to have negligible effect on the acquired AE.

A NIKKEN BT30-SZF10-90 zero-fit specialised toolholder, capable of adjusting a tool's $r_{runout}$, was employed to allow a systematic investigation of the effect a DCB's $r_{runout}$. Unlike other studies aiming to quantify the effect of $r_{runout}$, discussed in Section 2.1.4, the use of the NIKKEN toolholder enabled the $r_{runout}$ of a DCB to be varied continuously between $0-80\,\mu m$, whilst not introducing a highly unbalanced load onto the machine spindle, as seen through the use of an adjustable boring head. Additionally, the non-contact nature of NC4 tool measurements, allowed the $r_{runout}$ to be measured precisely on the plated Ni-diamond abrasive layer of each DCB, ensuring all causes of runout were accounted for. When adjusting the $r_{runout}$ of a DCB, measurements were conducted at multiple axial positions up the length of a DCB, to ensure the tilt term of $r_{runout}$ was minimal.

## 6.2 Wear Test Series

In total, 22 wear tests were conducted utilising the methodology detailed in Chapter 3, generating a large dataset of both AE and inspection data relating to DCB wear. Throughout this thesis three main testing series were completed; feasibility (Section 4.1.1), runout variation (Section 4.1.2), and control (Section 4.1.3). Each contributing to the understanding of wear mechanisms that a DCB experiences and aiding the development of an AE-based TCM approach.

Both the 2D and 3D (when implemented) NC4 tool scans allowed visualisation and tracking of the wear each DCB experienced. Through which, isolated regions, void of any Ni-diamond abrasive layer, were seen to develop over time. Which, with further wear, then formed surface craters spanning a large proportion of the DCB's circumference. Depending on the $r_{runout}$ level of the specific DCB, these craters either expanded radially or axially. In turn, leading to bands or strips of the DCB being removed from the grinding altogether and wearing below the mean surface height. This localised loss of grinding capability occurred during phase II - steady-state of each DCB's life, as the singular layer

of diamond grains within the Ni bond layer started to wear away. Once developed across a DCB's surface, the wear of surrounding areas accelerated due to a reduction in active cutting grains. Leading the formation of surface craters to be a good indicator of a DCB soon to transition into phase III - wear-out.

All DCBs were seen to follow the three-phase wear cycle of I - wear-in, II - steady-state, and III - wear-out. The $r_{mean}$ of each DCB throughout its respective wear test, is the wear metric most capable of showing this trend, following the expected wear curve of tooling. With $r_{mean}$ showing distinct decreases in gradient at the beginning and end of each tool's life, matching with the theoretical increased wear rate due to phases I and III. Separated by a region of slow but consistent radial wear, spanning the majority of each DCB's life, as a result of phase II - steady-state. Hence explaining, why $r_{mean}$ is the most suitable metric for the regression models target, as a representation of the overall RUL of a DCB. However, during the runout variation series a limitation of the NC4 system was encountered when measuring the DCBs with a "high" level of runout, leading to the $r_{mean}$ values potentially being restricted. Due to the fixed size of the NC4 laser beam and the extreme level of $r_{runout}$, the low side of the DCBs did not obscure the beam, therefore registering as empty space and setting the radius to the lower limit. Despite this, due to the majority of the tool's surface still being measured, importantly including the DCB high spot, the NC4 measurements were still useful and tracked the DCBs wear progression, albeit presenting a very different trend due to the increased $r_{runout}$.

In addition to the NC4 tool measurements, the OMP600 monitored a DCB's material removal from the SiC workpiece, producing a measure of $a_e'$ after every grinding pass. Results from the OMP600 $a_e'$ measurements complemented the NC4 tool wear data, relating the wear of a DCB to its actual grinding output, seen through the geometric deviation from the programmed $a_e$. A distinct "n" shaped curve was observed within the $a_e'$ measurements, shown in Fig. 4.25, matching the three-phase wear process seen in the NC4 tool wear measurements. These results provided additional confirmation that the DCBs underwent the theoretical and observed three-phase wear cycle, by detailing the effect each phase has on the tool's grinding capability. During phase I - wear-in of a DCB's life,

the DCB experiences rapid radial wear, whereby superfluous Ni bond material or weakly adhered diamond grains are removed from the DCB's surface. This effect is also seen through the DCB slowly building up to removing the programmed $a_e$ within the first few measurements of $a'_e$, indicating that initially the workpiece is grinding the DCB. Until, the DCB has undergone sufficient wear, exposing enough abrasive grains with adequate bond strength and protrusion, to grind the programmed $a_e$ from the workpiece. Similar alignment between the OMP600 $a'_e$ measurements and the hypothesised interaction between tool and workpiece, can also be seen across both phases II and III of a DCB's life.

A large concern, when using these DCBs, is defining the point at which a DCB is no longer useful, to continue grinding. Unlike in the NC4 $r_{mean}$ measurements, the OMP600 measurements of $a'_e$ presents a clear transition point between each DCB wear phase. Allowing a simple definition to be made, of when a DCB has reached phase III - wear-out, based on its ability to remove workpiece material to tolerance. However, whether this transition point between phase II and III is the ideal stopping point is unclear and application dependent. Whilst the DCB may be capable of still removing the asked $a_e$, meeting a defined geometric tolerance, it may not meet the surface roughness tolerance set by a manufacturer. No method of implementing surface roughness measurements in an automated manner was deemed suitable for this application, and as such a large improvement to the wear test methodology could be found through their inclusion. An additional example of this complexity in deciding a stopping point, can be seen through the measurements of $a'_e$ from DCBs with a "high" level of $r_{runout}$, in Fig. 4.31. Within each of the three wear tests conducted at this level of $r_{runout}$, the $a'_e$ reduced by $\sim$2.5 µm during the DCBs' phase II -steady-state. This decrease in $a'_e$, as a result of each DCB's high spot wearing fully, indicates a significant geometric error being imparted onto the workpiece with potentially degraded surface quality. Despite these manufacturing errors, the DCB could still be deemed useful for particular applications, as it is still capable of grinding the SiC workpiece, seen by each DCB continuing to grinding for at least another 30 passes. One such application would be roughing operations, aiming to remove a larger amount of workpiece material with a DCB, prior to a more tightly toleranced finishing operation

to bring a component to specification. As a result, the TCM approaches in this work have not been aimed to determine when a DCB is no longer useful to a manufacturer, but rather developing methods to provide a user with greater information about the current state of wear. Enabling the developed TCM approaches to be adapted for use within other grinding operations utilising DCBs.

Having been identified across the initial four wear tests of the feasibility series, a DCB's $r_{runout}$ was seen to have a large effect on the development of a DCB's wear. To investigate this further, 12 wear tests were completed within the runout variation series. In which a NIKKEN adjustable toolholder was utilised to set each DCB's $r_{runout}$ to a prescribed level prior to the start of each wear test. Three levels of DCB $r_{runout}$ were defined for investigation across the range of feasible values; "low" at $<15\,\mu m$, "medium" between $25-35\,\mu m$, and "high" between $75-80\,\mu m$. Through which the effects of $r_{runout}$ on the tool's life and wear mechanisms, as well as the generated AE from grinding, were isolated and verified.

Across the runout variation series, a significant increase in variability of a DCB's total life is observed, with increasing levels of initial DCB $r_{runout}$. An increase in range from 16 to 99 passes was seen when increasing a DCB's $r_{runout}$ from the "low" to "high" level. Furthermore, increasing a DCB's $r_{runout}$ from the "low" to "medium" level resulted in a decrease in total life by 39 % on average. Both of these changes to the overall grinding life of a DCB due to increasing $r_{runout}$ are significant to their usage within manufacturing. Perhaps more obviously of which, is the effect of reducing the average number of passes completed by a DCB, in effect increasing the tooling cost for every manufactured part. But the increased variability associated with higher $r_{runout}$ levels, can lead to simple but widespread time-based tool replacement strategies requiring lower limits to prevent unexpected tool failure, thus drastically underutilising the majority of DCBs and increasing tool wastage. As such, without the evaluation and consideration of a DCB's $r_{runout}$ level, it is difficult to implement any basic tool replacement strategy whilst maintaining an acceptable level of efficiency. Adjusting the $r_{runout}$ of a DCB to $<15\,\mu m$ however, significantly improves the repeatability of a DCB wear cycle. Therefore, allowing a con-

fidence interval based method to be used, with minimal wastage and a lowered chance of unexpected failure, for a tool replacement strategy. Even without the ability for $r_{runout}$ adjustment or direct measurements, an indication of the DCB's runout can provide significant contextual information about the wear mechanisms and collected indirect sensor signals. The importance of $r_{runout}$ for manufacturing with small diameter DCBs is critical, and amplified when considering these DCBs are not suitable for corrective dressing, prior to their usage.

However, it is important to also highlight the inherent variation in a DCB's total life, despite its level of $r_{runout}$. DCBs at a "low" level of runout still exhibited a range of 16 passes, with the control series wear tests resulting in a range of 10 passes. Which due to the consistent methodology, was seen to the result of varying DCB wear rates, stemming from the stochastic nature of DCB manufacture. Additionally, a 50 % reduction in overall life was observed across the five control series wear tests, explained in Section 4.1.3, to be the result of a lower quality batch of DCBs. Hence underscoring the importance of this work, to prevent wastage due to generic and conservative tool replacement strategies, but limit the necessity of expensive constant direct tool wear measurements.

Through the acquired AE during each grinding pass, the period of tool-workpiece contact is identifiable by sharp increases in amplitude of both the $AE_{raw}$ and rolling $AE_{RMS}$ signals, as seen in Fig. 4.4. Considering the DCB grit size of 15 µm (#1000) and the $a_e$ of 30 µm, the grinding pass is considered a fine operation, generating very low grinding forces. Regardless of the low grinding aggressiveness comparatively to other grinding operations, a good S/N of $>40\,\mathrm{dB_{AE}}$ is produced, as a result of the sensitivity of AE within the machine tool environment at the microscale. This sensitivity enabled the creation of a reliable trigger picking algorithm to isolate the grinding period based on the instantaneous amplitude from the signal's envelope, outlined in Section 3.5.3. Throughout this thesis a consistent AE sensor location, on the top of the workpiece, was used, preventing any effect of varying sensor location to be characterised. Sensor location is a crucial consideration for industrial implementation, in regard to both the signal attenuation and feasibility within a mass-manufacturing setup. Despite this, it

has been omitted from this work, due to both time constraints and the large number of other research works focusing on the area, showing minimal impact for TCM applications, detailed in Section 2.2.2.

In addition to its sensitivity, AE is capable of identifying a given DCB's $r_{runout}$ level by visualising the changing contact area between the workpiece and DCB. The $r_{runout}$ is identifiable through the periodic signal bursts within the $AE_{raw}$ signal, aligning with the rotational speed of the spindle. As seen in Fig. 4.33, AE is clearly effected by a DCB's $r_{runout}$. DCBs grinding with a "low" level of $r_{runout}$ generated a continuous $AE_{raw}$ signal throughout its rotation, as expected of a source producing overlapping transient AE signals. As $r_{runout}$ is introduced into the DCB's grinding process, a decreasing amount of the DCB's grinding surface will fully penetrate the workpiece as the tool rotates. Therefore, leading to the periodic burst of $AE_{raw}$ generated by DCBs at "medium" and "high" $r_{runout}$ levels. This observation led to the sectioning and alignment of the $AE_{raw}$ signals, based on the rotational speed of the DCB. Through which, the severity of a DCB's high spot and thus $r_{runout}$ level, is observed, and its subsequent wear monitored, as seen in Figs. 4.34–4.36. Visualisation of the AE over a single revolution of the spindle captured the progression of surface crater wear around the circumference of "high" $r_{runout}$ DCBs. Presenting a clear advantage of using AE over the NC4 system for measurements of higher $r_{runout}$ DCBs, due to the previously mentioned laser size limitations. With this technique, confirmation that the axial surface craters rejoined, having expanded around the entire DCB circumference, a result that was only suggested through both the 2D and 3D NC4 measurements.

The runout variation series allowed for detailed analysis into the effect $r_{runout}$ plays on the generated AE from a DCB. Clear changes were observed, mainly presenting as a change from continuous $AE_{raw}$ to a more burst-like periodic signal. However, these distinct changes also enable a visualisation technique to be employed, allowing a DCB's $r_{runout}$ level to be estimated, and tracking of axial surface crater wear progression. Overall, when utilising a TCM approach based on AE, the signal changes stemming from a DCB's $r_{runout}$ could lead to premature tool replacement without the knowledge of these effects, further

increasing the existing tool-life wastage. However, with greater understanding of the process and the correct implementation of processing techniques it could also potentially allow for an on-machine, indirect and passive sensing methodology of determining a DCB's $r_{runout}$ and monitoring its wear simultaneously.

Alongside this utilisation of the $AE_{raw}$ signals, simpler AE features were extracted during each grinding pass for investigation. A range of AE time-domain features and frequency-domain partial powers were calculated, aiming to identify features correlating to DCB wear metrics with reduced computational expense.

Of the time-domain features, $AE_{kurt}$ is observed to be an indicator of a DCB's $r_{runout}$, also signifying the point of surface crater formation. Kurtosis, as a measure of a distributions "tailedness", signifies how continuous the $AE_{raw}$ signals are, explaining why the $AE_{kurt}$ of a "high" $r_{runout}$ DCB is considerably greater. The $AE_{kurt}$ throughout a wear test, starts very high, falling to a baseline level during phase I - wear-in, where the baseline level then indicates the severity of the tool's $r_{runout}$. As each DCB wears further, the $AE_{kurt}$ then slowly decreases, suggesting the DCB is wearing into a more circular form, producing a more continuous AE signal. However, once a surface crater has formed, a large increase in $AE_{kurt}$ occurs, due to the reduced tool-workpiece contact. Overall, $AE_{kurt}$ is a highly useful AE feature, providing contextual information about the current DCB wear state. But, whilst the changing baseline levels and scaling increases of the $AE_{kurt}$ align with the DCB's $r_{runout}$, it also makes it difficult to set reliable thresholds for TCM approaches.

Complementing $AE_{kurt}$ as a wear metric for TCM, the $AE_{RMS}$ time-domain feature is seen to be an indicator of the grinding aggressiveness across the entire pass completed by a DCB. Much like $AE_{kurt}$, the DCB's level of $r_{runout}$ is also seen through the changing overall levels of $AE_{RMS}$, whilst not as linearly as seen in $AE_{kurt}$. Generally, when using "low" $r_{runout}$ DCBs, the $AE_{RMS}$ increases to a plateau during the tool's phase I - wear-in, shown in Fig. 4.41. After which large reductions in tool-workpiece contact, such as those seen from surface crater wear, result in large fluctuations in $AE_{RMS}$ depending on the overall tool wear state. However, akin to the problems of utilising $AE_{kurt}$, the varying

levels of $AE_{RMS}$ require both operator knowledge and input to extract useful information.

Through the use of a consistent type of AE sensor across the wear tests, a MISTRAS WD sensor, a consistent spectrum shape is produced. As such, variations in power across a DCB's life, within set frequency bands, seen in Fig. 4.12, are due to DCB wear and the resulting loss of tool-workpiece contact. A range of different $PP$s correlate well to the overall RUL of a DCB, indicated through the $r_{mean}$ metric. From the PSD, five frequency bands are seen to be of interest; 10, 35, 134, 350 and 900 kHz. Of particular note is $PP_{350}$, shown in Fig. 4.51, which shows very good correlation to both the DCB $r_{mean}$ and $a'_e$, allowing clear identification of the three DCB wear phases. Whilst not a concern across a single wear test due to the minimal material removed, source location has a clear effect at the higher end of the frequency range of the PSD. This effect is seen across the control series in Fig. 4.50, whereby tests 21 and 22 were conducted on a different and previously used workpiece, with the cutting surface considerably closer to the AE sensor location, resulting in less attenuation of the PSD above 250 kHz. Despite this effect, the trend of the $PP$s at the higher frequency ranges remaining consistent across the wear tests.

A short study into the effect grinding parameters play on the acquired AE signals was also conducted, presented in Section 4.2. Reduction of both the DCB's feedrate and spindle speed are seen to have a direct effect on the $AE_{raw}$ signals and extracted features. Initial results show that both $AE_{RMS}$ and $PP_{35}$ reduce in line with reductions in the feedrate, as a result of the lowered grinding forces, and spindle speed. Further work, including full wear tests at these parameters, should be carried out to conclusively determine the effect on developed TCM approaches. Similarly, prior to implementation of an AE-based TCM approach, analysis into the effect of different workpiece materials should also be conducted. As other workpiece materials could not only impact the characteristics or attenuation of acquired AE, but also how a DCB wears, a critical consideration when expanding this work to a wider application base.

## 6.3 TCM Approaches

To take advantage of the knowledge gained through the three testing series, two approaches were investigated for implementation as a TCM system; a threshold-based criterion approach utilising the correlating AE features, and the use of ANNs to determine the DCB $r_{mean}$, wear phase or $a'_e$ tolerance. Both approaches show promise for the TCM of DCBs, despite targetting different aspects of a DCB's wear with vastly different computational expenses.

Through the presented analysis of the wear test data in Chapter 4, multiple correlated AE features were found relating to a DCB's wear state. A common technique within AE monitoring, is the implementation of manually set thresholds indicating anomalies, damage, or oncoming failure. However, as discussed previously in Section 5.1, this threshold-based criterion approach was not suitable for use with the presented AE features, due to their volatile baseline levels. Therefore, to enable a static threshold to be used, two metrics were utilised derived from the absolute gradient of selected AE features.

The first metric, $|\nabla PP_{350}|$, shows the benefit of using the absolute gradient, transforming the AE feature into a consistent metric with a steady baseline across each DCBs' phase II - steady-state, with large increases seen resulting from both phases I and III. A static threshold of 0.175 was manually chosen based on the five control series wear tests, shown in Fig. 5.1, aiming to pick the transition from phase II to III of each DCB. Which, when evaluated over the twelve wear tests from the runout variation series, is capable of precisely pick the transition point no matter the level of $r_{runout}$. Despite its precision, due to the level of noise within the $|\nabla PP_{350}|$ metric, two of the twelve wear tests prematurely exceed the set threshold, leading to significant errors when compared to the true values seen in Appendix G. Furthermore, in order for this approach to work the initial grinding passes associated with each DCBs' phase I - wear-in, were required to be ignored to prevent further false triggers. This requirement, whilst reasonable, could prevent a TCM system utilising this approach from detecting failure during phase I - wear-in of a DCB's life. Which would limit this approach's use to DCBs known to have completed phase I -

wear-in.

To combat this limitation the second metric, $|\nabla(AE_{RMS} \cdot AE_{kurt})| \cdot n$, is calculated from the product of $AE_{RMS}$ and $AE_{kurt}$, but critically also employs $n$, the number of passes completed by the DCB at that point. The inclusion of $n$, greatly lowers the effect of the DCB's phase I - wear-in on the calculated metric. The use of $AE_{kurt}$ and $AE_{RMS}$ also reduces the overall noise prior to the transition point of interest, allowing a more accurate and reliable threshold to be chosen. Across the runout variation series, the picked point using $|\nabla(AE_{RMS} \cdot AE_{kurt})| \cdot n$, is seen to align with the formation of surface craters on the DCB surface, unlike the result seen using the $|\nabla PP_{350}|$ metric picking the transition between phases II and III. Additionally, with the $|\nabla(AE_{RMS} \cdot AE_{kurt})| \cdot n$ metric, no false triggers occurred and only three of the twelve wear tests had to have their phase I - wear-in ignored.

Overall, a threshold-based criterion approach is an effective method of reliably identifying a DCB's transition into phase III or the formation of surface craters. By using the five control series wear tests to set both static thresholds, validation of the technique is representative of a true scenario. Both metrics show very good precision, with only the $|\nabla PP_{350}|$ metric resulting in false triggers due to noise during a DCB's phase II - steady-state. Furthermore, whilst a DCB's $r_{runout}$ has a clear effect on the generated AE, it does not affect the capability of both metrics in this threshold-based approach. A major benefit of this approach is the reduced computational expense to implement and utilise in real-time. But prior to its implementation, significant time is required to develop the approach; finding correlating features within the AE, constructing reliable metrics through feature transformations, and choosing adequate thresholds. The presented threshold-based approaches, would be highly suited to indicate when more time-consuming direct measurements should be conducted, particularly using the $|\nabla(AE_{RMS} \cdot AE_{kurt})| \cdot n$ metric. Thus removing the need for periodic direct tool/workpiece measurements, and in turn reducing process downtime whilst still enabling minimal operator input. Additionally, more useful and informative features may exist, better suited to this task, enabling this simple threshold-based criterion approach to be further developed for particular applications. As

such the use of ML feature extraction techniques, such as principal component analysis or unsupervised autoencoders, could be utilised to great effect.

In addition to the threshold-based criterion approach, ANNs were also developed for TCM, leading to a regression and classification approach being investigated. All trained ANNs utilise the same nine AE features as inputs, aiming to predict either the DCB $r_{mean}$ within the regression models, the DCB wear phase or $a'_e$ tolerance with the classification models. A supervised approach was enabled through the large quantity of both NC4 tool wear and OMP600 $a'_e$ workpiece measurements. The final ANNs are all capable of generalising the AE input data sufficiently to predict with a low error, no matter the objective of the model. Despite the success of all the ANNs there are other ML and statistical techniques that could be investigated and found to outscore the presented approaches, with a lower computational expense or time cost.

Three architectures; a MLP, MLP-WIN, and LSTM, were optimised and evaluated for a supervised regression problem aiming to predict the DCB $r_{mean}$, representing the tool's RUL. Whilst each architecture is able to generalise and learn from the AE features, significant differences across the scoring metrics were observed, as presented in Table 5.5. The LSTM architecture shows a clear advantage in its predictive capability when compared to the other architectures, resulting in significantly better scores over the test dataset. This improved capability likely stemming from the complex recurrent nature of LSTMs, as laid out in Section 5.2.1, enabling significant improvements when utilising time-series data. One such advantage of an ANN that is able to consider the temporal nature of a TCM dataset, is that wear is linear in its progression, and as such a DCB's $r_{mean}$ will not increase with time. Therefore, not only does the LSTM architecture perform best with the maximal allowed input sequence length of 15, but it also is the most computationally expense architecture. During training, the LSTM models utilise significantly more computer memory and required approximately three times longer to train than the other optimised regression architectures.

Comparison between the MLP and MLP-WIN architectures shows a clear benefit to the inclusion of historical data, even when not utilising a RNN architecture, like the

LSTM. Whilst being a less complex model, consisting of three dense layers of 128 neurons in place of four, the MLP-WIN results in better prediction scores across both its training and test datasets. An additional benefit of the less complex architecture of the optimal MLP-WIN model, is a slight decrease in computational expense; whereby the increased input size is outweighed by the removal of a dense hidden layer. Overall, improvements are observed across predictions at the higher range of $r_{mean}$ values, seen in Fig. 5.16(a–b). Consequently, an MLP-WIN architecture is positioned as a notable enhancement to a standard MLP architecture, due to its reduced model complexity and enhanced scoring. Therefore, relegating the MLP architecture to be suboptimal, in light of the improved capability and cost-efficiency of an MLP-WIN model.

Of interest, a previously published work by this author [38], utilising the same regression ANN approach for the three architectures, but trained over a reduced dataset including only the feasibility testing series, resulted in an opposing finding. The outcome of the paper still presented LSTM as a superior architecture from a predictive standpoint, but showed the MLP as a more capable architecture when compared to an MLP-WIN. As alluded to in the work, and verified when trained on a larger dataset in this thesis, the architectures were likely limited by the small dataset size used at the time. Therefore, with a larger training dataset covering a broader range of $r_{mean}$ values, the ANNs presented in this thesis are more representative of the true capability of the architectures.

With regard to the implementation of a regression model for a TCM system, the choice between employing an MLP-WIN and an LSTM is a trade-off between predictive accuracy and computational expense. Where computational power is limited, such as on an edge device or within a machine controller, an MLP-WIN may be a suitable compromise on accuracy to enable a real-time prediction strategy. However, an LSTM model has lower predictive error across the whole range of $r_{mean}$ values when predicting on unseen input data, and therefore is the clear favourite where computationally affordable. Once trained, an LSTM could be utilised to enable a radius compensation routine within the machine controller, foregoing the need for direct tool radius measurements. Which, due to its low prediction errors, would prevent the reduction in $a'_e$ seen to occur midway through the

lives of both "medium" and "high" level $r_{runout}$ DCBs in Figs. 4.28 and 4.31.

As a result of the collected OMP600 $a_e'$ measurements during the runout variation and control testing series, a supervised classification approach was also enabled. From these workpiece measurements, two labelling methods were used; the first a multi-class method based on the DCB wear phases, and the second a binary classification dependent on the $a_e'$ measurements falling into a tolerance band ($30\pm1.5\,\mu m$). Both methods of labelling the dataset resulted in imbalanced distributions of class labels, seen in Table 5.6, with class 0 comprising just 3.52 % of the multi-class dataset. An MLP classification model trained for both supervised datasets, yields balanced accuracy scores across the unseen test dataset of 0.896 and 0.938 respectively. With each MLP's recall over the smaller sized classes resulting in the majority of their prediction errors.

Considering the imbalance of both classification approaches, both can be seen to have generalised well, resulting in good predictive capabilities. The binary classification MLP produces slight improvements to the CV scoring metric standard deviations, likely because of the less severe data imbalance between the two classes. Therefore, to combat the limitations of training with an imbalanced dataset, the multi-class approach could benefit from particular imbalanced classification techniques; this could include expansion of the dataset as a whole, weighting the loss function to focus on classes with lower dataset proportion [200], or even under/oversampling of the dataset to artificially even the class distributions [210]. Additionally, unlike the regression approaches detailed in Section 5.2.2, investigation of different ANN architectures or optimisation of the MLP was not conducted and as such, improvements to the predictive capabilities of both MLPs could be seen by tailoring the models for each labelling method.

Application specific improvements to the binary classification MLP were produced by optimising the classification threshold used to determine the predicted class from the softmax activated neuron's output. In this scenario whereby misclassifying a sample labelled as out of tolerance could result in unexpected tool failure and workpiece damage, the MLP's recall over class 1: out-tolerance is critical. As incorrect predictions of in tolerance samples would, at worst, prompt direct tool/workpiece measurements, a less

expensive impact on the overall process. Threshold moving to optimise the binary MLP's based on its ROC curve, seen in Fig. 5.20, not only yields a slight increase to its balanced accuracy, but crucially a large increase in its recall over class 1. Leading to a slight bias in predictive outcome towards class 1, but with no detrimental effect due to the given application.

Overall, whilst no optimisation occurred, both MLP approaches to enact TCM as a supervised classification problem are successful. The multi-class labelling approach enables the indirect prediction of a DCB's wear phase, potentially allowing more efficient use of each DCB's phase II - steady-state. Furthermore, tracking of phase I - wear-in of a DCB, could enable it to be conducted whilst grinding a sacrificial workpiece instead of a presumably expensive component. The binary labelling approach, based on the tolerancing of $a'_e$ measurements, could directly be utilised to minimise the required number of direct tool or workpiece measurements. In combination with the developed regression LSTM, a reliable but indirect tool wear compensation method could be implemented. Whereby, the binary MLP is used to determine when or if compensation is required, the LSTM could provide predictions for the updated values of tool radius and then the classification model could be used again for validation of the compensation. This methodology would take advantage of the significantly less complex MLP architecture used for both classification approaches during the majority of a DCB's life, only requiring the more computationally expensive LSTM model when indicated.

Moreover, the two labelling methods detailed in Section 5.2.1 to frame this work into a supervised classification approach, are by no means exhaustive or optimal for this application. Other labelling methods not investigated could include; binary classification for phase II - steady-state or any of the individual wear phases, identification of surface crater formation or even an unsupervised approach through the use of autoencoders or clustering. Additionally, due to the success of all the TCM avenues investigated across Chapter 5, the combination of approaches through the use of multi-output ANNs [211] or data fusion techniques [212, 213], could be employed to obtain further improvements or more useful outcomes for a TCM system.

# 7 Conclusion

This thesis investigated the use of AE, as an indirect and passive sensing method, to monitor and predict the wear state of DCBs during their use, with the aim of optimising tool replacement strategies, thus reducing wastage, improving cycle times, and preventing unexpected tool failure.

In order to achieve this aim, a wear test methodology was developed and implemented to systematically wear DCBs, whilst acquiring continuous AE throughout each grinding pass. Regular direct tool and workpiece measurements, conducted by two on-machine tool-setting and metrology systems, enabled tracking of each DCB's wear state to validate the developed AE-based approaches. The autonomous nature of this methodology enabled a large number of wear tests to be completed, under constant specifications. Therefore, allowing an investigation of DCB wear mechanisms, and quantification of the effect of DCB runout. Leading to the the development and validation of a range of AE-based prediction approaches for TCM.

This concluding chapter, first summaries the main contributions of this thesis, and then presents directions for future work, to further develop the presented research.

## 7.1 Contributions

The presented methodology in Chapter 3, used to autonomously wear DCBs, whilst acquiring both sensor signals (AE) and validation/wear monitoring measurements (NC4 and OMP600), is the backbone of this thesis. Without which, knowledge of DCB wear mechanisms would be unknown or invalidated, and the development of useful TCM approaches would not be possible. As identified through a review of current wear test meth-

odologies, detailed in Section 2.3, the use of manually operated inspection techniques to acquire direct tool wear measurements, leads to a low resolution view of a tool's continuous wear cycle. The use of an NC4 laser tool setter and an OMP600 contact spindle probe enabled direct measurements to be acquired after every grinding pass, resulting in the acquisition of a more accurate and continuous representation of a DCB's wear state. The developed inspection cycle included 2D NC4 tool surface scans and measurements of the $a'_e$ removed from the SiC workpiece, after every grinding pass, as well as a less frequent qualitative 3D NC4 tool scan of the whole DCB grinding surface. Wear of each DCB was conducted systematically through a repeated side-milling operation, with constant grinding parameters across all wear tests, focusing the monitoring methods solely on mechanisms of wear and not changing grinding conditions or aggressiveness. AE signals, generated by the tool-workpiece interaction, were acquired through a MISTRAS WD sensor coupled to the top face of the SiC workpiece. An NI DAQ system enabled the continuous acquisition of AE, at a sample rate of 2 MHz, throughout each grinding pass, having been triggered directly by the machine tool's g-code. Additionally, the use of a NIKKEN adjustable tool-holder, enabled the effect of a DCB's $r_{runout}$ to be quantified, through the removal or addition of $r_{runout}$ to a DCB prior to carrying out a wear test.

The implementation of this developed DCB wear test methodology, resulted in the completion of 22 wear tests, across three different testing series, as presented in Chapter 4. Each DCB was seen to follow the theoretical three-phase wear cycle of phase I - wear-in, phase II - steady-state, and phase III - wear-out. Further analysis of the inspection data, revealed a common wear mechanism experienced by all DCBs, in which large regions of the abrasive Ni-diamond layer were fully removed. Formation of these identified surface craters, results in the acceleration of wear rate across the remaining DCB surface. Variation was seen between the total life of DCBs of the same specification, despite being worn by the same methodology, which was deemed to be the result of the random nature of the Ni-diamond electroplating process. Increased DCB $r_{runout}$ led to the modification of the surface crater formation process, whereby the crater first expanded axially along the tool's high spot, prior to expanding around the circumference of the DCB. Additionally,

a large increase in variability of their failure points, was seen across DCBs with increased $r_{runout}$. From a range of 16 passes between the DCBs at a "low" level of $r_{runout}$, to 99 passes when utilising a DCB with a "high" level of $r_{runout}$.

Alongside the developed understanding of DCB wear mechanisms, analysis of the acquired AE in Chapter 4, presents multiple features and techniques to aid a TCM system. The high sensitivity of AE, even when grinding at the microscale, enables a reliable triggering process to isolate the period of tool-workpiece contact. From which, a range of AE features, extracted from both the time and frequency domain, correlate to different aspects of a DCB's wear. Certain partial powers from the PSD, align well with the overall wear of a DCB and time domain features, such as $AE_{kurt}$ and $AE_{RMS}$, indicate the level of $r_{runout}$ a DCB is grinding with. Validation, with the collected direct tool wear measurements, showed the AE features were indirectly capable of identifying the DCB's wear phase, $r_{runout}$ level, and the point of surface crater formation, no matter the DCB's level of $r_{runout}$. Additionally, through isolating the AE power during a single revolution, the wear of DCBs with "medium" and "high" $r_{runout}$ can be visualised throughout their life cycle. Enabling monitoring of surface crater formation and expansion to be captured indirectly.

Finally, the highlighted AE features were utilised in three TCM methods, to predict the wear state of a DCB in use, presented in Chapter 5. The first method, utilises a AE threshold-based criterion approach to indicate the point at which a DCB has reached phase III - wear-out or the initial formation point of surface craters. Two different metrics are calculated by transforming AE features into metrics suitable for a static threshold approach. Both metrics show a good level of precision when identifying these points of interest, with only two instances of false triggers across the runout variation series wear tests, used for validation. Importantly, this threshold-based criterion approach requires little computational power and therefore could be implemented in real-time, indicating when direct tool measurements should be conducted. In addition to the relatively simple threshold-based criterion method, more computationally expensive ANNs were also used, framing the TCM of a DCB as both a regression and classification problem. Three re-

gression ANN architectures, MLP, MLP-WIN, and LSTM, were optimised, trained and evaluated, aiming to predict the $r_{mean}$ of a DCB, from only AE features. All architectures are capable of generalising sufficiently to make good predictions over the held out test dataset, leading to RMSE errors of less than 3.408 µm. But, as a consequence of the LSTM's recurrent nature, enabling the consideration of the temporal nature of tool wear, the LSTM results in significantly improved predictive capabilities, yielding a RMSE of 1.407 µm across the unseen test dataset. However, due to the more complex architecture used by LSTM models, a considerable increase in computational expense when training an LSTM model is required. Alongside this regression approach, labelling of the acquired OMP600 $a'_e$ measurements enabled a supervised classification approach to be developed. Two methods of labelling the acquired dataset were investigated; the first a multi-class method based on the three DCB wear phases, and the second a binary method dependent on the $a'_e$ measurements falling within a tolerance band (30±1.5 µm). Despite the imbalanced nature of both labelled datasets, an MLP classification model trained for each approach, yields balanced accuracy scores of 0.896 and 0.938 respectively, across the test datasets. As a result of both the regression and classification ANNs success and predictive ability, a combination of all three approaches could enable an optimised tool replacement strategy to be employed without the requirement of time-consuming direct tool measurements. An outline of a potential strategy would be as follows: use of the binary classification MLP to determine when a DCB is no longer grinding to tolerance, a which point the LSTM regression ANN would predict an updated value for the DCB's radial offset within the g-code, to compensate for its wear, with the threshold-based criterion approach verifying the compensation is appropriate or if direct tool measurements are needed for confirmation. Simultaneously, maximising the usage of each DCB, reducing the required number of direct tool/workpiece measurements, and indicating the wear phase a DCB is undergoing preventing unexpected tool failures, solely through the indirect and passive AE generated during grinding.

## 7.2 Directions for Future Research

Despite the advancements in both the understanding of DCB wear mechanisms and development in AE-based TCM approaches, continuation of this research is required prior to its industrial implementation. Avenues for future work are divided into three key areas: implementation scenarios, methodology improvements, and TCM systems.

To validate the proposed AE-based TCM approaches for a wider variety of applications, a range of further wear test series could be investigated, isolating other variables. Future work could extend this research by evaluating the AE-based monitoring approach when grinding a wider range of workpiece materials, allowing assessment of how material properties influence AE generation and feature robustness. Further investigation into alternative AE sensor locations within the machine tool would help quantify the effects of structural damping, signal attenuation, and noise coupling on monitoring performance. Full wear-progression tests conducted under varied grinding parameters, such as spindle speed, feed rate, and depth of cut would clarify the sensitivity of AE features to process conditions and support the development of more adaptive models. Alongside this, additional studies should also examine how changes in DCB specification, including diameter, abrasive grain size, and tool form, affect AE and wear behaviour. With a larger aim of testing the framework across different grinding operations, tool paths, and real component-manufacturing scenarios, to provide insight into its robustness under more complex and transient engagement conditions. Finally, applying the methodology to a broader range of grinding machine tools would help determine its generalisability and identify any machine-specific considerations required for industrial deployment.

Improvements to the developed wear test methodology could further improve analysis of the acquired AE, which may be beneficial when conducting additional wear series, investigating other variables. These improvements consist of incorporating automated measurement of the workpiece's surface roughness to provide a more objective link between grinding performance, tool wear, and AE. Real-time adjustment of the NC4 macros to compensate for the DCB's runout would help ensure that all regions of the tool consistently

register within the laser beam, improving the reliability of diameter and wear measurements. The use of an on-machine camera or microscope would enable rapid qualitative checks of DCB condition during testing, offering a practical means of validating AE-based wear indicators. Additionally, integrating high-resolution imaging, such as SEM or optical microscopy, throughout the wear tests would allow direct observation of abrasive grain degradation, supporting a more in-depth understanding of the wear mechanisms.

Finally, investigations into the use of different ML approaches, other than those presented in this thesis, could also be conducted. Methods such as Gaussian processes for a statistical approach to the TCM problem, autoencoders to approach TCM as an unsupervised problem, or even CNNs to utilise time-frequency domain images as inputs. But, as well as different ML approaches and architectures, further work can be conducted to improve or further validate the existing TCM approaches. A focus on system-level integration by deploying the proposed TCM approaches directly onto an edge device or machine controller could be investigated. Therefore, enabling tighter coupling between monitoring outputs and machine behaviour. Real-time implementation of these methods during wear tests would also further demonstrate their responsiveness and suitability for in-process decision-making. The utilisation of regression LSTM models for in-process radius compensation, offering the potential to predict and correct tool geometry changes dynamically. Continued optimisation of the ANN classification architecture could improve diagnostic accuracy and reduce computational overhead, supporting more efficient on-machine deployment. Finally, combining the outputs of multiple TCM approaches presented, may yield a more robust and reliable monitoring framework.

# References


[1] I. D. Marinescu, B. Rowe, Y. Ling and H. G. Wobker, 'Chapter 3 - Abrasive Processes', in *Handbook of Ceramics Grinding and Polishing*, I. D. Marinescu, T. K. Doi and E. Uhlmann, Eds., Boston: William Andrew Publishing, 1st Jan. 2015, pp. 67–132. DOI: 10.1016/B978-1-4557-7858-4.00003-0.

[2] I. D. Marinescu, M. Hitchiner, E. Uhlmann, W. B. Rowe and I. Inasaki, *Handbook of Machining with Grinding Wheels* (Manufacturing Engineering And Materials Processing). Taylor & Francis Group, 2007.

[3] D. Zhu, 'Aerospace Ceramic Materials: Thermal, Environmental Barrier Coatings and SiC/SiC Ceramic Matrix Composites for Turbine Engine Applications', E-19506, 1st May 2018.

[4] S. Dhanasekar *et al.*, 'A Comprehensive Study of Ceramic Matrix Composites for Space Applications', *Advances in Materials Science and Engineering*, vol. 2022, no. 1, p. 6 160 591, 2022. DOI: 10.1155/2022/6160591.

[5] K. O. Shvydyuk, J. Nunes-Pereira, F. F. Rodrigues and A. P. Silva, 'Review of Ceramic Composites in Aeronautics and Aerospace: A Multifunctional Approach for TPS, TBC and DBD Applications', *Ceramics*, vol. 6, no. 1, pp. 195–230, 1 Mar. 2023. DOI: 10.3390/ceramics6010012.

[6] Z. Valdez-Nava, D. Kenfaui, M.-L. Locatelli, L. Laudebat and S. Guillemet, 'Ceramic substrates for high voltage power electronics: Past, present and future', in *2019 IEEE International Workshop on Integrated Power Packaging (IWIPP)*, Apr. 2019, pp. 91–96. DOI: 10.1109/IWIPP.2019.8799084.

[7] H. Matsunami, 'Fundamental research on semiconductor SiC and its applications to power electronics', *Proceedings of the Japan Academy, Series B*, vol. 96, no. 7, pp. 235–254, 2020. DOI: 10.2183/pjab.96.018.

[8] X.-F. Song, H.-T. Ren and L. Yin, 'Machinability of lithium disilicate glass ceramic in in vitro dental diamond bur adjusting process', *Journal of the Mechanical Behavior of Biomedical Materials*, vol. 53, pp. 78–92, 1st Jan. 2016. DOI: 10.1016/j.jmbbm.2015.08.003.

[9] J. Kelly and P. Benetti, 'Ceramic materials in dentistry: Historical evolution and current practice', *Australian Dental Journal*, vol. 56, no. s1, pp. 84–96, 2011. DOI: 10.1111/j.1834-7819.2010.01299.x.

[10] W. König, L. Cronjäger, G. Spur, H. K. Tönshoff, M. Vigneau and W. J. Zdeblick, 'Machining of New Materials', *CIRP Annals*, vol. 39, no. 2, pp. 673–681, 1st Jan. 1990. DOI: 10.1016/S0007-8506(07)63004-2.

[11] A. Choudhary and S. Paul, 'The wear mechanisms of diamond grits in grinding of alumina and yttria-stabilized zirconia under different cooling-lubrication schemes', *Wear*, vol. 454–455, p. 203 315, 15th Aug. 2020. DOI: 10.1016/j.wear.2020.203315.

[12] L. E. A. Sanchez, J. F. G. Oliveira and R. T. Coelho, 'Detection of cracks in scratching tests in ceramic materials through acoustic emission', *Proceedings of the Institution of Mechanical Engineers, Part B*, vol. 219, no. 9, pp. 685–693, 1st Sep. 2005. DOI: 10.1243/095440505X32616.

[13] M. S. Lan and D. A. Dornfeld, 'In-Process Tool Fracture Detection', *Journal of Engineering Materials and Technology*, vol. 106, no. 2, pp. 111–118, 1st Apr. 1984. DOI: 10.1115/1.3225684.

[14] T. F. De Barrena, J. L. Ferrando, A. García, X. Badiola, M. S. de Buruaga and J. Vicente, 'Tool remaining useful life prediction using bidirectional recurrent neural networks (BRNN)', *The International Journal of Advanced Manufacturing Technology*, vol. 125, no. 9, pp. 4027–4045, 1st Apr. 2023. DOI: 10.1007/s00170-023-10811-9.

[15] P. W. Prickett and C. Johns, 'An overview of approaches to end milling tool monitoring', *International Journal of Machine Tools and Manufacture*, vol. 39, no. 1, pp. 105–122, 1st Jan. 1999. DOI: 10.1016/S0890-6955(98)00020-0.

[16] P. Twardowski, M. Tabaszewski, M. Wiciak – Pikuła and A. Felusiak-Czyryca, 'Identification of tool wear using acoustic emission signal and machine learning methods', *Precision Engineering*, vol. 72, pp. 738–744, 1st Nov. 2021. DOI: 10.1016/j.precisioneng.2021.07.019.

[17] D. Dornfeld and H. G. Cai, 'An Investigation of Grinding and Wheel Loading Using Acoustic Emission', *Journal of Engineering for Industry*, vol. 106, no. 1, pp. 28–33, 1st Feb. 1984. DOI: 10.1115/1.3185907.

[18] V. Pandiyan and T. Tjahjowidodo, 'Use of Acoustic Emissions to detect change in contact mechanisms caused by tool wear in abrasive belt grinding process', *Wear*, vol. 436–437, p. 203 047, 15th Oct. 2019. DOI: 10.1016/j.wear.2019.203047.

[19] D. Y. Pimenov, L. R. Ribeiro da Silva, M. Kuntoğlu, B. S. Abrão, L. E. dos Santos Paes and E. Linul, 'Review of advanced sensor system applications in grinding operations', *Journal of Advanced Research*, 10th Jan. 2025. DOI: 10.1016/j.jare.2025.01.013.

[20] S. Kurada and C. Bradley, 'A review of machine vision sensors for tool condition monitoring', *Computers in Industry*, vol. 34, no. 1, pp. 55–72, 1st Oct. 1997. DOI: 10.1016/S0166-3615(96)00075-9.

[21] O. Ohnishi *et al.*, 'Chapter 4 - Grinding', in *Handbook of Ceramics Grinding and Polishing*, I. D. Marinescu, T. K. Doi and E. Uhlmann, Eds., Boston: William Andrew Publishing, 1st Jan. 2015, pp. 133–233. DOI: 10.1016/B978-1-4557-7858-4.00004-2.

[22] W. B. Rowe, '3 - Grinding Wheel Developments', in *Principles of Modern Grinding Technology (Second Edition)*, W. B. Rowe, Ed., Oxford: William Andrew Publishing, 1st Jan. 2014, pp. 35–62. DOI: 10.1016/B978-0-323-24271-4.00003-8.

[23] C. Wang, Y. Gong, J. Cheng, X. Wen and Y. Zhou, 'Fabrication and evaluation of micromill-grinding tools by electroplating CBN', *The International Journal of Advanced Manufacturing Technology*, vol. 87, no. 9, pp. 3513–3526, 1st Dec. 2016. DOI: 10.1007/s00170-016-8730-1.

[24] N. Pietrow, D. Curtis, H. Ghadbeigi, D. Novovic and J. McGourlay, 'An investigation into the challenges of the point grinding machining process', *Procedia CIRP*, 9th CIRP Conference on High Performance Cutting, vol. 101, pp. 190–193, 1st Jan. 2021. DOI: 10.1016/j.procir.2020.09.195.

[25] R. Teti, K. Jemielniak, G. O'Donnell and D. Dornfeld, 'Advanced monitoring of machining operations', *CIRP Annals*, vol. 59, no. 2, pp. 717–739, 1st Jan. 2010. DOI: 10.1016/j.cirp.2010.05.010.

[26] D. A. Dornfeld, Y. Lee and A. Chang, 'Monitoring of ultraprecision machining processes', *The International Journal of Advanced Manufacturing Technology*, vol. 21, no. 8, pp. 571–578, 2003. DOI: 10.1007/s00170-002-1294-2.

[27] I. Yesilyurt, A. Dalkiran, O. Yesil and O. Mustak, 'Scalogram-Based Instantaneous Features of Acoustic Emission in Grinding Burn Detection', *Journal of Dynamics, Monitoring and Diagnostics*, vol. 1, no. 1, pp. 19–28, 1 2022. DOI: 10.37965/jdmd.2021.49.

[28] S. H. Lee, 'Analysis of ductile mode and brittle transition of AFM nanomachining of silicon', *International Journal of Machine Tools and Manufacture*, vol. 61, pp. 71–79, 1st Oct. 2012. DOI: 10.1016/j.ijmachtools.2012.05.011.

[29] J. L. Ferrando Chacón, T. Fernández de Barrena, A. García, M. Sáez de Buruaga, X. Badiola and J. Vicente, 'A Novel Machine Learning-Based Methodology for Tool Wear Prediction Using Acoustic Emission Signals', *Sensors*, vol. 21, no. 17, p. 5984, 17 Jan. 2021. DOI: 10.3390/s21175984.

[30] M. Shah, V. Vakharia, R. Chaudhari, J. Vora, D. Y. Pimenov and K. Giasin, 'Tool wear prediction in face milling of stainless steel using singular generative adversarial network and LSTM deep learning models', *The International Journal of Advanced Manufacturing Technology*, vol. 121, no. 1, pp. 723–736, 1st Jul. 2022. DOI: 10.1007/s00170-022-09356-0.

[31] R. E. Haber, J. E. Jiménez, C. R. Peres and J. R. Alique, 'An investigation of tool-wear monitoring in a high-speed machining process', *Sensors and Actuators A: Physical*, vol. 116, no. 3, pp. 539–545, 29th Oct. 2004. DOI: 10.1016/j.sna.2004.05.017.

[32] X. Han and T. Wu, 'Analysis of acoustic emission in precision and high-efficiency grinding technology', *The International Journal of Advanced Manufacturing Technology*, vol. 67, no. 9, pp. 1997–2006, 1st Aug. 2013. DOI: 10.1007/s00170-012-4626-x.

[33] Z. Wang, P. Willett, P. R. DeAguiar and J. Webster, 'Neural network detection of grinding burn from acoustic emission', *International Journal of Machine Tools and Manufacture*, vol. 41, no. 2, pp. 283–309, 1st Jan. 2001. DOI: 10.1016/S0890-6955(00)00057-2.

[34] M. Yiming, Y. Zhonghua and Y. Zhensheng, 'Experimental investigation of correlation between attrition wear and features of acoustic emission signals in single-grit grinding', *The International Journal of Advanced Manufacturing Technology*, vol. 93, no. 5, pp. 2275–2287, 1st Nov. 2017. DOI: 10.1007/s00170-017-0687-1.

[35] P. Suya Prem Anand, N. Arunachalam and L. Vijayaraghavan, 'Evaluation of grinding strategy for bioceramic material through a single grit scratch test using force and acoustic emission signals', *Journal of Manufacturing Processes*, vol. 37, pp. 457–469, 1st Jan. 2019. DOI: 10.1016/j.jmapro.2018.12.006.

[36] D. Y. Pimenov, A. Bustillo, S. Wojciechowski, V. S. Sharma, M. K. Gupta and M. Kuntoğlu, 'Artificial intelligence systems for tool condition monitoring in machining: Analysis and critical review', *Journal of Intelligent Manufacturing*, vol. 34, no. 5, pp. 2079–2121, 1st Jun. 2023. DOI: 10.1007/s10845-022-01923-2.

[37] Y. Cheng, R. Guan, Y. Jin, X. Gai, M. Lu and Y. Ding, 'Research on intelligent tool condition monitoring based on data-driven: A review', *Journal of Mechanical Science and Technology*, vol. 37, no. 7, pp. 3721–3738, 1st Jul. 2023. DOI: 10.1007/s12206-023-0637-9.

[38] T. Jessel, C. Byrne, M. Eaton, B. Merrifield, S. Harris and R. Pullin, 'Tool condition monitoring of diamond-coated burrs with acoustic emission utilising machine learning methods', *The International Journal of Advanced Manufacturing Technology*, vol. 130, no. 3, pp. 1107–1124, 1st Jan. 2024. DOI: 10.1007/s00170-023-12700-7.

[39] T. Jessel, C. Byrne, M. J. Eaton and R. Pullin, 'The capability of Acoustic Emission features to monitor diamond-coated burr grinding wear and effectiveness', *e-Journal of Nondestructive Testing*, vol. 29, no. 10, 10 1st Oct. 2024. DOI: 10.58286/30231.

[40] T. Jessel, 'The monitoring of diamond-coated burrs with acoustic emission techniques', presented at the CIRP UK Meeting (Cardiff, UK), 23rd May 2024.

[41] T. Jessel, C. Byrne, M. Eaton, B. Merrifield and R. Pullin, 'Monitoring the effect of runout on a Diamond-Coated Burrs' wear progression with Acoustic Emission', *Wear*, vol. 584–585, p. 206 420, 15th Jan. 2026. DOI: 10.1016/j.wear.2025.206420.

[42] T. Jessel, C. Byrne, M. Eaton and R. Pullin, 'Predicting the wear state of diamond-coated burrs, using acoustic emission features and machine learning techniques', *Procedia CIRP*, [Accepted, Pending Publication],

[43] T. Jessel, 'A machine learning approach to tool state classification utilising in-process acoustic emission features', presented at the 65th Acoustic Emission Working Group (AEWG) Meeting (Chicago, USA), 14th May 2025.

[44] T. Jessel, C. Byrne, M. Eaton and R. Pullin, 'Utilising Machine Learning for Tool Condition Monitoring of Diamond-Coated Burrs with Acoustic Emission', presented at the BSSM 17th International Conference on Advances in Experimental Mechanics (Glasgow, UK), 31st Aug. 2023.

[45] D. K. Aspinwall, S. L. Soo, D. T. Curtis and A. L. Mantle, 'Profiled Superabrasive Grinding Wheels for the Machining of a Nickel Based Superalloy', *CIRP Annals*, vol. 56, no. 1, pp. 335–338, 1st Jan. 2007. DOI: 10.1016/j.cirp.2007.05.077.

[46] M. C. Shaw, *Principles of Abrasive Processing* (Oxford Series on Advanced Manufacturing). Oxford: Clarendon, 1996, vol. 13.

[47] C. A. Huang, C. H. Shen, W. Z. Huang, J. S. Lo and P. L. Lai, 'Grinding performance of electroplated diamond tools strengthened with Cr-C deposit using D-150 diamond particles', *The International Journal of Advanced Manufacturing Technology*, vol. 121, no. 7, pp. 4549–4558, 1st Aug. 2022. DOI: 10.1007/s00170-022-09604-3.

[48] T. Bergs and F. Klocke, 'Electroplating', in *Manufacturing Processes 3: Electrical Discharge Machining, Electrochemical Manufacturing and Beam Processes*, T. Bergs and F. Klocke, Eds., Berlin, Heidelberg: Springer, 2025, pp. 243–256. DOI: 10.1007/978-3-662-70580-3_5.

[49] C. A. Huang, S. W. Yang, C. H. Shen, K. C. Cheng, H. Wang and P. L. Lai, 'Fabrication and evaluation of electroplated Ni–diamond and Ni–B–diamond milling tools with a high density of diamond particles', *The International Journal of Advanced Manufacturing Technology*, vol. 104, no. 5, pp. 2981–2989, 1st Oct. 2019. DOI: 10.1007/s00170-019-04174-3.

[50] E. C. Lee and J. W. Choi, 'A study on the mechanism of formation of electrocodeposited Ni–diamond coatings', *Surface and Coatings Technology*, vol. 148, no. 2, pp. 234–240, 3rd Dec. 2001. DOI: 10.1016/S0257-8972(01)01352-4.

[51] H. Zhou, N. Du, L. Zhu, J. Shang, Z. Qian and X. Shen, 'Characteristics investigation of Ni-diamond composite electrodeposition', *Electrochimica Acta*, vol. 151, pp. 157–167, 1st Jan. 2015. DOI: 10.1016/j.electacta.2014.10.122.

[52] I. D. Marinescu, W. B. Rowe, B. Dimitrov and I. Inasaki, *Tribology of Abrasive Machining Processes*. William Andrew Publishing, 2004, vol. 1.

[53] Y. Lyu, H. Yu, J. Wang, G. Zhao and Z. Liu, 'Improved performance of electroplated grinding wheels using a new method of controlled grain size sorting', *Journal of Manufacturing Processes*, vol. 30, pp. 336–342, 1st Dec. 2017. DOI: 10.1016/j.jmapro.2017.10.004.

[54] B. Li *et al.*, 'Ultrasonic-assisted electrodeposition of Ni/diamond composite coatings and its structure and electrochemical properties', *Ultrasonics Sonochemistry*, vol. 73, p. 105 475, 1st May 2021. DOI: 10.1016/j.ultsonch.2021.105475.

[55] C. Feng, Z. Cui, Y. Zhang and T. Yang, 'Electroplating technology of suspended diamond particles surface based on rotating electrode', *Diamond and Related Materials*, vol. 128, p. 109 270, 1st Oct. 2022. DOI: 10.1016/j.diamond.2022.109270.

[56] X. Shen, X. Wang and F. Sun, 'Fabrication and evaluation of monolayer diamond grinding tools by hot filament chemical vapor deposition method', *Journal of Materials Processing Technology*, vol. 265, pp. 1–11, 1st Mar. 2019. DOI: 10.1016/j.jmatprotec.2018.10.001.

[57] D. Bhaduri, R. Kumar, A. K. Jain and A. K. Chattopadhyay, 'On tribological behaviour and application of TiN and MoS2-Ti composite coating for enhancing performance of monolayer cBN grinding wheel', *Wear*, vol. 268, no. 9, pp. 1053–1065, 25th Mar. 2010. DOI: 10.1016/j.wear.2010.01.013.

[58] Nickel Institute. 'Nickel Plating Handbook'. (2023), [Online]. Available: https://nickelinstitute.org/en/library/publications/nickel-plating-handbook-en/ (visited on 10/06/2025).

[59] A. Karimzadeh, M. Aliofkhazraei and F. C. Walsh, 'A review of electrodeposited Ni-Co alloy and composite coatings: Microstructure, properties and applications', *Surface and Coatings Technology*, vol. 372, pp. 463–498, 25th Aug. 2019. DOI: 10.1016/j.surfcoat.2019.04.079.

[60] L. Wang, Y. Gao, H. Liu, Q. Xue and T. Xu, 'Effects of bivalent Co ion on the co-deposition of nickel and nano-diamond particles', *Surface and Coatings Technology*, vol. 191, no. 1, pp. 1–6, 1st Feb. 2005. DOI: 10.1016/j.surfcoat.2004.03.047.

[61] M. Pushpavanam, H. Manikandan and K. Ramanathan, 'Preparation and characterization of nickel–cobalt-diamond electro-composites by sediment co-deposition', *Surface and Coatings Technology*, vol. 201, no. 14, pp. 6372–6379, 2nd Apr. 2007. DOI: 10.1016/j.surfcoat.2006.12.004.

[62] Y. Liang, Y.-S. Li, Q.-Y. Yu, Y.-X. Zhang, W.-j. Zhao and Z.-X. Zeng, 'Structure and wear resistance of high hardness Ni-B coatings as alternative for Cr coatings', *Surface and Coatings Technology*, vol. 264, pp. 80–86, 25th Feb. 2015. DOI: 10.1016/j.surfcoat.2015.01.016.

[63] X. Fang, G. Jin, X. F. Cui and J. N. Liu, 'Evolution characteristics of residual stress in metastable Ni-B alloy coatings identified by nanoindentation', *Surface and Coatings Technology*, vol. 305, pp. 208–214, 15th Nov. 2016. DOI: 10.1016/j.surfcoat.2016.08.042.

[64] C. A. Huang, C. H. Shen, C. J. Lee, H. Wang and P. L. Lai, 'Grinding performances of electroplated Ni–B-diamond tools prepared through composite electroplating with intermittent stirring', *The International Journal of Advanced Manufacturing*

*Technology*, vol. 124, no. 5, pp. 1891–1903, 1st Jan. 2023. DOI: 10.1007/s00170-022-10574-9.

[65] T. Suzuki and T. Konno, 'Improvement in tool life of electroplated diamond tools by Ni-based carbon nanotube composite coatings', *Precision Engineering*, vol. 38, no. 3, pp. 659–665, 1st Jul. 2014. DOI: 10.1016/j.precisioneng.2014.03.003.

[66] B. Azarhoushang and A. Daneshi, '13 - Mechanisms of tool wear', in *Tribology and Fundamentals of Abrasive Machining Processes (Third Edition)*, B. Azarhoushang, I. D. Marinescu, W. Brian Rowe, B. Dimitrov and H. Ohmori, Eds., William Andrew Publishing, 1st Jan. 2022, pp. 539–554. DOI: 10.1016/B978-0-12-823777-9.00020-3.

[67] M. J. Jackson and M. P. Hitchiner, 'Abrasive Tools and Bonding Systems', in *Machining with Abrasives*, M. J. Jackson and J. P. Davim, Eds., Boston, MA: Springer US, 2011, pp. 1–77. DOI: 10.1007/978-1-4419-7302-3_1.

[68] W. B. Rowe, '5 - Wheel Contact and Wear Effects', in *Principles of Modern Grinding Technology (Second Edition)*, W. B. Rowe, Ed., Oxford: William Andrew Publishing, 1st Jan. 2014, pp. 83–99. DOI: 10.1016/B978-0-323-24271-4.00005-1.

[69] S. Malkin and N. H. Cook, 'The Wear of Grinding Wheels: Part 2—Fracture Wear', *Journal of Engineering for Industry*, vol. 93, no. 4, pp. 1129–1133, 1st Nov. 1971. DOI: 10.1115/1.3428052.

[70] A. Ghosh and A. K. Chattopadhyay, 'Performance enhancement of single-layer miniature cBN wheels using CFUBMS-deposited TiN coating', *International Journal of Machine Tools and Manufacture*, vol. 47, no. 12, pp. 1799–1806, 1st Oct. 2007. DOI: 10.1016/j.ijmachtools.2007.04.008.

[71] Z. Shi and S. Malkin, 'Wear of Electroplated CBN Grinding Wheels', *Journal of Manufacturing Science and Engineering*, vol. 128, no. 1, pp. 110–118, 5th Jul. 2005. DOI: 10.1115/1.2122987.

[72] W. B. Rowe, '4 - Grinding Wheel Dressing', in *Principles of Modern Grinding Technology (Second Edition)*, W. B. Rowe, Ed., Oxford: William Andrew Publishing, 1st Jan. 2014, pp. 63–82. DOI: 10.1016/B978-0-323-24271-4.00004-X.

[73] E. J. Krabacher, 'Factors Influencing the Performance of Grinding Wheels', *Journal of Engineering for Industry*, vol. 81, no. 3, pp. 187–199, 1st Aug. 1959. DOI: 10.1115/1.4008296.

[74] H. Grisbrook, R. H. Hollier and P. G. Varley, 'Related Patterns of Grinding Forces, Wheel Wear and Surface Finish', *International Journal of Production Research*, vol. 1, no. 3, pp. 57–74, 1st Jan. 1961. DOI: 10.1080/00207546108943089.

[75] T. W. Hwang, C. J. Evans, E. P. Whitenton and S. Malkin, 'High Speed Grinding of Silicon Nitride With Electroplated Diamond Wheels, Part 1: Wear and Wheel Life', *Journal of Manufacturing Science and Engineering*, vol. 122, no. 1, pp. 32–41, 1st Jun. 1999. DOI: 10.1115/1.538908.

[76] T. Liao, K. Li, S. McSpadden and L. O'Rourke, 'Wear of diamond wheels in creep-feed grinding of ceramic materials I. Mechanisms', *Wear*, vol. 211, no. 1, pp. 94–103, 1st Oct. 1997. DOI: 10.1016/S0043-1648(97)00075-6.

[77] W. B. Rowe, '17 - Mechanics of Abrasion and Wear', in *Principles of Modern Grinding Technology (Second Edition)*, W. B. Rowe, Ed., Oxford: William Andrew Publishing, 1st Jan. 2014, pp. 349–379. DOI: 10.1016/B978-0-323-24271-4.00017-8.

[78] N. Pietrow, D. Curtis, D. Novovic, J. McGourlay and H. Ghadbeigi, 'Evolution of Electroplated Cubic Boron Nitride Tool Surface Texture Parameters During Point Grinding', *Journal of Manufacturing Science and Engineering*, vol. 144, no. 121007, 25th Aug. 2022. DOI: 10.1115/1.4054990.

[79] A. Attanasio, 'Tool Run-Out Measurement in Micro Milling', *Micromachines*, vol. 8, no. 7, 2017. DOI: 10.3390/mi8070221.

[80] X. Zhang, K. F. Ehmann, T. Yu and W. Wang, 'Cutting forces in micro-end-milling processes', *International Journal of Machine Tools and Manufacture*, vol. 107, pp. 21–40, 1st Aug. 2016. DOI: 10.1016/j.ijmachtools.2016.04.012.

[81] E. Diez, H. Perez, M. Guzman and A. Vizan, 'An improved methodology for the experimental evaluation of tool runout in peripheral milling', *The International Journal of Advanced Manufacturing Technology*, vol. 65, no. 1, pp. 283–293, 1st Mar. 2013. DOI: 10.1007/s00170-012-4168-2.

[82] J. Badger, S. Murphy and G. O'Donnell, 'The effect of wheel eccentricity and run-out on grinding forces, waviness, wheel wear and chatter', *International Journal of Machine Tools and Manufacture*, vol. 51, no. 10, pp. 766–774, 1st Oct. 2011. DOI: 10.1016/j.ijmachtools.2011.06.006.

[83] J. Baumann, T. Siebrecht, P. Wiederkehr and D. Biermann, 'The effect of runout errors on process forces and tool wear', *Procedia CIRP*, 12th CIRP Conference on Intelligent Computation in Manufacturing Engineering, 18-20 July 2018, Gulf of Naples, Italy, vol. 79, pp. 39–44, 1st Jan. 2019. DOI: 10.1016/j.procir.2019.02.008.

[84] K. Li, K. Zhu and T. Mei, 'A generic instantaneous undeformed chip thickness model for the cutting force modeling in micromilling', *International Journal of Machine Tools and Manufacture*, vol. 105, pp. 23–31, 1st Jun. 2016. DOI: 10.1016/j.ijmachtools.2016.03.002.

[85] M. E. Nakai, P. R. Aguiar, H. Guillardi, E. C. Bianchi, D. H. Spatti and D. M. D'Addona, 'Evaluation of neural models applied to the estimation of tool wear in the grinding of advanced ceramics', *Expert Systems with Applications*, vol. 42, no. 20, pp. 7026–7035, 15th Nov. 2015. DOI: 10.1016/j.eswa.2015.05.008.

[86] Z. Si, S. Si and D. Mu, 'Precision forecasting of grinding wheel Wear: A TransBi-GRU model for advanced industrial predictive maintenance', *Measurement*, vol. 234, p. 114 859, 1st Jul. 2024. DOI: 10.1016/j.measurement.2024.114859.

[87] J. V. Abellan-Nebot and F. Romero Subirón, 'A review of machining monitoring systems based on artificial intelligence process models', *The International Journal of Advanced Manufacturing Technology*, vol. 47, no. 1, pp. 237–257, 1st Mar. 2010. DOI: 10.1007/s00170-009-2191-8.

[88] E. T. Lee, Z. Fan and B. Sencer, 'Estimation of cBN grinding wheel condition using image sensor', *Procedia Manufacturing*, 49th SME North American Manufacturing Research Conference (NAMRC 49, 2021), vol. 53, pp. 286–292, 1st Jan. 2021. DOI: 10.1016/j.promfg.2021.06.031.

[89] E. T. Lee, Z. Fan and B. Sencer, 'Real-time Grinding Wheel Condition Monitoring Using Linear Imaging Sensor', *Procedia Manufacturing*, Proceedings of the 8th International Conference on Through-Life Engineering Services – TESConf 2019, vol. 49, pp. 139–143, 1st Jan. 2020. DOI: 10.1016/j.promfg.2020.07.009.

[90] H. B. Hübner *et al.*, 'A comparative study of two indirect methods to monitor surface integrity of ground components', *Structural Health Monitoring*, vol. 19, no. 6, pp. 1856–1870, 1st Nov. 2020. DOI: 10.1177/1475921720903442.

[91] V. Pandiyan, S. Shevchik, K. Wasmer, S. Castagne and T. Tjahjowidodo, 'Modelling and monitoring of abrasive finishing processes using artificial intelligence techniques: A review', *Journal of Manufacturing Processes*, vol. 57, pp. 114–135, 1st Sep. 2020. DOI: 10.1016/j.jmapro.2020.06.013.

[92] J. A. Couey, E. R. Marsh, B. R. Knapp and R. R. Vallance, 'In-process force monitoring for precision grinding semiconductor silicon wafers', *International Journal of Manufacturing Technology and Management*, vol. 7, no. 5–6, pp. 430–440, Jan. 2005. DOI: 10.1504/IJMTM.2005.007695.

[93] T. W. Hwang, C. J. Evans and S. Malkin, 'High Speed Grinding of Silicon Nitride With Electroplated Diamond Wheels, Part 2: Wheel Topography and Grinding Mechanisms', *Journal of Manufacturing Science and Engineering*, vol. 122, no. 1, pp. 42–50, 1st Jun. 1999. DOI: 10.1115/1.538909.

[94] A. Gouarir, G. Martínez-Arellano, G. Terrazas, P. Benardos and S. Ratchev, 'In-process Tool Wear Prediction System Based on Machine Learning Techniques and Force Analysis', *Procedia CIRP*, 8th CIRP Conference on High Performance Cutting (HPC 2018), vol. 77, pp. 501–504, 1st Jan. 2018. DOI: 10.1016/j.procir.2018.08.253.

[95] E. Sauter, E. Sarikaya, M. Winter and K. Wegener, 'In-process detection of grinding burn using machine learning', *The International Journal of Advanced Manufacturing Technology*, vol. 115, no. 7–8, pp. 2281–2297, Aug. 2021. DOI: 10.1007/s00170-021-06896-9.

[96] E. Brazel, R. Hanley and G. E. O'Donnell, 'The effects of process parameters on spindle power consumption in abrasive machining of CoCr alloy', *Journal of machine Engineering*, vol. 11(4), pp. 59–69, 2011.

[97] M. Hacksteiner, H. Peherstorfer and F. Bleicher, 'Energy efficiency of state-of-the-art grinding processes', *Procedia Manufacturing*, vol. 21, pp. 717–724, 2018. DOI: 10.1016/j.promfg.2018.02.176.

[98] Y. Wang, J. Xiang, R. Markert and M. Liang, 'Spectral kurtosis for fault detection, diagnosis and prognostics of rotating machines: A review with applications', *Mechanical Systems and Signal Processing*, vol. 66–67, pp. 679–698, 1st Jan. 2016. DOI: 10.1016/j.ymssp.2015.04.039.

[99] V. H. Nguyen, T. H. Vuong and Q. T. Nguyen, 'Feature representation of audible sound signal in monitoring surface roughness of the grinding process', *Production & Manufacturing Research*, vol. 10, no. 1, pp. 606–623, 31st Dec. 2022. DOI: 10.1080/21693277.2022.2108927.

[100] Z. He, T. Shi, J. Xuan and T. Li, 'Research on tool wear prediction based on temperature signals and deep learning', *Wear*, vol. 478–479, p. 203 902, 15th Aug. 2021. DOI: 10.1016/j.wear.2021.203902.

[101] J. Webster, W. P. Dong and R. Lindsay, 'Raw Acoustic Emission Signal Analysis of Grinding Process', *CIRP Annals*, vol. 45, no. 1, pp. 335–340, 1st Jan. 1996. DOI: 10.1016/S0007-8506(07)63075-3.

[102] L. Wan, X. Zhang, Q. Zhou, D. Wen and X. Ran, 'Acoustic emission identification of wheel wear states in engineering ceramic grinding based on parameter-adaptive VMD', *Ceramics International*, vol. 49, pp. 13 618–13 630, 9, Part A 1st May 2023. DOI: 10.1016/j.ceramint.2022.12.238.

[103] J. Liu, C. Jiang, X. Yang and S. Sun, 'Review of the Application of Acoustic Emission Technology in Green Manufacturing', *International Journal of Precision Engineering and Manufacturing-Green Technology*, vol. 11, no. 3, pp. 995–1016, 1st May 2024. DOI: 10.1007/s40684-023-00557-w.

[104] J. Webster, I. Marinescu, R. Bennett and R. Lindsay, 'Acoustic Emission for Process Control and Monitoring of Surface Integrity during Grinding', *CIRP Annals*, vol. 43, no. 1, pp. 299–304, 1st Jan. 1994. DOI: 10.1016/S0007-8506(07)62218-5.

[105] J. Jia *et al.*, 'Applications of Acoustic Emission Monitoring in Grinding: A Review', *International Journal of Precision Engineering and Manufacturing-Green Technology*, 11th May 2025. DOI: 10.1007/s40684-025-00749-6.

[106] H. K. Tönshoff, T. Friemuth and J. C. Becker, 'Process Monitoring in Grinding', *CIRP Annals*, vol. 51, no. 2, pp. 551–571, 1st Jan. 2002. DOI: 10.1016/S0007-8506(07)61700-4.

[107] R. Unnthorsson, 'Hit Detection and Determination in AE Bursts', in *Acoustic Emission - Research and Applications*, IntechOpen, 6th Mar. 2013. DOI: 10.5772/54754.

[108] D. E. Lee, I. Hwang, C. M. O. Valente, J. F. G. Oliveira and D. A. Dornfeld, 'Precision Manufacturing Process Monitoring with Acoustic Emission', in *Condition Monitoring and Control for Intelligent Manufacturing*, ser. Springer Series in Advanced Manufacturing, L. Wang and R. X. Gao, Eds., London: Springer, 2006, pp. 33–54. DOI: 10.1007/1-84628-269-1_2.

[109] R. Unnthorsson, T. P. Runarsson and M. T. Jonsson, 'Acoustic emission based fatigue failure criterion for CFRP', *International Journal of Fatigue*, vol. 30, no. 1, pp. 11–20, 1st Jan. 2008. DOI: 10.1016/j.ijfatigue.2007.02.024.

[110] C. B. Scruby, 'An introduction to acoustic emission', *Journal of Physics E: Scientific Instruments*, vol. 20, no. 8, pp. 946–953, Aug. 1987. DOI: 10.1088/0022-3735/20/8/001.

[111] K. Ono, H. Cho and T. Matsuo, 'Experimental Transfer Functions of Acoustic Emission Sensors', *e-Journal of Nondestructive Testing*, vol. 16, no. 07, 1st Jul. 2011.

[112] ASTM, *Standard Guide for Mounting Piezoelectric Acoustic Emission Sensors*, ASTM Int'l, 2017.

[113] C.-H. Shen, 'Acoustic emission based grinding wheel wear monitoring: Signal processing and feature extraction', *Applied Acoustics*, vol. 196, p. 108 863, 1st Jul. 2022. DOI: 10.1016/j.apacoust.2022.108863.

[114] P. Theobald, B. Zeqiri and J. Avison, 'Couplants and their influence on AE sensor sensitivity', *Journal of Acoustic Emission*, vol. 26, pp. 91–97, 2008.

[115] G. Bi, S. Liu, S. Su and Z. Wang, 'Diamond Grinding Wheel Condition Monitoring Based on Acoustic Emission Signals', *Sensors*, vol. 21, no. 4, 2021. DOI: 10.3390/s21041054.

[116] G. Bi, S. Zheng and L. Zhou, 'Online monitoring of diamond grinding wheel wear based on linear discriminant analysis', *The International Journal of Advanced Manufacturing Technology*, vol. 115, no. 7, pp. 2111–2124, 1st Aug. 2021. DOI: 10.1007/s00170-021-07190-4.

[117] B.-S. Wan, M.-C. Lu and S.-J. Chiou, 'Analysis of Spindle AE Signals and Development of AE-Based Tool Wear Monitoring System in Micro-Milling', *Journal of Manufacturing and Materials Processing*, vol. 6, no. 2, p. 42, 2 Apr. 2022. DOI: 10.3390/jmmp6020042.

[118] H. Murakami, A. Katsuki, T. Sajima, K. Uchiyama, K. Houda and Y. Sugihara, 'Spindle with built-in acoustic emission sensor to realize contact detection', *Precision Engineering*, vol. 70, pp. 26–33, 1st Jul. 2021. DOI: 10.1016/j.precisioneng.2021.01.017.

[119] T. Kon *et al.*, 'Effect of Acoustic Emission Sensor Location on the Detection of Grinding Wheel Deterioration in Cylindrical Grinding', *Lubricants*, vol. 12, no. 3, p. 100, 3 Mar. 2024. DOI: 10.3390/lubricants12030100.

[120] I. Inasaki, 'Application of acoustic emission sensor for monitoring machining processes', *Ultrasonics*, Ultrasonics International 1997, vol. 36, no. 1, pp. 273–281, 1st Feb. 1998. DOI: 10.1016/S0041-624X(97)00052-8.

[121] W. B. Rowe, X. Chen and D. R. Allanson, 'The Coolant Coupling Method Applied to Touch Dressing in High Frequency Internal Grinding', in *Proceedings of the Thirty-Second International Matador Conference*, A. K. Kochhar *et al.*, Eds., London: Macmillan Education UK, 1997, pp. 337–340. DOI: 10.1007/978-1-349-14620-8_53.

[122] P. Sutowski, K. Nadolny and W. Kaplonek, 'Monitoring of cylindrical grinding processes by use of a non-contact AE system', *International Journal of Precision Engineering and Manufacturing*, vol. 13, no. 10, pp. 1737–1743, 1st Oct. 2012. DOI: 10.1007/s12541-012-0228-7.

[123] M. G. R. Sause, M. A. Hamstad and S. Horn, 'Finite element modeling of conical acoustic emission sensors and corresponding experiments', *Sensors and Actuators A: Physical*, vol. 184, pp. 64–71, 1st Sep. 2012. DOI: 10.1016/j.sna.2012.06.034.

[124] C. U. Grosse, M. Ohtsu, D. G. Aggelis and T. Shiotani, Eds., *Acoustic Emission Testing: Basics for Research – Applications in Engineering* (Springer Tracts in Civil Engineering). Cham: Springer International Publishing, 2022. DOI: 10.1007/978-3-030-67936-1.

[125] N. Hsu and F. Breckenridge, 'Characterization and calibration of acoustic emission sensors', *Materials Evaluation*, vol. 39, no. 1, pp. 60–68, 1981.

[126] A. Nielsen, 'Acoustic emission source based on pencil lead breaking', *Svejsecentralen*, Svejsecentralen, vol. 15, 1980.

[127] M. G. Sause, 'Investigation of pencil-lead breaks as acoustic emission sources', *Journal of Acoustic Emission*, vol. 29, 2011.

[128] ASTM, *Standard Guide for Determining the Reproducibility of Acoustic Emission Sensor Response*, ASTM Int'l, 2021.

[129] R. K. Miller, E. v. K. Hill, P. O. Moore and American Society for Nondestructive Testing, *Acoustic Emission Testing* (Nondestructive Testing Handbook, Third Edition ; v. 6). Columbus, OH: American Society for Nondestructive Testing, 2005, x+446.

[130] J. P. McCrory, M. R. Pearson, R. Pullin and K. M. Holford, 'Optimisation of acoustic emission wavestreaming for structural health monitoring', *Structural Health Monitoring*, vol. 19, no. 6, pp. 2007–2022, 1st Nov. 2020. DOI: 10.1177/1475921720912174.

[131] J. L. Ferrando Chacon, 'Fault Detection in Rotating Machinery Using Acoustic Emission', Ph.D. dissertation, Brunel University London, 7th Oct. 2015. DOI: 10.13140/RG.2.1.2369.5444.

[132] S. Hutt, A. Clarke, R. Pullin and H. P. Evans, 'The acoustic emission from asperity interactions in mixed lubrication', *Proceedings of the Royal Society A: Mathematical, Physical and Engineering Sciences*, vol. 475, no. 2227, p. 20 180 900, 10th Jul. 2019. DOI: 10.1098/rspa.2018.0900.

[133] I. Inasaki and K. Okamura, 'Monitoring of Dressing and Grinding Processes with Acoustic Emission Signals', *CIRP Annals*, vol. 34, no. 1, pp. 277–280, 1st Jan. 1985. DOI: 10.1016/S0007-8506(07)61772-7.

[134] J.-J. B. Liu, 'Monitoring the precision machining process: Sensors, signal processing and information analysis', Ph.D. dissertation, University of California, Berkeley, United States – California, 1991, 185 pp.

[135] J. F. G. De Oliveira and D. A. Dornfeld, 'Dimensional Characterization of Grinding Wheel Surface through Acoustic Emission', *CIRP Annals*, vol. 43, no. 1, pp. 291–294, 1st Jan. 1994. DOI: 10.1016/S0007-8506(07)62216-1.

[136] B. Denkena, J. Jacobsen and N. Kramer, 'Dressing Monitoring by Acoustic Emission', *Key Engineering Materials*, vol. 291–292, pp. 195–200, 2005. DOI: 10.4028/www.scientific.net/KEM.291-292.195.

[137] P. Sutowski and S. Plichta, 'An investigation of the grinding wheel wear with the use of root-mean-square value of acoustic emission', *Archives of Civil and Mechanical Engineering*, vol. 6, no. 1, pp. 87–98, 1st Mar. 2006. DOI: 10.1016/S1644-9665(12)60078-8.

[138] Y.-K. Lin, B.-F. Wu and C.-M. Chen, 'Characterization of Grinding Wheel Condition by Acoustic Emission Signals', in *2018 International Conference on System Science and Engineering (ICSSE)*, Jun. 2018, pp. 1–6. DOI: 10.1109/ICSSE.2018.8520249.

[139] J. Akbari, Y. Saito, T. Hanaoka and S. Enomoto, 'Using Acoustic Emission for Monitoring of Grinding Process of Fine Ceramics : Sensitivity of AE to Grain Depth of Cut', *JSME international journal. Ser. C, Dynamics, control, robotics, design and manufacturing*, vol. 38, no. 1, pp. 175–180, 1995. DOI: 10.1299/jsmec1993.38.175.

[140] Y. Qu, E. Bechhoefer, D. He and J. Zhu, 'A New Acoustic Emission Sensor Based Gear Fault Detection Approach', *International Journal of Prognostics and Health Management*, vol. 4, no. 3, 3 2013. DOI: 10.36001/ijphm.2013.v4i3.2141.

[141] J. Akbari, Y. Saito, T. Hanaoka, S. Higuchi and S. Enomoto, 'Effect of grinding parameters on acoustic emission signals while grinding ceramics', *Journal of Materials Processing Technology*, 2nd International Conference on Production Engineering, vol. 62, no. 4, pp. 403–407, 1st Dec. 1996. DOI: 10.1016/S0924-0136(96)02443-0.

[142] T. W. Hwang, E. P. Whitenton, N. N. Hsu, G. V. Blessing and C. J. Evans, 'Acoustic emission monitoring of high speed grinding of silicon nitride', *Ultrasonics*, vol. 38, no. 1, pp. 614–619, 1st Mar. 2000. DOI: 10.1016/S0041-624X(99)00064-5.

[143] A. A. Mokbel and T. M. A. Maksoud, 'Monitoring of the condition of diamond grinding wheels using acoustic emission technique', *Journal of Materials Processing Technology*, vol. 101, no. 1, pp. 292–297, 14th Apr. 2000. DOI: 10.1016/S0924-0136(00)00433-7.

[144] H. Suzuki, T. Kinjo, Y. Hayashi and M. Takemoto, 'Wavelet Transform of Acoustic Emission Signals', *Journal of Acoustic Emission*, vol. 14, pp. 69–84, 1996.

[145] M. A. Hamstad, A. OíGALLAGHER and J. Gary, 'A Wavelet Transform Applied to Acoustic Emission Signals: Part 1: Source Identification', *Journal of Acoustic Emission*, vol. 20, pp. 39–61, 2002.

[146] Q. Liu, X. Chen and N. Gindy, 'Investigation of acoustic emission signals under a simulative environment of grinding burn', *International Journal of Machine Tools and Manufacture*, vol. 46, no. 3, pp. 284–292, 1st Mar. 2006. DOI: 10.1016/j.ijmachtools.2005.05.017.

[147] T. W. Liao, C.-F. Ting, J. Qu and P. J. Blau, 'A wavelet-based methodology for grinding wheel condition monitoring', *International Journal of Machine Tools and Manufacture*, vol. 47, no. 3, pp. 580–592, 1st Mar. 2007. DOI: 10.1016/j.ijmachtools.2006.05.008.

[148] M. Li, Y. Chen, X. Jiang and X. Yang, 'Surface damage characteristics and identification based on acoustic emission in diamond point grinding carbon/carbon ceramic matrix composites', *Proceedings of the Institution of Mechanical Engineers, Part B: Journal of Engineering Manufacture*, vol. 238, no. 13, pp. 2014–2025, 1st Nov. 2024. DOI: 10.1177/09544054231209792.

[149] W. Huang, Y. Li, X. Wu and J. Shen, 'The wear detection of mill-grinding tool based on acoustic emission sensor', *The International Journal of Advanced Manufacturing Technology*, vol. 124, no. 11, pp. 4121–4130, 1st Feb. 2023. DOI: 10.1007/s00170-022-09058-7.

[150] R. Zhao, J. Wang, R. Yan and K. Mao, 'Machine health monitoring with LSTM networks', in *2016 10th International Conference on Sensing Technology (ICST)*, Nov. 2016, pp. 1–6. DOI: 10.1109/ICSensT.2016.7796266.

[151] Q. An, Z. Tao, X. Xu, M. El Mansori and M. Chen, 'A data-driven model for milling tool remaining useful life prediction with convolutional and stacked LSTM network', *Measurement*, vol. 154, p. 107 461, 15th Mar. 2020. DOI: 10.1016/j.measurement.2019.107461.

[152] G. Serin, B. Sener, A. M. Ozbayoglu and H. O. Unver, 'Review of tool condition monitoring in machining and opportunities for deep learning', *The International Journal of Advanced Manufacturing Technology*, vol. 109, no. 3, pp. 953–974, 1st Jul. 2020. DOI: 10.1007/s00170-020-05449-w.

[153] P. Sachin Krishnan and K. Rameshkumar, 'Grinding wheel condition prediction with discrete hidden Markov model using acoustic emission signature', *Materials Today: Proceedings*, International Mechanical Engineering Congress 2019, vol. 46, pp. 9168–9175, 1st Jan. 2021. DOI: 10.1016/j.matpr.2019.12.428.

[154] I. Abu-Mahfouz, 'Drilling wear detection and classification using vibration signals and artificial neural network', *International Journal of Machine Tools and Manufacture*, vol. 43, no. 7, pp. 707–720, 1st May 2003. DOI: 10.1016/S0890-6955(03)00023-3.

[155] D. F. G. Moia, I. H. Thomazella, P. R. Aguiar, E. C. Bianchi, C. H. R. Martins and M. Marchi, 'Tool condition monitoring of aluminum oxide grinding wheel in dressing operation using acoustic emission and neural networks', *Journal of the Brazilian Society of Mechanical Sciences and Engineering*, vol. 37, no. 2, pp. 627–640, 1st Mar. 2015. DOI: 10.1007/s40430-014-0191-6.

[156] J. Gu *et al.*, 'Recent advances in convolutional neural networks', *Pattern Recognition*, vol. 77, pp. 354–377, 1st May 2018. DOI: 10.1016/j.patcog.2017.10.013.

[157] Y. Zhang, X. Qi, T. Wang and Y. He, 'Tool Wear Condition Monitoring Method Based on Deep Learning with Force Signals', *Sensors*, vol. 23, no. 10, p. 4595, 10 Jan. 2023. DOI: 10.3390/s23104595.

[158] Z. Li, X. Liu, A. Incecik, M. K. Gupta, G. M. Królczyk and P. Gardoni, 'A novel ensemble deep learning model for cutting tool wear monitoring using audio sensors', *Journal of Manufacturing Processes*, vol. 79, pp. 233–249, 1st Jul. 2022. DOI: 10.1016/j.jmapro.2022.04.066.

[159] J. Duan, J. Duan, H. Zhou, X. Zhan, T. Li and T. Shi, 'Multi-frequency-band deep CNN model for tool wear prediction', *Measurement Science and Technology*, vol. 32, no. 6, p. 065 009, Apr. 2021. DOI: 10.1088/1361-6501/abb7a0.

[160] X. Cao, B. Chen, B. Yao and S. Zhuang, 'An Intelligent Milling Tool Wear Monitoring Methodology Based on Convolutional Neural Network with Derived Wavelet Frames Coefficient', *Applied Sciences*, vol. 9, no. 18, p. 3912, 18 Jan. 2019. DOI: 10.3390/app9183912.

[161] S. Hochreiter and J. Schmidhuber, 'Long Short-Term Memory', *Neural Computation*, vol. 9, no. 8, pp. 1735–1780, 15th Nov. 1997. DOI: 10.1162/neco.1997.9.8.1735.

[162] Y. Yu, X. Si, C. Hu and J. Zhang, 'A Review of Recurrent Neural Networks: LSTM Cells and Network Architectures', *Neural Computation*, vol. 31, no. 7, pp. 1235–1270, 1st Jul. 2019. DOI: 10.1162/neco_a_01199.

[163] A. Graves, N. Jaitly and A.-r. Mohamed, 'Hybrid speech recognition with Deep Bidirectional LSTM', in *2013 IEEE Workshop on Automatic Speech Recognition and Understanding*, Dec. 2013, pp. 273–278. DOI: 10.1109/ASRU.2013.6707742.

[164] N. Tavakoli, 'Modeling Genome Data Using Bidirectional LSTM', in *2019 IEEE 43rd Annual Computer Software and Applications Conference (COMPSAC)*, vol. 2, Jul. 2019, pp. 183–188. DOI: 10.1109/COMPSAC.2019.10204.

[165] Q. Chen, X. Zhu, Z. Ling, S. Wei, H. Jiang and D. Inkpen. 'Enhanced LSTM for Natural Language Inference', arXiv.org. (20th Sep. 2016).

[166] W. Guo, B. Li and Q. Zhou, 'An intelligent monitoring system of grinding wheel wear based on two-stage feature selection and Long Short-Term Memory network', *Proceedings of the Institution of Mechanical Engineers, Part B: Journal of Engineering Manufacture*, vol. 233, no. 13, pp. 2436–2446, 1st Nov. 2019. DOI: 10.1177/0954405419840556.

[167] Z. Liu, B. Chen, H. Xu, G. Liu, W. Ou and J. Wu, 'A study of diamond grinding wheel wear condition monitoring based on acoustic emission signals', *The International Journal of Advanced Manufacturing Technology*, vol. 134, no. 9, pp. 4367–4385, 1st Oct. 2024. DOI: 10.1007/s00170-024-14392-z.

[168] 'LOCTITE-SI-595-en_GL'. (), [Online]. Available: https://datasheets.tdx.henkel.com/LOCTITE-SI-595-en_GL.pdf (visited on 11/08/2025).

[169] R. G. Lyons, *Understanding Digital Signal Processing*. Pearson Education International, 2011, 925 pp. Google Books: c8IT_gAACAAJ.

[170] Renishaw plc. 'Renishaw: NC4', Renishaw. (), [Online]. Available: http://www.renishaw.com/en/high-accuracy-laser-tool-setting-systems--6099 (visited on 20/04/2022).

[171] Renishaw plc. 'White paper: Innovative laser tool setting technology provides accuracy, flexibility and robust operation'. (), [Online]. Available: https://www.renishaw.com/resourcecentre/en/details/white-paper-innovative-laser-tool-setting-technology-provides-accuracy-flexibility-and-robust-operation--4738 (visited on 02/06/2025).

[172] Renishaw plc, *Understanding non-contact tool setting*, 25th Oct. 2003.

[173] K. Kanatani and P. Rangarajan, 'Hyper least squares fitting of circles and ellipses', *Computational Statistics & Data Analysis*, vol. 55, no. 6, pp. 2197–2208, 1st Jun. 2011. DOI: 10.1016/j.csda.2010.12.012.

[174] A. Woźniak and K. Męczyńska, 'Measurement hysteresis of touch-trigger probes for CNC machine tools', *Measurement*, vol. 156, p. 107 568, 1st May 2020. DOI: 10.1016/j.measurement.2020.107568.

[175] Renishaw plc, 'White paper: Innovations in touch-trigger probe sensor technology'.

[176] M. Weck, P. McKeown, R. Bonse and U. Herbst, 'Reduction and Compensation of Thermal Errors in Machine Tools', *CIRP Annals*, vol. 44, no. 2, pp. 589–598, 1st Jan. 1995. DOI: 10.1016/S0007-8506(07)60506-X.

[177] J.-S. Chen and W.-Y. Hsu, 'Characterizations and models for the thermal growth of a motorized high speed spindle', *International Journal of Machine Tools and Manufacture*, vol. 43, no. 11, pp. 1163–1170, 1st Sep. 2003. DOI: 10.1016/S0890-6955(03)00103-2.

[178] C. Ma, X. Mei, J. Yang, L. Zhao and H. Shi, 'Thermal characteristics analysis and experimental study on the high-speed spindle system', *The International Journal of Advanced Manufacturing Technology*, vol. 79, no. 1, pp. 469–489, 1st Jul. 2015. DOI: 10.1007/s00170-015-6821-z.

[179] B. Chen, X. Guan, D. Cai and H. Li, 'Simulation on thermal characteristics of high-speed motorized spindle', *Case Studies in Thermal Engineering*, vol. 35, p. 102 144, 1st Jul. 2022. DOI: 10.1016/j.csite.2022.102144.

[180] Y.-C. Chen, P.-Z. Chang and Y.-C. Tsai, 'Runout parameters identification in milling process', *Procedia CIRP*, 57th CIRP Conference on Manufacturing Systems 2024 (CMS 2024), vol. 130, pp. 656–661, 1st Jan. 2024. DOI: 10.1016/j.procir.2024.10.144.

[181] C. Baumeister, T. Schlech, Q. R. Luong, E. Sasani and M. G. R. Sause, 'Optimising Sensor Placement for Tool Condition Monitoring: A Comparative Analysis of Acoustic Emission Data', *e-Journal of Nondestructive Testing*, vol. 29, no. 10, 1st Oct. 2024. DOI: 10.58286/30267.

[182] K. M. Holford *et al.*, 'A new methodology for automating acoustic emission detection of metallic fatigue fractures in highly demanding aerospace environments: An overview', *Progress in Aerospace Sciences*, vol. 90, pp. 1–11, 1st Apr. 2017. DOI: 10.1016/j.paerosci.2016.11.003.

[183] A. Géron, *Hands-On Machine Learning with Scikit-Learn, Keras, and TensorFlow*. "O'Reilly Media, Inc.", 4th Oct. 2022, 879 pp.

[184] V. Maiorov and A. Pinkus, 'Lower bounds for approximation by MLP neural networks', *Neurocomputing*, vol. 25, no. 1, pp. 81–91, 1st Apr. 1999. DOI: 10.1016/S0925-2312(98)00111-8.

[185] B. Ding, H. Qian and J. Zhou, 'Activation functions and their characteristics in deep neural networks', in *2018 Chinese Control And Decision Conference (CCDC)*, Jun. 2018, pp. 1836–1841. DOI: 10.1109/CCDC.2018.8407425.

[186] A. Graves, *Supervised Sequence Labelling with Recurrent Neural Networks* (Studies in Computational Intelligence). Berlin, Heidelberg: Springer, 2012, vol. 385. DOI: 10.1007/978-3-642-24797-2.

[187] S. Hochreiter, 'The Vanishing Gradient Problem During Learning Recurrent Neural Nets and Problem Solutions', *International Journal of Uncertainty, Fuzziness and Knowledge-Based Systems*, vol. 06, no. 02, pp. 107–116, Apr. 1998. DOI: 10.1142/S0218488598000094.

[188] M. Sundermeyer, R. Schlüter and H. Ney, 'LSTM neural networks for language modeling', in *Thirteenth Annual Conference of the International Speech Communication Association*, 2012.

[189] T. Boulmaiz, M. Guermoui and H. Boutaghane, 'Impact of training data size on the LSTM performances for rainfall–runoff modeling', *Modeling Earth Systems and Environment*, vol. 6, no. 4, pp. 2153–2164, 1st Dec. 2020. DOI: 10.1007/s40808-020-00830-w.

[190] X. Bao, Y. Xu and E. N. Kamavuako, 'The Effect of Signal Duration on the Classification of Heart Sounds: A Deep Learning Approach', *Sensors*, vol. 22, no. 6, p. 2261, 6 Jan. 2022. DOI: 10.3390/s22062261.

[191] A. Graves and J. Schmidhuber, 'Framewise phoneme classification with bidirectional LSTM and other neural network architectures', *Neural Networks*, IJCNN 2005, vol. 18, no. 5, pp. 602–610, 1st Jul. 2005. DOI: 10.1016/j.neunet.2005.06.042.

[192] M. Vafaeipour, O. Rahbari, M. A. Rosen, F. Fazelpour and P. Ansarirad, 'Application of sliding window technique for prediction of wind velocity time series', *International Journal of Energy and Environmental Engineering*, vol. 5, no. 2, p. 105, 18th May 2014. DOI: 10.1007/s40095-014-0105-5.

[193] H. Izzeldin, V. S. Asirvadam and N. Saad, 'Online sliding-window based for training MLP networks using advanced conjugate gradient', in *2011 IEEE 7th International Colloquium on Signal Processing and Its Applications*, Mar. 2011, pp. 112–116. DOI: 10.1109/CSPA.2011.5759854.

[194] P. Schober, C. Boer and L. A. Schwarte, 'Correlation Coefficients: Appropriate Use and Interpretation', *Anesthesia & Analgesia*, vol. 126, no. 5, p. 1763, May 2018. DOI: 10.1213/ANE.0000000000002864.

[195] M. Sivakumar, S. Parthasarathy and T. Padmapriya, 'Trade-off between training and testing ratio in machine learning for medical image processing', *PeerJ Computer Science*, vol. 10, e2245, 6th Sep. 2024. DOI: 10.7717/peerj-cs.2245. PMID: 39314694.

[196] K. K. Dobbin and R. M. Simon, 'Optimally splitting cases for training and testing high dimensional classifiers', *BMC Medical Genomics*, vol. 4, p. 31, 8th Apr. 2011. DOI: 10.1186/1755-8794-4-31. PMID: 21477282.

[197] I. H. Witten, E. Frank and M. A. Hall, 'Chapter 5 - Credibility: Evaluating What's Been Learned', in *Data Mining: Practical Machine Learning Tools and Techniques (Third Edition)*, ser. The Morgan Kaufmann Series in Data Management Systems, I. H. Witten, E. Frank and M. A. Hall, Eds., Boston: Morgan Kaufmann, 1st Jan. 2011, pp. 147–187. DOI: 10.1016/B978-0-12-374856-0.00005-5.

[198] L. Huang, J. Qin, Y. Zhou, F. Zhu, L. Liu and L. Shao, 'Normalization Techniques in Training DNNs: Methodology, Analysis and Application', *IEEE Transactions on Pattern Analysis and Machine Intelligence*, vol. 45, no. 8, pp. 10 173–10 196, Aug. 2023. DOI: 10.1109/TPAMI.2023.3250241.

[199] Q. Wang, Y. Ma, K. Zhao and Y. Tian, 'A Comprehensive Survey of Loss Functions in Machine Learning', *Annals of Data Science*, vol. 9, no. 2, pp. 187–212, 1st Apr. 2022. DOI: 10.1007/s40745-020-00253-5.

[200] Z.-H. Zhou and X.-Y. Liu, 'Training cost-sensitive neural networks with methods addressing the class imbalance problem', *IEEE Transactions on Knowledge and Data Engineering*, vol. 18, no. 1, pp. 63–77, Jan. 2006. DOI: 10.1109/TKDE.2006.17.

[201] F. Provost. 'Machine Learning from Imbalanced Data Sets 101', AAAI. (Jan. 2000), [Online]. Available: https://aaai.org/papers/ws00-05-001-machine-learning-from-imbalanced-data-sets-101/ (visited on 31/08/2025).

[202] L. A. Yates, Z. Aandahl, S. A. Richards and B. W. Brook, 'Cross validation for model selection: A review with examples from ecology', *Ecological Monographs*, vol. 93, no. 1, e1557, 2023. DOI: 10.1002/ecm.1557.

[203] M. Grandini, E. Bagli and G. Visani. 'Metrics for Multi-Class Classification: An Overview'. arXiv: 2008.05756. (13th Aug. 2020), pre-published.

[204] D. Hand and P. Christen, 'A note on using the F-measure for evaluating record linkage algorithms', *Statistics and Computing*, vol. 28, no. 3, pp. 539–547, 1st May 2018. DOI: 10.1007/s11222-017-9746-6.

[205] D. Chicco and G. Jurman, 'The advantages of the Matthews correlation coefficient (MCC) over F1 score and accuracy in binary classification evaluation', *BMC Genomics*, vol. 21, no. 1, p. 6, 2nd Jan. 2020. DOI: 10.1186/s12864-019-6413-7.

[206] G. James, D. Witten, T. Hastie, R. Tibshirani and J. Taylor, *An Introduction to Statistical Learning: With Applications in Python* (Springer Texts in Statistics). Cham: Springer International Publishing, 2023. DOI: 10.1007/978-3-031-38747-0.

[207] R. R. Bouckaert, 'Choosing between two learning algorithms based on calibrated tests', in *Proceedings of the Twentieth International Conference on International Conference on Machine Learning*, ser. ICML'03, Washington, DC, USA: AAAI Press, 21st Aug. 2003, pp. 51–58.

[208] G. E. Hinton, N. Srivastava, A. Krizhevsky, I. Sutskever and R. R. Salakhutdinov. 'Improving neural networks by preventing co-adaptation of feature detectors'. arXiv: 1207.0580 [cs]. (3rd Jul. 2012), pre-published.

[209] R. Zhao, R. Yan, Z. Chen, K. Mao, P. Wang and R. X. Gao, 'Deep learning and its applications to machine health monitoring', *Mechanical Systems and Signal Processing*, vol. 115, pp. 213–237, 15th Jan. 2019. DOI: 10.1016/j.ymssp.2018.05.050.

[210] B. W. Yap, K. A. Rani, H. A. A. Rahman, S. Fong, Z. Khairudin and N. N. Abdullah, 'An Application of Oversampling, Undersampling, Bagging and Boosting in Handling Imbalanced Datasets', in *Proceedings of the First International Conference on Advanced Data and Information Engineering (DaEng-2013)*, T. Herawan, M. M. Deris and J. Abawajy, Eds., vol. 285, Singapore: Springer Singapore, 2014, pp. 13–22. DOI: 10.1007/978-981-4585-18-7_2.

[211] D. Xu, Y. Shi, I. W. Tsang, Y.-S. Ong, C. Gong and X. Shen, 'Survey on Multi-Output Learning', *IEEE Transactions on Neural Networks and Learning Systems*, vol. 31, no. 7, pp. 2409–2429, Jul. 2020. DOI: 10.1109/TNNLS.2019.2945133.

[212] F. Castanedo, 'A Review of Data Fusion Techniques', *The Scientific World Journal*, vol. 2013, no. 1, p. 704 504, 2013. DOI: 10.1155/2013/704504.

[213] S. Hassani, U. Dackermann, M. Mousavi and J. Li, 'A systematic review of data fusion techniques for optimized structural health monitoring', *Information Fusion*, vol. 103, p. 102 136, 1st Mar. 2024. DOI: 10.1016/j.inffus.2023.102136.

# Appendices

## A Wear Test G-code

The following appendix shows the G-code files for conducting wear tests within the JD machine tool. The main program, seen in Listing 1, controls data output, grinding parameters setting and the control loop. Within Listing 1 multiple other sub-programs are called to carry out macros for inspection or setup, these are found in Listings 2–6.

**Listing 1:** O0021 - DCB wear test.nc.

```
; (DATE=02-02-2021 TIME=11:29:56 - Wear test with AE)
%
O21
G0 G17 G40 G49 G54 G90 G98
;OUTPUT FILE CREATION
; MUST CHANGE TO MATCH BELOW
G100 P221 L10 F1 T1 (E:\FTP\TOM\RESULTS\240610-WEARTEST.csv)

M12
M103 P2
M105 P2
M107 P2
M104 P2

; GRINDING PARAMETERS
#1 = 0          ; LOOP COUNTER
#2 = 250        ; LOOP TARGET
#3 = 24         ; BURR TOOL NUMBER
#4 = 1.3        ; BURR TOOL DIAMETER
#5 = 1          ; PROBE TOOL NUMBER
#6 = 20         ; WORKPIECE Y LENGTH
;#7
#8 = 24000      ; SPINDLE SPEED(CUT)
#9 = 3000       ; SPINDLE SPEED(OTHER)
#10 = 60        ; FEED RATE(CUT)
#11 = 5.        ; Z CUT DEPTH
```

```
#12 = 0.03     ; X CUT DEPTH
;#13
#14 = 0.       ; TOLERANCE FLAG NC4
#15 = 0        ; TOTAL CUTS
#16 = 0        ; CUT REPEAT COUNTER
#17 = 1        ; SIC CUTS PER PROBE
#18 = 1        ; NO. OF CUTS BEFORE NC4 MEASURE
#29 = 5        ; NO. OF CUTS BEFORE OWL/SPRIAL SCAN
#30 = 1        ; NO. OF CUTS BEFORE THERMAL DRIFT PROBE

;Date & Time
#40 = #2400/10000                ; Year
#41 = [#40-FIX[#40]]*100         ; Month
#42 = ROUND[[#41-FIX[#41]]*100]  ; Day
#43 = #2401/10000                ; Hour
#44 = [#43-FIX[#43]]*100         ; Minute
#45 = ROUND[[#44-FIX[#44]]*100]  ; Second

; Output file headings
G100 P221 L20 F1 (<ELN:1>)
G100 P221 L20 F1 (DATE,<FMT:.2D,#42>-<FMT:.2D,#41>-<FMT:.4D,#40><ELN:1>)
G100 P221 L20 F1 (TIME,<FMT:.2D,#43>:<FMT:.2D,#44>:<FMT:.2D,#45><ELN:1>)
G100 P221 L20 F1 (<ELN:1>)
G100 P221 L20 F1 (Cut No,NC4 Radius,PROBE1,PROBE2,PROBE3,PROBE4,)
G100 P221 L20 F1 (AVGPROBE,REFBORE-X,REFBORE-Y,REFBORE-S<ELN:>)
G100 P221 L11 F1

GOTO 3
N1
#16=0.              ; Reset cut repeat counter

N2
;----------------CUT SIC---------------
WHILE[#16LT#18]DO 1
T#3M6
G54.1000 P7
G90 G0 X-#4 Y-#4
G0 G43 H#2233 Z50 F5000
M3 S#8
M8
G1 Z-#11
G01 X[[#12*#15]-#[6300+#3]] F#10
;ACOUSTICS SIGNAL
```

```
M107 P1
;CUTTING PASS
G01 Y#6
M107 P2
G40
G1 Z50 F5000
M9
M5
IF[#1GE#2]GOTO 3
#1=#1+1              ; Increment loop counter
#15=#15+1            ; Increment total cuts
#16=#16+1            ; Increment cut repeat counter
END 1

N3
;-------------MEASURE TOOL--------------
;MEASURE
T#3M6
G53
; Wait for coolant to stop
G91 G28 Z0
G90
G4X20
M3 S24000
G4X10
M7
G4X5
M9
M5

G65 P7862 B3 R#4 Z[#11/2] S#9 H1 D99 M1; changed to save to T99
#604=#[6300+99]; changed to 99 from #3
#14 = #148  ; Set NC4 tolerance flag

N4
;----ANALOGUE TRACE AT Z BOTH SIDES-----
G54
G65 P1000 Z[#11/2] D#4

N5
;-----------OWL/SPRIAL SCAN-------------
IF[[#15/#29]NE[FIX[#15/#29]]]GOTO 6
G65 P1004 T#3 D#4 S60. F2. Z7. Y0.03
```

```
113
114 N6
115 ;--------PROBE SIC - PRE CUTTING--------
116 IF[#1GT0]GOTO 7
117 G65 P1001
118
119 N7
120 ;---------------PROBE SIC---------------
121 ; Check whether to probe after this cut if not then skip
122 IF[[#15/#17]NE[FIX[#15/#17]]]GOTO 8
123 G65 P1002 X[#12 * #15] T1 W20
124
125 N8
126 ;----------THERMAL DRIFT PROBE----------
127 IF [[#15/#30]NE[FIX[#15/#30]]]GOTO 9
128 G65 P1003
129 #673 = #135         ; REF BORE X
130 #674 = #136         ; REF BORE Y
131 #675 = #138         ; REF BORE SIZE
132
133 N9
134 ;PRINT OUT DATA
135 ; #1 - Cut No
136 ; #604 - NC4 Radius measurement
137 ; #668 - Relative probe measurement between ref and cut surface at P1
138 ; #669 - Relative probe measurement between ref and cut surface at P2
139 ; #670 - Relative probe measurement between ref and cut surface at P3
140 ; #671 - Relative probe measurement between ref and cut surface at P4
141 ; #672 - Avg of P1,P2,P3,P4
142 ; #673 - REF BORE X
143 ; #674 - REF BORE Y
144 ; #675 - REF BORE SIZE
145
146 G100 P221 L10 F1 T1 (E:\FTP\TOM\RESULTS\240610-WEARTEST.csv)
147 IF [#14 EQ 1] G100 P221 L20 F1 (NC4 Length Triggered Tool Broken <ELN:>)
148 G100 P221 L20 F1 (<FMT:.1F,#1>,<FMT:.4F,#604>,<FMT:.4F,#668>,)
149 G100 P221 L20 F1 (<FMT:.4F,#669>,<FMT:.4F,#670>,<FMT:.4F,#671>,)
150 G100 P221 L20 F1 (<FMT:.4F,#672>,<FMT:.4F,#673>,<FMT:.4F,#674>,)
151 G100 P221 L20 F1 (<FMT:.4F,#675><ELN:>)
152 G100 P221 L11 F1
153 M1
154
155 ;-------------NO. CUT CHECK-------------
```

```
IF[#14 EQ 1]GOTO 10  ; Check if tool broken to stop
IF[#1 GE #2]GOTO 10
GOTO 1

N10
;---------------PROGRAM END-------------
G100 P221 L11 F1
M30
%
```

**Listing 2:** O1000 - NC4-AnalogScan.nc.

```
;(Analog Scan of a tool with NC4)
;(E.G. G65 P1000 D1.3 Z2.5)
;(Inputs:)
;(D [#07] - Nominal Tool Diameter)
;(Z [#26] - Axial Scan Pos up from Tool Tip)
%
O1000 ;(NC4-AnalogScan)

#19 = 60    (Spindle RPM)
#20 = 1.    (Beam Side)
#21 = 0.04  (Relative Scan Y Pos)

;(Turn on NC4 Air Blast)
M105 P1
G4 X1
;(Start NC4 Acquisition)
M103 P1

N1
G53 G49
;(Y Position Calc)
; #522, #523 NC4 calibration values for Y pos either side of beam
#22 = [[#522 + #523] / 2] + #20 * [[#7 / 2] + #21]
;(Z Position Calc)
; #520, #521 NC4 calibration values for Z pos either side of beam
; #[6100 + #2233] is the tool length offset for current tool
#23 = [[[#520 + #521] / 2] - #26] + #[6100 + #2233]

N2
G53 G1 X#524 Y#22 F8000

G53 G1 Z#23 F8000
```

```
M3 S#19
G4 X4

N3
;(Increment Scan Y Position)
#21 = #21 - 0.01
;(Check if scanned all Y pos 0.04, 0.03, 0.02, 0.01, 0.00, -0.01)
IF [#21 GE -0.01] GOTO 1

;(Repeat Scan for other side of beam)
#21 = 0.04
#20 = #20 - 2.
IF[#20 GE - 1.] GOTO 1

;(Stop Acquisition and Air Blast)
M103 P2
M105 P2

M5
;(Retract to Safe Position)
G91 G28 Z0
G90

M99
%
```

**Listing 3:** O1001 - Probe-SetupWorkpiece.nc.

```
;(Probe of SiC Workpiece to set work coords)
;(Cutting Surface    -   G54.1000 P7)
;(Reference Surface  -   G54.1000 P6)

%
O1001 ;(Probe-SetupWorkpiece)
G0 G17 G40 G49 G54 G90 G98
M104 P2
G28 G91 Z0
G90

T1 M6
G54.1000 P7
G0 X5 Y5
G1 G43 H#2233 Z150 F5000
M104 P1
```

```
G4 X1

;(Cutting Surface    -   G54.1000 P7)
G54.1000 P7
; Z Work Offset
G65 P7810 X5 Y5
G65 P7810 Z10
G65 P7811 Z0 S107
; Corner Probe
G65 P7810 X-6 Y -6
G65 P7810 Z-4.5
G65 P7816 X0 Y0 D6 E6 S107
G65 P7810 Z10

;(Reference Surface  -   G54.1000 P6)
; Z Work Offset = to cutting surface
; #5243 - Variable for Z G54.1000 P6
; #5263 - Variable for Z G54.1000 P7
#5243 = #5263
G54.1000 P6
G65 P7810 X-6 Y -6
G65 P7810 Z-9.5
G65 P7816 X0 Y0 D6 E6 S106
G65 P7810 Z100

M104 P2
G91 G28 Z0
G90
M99
%
```

**Listing 4:** O1002 - Probe-CutRefSurfaceMeasure.nc.

```
;(Probe of both SiC cutting and reference surfaces for difference
   measurement)
;(E.G. G65 P1002 X10 T1 W20)
;(Cutting Surface    -   G54.1000 P7)
;(Reference Surface  -   G54.1000 P6)
;(Inputs:)
;(X [#24] - Theoretical Cutting Surface X Position)
;(T [#20] - Tool Number for Probe)
;(W [#23] - Workpiece Width / mm)
%
O1002 ;(Probe-CutRefSurfaceMeasure)
```

```
G0 G17 G40 G49 G54 G90 G98
M104 P2
G28 G91 Z0
G90

;(Parameters:)
#1 = 1       ; Probe Measurement Count
#2 = 0       ; Y Start
#3 = #23     ; Y End
#4 = 4       ; Number of Measurement Points
#5 = [[#3 - #2] / [[#4 + 2] - 1]     ; Y Step

;(Outputs:)
; #659 = Avg Reference Surface X
; #660 - #663 = Reference Surface X Measurements
; #664 - #667 = Cutting Surface X Measurements
; #668 - #671 = Difference Measurements
; #672 = Avg Difference

N1 ;(Probe Setup)
T#20 M6
M104 P1
G4 X1

N2 ;(Probe Reference Surface)
G54.1000 P6
G0 X-5 Y-5
G1 G43 H#2233 Z20 F5000
G65 P7810 Z-6.5

N21
G65 P7810 Y[#2 + [#5 * #1]]
G65 P7811 X0
; #135 Probe Measurement, #5241 Reference Surface X Coord
#[659 + #1] = #135 + #5241
M12
#1 = #1 + 1
IF [#1 LE #4] GOTO 21
#659 = [#660 + #661 + #662 + #663] / #4
G65 P7810 Z20

N3 ;(Probe Cutting Surface)
G54.1000 P7
```

```
G0 X-5 Y-5
G65 P7810 Z-1.5

N31
G65 P7810 Y[#2 + [#5 * [#1 - #4]]
G65 P7811 X#24
; #135 Probe Measurement, #5261 Cutting Surface X Coord
#[659 + #1] = #135 + #5261
#[[659 + #1] + #4] = #[659 + #1] - #659
M12
#1 = #1 + 1
IF [#1 LE [#4 * 2]] GOTO 31
#672 = [#668 + #669 + #670 + #671] / #4
G65 P7810 Z20

N4 ;(END OF PROGRAM)
M104 P2
G91 G28 Z0
G90
M99
%
```

**Listing 5:** O1003 - Probe-RefBore.nc.

```
;(Probe ref bore for thermal drift measurements)
%
O1003
G54
G0 G90 G98

M104 P2

G28 G91 Z0
G90

T1 M6

G0 X260.8714 Y41.9922
G01 G43 H#2233 Z5. F5000

M104 P1
G4 X1

G65 P7810 Z-78 ;(Move into the Ref Bore)
```

```
G65 P7814 D30 ;(Measure the Ref Bore)
G65 P7810 Z0 ;(Protected move to Z0)

M104 P2 ;(Turn off probe)
G91 G28 Z0
G90
M99
```

**Listing 6:** O1004 - NC4-SpiralScan.nc.

```
;(Spiral Scan of the tool with NC4)
;(E.G G65 P1004 T24 D1.3 S60 F4 Z10 Y0)
;(Inputs:)
;(T [#20] - Tool Number)
;(D [#07] - Nominal Tool Diameter)
;(S [#19] - Spindle Speed RPM)
;(F [#09] - FeedRate)
;(Z [#26] - Z Depth of Scan)
;(Y [#25] - Y Postion Offset)
%
O1004 ;(NC4 Spiral Scan)
G0 G17 G40 G49 G54 G90 G98

M12
M103 P2
M105 P2
M107 P2
M104 P2

#10 = 1. ;(Beam Side)

T#20 M6

;(X Position)
;(NC4 middle X pos)
#1 = #524

;(Y Position)
;(NC4 middle of beam + offset for tool diameter and Y offset)
#2 = [[#522 + #523] / 2] + [#10 * [[#7 / 2] + #25]]

;(Z Position)
;(NC4 middle of beam + offset for tool length)
#3 = [[#520 + #521] / 2] + #[6100 + #2233]
```

```
35
36 ;(Move to start location)
37 G53 G1 X#1 Y#2 F8000
38 G53 G1 Z[#3 + 0.25] F5000
39
40 ;(Start NC4 Acquisition)
41 M105 P1
42 M103 P1
43 G4 X0.5
44
45 ;(Rotate Spindle)
46 M3 S#19
47 ;(Move spindle down at correct feedrate)
48 G53 G1 Z[#3 - #26] F#9
49
50 ;(Stop spindle)
51 M5
52
53 ;(End NC4 Acquisition)
54 M103 P2
55 M105 P2
56
57 G91 G28 Z0
58 G90
59
60 M99
61 %
```

# B MISTRAS WD Sensor Datasheet

MISTRAS
A World of NDT Solutions
Products & Systems Division

PHYSICAL ACOUSTICS CORPORATION

PRODUCT DATA SHEET

## WD Sensor

### Wideband Differential Sensor

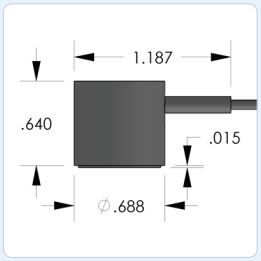


#### DESCRIPTION AND FEATURES

WD is a true differential wideband sensor with a very high sensitivity and bandwidth. It has a very good frequency response over the range of 100 – 900 kHz. Differential sensors differ from their general purpose counterparts by employing two sensing elements with opposite polarization directions. The two signal leads feed into a differential pre-amplifier which eliminates common-mode noise resulting in a lower noise output from the pre-amplifier. Noise improvements to the tune of 2 dB can be achieved using differential sensors over a single ended sensor. This sensor features a rugged steel construction with an integrated twin axial cable exiting on the side.

#### APPLICATIONS

This sensor is well suited for structural health monitoring of large structures like storage tanks, pipelines etc. This sensor is an ideal candidate for applications requiring high bandwidth for frequency analysis of the AE signals for noise discrimination and source identification. Wideband sensors are particularly well suited for research applications where a high fidelity AE response is required. It can be easily mounted using epoxy.

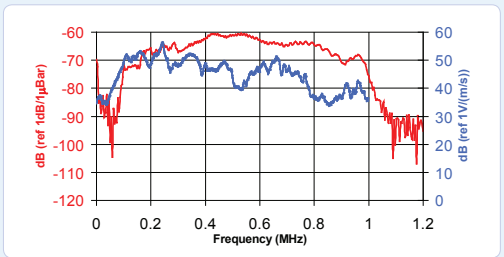


#### OPERATING SPECIFICATIONS

*Dynamic*

| | |
|---|---|
| Peak Sensitivity, Ref V/(m/s) | 56 dB |
| Peak Sensitivity, Ref V/µbar | -61 dB |
| Operating Frequency Range | 125-1000 kHz |
| Resonant Frequency, Ref V/(m/s) | 125 kHz |
| Resonant Frequency, Ref V/µbar | 450 kHz |
| Directionality | +/-1.5 dB |

*Environmental*

| | |
|---|---|
| Temperature Range | -65 to 177ºC |
| Shock Limit | 500 g |

Completely enclosed crystal for RFI/EMI immunity

*Physical*

| | |
|---|---|
| Dimensions | 0.7"OD X 0.65"H<br>17.8 mm OD X 16.5 mm H |
| Weight | 20 grams |
| Case Material | Stainless Steel |
| Face Material | Ceramic |
| Connector | BNC |
| Connector Locations | Side |

#### ORDERING INFORMATION AND ACCESSORIES

| | |
|---|---|
| WD | WD |
| Cable (specify length in '-XX' m at end of PN) | 1 m |
| Magnetic Hold-Down | MHSTD |
| Pre-Amplifier | 0/2/4, 2/4/6 |
| Preamp to System Cable (specify length in 'm') | 1234-X |
| Amplifier Subsystems | AE2A or AE5A |

*Sensors include*

NIST Calibration Certificate & Warranty

ISO 9001

**WORLDWIDE HEADQUARTERS:**
195 Clarksville Rd •
Princeton Jct, NJ 08550 • USA
T: +1.609.716.4000 • F: +1.609.716.0706
E-MAIL: sales.systems@mistrasgroup.com

| | | | | | | | |
|---|---|---|---|---|---|---|---|
| **CANADA** | T: +1.403.556.1350 | **HOLLAND** | T: +31.010.245.0325 | **RUSSIA** | T: +7495.789.4549 |
| **CHINA** | T: +86.10.5877.3631 | **INDIA** | T: +91.22.2586.2444 | **SCANDINAVIA** | T: +46(0)31.252040 |
| **FRANCE** | T: +331.498.26040 | **JAPAN** | T: +81.33.498.3570 | **S. AMERICA** | T: +55.11.3082.5111 |
| **GERMANY** | T: +49.040 2000.4025 | **MALAYSIA** | T: +60.9.517.3788 | **UK** | T: +44(0)1954.231.612 |
| **GREECE** | T: +30.210.2846.801-4 | **MIDDLE EAST** | T: +973.17.729.356 | | |

 #210D-11-133-01 www.mistrasgroup.com

# C MISTRAS 2/4/6 Pre-Amplifier Datasheet

MISTRAS
A World of NDT Solutions
Products & Systems Division

## 2/4/6 Preamplifier

### Description:

The 2/4/6 preamplifier was designed to be used with all available AE systems that have power supplied via the output signal BNC. It is supplied with 20/40/60 dB gain (switch selectable) and operates with either a single ended or differential sensor. Plug in filters provide the user with flexibility to optimize sensor selectivity and noise rejection. These filters are provided in the Low Pass (LP), High Pass (HP), and Band Pass (BP) configurations, and offers constant insertion loss for easy filter swapping without the need for recalibration. Automatic Sensor Test (AST) is standard. This option provides the sensor with the ability to characterize its own condition as well as send out a simulated acoustic emission wave that other sensors can detect.


### Features:

- 20/40/60 Selectable Gain
- Wide Dynamic Range > 90dB Standard
- Low Noise < 2¤V (With Standard* Filter & Input Shorted)
- Large Output Signal 20Vpp into 50¤
- Single Power/Signal BNC or Optional Separate Power/ Signal BNC
- Plug-in Filters (Utilizes the same filter as the SPARTAN 2000)
- High Input Impedance
- Standard Auto Sensor Test
- Input Protection

### Electrical Specifications:

- Gain Selectable: 20/40/60 dB + 0.5% dB
- Input Impedance: 10KΩ // 15pF
- Power Required: 18-28V DC
- Operating Current: 30mA (With AST Installed)
- 28mA (Without AST Installed)
- Dynamic Range: 80dB (Utilizing an R15 Sensor)
  90dB (50Ω Input

### Environmental Specifications:

- Temperature: -40 C to +65 C

| Gain Selection | 20dB | 40dB | 60dB |
|---|---|---|---|
| • Bandwidth (-3dB): | 10kHz-2.5MHz | 10kHz-2.0MHz | 10kHz-900kHz |
| • Output Voltage (50Ω Load): | 6Vpp | 20Vpp | 20Vpp |
| • CMRR (500kHz): | 42dB | 42dB | 42dB |
| • Noise (RMS rti): | | | |

| Filter Frequency Response Hz | 20dB With R15 Sensor | 40dB With R15 Sensor | 60dB With R15 Sensor | 20dB Input Shorted | 40dB Input Shorted | 60dB Input Shorted |
|---|---|---|---|---|---|---|
| 135k-185k | 3 µV | 1.4 µV | 1.5 µV | 2.0 µV | 0.6 µV | 0.42 µV |
| 100k-300k* | 3 µV | 1.8 µV | 1.8 ¤V | 2.3 µv | 1 µV | 0.8 µV |
| 10k-2.0M | 5 µV | 4 µV | 3 µV | 4 µV | 3 µV | 2.5 µV |

**Standard filter*

195 Clarksville Road, Princeton Junction, NJ 08550 USA
Phone: (609) 716-4000 • Fax: (609) 716-0706
Email: sales.systems@mistrasgroup.com • www.mistrasgroup.com

# D Renishaw NC4+ Blue Datasheet

RENISHAW
apply innovation™

## NC4+ Blue non-contact tool setting range

### Specification

| | | |
|---|---|---|
| **Principal application** | High-precision, high-speed non-contact tool setting and tool breakage detection on all sizes of vertical and horizontal machining centres, multi-tasking machines and gantry machining centres. | |
| **Transmission type** | Hard-wired transmission | |
| **Compatible interfaces** | NCi-6 | |
| **Repeatability** | F115 and F145 | ±0.5 µm (19.69 µin) 2σ |
| | F230 and F300 | ±0.75 µm (29.53 µin) 2σ |
| **Tool setting and tool breakage detection** (minimum tool or feature size) | F115 systems | Ø0.03 mm (0.0012 in) |
| | F145 systems | Ø0.05 mm (0.0020 in) |
| | F230 systems | Ø0.1 mm (0.0039 in) |
| | F300 systems | Ø0.2 mm (0.0079 in) |
| **Output signal** (from interface unit) | Two voltage-free, solid-state relays (SSR). Each can be either normally open or normally closed (selectable via a switch). Current (maximum) 50 mA, voltage (maximum) ±50 V.<br>The interface contains an auxiliary relay which can be used for switching the output between the NC4+ Blue and a spindle probe. This relay can also be used to control an air blast solenoid (optional). | |
| **Supply voltage** (to interface) | 11 Vdc to 30 Vdc | |
| **Supply current** (to interface) | 120 mA @ 12 Vdc, 70 mA @ 24 Vdc | |
| **Supply protection** | Resettable fuses in interface. Reset by removing power and cause of fault. | |
| **Electrical connection arrangement** | **Systems with connector:** Connector socket.<br>**Hard-wired systems:** Cable on the end of the unit.<br>Other configurations are available on request. | |
| **Cable** (to interface) | **Specification** | Ø6.0 mm (0.24 in), two twisted pairs, two individual cores plus screen, each core 18 × 0.1 mm insulated. |
| | **Length** | 12.5 m (41.01 ft) |
| | **Electrical connection** | **Systems with connector:** cable with bayonet-type plug, connector socket on the end of the unit.<br>**Hard-wired systems:** cable on the end of the unit.<br>Other configurations are available on request. |
| **NC4+ Blue pneumatic supply** | Air supply to the NC4 must conform to BS ISO 8573-1: 2010 Class 1.4.2. 6.0 bar (87.02 psi) maximum.<br>**Systems with connector:** Ø4.0 mm (0.16 in) × 5.0 m (16.40 ft)<br>**Hard-wired systems:** Ø3.0 mm (0.12 in) × 5.0 m (16.40 ft) | |
| **Air blast pneumatic supply** | Air supply to the air blast must conform to BS ISO 8573-1: 2010 Class 2.9.4.<br>Ø6.0 mm (0.24 in) air pipe × 5.0 m (16.40 ft), 6.0 bar (87.02 psi) maximum. | |
| **Laser type** | Class 2 laser product:<br>1 mW maximum output emitted wavelength 405 nm.<br>**WARNING:** Laser radiation. Do not stare into beam. | |
| **Laser beam alignment** | The unit is supplied with an adjustable mounting plate on the underside. | |
| **Weight** (including 12.5 m (41.01 ft) of cable) | 1080 g (2.38 lb) to 2000 g (4.4 lb) depending on configuration. | |

**www.renishaw.com/nc4** #renishaw

RENISHAW
apply innovation™

## Specification (continued)

| | | |
|---|---|---|
| **Mounting** | M4 (× 3), M10 (3/8 in) or M12 (½ in) bolts for mounting via adjuster plate (not supplied).<br>Other fixing arrangements are available on request. | |
| **Environment** | IP rating | IPX6 and IPX8, BS EN 60529:1992+A2:2013 (IEC 60529:1989+A1:1999+A2:2013) |
| | Storage temperature | –25 °C to +70 °C (–13 °F to +158 °F) |
| | Operating temperature | +5 °C to +55 °C (+41 °F to +131 °F) |

## NC4+ Blue hard-wired system dimensions

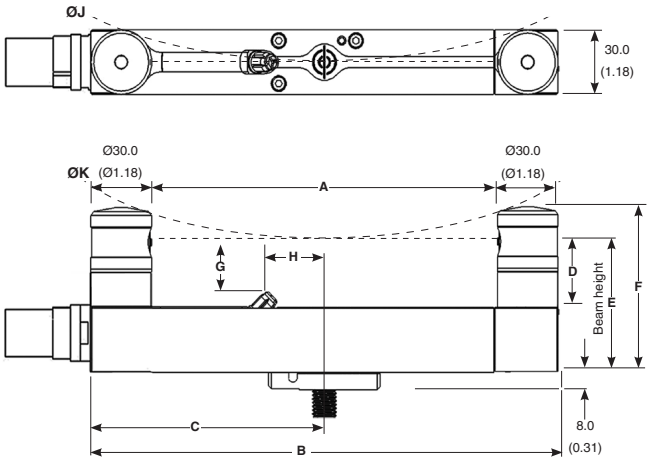


| Model | Dimensions | | | | | | | | | |
|---|---|---|---|---|---|---|---|---|---|---|
| | A | B | C | D | E | F | G | H | ØJ | ØK |
| **F145** | 85.0 (3.35) | 145.0 (5.71) | 72.5 (2.85) | 31.0 (1.22) | 61.0 (2.40) | 77.0 (3.03) | 20.4 (0.80) | 24.5 (0.96) | 205.0 (8.07) | 147.0 (5.79) |
| **F230** | 170.0 (6.69) | 230.0 (9.06) | 115.0 (4.53) | 31.0 (1.22) | 61.0 (2.40) | 77.0 (3.03) | 21.3 (0.84) | 25.3 (1.00) | 652.0 (25.67) | 535.0 (21.06) |

Dimensions given in mm (in)

# E Renishaw OMP600 Machine Probe Datasheet

RENISHAW
apply innovation™

## OMP600 optical machine probe

### Specification

| | | | |
|---|---|---|---|
| **Principal application** | | Workpiece inspection and job set-up on all sizes of machining centres and small to medium multi-tasking machines | |
| **Transmission type** | | 360° infra-red optical transmission | |
| **Compatible interfaces** | | **Modulated**<br>OMI-2, OMI-2T, OMI-2H, OMI-2C or OMM-2 / OMM-2C with OSI / OSI-D | **Legacy**<br>OMI or OMM with MI 12 |
| **Operating range** | | Up to 6 m (19.7 ft) | |
| **Recommended styli** | | High modulus carbon fibre, lengths 50 mm (1.97 in) to 200 mm (7.88 in) | |
| **Weight (without shank)** | | including batteries | 1029 g (36.3 oz) |
| **Switch-on / switch-off options** | | Optical on → Optical off or timer off<br>Shank on → Shank switch off<br>Spin on → Spin off or timer off | |
| **Battery life (2 × AA 3.6 V lithium-thionyl chloride)** | Standby life | 800 days maximum dependent on switch-on / switch-off option | |
| | Continuous life | **Modulated**<br>380 hours maximum, dependent on switch-on / switch-off option. | **Legacy**<br>410 hours maximum, dependent on switch-on / switch-off option. |
| **Sense directions** | | ±X, ±Y, +Z | |
| **Unidirectional repeatability** | | 0.25 µm (10 µin) 2σ – 50 mm stylus length [1]<br>0.35 µm (14 µin) 2σ – 100 mm stylus length | |
| **X, Y (2D) form measurement deviation** | | ±0.25 µm (10 µin) – 50 mm stylus length [1]<br>±0.25 µm (10 µin) – 100 mm stylus length | |
| **X, Y, Z (3D) form measurement deviation** | | ±1.00 µm (40 µin) – 50 mm stylus length [1]<br>±1.75 µm (70 µin) – 100 mm stylus length | |
| **Stylus trigger force** [2] [3]<br>XY plane (typical minimum)<br>+Z plane (typical minimum) | | <br>0.15 N, 15 gf (0.54 ozf)<br>1.75 N, 178 gf (6.03 ozf) | |
| **Stylus overtravel force**<br>XY plane (typical minimum)<br>+Z plane (typical minimum) | | <br>3.05N, 311gf (10.98 ozf) [4]<br>10.69 N, 1090 gf (38.51 ozf) [5] | |
| **Probe feedrate (minimum)** | | 3 mm/min (0.12 in/min) [6] | |
| **Environment** | | IP rating | IPX8, BS EN 60529:1992+A2:2013 |
| | | IK rating (typical) | IK01, BS EN 62262:2002+A1:2021 [for glass window] |
| | | Storage temperature | –25 °C to +70 °C (–13 °F to +158 °F) |
| | | Operating temperature | +5 °C to +55 °C (+41 °F to +131 °F) |

[1] Performance specification is tested at a standard test velocity of 240 mm/min (9.45 in/min) with a 50 mm carbon fibre stylus. Significantly higher velocity is possible depending on application requirements.

[2] Trigger force, which is critical in some applications, is the force exerted on the component by the stylus when the probe triggers. The maximum force applied will occur after the trigger point (overtravel). The force value depends on related variables, including measuring speed, machine deceleration and system latency. RENGAGE equipped probes offer ultra-low trigger forces when probing at low feedrates.

[3] These are the factory settings: manual adjustment is not possible.

[4] Stylus overtravel force in the XY plane occurs 70 µm (2755.91 µin) after the trigger point and rises by 0.1 N/mm,10 gf/mm (9.1 ozf/in) until the machine tool stops (in the high force direction and using a 50 mm (1.97 in) carbon fibre stylus).

[5] Stylus overtravel force in +Z direction occurs 10 µm (393.70 µin) to 11 µm (433.07 µin) after the trigger point and rises by 1.2 N/mm, 122 gf/mm (109.6 ozf/in) until the machine tool stops.

[6] Speeds below 3 mm/min commonly occur when manually moving the probe using the handwheel with a very fine feedrate.

For further information and the best possible application and performance support, contact Renishaw or visit **www.renishaw.com/OMP600**

**www.renishaw.com/omp600** **#renishaw**

# F NIKKEN Zero-Fit Tool Holder Datasheet



## ZERO FIT TYPE SLIM CHUCK

NIKKEN

SZF

Fig.1

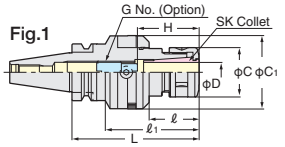


Fig.2

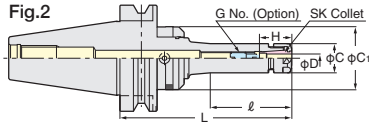


Explanation of the Code No.

BT40 SZF10 – 90

- 90: Nominal Gauge Length
- SZF10: Chucking Capacity
- SZF: Zero Fit Type Slim Chuck
- BT40: Shank No.

| MAX. run-out at 100mm | | |
|---|---|---|
| SZF 6 | L<150 | 0.050mm/dia. |
| | L≥150 | 0.040mm/dia. |
| SZF10 | | 0.050mm/dia. |
| SZF16 | | 0.040mm/dia. |
| SZF25 | | 0.025mm/dia. |

**JAPAN, USA, UK, GERMANY, KOREA, TAIWAN PAT.**

| TAPER | Code No. | D | L | ℓ | ℓ1 | C | C1 | H | G No. (Option) | Weight (kg) | Fig. | Collet |
|---|---|---|---|---|---|---|---|---|---|---|---|---|
| No.30 | BT30-SZF 6- 90 | 0.7～6.0 | 90 | 42 | - | 19.5 | 40.5 | 21～35 | SKG- 8 | 0.9 | 2 | SK 6 |
| | -SZF10- 90 | 1.75～10.0 | | 35 | 61 | 27.5 | 48.5 | 30～50 | SKG-12L | 1.3 | 1 | SK10 |
| | -SZF16-105 | 2.75～16.0 | 105 | 40 | 76 | 40 | 59.5 | 45～65 | SKG-18L | 1.6 | | SK16 |
| No.40 | BT40-SZF 6- 90 | 0.7～6.0 | 90 | 37 | - | 19.5 | 40.5 | 21～35 | SKG- 8 | 1.3 | 2 | SK 6 |
| | -150 | | 150 | 60 | | | 48.5 | | | 1.7 | | |
| | BT40-SZF10- 90 | 1.75～10.0 | 90 | 37 | | 27.5 | 48.5 | 30～50 | SKG-12L | 1.5 | | SK10 |
| | -150 | | 150 | 97 | | | | | | 1.9 | | |
| | BT40-SZF16- 90 | 2.75～16.0 | 90 | 37 | | 40 | 59.5 | 40～70 | SKG-18L | 1.8 | | SK16 |
| | -150 | | 150 | 97 | | | | | | 2.2 | | |
| | -SZF25-120 | 7.5～25.4 | 120 | 55 | 84 | 55 | 66.5 | 55～85 | SKG-28 | 2.4 | 1 | SK25 |
| | -150 | | 150 | 86 | 114 | | | | | 2.9 | | |
| No.50 | BT50-SZF 6-105 | 0.7～6.0 | 105 | 41 | - | 19.5 | 40.5 | 21～35 | SKG- 8 | 4.0 | 2 | SK 6 |
| | -165 | | 165 | 63 | | | 59.5 | | | 4.2 | | |
| | -SZF10-105 | 1.75～10.0 | 105 | 41 | | 27.5 | 48.5 | 30～50 | SKG-12L | 4.5 | | SK10 |
| | -165 | | 165 | 101 | | | | | | 4.9 | | |
| | -SZF16-105 | 2.75～16.0 | 105 | 41 | | 40 | 59.5 | 40～70 | SKG-18L | 5.0 | | SK16 |
| | -165 | | 165 | 101 | | | | | | 5.4 | | |
| | -SZF25-135 | 7.5～25.4 | 135 | 71 | | 55 | 66.5 | 55～85 | SKG-28 | 5.8 | | SK25 |
| | -165 | | 165 | 101 | | | | | | 6.0 | | |

★Adjust screw (G No.), wrench to adjust run-out (**9ZFL**) and **SKL** spanner are available as an option. **SZF6: SKL-6W, SZF10: SKL-10, SZF16: 9HC16, SZF25: 9HC25**

★**Please use "P" class or "A" type SK collet.** ☞P.47

★For centre through coolant application please use **SK J** type nut and cap for your preference. Please note that the length of **J** type nut is 6mm longer than the standard **SK** nut. ☞P.53

★For High Speed type, Code No. is **"SZF-P"**. **e.g. BT40-SZF10-90P** **GH handle** ☞P.52 is necessary for High Speed Milling Chuck.

★Multi-Cam style is available. **e.g. BT40-SZF16-90-C3**. (3 Cams) Please contact us for more detail.

**•When using SK-A collets or SK-AC collets, or when gripping a cutting tool smaller than the nominal diameter on SK collets, the total length will be shortened by about 3 mm. Please be careful when you check the interference.**

Wrench to adjust **9ZFL**

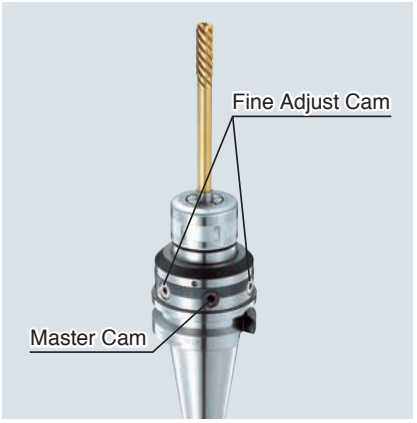


### Multi-Cam Style

The minute run-out after adjusting by a master cam can be adjusted by fine adjust cams at the same position.
**e.g. BT40-SZF16-90-C3** (3 Cams)
The multi-cam style can not be made for all zero fit holders.

# G Multi-class Wear Phase Labelling Points

**Table G1:** Manually picked transition points between wear phases of test 6 – 22.

| Wear Test No. | Transition Points | | No. of Grinding Passes Completed |
|---|---|---|---|
| | Phase I to II | Phase II to III | |
| 6 | 6 | 100 | 125 |
| 7 | 6 | 131 | 141 |
| 8 | 6 | 123 | 141 |
| 9 | 6 | 122 | 139 |
| 10 | 6 | 119 | 135 |
| 11 | 4 | 115 | 140 |
| 12 | 0 | 100 | 107 |
| 13 | 2 | 89 | 101 |
| 14 | 6 | 78 | 87 |
| 15 | 2 | 148 | 158 |
| 16 | 3 | 57 | 59 |
| 17 | 5 | 102 | 110 |
| 18 | 2 | 55 | 71 |
| 19 | 5 | 55 | 68 |
| 20 | 1 | 60 | 78 |
| 21 | 2 | 50 | 67 |
| 22 | 1 | 59 | 77 |